UNIVERSITÀ DEGLI STUDI DI PADOVA

Dipartimento di Ingegneria Meccanica, Settore Materiali

SCUOLA DI DOTTORATO DI RICERCA IN SCIENZA ED INGEGNERIA DEI MATERIALI

XX CICLO

MESOPOROUS FILMS OBTAINED BY SUPRAMOLECULAR SELF-ASSEMBLY AND THEIR CHARACTERISATION BY ADVANCED TECHNIQUES

Direttore della Scuola: Ch.mo Prof. Gaetano Granozzi

Supervisore: Ch.mo Prof. Massimo Guglielmi

Co-supervisore: Ch.mo Prof. Plinio Innocenzi

Dottorando: Stefano Costacurta

Gennaio 2008

Abstract

Mesoporous films are characterised by the presence of ordered porosity in the 2 to 50 nm range. These systems are extremely interesting from a technological viewpoint due to the very high specific surface area (on the order of 1000 m$^2 \cdot$g^{-1}) and the possibility to tune important parameters such as chemical composition, pore size and shape, pore accessibility. This doctorate work was aimed at the study on mesoporous thin films, a goal that has been tackled following two directions. The first goal was to promote a basic study on the synthetic and processing parameters through which mesoporous films are obtained: for example, using different precursors in order to vary the chemical composition of the films and modify physical parameters such as pore size and shape. The second direction followed in this work was to pursue an explorative study regarding applications of mesoporous coatings, for example for hierarchical multiscale porosity materials and in patterning of mesoporous thin films. Whilst dealing with these subjects, advanced characterisation techniques using synchrotron radiation were developed for the basic study of mesoporous films.

Riassunto

I film mesoporosi sono caratterizzati dalla presenza di pori ordinati di dimensioni comprese tra 2 e 50 nm. Questi sistemi sono estremamente interessanti da un punto di vista tecnologico poiché possiedono un'elevata area superficiale specifica (dell'ordine di 1000 m$^2 \cdot$g^{-1}) e vi è la possibilità di controllare importanti parametri come la composizione chimica, la forma, la dimensione e l'accessibilità dei pori. Questo lavoro di dottorato è stato finalizzato allo studio sui film mesoporosi, un compito che può essere diviso in due parti. Il primo obiettivo è costituito da uno studio di base sui parametri di sintesi attraverso i quali si ottengono film mesoporosi: ad esempio, ciò include l'impiego di diversi precursori per variare la composizione chimica dei film e per modificare parametri fisici come ad esempio la forma e la dimensione dei pori. La seconda direzione seguita in questo lavoro riguarda lo studio esplorativo di applicazioni di ricoprimenti mesoporosi, ad esempio in materiali a porosità gerarchica multiscala e nel patterning di film mesoporosi. Queste tematiche sono state affrontate anche attraverso lo sviluppo di tecniche avanzate di caratterizzazione utilizzando radiazione di sincrotrone per lo studio di base di film mesoporosi.

Preface

Writing this thesis has been both a challenge and a pleasure. The *challenge* appeared early in the draft of the introductory chapter, when I had to do a thorough literature search drawing on publications, books and the internet, retrieving old documents and finding new ones. Writing the experimental part represented another challenge in that I had to gather all the experimental data collected in three years, which was mostly spread about in the hard drive of my laptop—and in the old laptop, and in that CD forgotten under a pile of papers... Even though much of that stuff had already been published, many concepts needed thorough revision. I had to refresh my ideas and make them more accurate, adding detail to come up with a comprehensive scientific dissertation, a text showing also some sort of "soul" in order to catch the reader's interest and keep it throughout the notions and the experiments presented. This process was most instructive—and of course, a valuable exercise in English language!

The *pleasure* of writing this thesis has come in small sips, originating from the pattern that steadily unravels after the continuous work of organising thoughts and data in a coherent framework, eventually giving meaning to three years of doctorate. I compare this pleasure of writing, to the emotions arising in the author that's writing a novel, studying the characters, providing them with the right words and actions, unveiling the plot little by little with careful timing. And still, scientific writing and fiction writing couldn't be more different both in style and purpose!

The experimental part of this thesis reflects my "learning curve" as a scientific researcher. The goal of this work was to gain a better understanding of mesoporous films in terms of physicochemical properties and processing parameters: this is the starting point of a project with the final aim of developing functional materials based on mesoporous systems. The strategy appears often to be that of a "solution looking for a problem" rather than of a "problem looking for a solution". In other words, the method was, more often than not, to *explore* possibilities in a creative and sometimes serendipic fashion. In fact, these two approaches are not mutually exclusive, and it is often the case that a new unexpected property or idea for an application emerges from a study that is being conducted with a different goal. In writing this thesis I have tried to reflect both aspects, devising a logical breakdown of the experimental work into chapters and sections, even if this does not necessarily match the chronology of my research.

This thesis is divided into five chapters. Chapter 1 introduces the topic of mesostructured materials, with particular attention to films. This part took shape little by little, in a "successive approximations" fashion: at first it was based on the notes that I had jotted down at different times in these three years; these were then expanded and rearranged according to literature search, laboratory feedback and discussion with fellow researchers. Chapter 2 deals with the characterisation

techniques used in the experimental part. The two most used techniques, small-angle X-ray scattering and Fourier-transform infrared spectroscopy, deserved description in full detail. Chapter 3 is the first of the three experimental chapters: it revolves around mesoporous silica and hybrid organosilica films. Chapter 4 shows a few prospected applications of these materials, such as hierarchical porosity and a microfabrication technique for patterning mesoporous silica films utilising synchrotron radiation. Chapter 5 describes an interesting study on the basic principles of self-assembly, as well as a novel experimental technique for the simultaneous structural and chemical study of mesostructured films. The appendices contain further information which would have otherwise burdened the text.

Having said that, I believe that from the reader's viewpoint this thesis should be, first of all, *useful*. So, this is my hope: that this thesis will be of some interest to the reader—be it as a simple instructive reading or as a help specific to the research work on mesoporous materials—as it was useful for me to write it. I'll let you judge, now read on...

November 2007

Contents

List of Symbols and Abbreviations

ΔG Gibbs free energy variation, page 19

χ Flory-Huggins interaction parameter, page 31

cmc critical micelle concentration, page 9

f copolymer architecture, page 33

g surfactant packing factor, $g = v/l_c a_0$, page 23

k_i kinetic constant of process i, page 20

ABC   amphiphilic block copolymer, page 30

ATR   attenuated total reflection, page 136

BC   block copolymer, page 29

BET   Brunauer-Emmett-Teller, page 86

CTAB   cetyltrimethylammonium bromide, $C_{16}H_{33}(CH_3)_3N^+Br^-$, page 16

DWBA   distorted wave Born approximation, page 98

EISA   evaporation-induced self-assembly, page 42

FTIR   Fourier-transform infrared spectroscopy, page 82

FWHM   full width at half maximum, page 116

GISAXS   grazing incidence small-angle X-ray scattering, page 74

GLYMO   glycidoxypropyltrimethoxysilane, page 36

HI   hybrid interface, page 19

MCM   Mobil composition of matter, page 16

MCT   mercury-cadmium-telluride (infrared detector), page 117

MW   molecular weight, page 30

NBB   nano-building block, page 6

NMR   nuclear magnetic resonance, page 17

PEO   polyethylene oxide, page 34

PI   polyisoprene, page 36

PMMA   poly-methyl-methacrylate, page 8

PPO   polypropylene oxide, page 34

PS   polystyrene, page 27

SA   self-assembly, page 6

SAXS   small-angle X-ray scattering, page 66

STEM   scanning transmission electron microscopy, page 82

TEM   transmission electron microscopy, page 78

TEOS   tetraethoxysilane, $Si(OCH_2CH_3)_4$, page 11

TLCT   true liquid crystal templating, page 28

TMOS   tetramethoxysilane, $Si(OCH_3)_4$, page 12

XRD   X-ray diffraction, page 66

Chapter 1

An overview on mesoporous materials

Abstract

The importance of porous materials is testified to by their widespread use both in industrial and in household products. Well-known applications include catalysis, filtration, extraction, cleaning and sorption. In the past years, one of the major limitations to overcome was the size and accessibility of pores, which were restrained to the sub-nanometre scale in molecular sieves such as natural and synthetic zeolites: this limited the application of these porous systems to small molecules. The discovery of mesoporous silica and aluminosilicates with ordered pore arrangement and tunable pore size ranging from 1 to tens of nanometres provided a solution and constituted a starting point for new porous materials for traditional (e.g. catalytic and separation) and advanced (e.g. sensing, electronics) applications. The synthesis of mesoporous materials in the form of homogeneous films was a very important breakthrough because it allowed the development of materials for advanced applications, e.g. in optics, sensing and microelectronics.

Mesoporous films are obtained by templated self-assembly, which is a soft chemistry synthetic approach involving organic and inorganic colloidal chemistry. This process involves self-assembly of surfactants into ordered micellar aggregates (mesostructure) and inorganic polycondensation reactions triggered by solvent evaporation, in a technique called evaporation-induced self-assembly (EISA). Different compositions of the inorganic framework can be obtained by this method, most notably silica, transition metal oxides, mixed oxides, phosphates.

In this chapter we report on the basic concepts regarding the synthesis of mesoporous materials, with particular attention to films. The models of mesostructure formation are illustrated by selected models and examples taken from the literature, discussing concepts regarding sol-gel and surfactant chemistry and physics. Particular attention is given to silica mesoporous films templated by amphiphilic block copolymers, due to their major importance in this doctorate work.

1.1 Nanoscience: an introduction

1.1.1 Nanostructured materials

Nanotechnology can be thought as a new approach to scientific research spanning and joining many branches of science. It consists essentially in the design, fabrication and application of structures with feature size defined on the nanometre scale (roughly 1 to 100 nm), be it individual particle size or interparticle distance. More precisely, the term "nanotechnology" implies two definitions: "nanoscience" describes the study and the comprehension of phenomena and physicochemical properties of matter at the nanoscale, whereas the term "nanotechnology" indicates the fabrication, application and commercialisation of devices based on nano-sized matter. Both terms encompass many different research areas, characterised by a marked interdisciplinarity (e.g. nanobiotechnology, nanoelectronics, nanomaterials, etc.). In the scope of this thesis, when using the generic term of nanotechnology or nanoscience we will refer mainly to the concept of nanoscience applied to materials science.

In materials science and engineering, nanotechnology represents a new approach to research, in that it can offer concepts, tools and models for the preparation of *nanomaterials* with highly innovative properties. In other words, «the nanoworld is a weird borderland between the realm of individual atoms and molecules (where quantum mechanics rules) and the macroworld (where the bulk properties of materials emerge from the collective behavior of trillions of atoms [...]). At the bottom end, in the region of one nanometer, nanoland bumps up against the basic building blocks of matter. As such, it defines the smallest natural structures and sets a hard limit to shrinkage: you just can't build things any smaller».[1] One could ask the simple question: "why should we be so interested in nanoscience?", or "why nano?".[2] The answer lies in the fact that when at least one characteristic length of a material is in the nanometre range, chemical and physical properties can be profoundly different than at the macroscopic scale. This gives rise to an ensemble of new functional properties upon which devices can be built that have a potential to contribute to a high level of scientific and technological development, and to dramatically improve the quality of life. Therefore, the so-called *nanostructured materials* constitute a bridge between the atomic and the macroscopic realms, a very promising and largely unexplored research area. The reason for this interesting—and sometimes curious—behaviour at the nanometre scale is twofold: increase in surface area and quantum size effects.

Surface area As the size of a material decreases, the ratio between the number of atoms that lie on the surface (a_s) and the total number of atoms (a_{tot}) increases. Let us consider a cube of size $l = 1$ cm that has a volume density of $\sim 10^{23}$ atoms·cm^{-3} and a surface density of $\sim 10^{15}$ atoms·cm^{-2}: the ratio $f = a_s/a_{tot}$ is $f \approx 6 \cdot 10^{-8}$. For smaller l values, f is correspondingly larger, e.g. if $l = 1$ nm, we obtain $f \approx 0.6$, that is to say 60% of the total atoms lies on the surface. Because the energy at the surface of a material is different than in the bulk, the energy of a material on the nanoscopic scale is different than at the macroscopic scale. This can be a very important property for applications that involve chemical reactions at interfaces, such as in catalysis: a nanomaterial, in fact, can account for catalytic properties which may be negligible in its macroscopic form. This is why nanopowders are

extremely reactive due to their high surface area and must be handled with care as there is the risk of self-ignition and even explosion.

Quantum size effects In this intermediate size range between matter at the molecular and at the macroscopic scale, individual energy states of molecules and continuous energy bands of solids become discrete and their energy separations display a dependence on the spatial dimension of the material, which in principle can be calculated by solving the Schrödinger equation for an electron in a box that has a size on the order of the Bohr radius of the electron. This causes particular electronic and optical properties to emerge as a function of size, e.g. plasmonic resonance frequency in metallic nanoparticles and tunable energy gap in semiconductor nanoparticles (quantum dots). These properties are exploited for advanced applications, e.g. in electronics, linear and non-linear optics.

Surface area and quantum size effects can explain a number of effects caused or enhanced by small size, such as magnetic, mechanical, tribological properties. The critical length below which matter shows interesting behaviour will obviously depend on the material itself and on the particular property we are considering, therefore one or more different critical lengths can be defined from case to case. Some systems may also have more than one feature size: in the case of multifunctional materials whose application requires a number n of properties, there may exist n critical dimensions related to these properties, that is to say the material is composed by elements with dimensions on n length scales. Sometimes these are arranged *hierarchically*, meaning that features of different length scales are arranged according to a relationship of subordination.

In its broadest meaning, nanoscience applied to materials has been exploited for decades, if not even for centuries. For example, the products of chemical industry may have nanometric size and be defined at the molecular level: this is the case of polymers, which are essentially nanometric structures obtained by successive additions of isolated monomers. Ancient glass-makers were *ante litteram* nanotechnologists who exploited the quantum size effects of colloidal metal nanoparticles (gold, silver) to obtain the colour red in glass, which was impossible to obtain by any other known chemical compound. Considering this, a large part of less recent science and technology could be considered as a part of nanoscience and nanotechnology, and these terms might appear deprived of their meanings. In fact, the key element that allows us to speak of "nano" as a new scientific/technological approach is twofold: (1) the possibility to *visualise and manipulate* matter at the nanoscale, even atom-by-atom, and (2) the understanding of the *relationship between structure and property* at the nanoscale, which was made possible by the invention of suitable analytical instrumentation.

Two crucial inventions in the 1980s enabled researchers to investigate and manipulate matter at the atomic level: the scanning tunnelling microscope (STM) in 1982 and the atomic force microscope (AFM) in 1986. In Eigler and Schweizer's well-known experiment, single Xe atoms were literally lifted and moved around on a Ni surface using an STM and were positioned to form the IBM logo.[3] Although this technique was extremely limited (the experiment was performed at 4 K in ultrahigh vacuum on a conducting surface), it opened the way to new approaches to manipulation of matter at the nanoscale. The invention of instruments which were able to image and fabricate nanostructures defined at the atomic level led to

a virtuous circle: new instrumentation permitted a more thorough comprehension of phenomena occurring at the nanoscale, which constituted a motivation for a better size and chemical control, which in turn was a stimulus to tweak the existing analytical instruments and invent new ones. As research progressed in the course of years, the field of nanoscience applied to materials thrived, catalysing the interest of more and more researchers trained in diverse scientific branches. Materials science could then develop as a discipline with a marked interdisciplinar character, and synergies could be established between disciplines traditionally considered separate, such as electronics, quantum mechanics, biochemistry.

From a historical viewpoint, the beginning of nanotechnology is generally considered to be the famous speech given by Richard P. Feynman in the annual meeting of the American Physical Society at CalTech in 1959, "There's plenty of room at the bottom".[4] This started a series of debates trying to settle the innovation (and the risks) that nanotechnology could bring about in the future. Some ideas appear way too futuristic, like the construction of a "space elevator" in which the cables are made of carbon nanotubes.[5,6] Other applications are much more feasible in the mid- or short term, e.g. a DNA sequencer composed of luminescent quantum dots that are functionalised with specific oligonucleotide, binding to a particular sequence of bases.[7] Important applications include, for example, battery-scale energy storage, nanostructured fuel cells, textiles (e.g. nanostructured fibers and fabrics), defense and security (e.g. surveillance, explosive detection and communications), medical research (e.g. scaled down gene and protein array-based diagnostics).[8]

1.1.2 Synthesis: bottom-up and top-down strategies

Though nanotechnology acquired strong elements of interdisciplinarity in the course of years, there are at least two elements that make it a homogeneous ensemble: (1) research is oriented towards the study of innovative properties which are determined by small feature size, (2) all synthetic approaches fall into two categories: top-down and bottom-up. *Top-down* techniques start from a bulk material and reduce its dimensions—by chemical etching, mechanical grinding, lithography—until a nanomaterial is obtained. Typical examples include the fabrication of integrated circuits by lithography, by which it is now possible to obtain structures smaller than 100 nm, and the production of nanopowders by ball milling. *Bottom-up* syntheses involve the assembly of small (generally atomic or molecular) units into the desired structure. An example is the wet-chemical synthesis of CdS quantum dots from a solution containing cadmium and sulphur ions, together with a suitable capping agent to control growth and prevent aggregation of the nanoparticles.[9]

Since both approaches have upsides and downsides, it is not possible to determine which is the best synthetic strategy regardless of the final structure that has to be obtained. However, we can say that the possibility of building structures defined at the atomic or molecular level is a prerogative of bottom-up syntheses, whereas complex structures such as micro- and nanoscopic interconnects and circuits can be obtained by top-down approaches. This consideration lets us grasp the potential of hybrid bottom-up and top-down syntheses (Figure 1.1).[10] For example, a photonic crystal obtained by the self-assembly of latex spheres can be grown selectively on
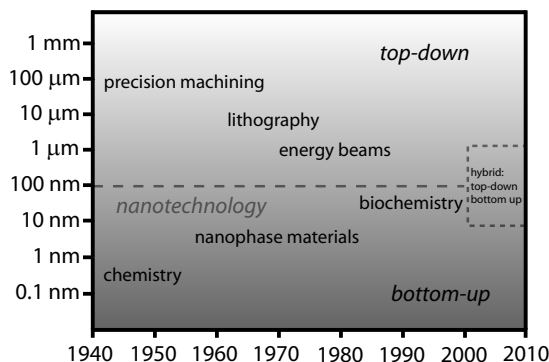
Figure 1.1. *Convergence of top down and bottom up synthesis techniques as a function of time.*

defined regions of a pre-patterned substrate, e.g. by microcontact printing, in order to fabricate an all-optical integrated circuit.[11]

In general, it is worth mentioning that every synthetic strategy should exert a fine control on chemical composition, spatial dimensions, nature of the interfaces, morphology, orientation, stability (e.g. thermal, temporal, chemical, dimensional, etc.). In addition, it is important to note that the industrial production of nanostructures requires low cost (in terms of chemical precursors, synthetic procedure and time) and full reproducibility of the products in large quantities; this is true both in the case the final product is a nanodevice, and in the case the product is a starting material for another synthesis.

1.2   Self-assembly

1.2.1   What is self-assembly?

As described previously, the strategies for the synthesis of nanomaterials using bottom-up approaches involve the assembly of small units, also called *nano-building blocks* (NBBs) into a nanostructure, where the NBBs are arranged according to a well-defined shape and architecture. Different bottom-up techniques that enable production of nanostructures with different degrees of quality, speed and cost have been devised. Here we will not make a list of all these techniques, since this would be outside the scope of this thesis. Instead, we will outline the synthetic approach of a bottom-up technique of outstanding interest, *self-assembly* (SA), upon which the syntheses of mesoporous materials are based. The distinctive aspect of SA is that the driving force that causes the NBBs to assemble into the final structure is strictly local, and there is no intervention of external forces. Starting from suitable NBBs with tailored size and shape, composition and surface structure, charge and functionality, one can obtain various nanostructures by a SA process which may be spontaneous, directed by templates or guided by chemically or lithographically defined surface patterns. These nanostructures are shaped into architectures that perform a function. When structure-directing species (often molecular and organic) are used that serve to fill space, balance charge and direct the formation of a specific structure in addition to the self-assembling NBBs, the process is referred to as *templated self-assembly* or *co-assembly*.

Indeed, it is easy to come across the concept of SA in science. SA is a term used to describe processes in which a disordered system of pre-existing components forms an organised structure or pattern as a consequence of *specific*, *local* interactions among the components themselves, *without external direction*.[12] Throughout this thesis we will use a connotation of SA that is often found in chemistry.

1.2.2 A definition of self-assembly

Self-assembly in chemistry can be defined as *the spontaneous and reversible organisation of molecular units into ordered structures by non-covalent interactions*.[13] The first property of a self-assembled system that this definition points out is the spontaneity of the self-assembly process: the interactions leading to the formation of the self-assembled system act on a strictly local scale—in other words, *the nanostructure builds itself*. At this point, one may argue that any chemical reaction driving atoms and molecules to assemble into larger structures, such as precipitation, could fall into the category of SA. However, there are at least three aspects that make SA a distinct concept. First, the self-assembled structure must have a higher order than the isolated components, be it a shape or a particular task that the self-assembled entity may perform. This is generally not true in chemical reactions, where an ordered state may proceed towards a disordered state depending on the thermodynamic parameters. The second important aspect of SA is the key role of weak interactions (e.g. Van der Waals, capillary, π-π, hydrogen bonds) with respect to more "traditional" covalent, ionic or metallic bonds. Although typically less energetic of a factor of 10, these weak interactions play an important role in materials synthesis. It can be instructive to note how weak interactions hold a prominent place in materials, but especially in biological systems, although they are often considered marginally with respect to "strong" (i.e. covalent, etc.) interactions. For example, they determine the physical properties of liquids, the solubility of solids, the organisation of molecules in biological membranes. The third distinctive aspect of SA is that the building blocks are not only atoms and molecules, but span a wide range of nano- and mesoscopic structures, with different chemical compositions, shapes and functionalities. These NBBs can in turn be synthesised through conventional chemical routes or by other SA strategies. Important examples of SA in materials science include the formation of molecular crystals, colloids, lipid bilayers, phase-separated polymers, and self-assembled monolayers.[14,15] The folding of polypeptide chains into proteins and the folding of nucleic acids into their functional forms are examples of self-assembled biological structures.[16]

Therefore, we can say that SA extends the scope of chemistry aiming at synthesising products with order and functionality properties, extending chemical bonds to weak interactions and encompassing the self-assembly of NBBs on all length scales.[2] In covalent synthesis and polymerisation, the scientist links atoms together in any desired conformation, which does not necessarily have to be the energetically most favoured position; self-assembling molecules, on the other hand, adopt a structure at the thermodynamic minimum, finding the best combination of interactions between subunits but not forming covalent bonds between them. In self-assembling structures, the scientist must predict this minimum, not merely place the atoms in the desired location.

Another characteristic that is common to nearly all self-assembled systems is

their *thermodynamic stability*: in order for SA to take place without the intervention of external forces, the process must lead to a lower Gibbs free energy, thus self-assembled structures are thermodynamically more stable than the single, unassembled components. A direct consequence is the general tendency of self-assembled structures to be relatively free of defects. An example is the formation of two-dimensional superlattices composed of an orderly arrangement of micron-sized poly-methyl-methacrylate (PMMA) spheres, starting from a solution containing the microspheres, in which the solvent is allowed to evaporate slowly in suitable conditions. In this case the driving force is capillary interaction, which originates from the deformation of the surface of a liquid caused by the presence of floating or submerged particles.[17]

These two properties—weak interactions and thermodynamic stability—can be recalled in order to rationalise another property which is often found in self-assembled systems: the *sensitivity to perturbations* exerted by the external environment: small fluctuations that alter the thermodynamic variables might lead to marked changes in the structure and even compromise it, either during or after SA. The weak nature of interactions accounts for the flexibility of the architecture and allows for rearrangements of the structure in the direction determined by thermodynamics. If fluctuations bring the thermodynamic variables back to the starting condition, the structure is likely to go back to its initial configuration. This leads us to identify one more property of SA, which is generally not observed in materials synthesised by other techniques: *reversibility*. For example, the most interesting example of reversibility in self-assembled mesostructured films is the so-called *tunable steady state*, a particular state of the as-deposited film that permits structural rearrangements that may increase or decrease the internal degree of order, and even change mesostructure symmetry (see page 49).

From what we have written so far, it should be evident that SA is a process which is easily influenced by external parameters: if this can make synthesis more problematic due to the many free parameters requiring control, on the other hand it has the exciting advantage that a large variety of shapes and functions on many length scales can be obtained.[18]

Generally speaking, the fundamental condition in order to have NBBs to self-assemble into an ordered structure is the simultaneous presence of long-range repulsive and short-range attractive forces.[19] Figure 1.2 exemplifies SA occurring
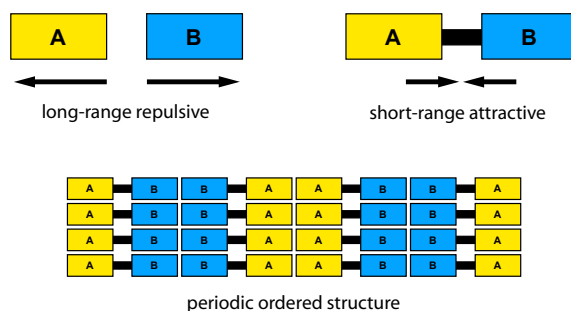
Figure 1.2. *Scheme of long-range repulsive interactions and short-range attractive interactions between two chemically different units A and B leading to a self-assembled periodic ordered structure.*

Table 1.1. *Examples of long-range repulsive and short-range attractive competing forces giving self-assembled systems (adapted from Förster and Plantenberg [19]).*

Long range repulsion	Short range attraction	Example
Hydrophobic-hydrophilic interactions	Covalent binding	Micelles, lyotropic liquid crystals
Coulomb repulsion	Electroneutrality	Ionic crystals
Excluded volume	Minimum space required	Thermotropic liquid crystals
Electric dipole field	Electric dipole interaction	Ferroelectric domains
Magnetic field	Magnetic dipole interaction	Magnetic domains

from building blocks constituted by two different units (A and B) which are covalently linked (short-range attraction) and repel each other by long-range interactions (e.g. because A is hydrophobic and B is hydrophilic). Since the energy of the system will unfavour configurations where A is close to B, and still no macrophase separation is possible due to the A–B covalent bonds, the system will adopt a configuration where the contact area between A and B is minimised. This results in a periodic ordered structure (in Figure 1.2 this is exemplified by a lamellar structure). In Table 1.1 we give a few examples of repulsive-attractive competing forces that can give rise to SA phenomena.

By choosing precursors with suitable physicochemical properties, it is possible to exert a fine control on the formation processes in order to obtain complex nanoarchitectures. Clearly, the most important tool when it comes to designing a synthesis strategy for a nanomaterial, is the knowledge of the chemistry of the building units. This is why in this chapter we will deal with inorganic sol-gel chemistry and macromolecular colloid chemistry and physics.

1.3 Templated self-assembly

Among the diversity of self-assembly processes, we concentrate on the so-called *self-assembly of templated inorganic materials*. As mentioned previously (page 6), a distinctive aspect of templated SA is that the resulting (typically inorganic) structure is templated by another self-assembled structure (typically organic and supramolecular) that serves to fill space or direct the formation of a specific structure as a scaffold, or balance charge. In the following of this thesis, when speaking of SA we will always refer to templated SA.

In the case of mesoporous materials, the self-assembly of molecular inorganic NBBs is directed by the presence of a *structure-directing agent*, which serves as a scaffold for the polycondensation of the inorganic NBBs (see Figure 1.3). The structure-directing agents are essentially supramolecular structures formed by the aggregation of *amphiphilic* molecules such as surfactants, which are molecules containing both hydrophilic and hydrophobic groups. Surfactants exhibit a particular behaviour in solution: above a certain concentration (*critical micellar concentration*, *cmc*) the surfactant molecules undergo a microphase segregation process in order to minimise the free Gibbs energy, forming supramolecular aggregates (*mi-*

surfactant   inorganic   NBB   mesostructure
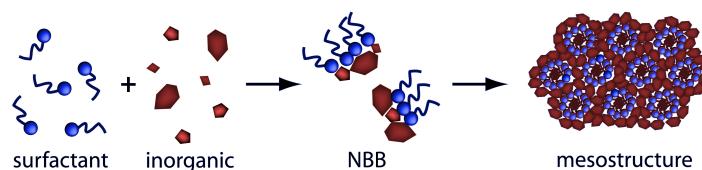
Figure 1.3. *Scheme of templated self-assembly. Surfactant molecules interact with inorganic species and form hybrid organic-inorganic nano-building blocks, which in turn self-assemble into an ordered mesostructure.*

celles), whose shape is determined by the nature and the architecture of the organic building units, as well as by other parameters such as nature of the solvent, pH and presence of ions. Inorganic polycondensation reactions take place around the templating supramolecular units (*mesophase*) and yield a hybrid network, constituted by a gel hydrated by solvent molecules.* A thermal treatment (*calcination*) is then performed to remove the templating agent and stiffen the inorganic framework by promoting further inorganic condensation obtaining a *mesoporous* material. Alternatively, the organic mesophase can be removed by solvent extraction.

The synthesis of mesoporous materials requires knowledge of the chemistry and the physics of the inorganic and organic component units. In many cases inorganic chemistry is that of sol-gel systems, since inorganic precursors are often alkoxides, organoalkoxides and inorganic salts that undergo hydrolysis and condensation reactions. On the other hand, supramolecular self-assembly of organic species borrows many concepts from colloidal and polymer chemistry and physics. Therefore, we will now deal briefly with the general concepts of self-assembly and sol-gel chemistry.

1.3.1 Supramolecular structures

In the synthesis of mesoporous materials, one exploits the self-assembly of amphiphilic molecules or macromolecules, which are constituted by a hydrophobic region (typically an aliphatic chain) and a hydrophilic region (typically an ion or a polar organic group). The most representative category goes under the name of *surfactants*, a term referring to the property of lowering the interface energy between a hydrophobic and a hydrophilic phase (*surf*ace *act*ive age*nt*). Their most known application in household products is as detergents: when surfactants come into contact with "dirt" organic particles, these are enclosed into a structure formed by the hydrophobic portions of the surfactant, while the hydrophilic portions are in contact with the hydrophilic medium (water). Therefore, surfactants can disperse organic particles in polar media, which accounts for their cleaning properties.

In general, amphiphilic molecules and macromolecules show a tendency to self-assemble forming micelles when their concentration in a polar solvent is higher than a critical micellar concentration ($c > cmc$). Micelles in a polar solvent are constituted by a finite number of amphiphilic units in which the hydrophobic regions form the core of the micelle, whereas the hydrophilic ends point towards the exterior and are swelled by solvent molecules (in an apolar medium it is the

---

*This process is similar to the biological process of biomineralisation. For further information regarding the biomimetic aspects of the synthesis of mesoporous materials, see Appendix B.

other way round: hydrophilic cores are surrounded by a hydrophobic corona).
An appealing vivid description pictures surfactant self-assembly as "chemical
schizophrenia": «In water, the hydrophilic headgroups are solvated and extrovert
in character, whereas the hydrophobic chains become chemical introverts intent
on shielding themselves from the uncomfortable polar interactions. A free energy
compromise is attained by self-assembly, in which the hydrophobic residues be-
come internalised within a supramolecular aggregate such as a micelle».[20] As we
will see, micelle shape is determined by the interactions between the amphiphilic
units and the solvent molecules. For higher concentrations ($c \gg cmc$) micelles
can form lyotropic phases, where micelles form periodic ordered patterns.[21] Some
examples of micellar aggregates are reported in Figure 1.4. We will discuss the
formation of supramolecular structures in more detail in Sections 1.5 and 1.6.

1.3.2 Inorganic polycondensation and sol-gel processes

Sol-gel processing is based on the controlled polymerisation of inorganic molec-
ular precursors in mild temperature conditions, organic solvents, and controlled
amounts of water. This technique is crucial in the development of synthesis routes
towards the inorganic NBBs.

Oxide formation by the sol-gel process implies connecting the metal centres
with oxo or hydroxo bridges, generating metal-oxo or metal-hydroxo polymers in
solution. A colloidal suspension (*sol*) evolves through polycondensation reactions
towards the formation of a continuous solid with the desired shape (e.g. monolith,
film, powder) in which a liquid phase is intercalated (*gel*). Upon drying, a solid
is formed, next thermal treatment may then be performed in order to favour fur-
ther polycondensation reactions and enhance mechanical properties. The sol-gel
approach is particularly interesting in that it allows for the fine control on the final
chemical composition, as even small quantities of dopants, such as organic dyes
and rare earth metals, can be introduced in the sol ending up in the final product
finely dispersed.

The precursor is either an alkoxide, i.e. a compound where a metal (e.g. Ti, B,
Al, Ga, Zr, Y, Ca) or metalloid (Si, Ge) is chemically bonded to one or more or-
ganic groups through an oxygen atom, or an inorganic salt, generally a transition
metal chloride. Silicon alkoxides, such as tetraethoxysilane (TEOS) and tetram-
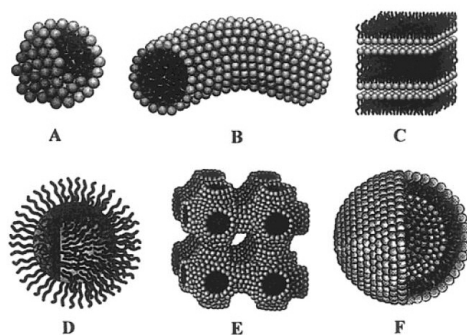
Figure 1.4. *Examples of micellar structures: (A) sphere, (B) cylinder, (C) planar bilayer, (D) reverse micelle, (E) bicontinuous phase, (F) liposomes. Reproduced from Soler-Illia et al.*[22]

ethoxysilane (TMOS), are widely used in order to produce silicon oxide (*silica*). TEOS is constituted by a Si atom bonded to 4 ethoxy groups (OCH_2CH_3) which are hydrolysed in the presence of water, an alcohol and a catalyst such as HCl to give $Si(OCH_2CH_3)_x(OH)_{4-x}$ ($0 \leq x \leq 3$). These, in turn, condense with other hydrolysed species and with unhydrolysed TEOS molecules, forming a larger macromolecule and yielding smaller molecules such as water or ethanol. Therefore, Si atoms end up linked by bridging oxygens or hydroxides in a SiO_2 network. Since this condensation process results in the assembly of a macromolecule starting from monomer units, freeing smaller molecules such as water and ethanol for each new unit linked to the forming structure, it is similar to organic living polymerisation, which somehow justifies the term "inorganic polymerisation" that is often used as a synonym for polycondensation. The resulting material framework can be purely inorganic (i.e. metal-oxo polymers) or hybrid organic-inorganic as in the case of hybrid precursors (i.e. organo-substituted alkoxides bearing non-hydrolysable organic groups or dyes dissolved in the solution).

The effect of catalysis has a dramatic effect on the microstructure of the solid that is obtained by hydrolysis and condensation reactions of the precursor sol.[23,24] Let us consider the case of silica, as it is the most relevant in the scope of this thesis. In acidic conditions an alkoxy group is protonated in a rapid first step; electron density is withdrawn from the Si atom, making it more electrophilic and thus more susceptible to attack from water: this results in the formation of a positively-charged five-coordinate transition state which decays by displacement of an alcohol and inversion of the silicon tetrahedron (Figure 1.5). Conversely, in basic conditions an OH^- group directly attacks a Si atom forming a five-coordination, negatively-charged transition state. Condensation reactions can involve elimination either of a water or an alcohol molecule (Figure 1.6). Thus, condensation can lead to an oxo bridge (*oxolation*), and water or alcohol is eliminated, whereas in the case of *olation* an addition reaction takes place, and a hydroxo bridge is formed.

The rate of hydrolysis and condensation of the 4 alkoxy groups bonded to a Si atom can be understood in terms of electronic effects, bearing in mind that alkoxy groups (OR) are electron-donating groups, whereas hydroxy groups (OH) are electron-withdrawing. Therefore, a substituting OH withdraws electron from the central Si atom and the positively-charged transition state in acid-catalysed hydrolysis becomes less stabilised as more alkoxy groups are substituted by hy-
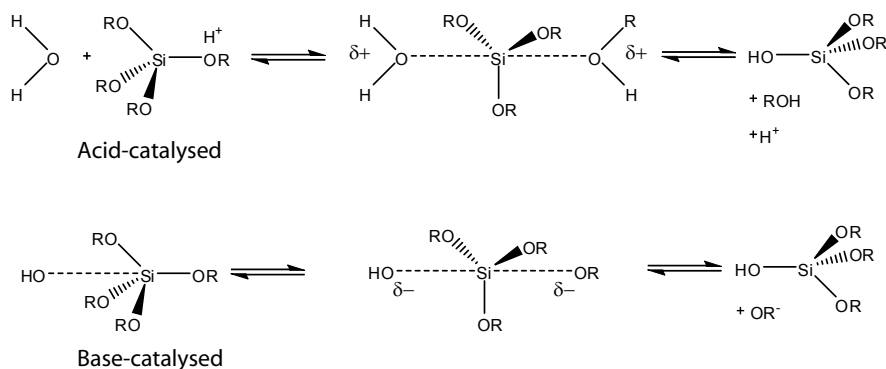
Figure 1.5. *Scheme of acid- and base-catalysed hydrolysis from silicon alkoxide.*

droxyl groups and the reaction rate decreases. Conversely, in base-catalysed hydrolysis the negatively-charged transition state becomes more stabilised as more alkoxy groups are substituted by hydroxyl groups, thus more highly hydrolysed silicones are more prone to attack and the reaction rate increases. This means that in acidic conditions one molecule of silicon alkoxide is one- or two-substituted by OH groups, whereas in basic conditions the silicate species will be almost fully hydrolysed. Condensation reactions proceed according to the same principle. In acidic conditions the transition state is positively charged and stabilised by electron-donating alkoxy groups, therefore less substituted $(RO)_3SiOH$ condense faster than $(RO)_2Si(OH)_2$, which condenses faster than $ROSi(OH)_3$ and $Si(OH)_4$. As a consequence, an open network forms initially, followed by further hydrolysis and cross-condensation reactions. In contrast, in base-catalysed condensation fully hydrolysed species condense and form branched clusters which eventually link to form gels with large pores between the interconnected clusters. Acid-catalysed sols are more suitable for depositing films by dip- or spin-coating, whereas base-catalysed sols are used for the synthesis of silica nano- and micro-spheres.[25]

The rate of reaction at different pH values shown in Figure 1.7 can be understood in these terms, considering that the isoelectric point of silica (i.e. where the equilibrium species have zero net charge) is $pH_{iep} = 2.2$. Below pH_{iep} the condensation rates are proportional to $[H^+]$. Between pH 2 and pH 6 condensation rates are proportional to $[OH^-]$. Above pH 7 condensed species are ionised and therefore mutually repulsive: growth occurs primarily through the addition of monomers to the more highly condensed particles rather then by particle aggregation. Due to the higher solubility of silica above pH 7, the reaction rate decreases again.

Transition metal alkoxides are very reactive due to the high electrophilicity of the metal atom that increases the rate of nucleophilic hydrolysis and condensation reactions, therefore inorganic salts are often used as the precursors. For example, titanium tetrachloride $TiCl_4$, which is widely used in the synthesis of titanium dioxide, gives $TiCl_{4-x}(EtO)_x$ species in an ethanolic solution, which in turn are hydrolysed by water.[26] Besides, a certain amount of HCl is formed upon dissolution of tetrachloride, which tends to quench fast and inhomogeneous condensation by forming complexes with the inorganic hydrolysed species. Furthermore, complexing agents such as acetyl acetone can be used in order to lower the polycondensation kinetics. Alternatively, non-hydrolytic routes can be used, especially
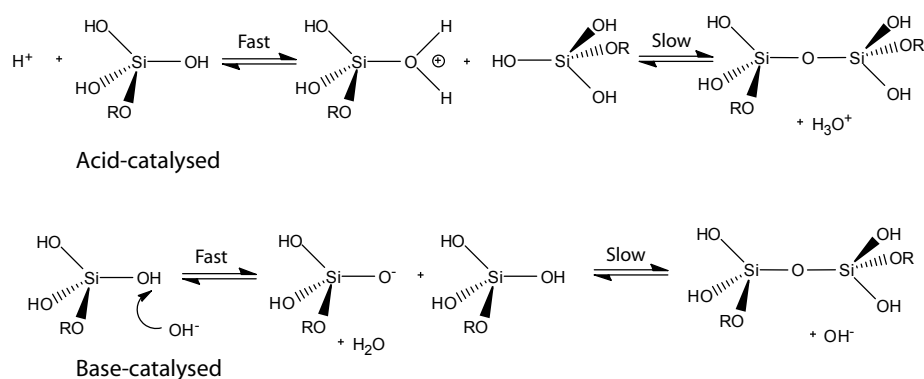
Figure 1.6. *Scheme of acid- and base-catalysed condensation from silicon alkoxide.*

for reactions which involve precursors of very different reactivity, e.g. in mixed oxides.[27]

Sol-gel methods allow creating nanometric inorganic and hybrid organic-inorganic building blocks with great variety in their nature, structure and functionality. The use of pre-formed species presents several advantages compared to alkoxide precursors, because pre-formed species are less reactive towards hydrolysis or attack of nucleophilic moieties. Furthermore, their size and composition can be carefully pre-synthesised. Thus, they can be used as model systems to understand the construction of hybrid materials, particularly at the inorganic-organic interface. For example, oligosilsesquioxanes can be used as building blocks for the preparation of nanocomposite siliceous thin films by a self-assembly approach.[28,29] Titanium oxo clusters can be obtained by hydrolysis of $Ti(OR)_4$ precursors in low water conditions, these clusters can be used to prepare mesostructured hybrid titania films.[30]

In this doctorate work we have focused mainly on mesoporous silica films, therefore we will discriminate between silica and non-silica systems. For a thorough revision on sol-gel, we address the reader to Brinker and Scherer's comprehensive text,[23] where in-depth information on reaction and formation mechanisms and applications of sol-gel derived materials can be found, as well as to other interesting books and publications in the literature.[24,31]

1.4   Porous and mesoporous materials

1.4.1   Importance of porous materials: the case of zeolites

Porous materials containing cavities in the nanometre and micrometre range (e.g. sponges, clay, zeolites) hold a significant position in industry owing to their widespread use both in industrial and in household products. Well-known applications include catalysis, filtration, extraction, cleaning and sorption. In all these cases, the synthesis of a porous material should allow for the control of the pore dimension and size distribution, which is generally required narrow and centred on a given value. Advanced applications of materials containing porosity require pores that may be either interconnected and open to the external environment, e.g. to allow for the diffusion of analytes in sensors, or isolated and inaccessible, e.g. in low dielectric constant materials in microelectronics.[32,33]
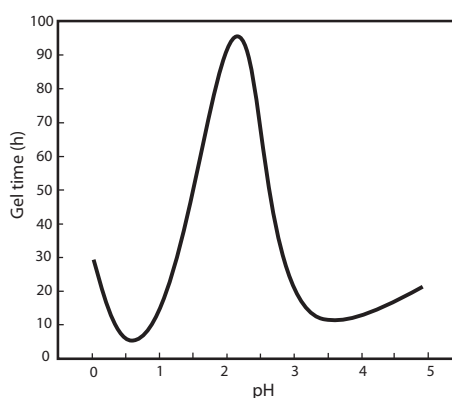
Figure 1.7. *Gel time as a function of pH for HCl-catalysed TEOS ($[H_2O]/[Si] = 4$).*

According to IUPAC classification,[34] porous solids fall into three categories according to pore size (*d*): *microporous* (*d* < 2 nm), *mesoporous* (2 nm < *d* < 50 nm) and *macroporous* (*d* > 50 nm). Microporous and mesoporous materials are generally referred to as *nanoporous* materials, which fall into the general class of nanostructured materials, since they possess features (pores) which are defined on the nanoscale. A useful and detailed review on porous materials, especially addressed to microporous and mesoporous systems, was written by Soler Illia et al.[22]

The distinction between the attributes meso*porous* and meso*structured* is not univocal. Whereas in the literature "mesoporous material" refers univocally to the presence of porosity in the 2–50 nm range, the term "mesostructured material" is less clear, referring to either "a mesoporous material with ordered disposition of pores" or "a material containing an organic mesophase in the 2–50 nm range". In the former case "mesostructured" is a special case of "mesoporous" where the pores are ordered, whereas in the latter case "mesostructured" means "containing a mesophase". In this thesis we will follow the latter case, therefore we define a "mesostructured material" as a material containing a (organic) phase in the 2–50 nm range. In this sense, the synthesis of a *mesoporous* film proceeds through the formation of a *mesostructured* film, which is then submitted to a treatment in order to remove the *mesophase*, yielding *mesoporosity*.

Zeolites were among the first porous materials with pores in the nanometre range to be synthesised, and they certainly represent the most known class of microporous materials. Zeolites are available from natural resources but there exist synthetic routes that permit obtaining zeolites with well-defined framework composition and pore size. Natural zeolites are hydrated aluminosilicates of alkali metals or alkaline earth metal ions, characterised by cavities and channels of molecular dimension that permeate the whole structure. Alkaline and alkaline earth cations are localised in the cavities and serve to maintain electroneutrality, so that the general formula for zeolites may be written as $M_{2/n}O \cdot Al_2O_3 \cdot xSiO_2 \cdot yH_2O$ (where M is a cation of valence *n* and $x \geq 2$). Albeit abundantly employed in catalysis (especially in the chemical and the oil industry), natural and synthetic zeolites have applications in other products of more common usage, such as detergents and filters for water purification. High surface area and mechanical strength make zeolites a class of materials of high technological interest and a topic of intense scientific research.

The synthetic strategy used in the industrial production of zeolites is based on a templating approach. Typically, the synthesis is carried out in hydrothermal conditions starting from a gel or a solution containing the aluminosilicate precursor together with the templating agents, such as alkaline or alkaline earth cations or organic molecules. These structure-directing agents control growth and morphology of the aluminosilicate phase. Pore size ranges from 2–3 Å to 1 nm with a narrow size distribution, and it reproduces the molecular templating units.[35]

1.4.2 A new class of materials: M41S

The motivation for research on mesoporous materials was the demand for porous materials similar to zeolites (narrow pore size distribution, thermal, chemical and mechanical properties), but with larger pores. In particular, larger pores could afford catalysis of larger molecules, thus extending applications to chemical reactions involving macromolecular reactants.
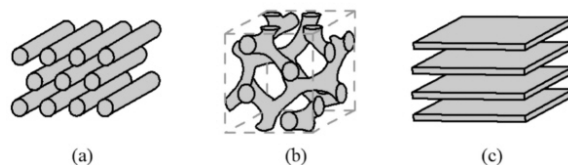
Figure 1.8. *The three structures of early M41S mesoporous materials. (a) MCM-41: 2d-hexagonal p*6mm*, (b) MCM-48: cubic bicontinuous I*a$\bar{3}$d*, (c) MCM-50 lamellar.*

The pioneering work of a Mobil Oil research group provided a first answer to the need for larger pores in 1992, when the first family of mesoporous materials, named M41S, was synthesised. The idea was to use a bundle of molecules as the porogen template, instead of the single-molecule templating approach used in zeolites. This new class of materials was based on silica or aluminosilicates, whose hydrothermal synthesis was directed by an ionic surfactant and yielded nanometric size-tunable pores.[36,37]

In a typical synthesis, an aqueous solution of an aluminosilicate or a silicon precursor (e.g. TEOS, Ludox, fumed silica, sodium silicate), a ionic surfactant (an alkyl trimethylammonium halogenide $C_nTA^+X^-$, such as cetyl-trimethylammonium bromide CTAB, $C_{16}H_{33}(CH_3)_3N^+Br^-$) and a base (e.g. NaOH) are heated to a temperature above 100°C for 24–144 hours (hydrothermal synthesis). The solid product is then washed, filtered and thermally treated at ≈500°C.

The main aspect of M41S is ordered porosity with size ranging from 18 to 100 Å. The pores are typically constituted by parallel channels, stacked with a two-dimensional hexagonal (*2d-hex*) cross section, but other structures are possible (Figure 1.8). Pore size can be tuned by selecting a surfactant with a suitable alkyl chain length. X-ray diffraction (XRD) performed on the products of syntheses carried out with surfactants having different alkyl chain lengths C_nH_{2n+1} ($n = 8, 9, 19, 12, 14, 16$) points out a direct proportion between n and the d-spacing values of the hexagonal mesostructure, which in turn are directly related to pore size. Moreover, the introduction of a swelling agent in the reaction vessel leads to a further increase in the d-spacing of the mesostructure. Different symmetries of the ordered porous mesostructure can be attained by varying the synthesis parameters, so that a total of three materials are reported, with different symmetries and pore shapes: MCM-41[†] has cylindrical pores packed in the 2d-hex stack of symmetry group *p*6mm,[‡] MCM-48 has spherical pores with cubic *I*a$\bar{3}$d symmetry ("cub"), and MCM-50 has a lamellar structure ("lam") which is mechanically unstable unless a post-synthesis treatment is performed, such as infiltration with TEOS vapours.[38] Other properties of M41S materials include thermal, mechanical and chemical stability and a surface area above 700 $m^2 \cdot g^{-1}$.

1.4.3   Formation mechanism of MCM-41

The Mobil Oil scientists proposed two mechanistic pathways in the formation of the ordered mesostructure in MCM-41, which were formulated based essentially

---

[†]From *M*obil *C*omposition of *M*atter
[‡]See Appendix A for an explanation of space group notation.

on XRD and transmission electron microscopy (TEM) data.[38] There is a striking
similarity between the ordered porous structures obtained in M41S materials and
the liquid crystal structures that the surfactant used in the synthesis (CTAB) forms
in water solution. Furthermore, there is a precise relationship between the pore size
and the alkyl chain length.

The first proposed mechanism (path 1 in Figure 1.9) is called *liquid crystal
templating* (LCT). It is based on the formation of a 2d-hex lyotropic phase and the
subsequent diffusion of the inorganic precursors towards the micelle surface due
to their high mobility in the solvent. The driving force for diffusion is the electro-
static interaction between the negative charge on the siliceous species (which are
protonated at high pH values) and the positive charge on the surfactant's quaternary
ammonium group $R(CH_3)_3N^+$. According to this mechanism the lyotropic phase
serves as a scaffold for inorganic polycondensation, which plays no other role on
the structure that is being formed but to balance electrostatic charge and to ensure
electroneutrality. The second mechanism (path 2 in Figure 1.9) involves a *coop-
erative process* where the self-assembly of the organic phase is mediated by the
inorganic phase, which therefore plays an active role in the formation and ordering
of the mesostructure.

Further studies have excluded the possibility that a type-1 mechanism could
account for mesostructure formation in MCM-41.[39] Considering a typical synthe-
sis, the concentration of CTAB in the solution turns out to be much lower than
the critical micelle concentration (*cmc*) for CTAB-water binary mixtures found in
the literature. Therefore, the formation of lyotropic structures appears to be very
unfavourable, and it is necessary to postulate some kind of interaction between the
organic and the inorganic precursors in the framework of a cooperative process, or
templated self-assembly mechanism. Consequently, the hybrid organic-inorganic
intermediates that are formed through this mechanism must be sufficiently compli-
ant in order to allow for the formation and the organisation of lyotropic ordered
phases. The fundamental role played by the inorganic precursors in this self-
assembly mechanism is underpinned by studies with ^2H and ^{29}Si NMR (nuclear
magnetic resonance), which demonstrate that CTAB forms an ordered mesophase
at these low concentrations only when siliceous anions are added.[40]

The correlation between alkyl chain length and pore size in the final product
can be readily explained by the formation of micellar supramolecular structures
composed of surfactant molecular units whose size scales with surfactant length.
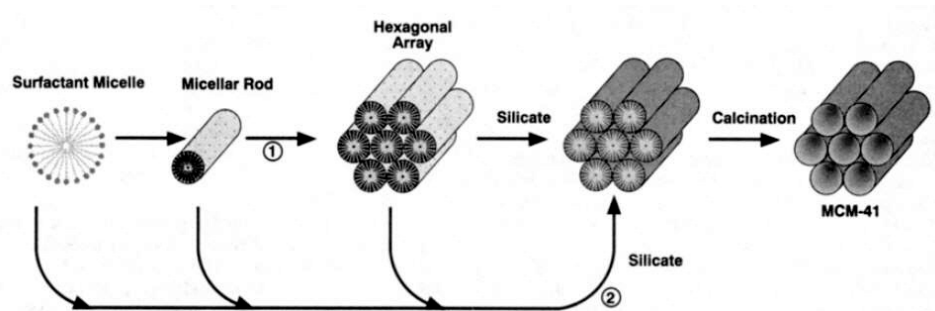
Figure 1.9. *Possible mechanistic pathways for the formation of MCM-41: (1) liquid
crystal-phase initiated and (2) silicate-anion initiated. Reproduced from Beck
et al.*[36]
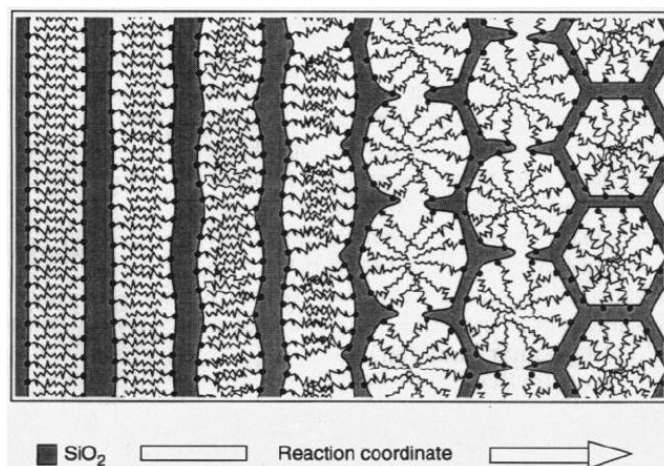
Figure 1.10. *Schematic diagram of the mechanism proposed for the transformation of a surfactant-silicate system from the lamellar to the hexagonal mesophase. On the left, small silica oligomers (not shown explicitly in the grey SiO_2 region) act as multidentate ligands, which have sufficiently high charge density to permit a lamellar surfactant configuration. As silica polycondensation proceeds, diminished charge density of larger silica polyanions increases the average headgroup area of the surfactant assembly, driving the transformation into the hexagonal mesophase. Reproduced from Monnier et al. [41]*

Micelles serve as the scaffold for polycondensation of the inorganic units, and their removal upon solvent extraction and thermal treatment eventually yields pores reflecting the micelles in their size and shape. A suitable hydrophobic solvent may selectively swell the hydrophobic micelle cores, thus increasing their size. Therefore, the design of a mesoporous material with well-defined pore size is accomplished by choosing a surfactant with the appropriate alkyl chain length, and optionally a swelling agent to get extra pore size.

The inorganic precursors play a key role in the formation of lyotropic phases. Electrostatic interactions between surfactant and inorganic NBBs are considered to function as stabilising agents in the formation of micelles. According to the charge matching model, supported by in situ XRD measurements, an initial lamellar phase is formed, made of alternate silicate and surfactant layers. Upon inorganic condensation, charge balance becomes altered since the negative charge on the inorganic phase decreases, therefore the silica/surfactant ratio must increase in order to maintain electroneutrality. As an effect, the curvature at the organic-inorganic interface increases, which results in the formation of cylindrical micelles packed according to a 2d-hex symmetry (Figure 1.10).[41,42] However, Regev et al. have observed the presence of intermediate structures made of cylindrical micelles bundled in clusters, each cluster being covered by siliceous units which only at a second time diffuse inside and eventually cover each single micelle.[43] Therefore, the presence of clusters implies the achievement of short-range order before long-range order is reached. This explains the existence in the final material of ordered mesoporous domains which are randomly oriented with respect to one another, as typically observed in TEM micrographs.

1.5 Main concepts on the synthesis of mesoporous materials

The discovery of M41S had a profound impact on research on catalysis and separation. This discovery provided also important *proof of concept* evidence for bio-inspired synthesis of organised matter by soft chemistry, i.e. chemistry at low temperatures and pressures, from molecular or colloidal precursors.[44] Using this approach, a new generation of advanced materials could be foreseen, obtained by the self-assembly of organic, inorganic and hybrid NBBs interconnected by specific molecular and supramolecular interactions. Several publications reporting new types of mesoporous materials and mechanisms of mesostructure formation appeared in the following years. Since a key factor in the design of materials is the understanding of the relation between the synthesis method and the final structure, it is no surprise that many among these first works were devoted to the mechanistic aspects of mesostructure formation. Another strong interest was obviously to determine the synthesis conditions for a reproducible control of mesoporosity, namely symmetry of the mesophase, pore size and size distribution. In 1994 a general model describing cooperative synthesis was proposed by Huo et al.[45] This model takes into consideration chemical, thermodynamic and kinetic parameters to explain the formation of an ordered mesostructure and guide the design of new mesoporous materials of different compositions, beyond the early M41S family. We will now tackle the main issues regarding the synthesis of mesoporous materials, using this paper of central importance as a starting point and further expanding our considerations to include more recent works.

1.5.1 Thermodynamic and kinetic considerations

The formation of an ordered mesostructure consists in the spatial organisation of hydrophilic and hydrophobic species, which are separated by a so-called *hybrid interface* (HI). Four different contributions to the Gibbs free energy of mesostructure formation, ΔG_{ms}, can be devised:

$$\Delta G_{ms} = \Delta G_{inter} + \Delta G_{org} + \Delta G_{inorg} + \Delta G_{sol}. \tag{1.1}$$

The term ΔG_{inter} accounts for the Van der Waals and electrostatic interactions between the organic and the inorganic species at the HI. ΔG_{org} contains the electrostatic interactions between the hydrophilic groups, together with the Van der Waals interactions and the conformational energy of the hydrophobic surfactant chains. As the inorganic phase contains units that may undergo polycondensation, the term ΔG_{inorg} describes the energetics of the electrostatic and intermolecular interactions of the inorganic units in the polycondensation process. The solution chemical potential is given by ΔG_{sol}.

In cooperative pathways leading to the formation of a mesostructure, the surfactant concentration is much lower than in water-surfactant lyotropic phases. This fact has been rationalised with the formation of hybrid intermediate states as NBBs in the formation of the mesostructure, which results in a lower *cmc*. As a consequence, the creation of a HI between the organic and inorganic species is a fundamental requisite for the formation of micelles with a well-defined curvature. This leads us to conclude that the term ΔG_{inter} predominates over the other free energy contributes, in particular: $|\Delta G_{org}| \ll |\Delta G_{inter}|$.

This is evident in the syntheses of mesoporous silica performed at high pH val-

ues (pH>13) where the formation of small oligomeric silica species prevails over long-range condensation, i.e. extended silica polycondensation is "turned off". In such system, the process of mesostructure formation can be decoupled from inorganic polycondensation and we can consider $|\Delta G_{inorg}| \to 0$. Since an ordered mesophase appears at low surfactant concentrations, the free energy of HI formation is confirmed to be the most important term.[46] On the other hand, in conditions where inorganic condensation is not inhibited, further rearrangements of the mesostructure can take place through siliceous condensation, which can be brought about by adjusting pH and temperature. In this case, inorganic condensation alters the charge balance at the interface, therefore the system responds by adopting a new morphology in order to re-establish electroneutrality. This accounts for rearrangements in mesophase symmetry, i.e. mesophase transitions, which are commonly observed in structural studies performed in situ, typically small-angle XRD using synchrotron radiation.

The thermodynamic aspect on the formation of a mesostructure should be combined with kinetic considerations. The formation of a well-ordered mesostructure can be hindered if inorganic condensation is too fast, eventually leading to a product with disordered or even absent porosity. No matter if the creation of an ordered mesostructure is thermodynamically favoured: if inorganic polycondensation is too fast, no order will be obtained. When inorganic condensation is slow, the kinetic constants (k_i) are ordered such that $k_{inter} > k_{org} > k_{inorg}$. Therefore, mesostructure formation is controlled by the formation of a HI: in such case we can speak of "inorganic-templated self-assembly" with reason. On the other hand, if inorganic condensation is too fast ($k_{inorg} > k_{inter}$ or $k_{inorg} > k_{org}$) the formation of a HI may be inhibited even in favourable thermodynamic conditions.[46] This is clear in reactive systems involving fast sol-gel hydrolysis and condensation reactions, such as transition metal alkoxides. A complexing agent (e.g. acetyl acetone) may be used in order to slow down inorganic condensation and permit the formation of an ordered mesostructure.

To summarise, there are two aspects of thermodynamic and kinetic order which are at play in the synthesis of mesostructured materials: interactions between inorganic and organic precursors which cooperate in forming a well-defined hybrid interface, and reactivity of inorganic precursors.

1.5.2 Self-assembled aggregates

It is a well-known fact that amphiphilic molecules in water solution can form a variety of supramolecular aggregates (spherical, cylindrical, lamellar, etc.) arranged in ordered structures with different symmetries (cubic, hexagonal, gyroid, etc.). Their symmetries and morphologies show a strong dependence on solution parameters such as pH or electrolyte concentration. These self-assembly processes are now well understood from the theoretical point of view, and there are several works on this topic which researchers on mesoporous materials have taken advantage of in order to rationalise the mesophase formation processes and design better syntheses.

At low concentration, amphiphilic molecules in an aqueous solvent are present as free molecules, whose polar head is solvated. When the concentration is raised above the *cmc*, the molecules self-assemble into micelles with a well-defined shape and aggregation number (i.e. average number of molecules per aggregate). At

higher concentrations a series of phase transformations may take place, related to changes in the curvature radius of the micelles. This phase transitions follow a general sequence with increasing concentration: direct spheres, direct cylinders, lamellae, inverse cylinders and inverse spheres (see also Figure 1.4). It should be noted how this sequence corresponds to a monotonic change in the curvature at the interface. In order to rationalise this phase transition phenomenology, several models have been proposed which take into consideration such parameters as: hydrophobic interactions between organic chains, geometric constraints due to molecular packing, molecular exchange between aggregates, repulsion between polar heads.

Israelachvili et al. proposed a simple model based on thermodynamic and geometric considerations, which predicts the shape of self-assembled structures formed by surfactants in an aqueous solvent, as well as their aggregation number.[21,47] Essentially, equilibrium thermodynamics requires that in a system of molecules that form aggregated structures in solution with aggregation number N, the chemical potential of all identical molecules in different aggregates be the same. Therefore, we may express the chemical potential of a molecule as:

$$\mu = \mu_N = \mu_N^0 + \frac{k_B T}{N} \log\left(\frac{X_N}{N}\right) = \text{const}, \qquad N = 1, 2, 3, \ldots, \qquad (1.2)$$

where μ_N is the mean chemical potential of a molecule in an aggregate of aggregation number N, μ_N^0 is the standard part of the chemical potential (i.e. the mean interaction free energy per molecule) and X_N is the concentration of molecules that are part of aggregates with aggregation number N. We may define a dynamic equilibrium according to which the molecules that make up an aggregate with aggregation number N constantly exchange with free molecules ($N = 1$ taken as the reference state), with equilibrium constant $K = \exp[-N(\mu_N^0 - \mu_1^0)/kT]$ (Figure 1.11). Equation 1.2 can thus be written in the more useful form:

$$X_N = N\left[X_1 \exp[(\mu_1^0 - \mu_N^0)]\right]^N. \qquad (1.3)$$

Aggregates form when there is a difference in the cohesive energies between the molecules in the aggregated and the dispersed ($N = 1$) states. The necessary condition for the formation of large stable aggregates is that $\mu_N^0 < \mu_1^0$ for some value of N, for example when μ_N^0 progressively decreases as N increases, or when μ_N^0 has a minimum value at some finite value of N. The exact functional variation of μ_N^0 with N determines many of the physical properties of aggregates, such as their mean size and polydispersity.

For the simplest shaped structures (rods, sheets, spheres) the interaction free energy of the molecules can be expressed as

$$\mu_N^0 = \mu_\infty^0 + \frac{\alpha k_B T}{N^p}, \qquad (1.4)$$

where α is a positive constant which depends on the strength of the intermolecular interactions and p is a number that depends on the shape of the aggregates. Inserting this expression into Equation 1.3 gives:

$$X_N = N\left[X_1 \exp\left(1 - \frac{1}{N^p}\right)\right]^N \approx N[X_1 e^\alpha]^N. \qquad (1.5)$$

We may note that for low monomer concentrations X_1, such that $X_1 \exp[(\mu_1^0 - \mu_N^0)/k_B T] \ll 1$, we have $X_1 > X_2 > X_3 > \dots$ for all α: thus, most of the molecules in solution will be present as isolated monomers. However, once X_1 approaches $\exp[(\mu_1^0 - \mu_N^0)/k_B T]$, it can increase no further, since X_N can never exceed unity. The monomer concentration $(X_1)_{crit}$ at which this occurs may be called critical micellar concentration (*cmc*). Therefore,

$$(X_1)_{crit} = cmc \approx \exp\left[-\frac{\mu_1^0 - \mu_N^0}{k_B T}\right] \approx e^{-\alpha} \quad \forall\, p. \tag{1.6}$$

This defines the concentration at which further addition of solute molecules results in the formation of more aggregates while leaving the monomer concentration more or less unchanged at the *cmc* value. Above *cmc*, free molecules will form aggregated structures, whose shape and aggregation number N essentially depend on the molecules we are considering. Note that this is true in general, both for hydrocarbon and for amphiphilic molecules. For example, alkane molecules in water form aggregates of infinite shape ($N \to \infty$) since α has typically high values (α is related to the solubility of the alkane in water, and can be seen as the free energy of transferring a molecule into the solvent phase). On the other hand, in the case of surfactant molecules being transferred into micelles or bilayers (N finite), α is significantly lower. In other words, the important difference between alkanes and amphiphilic molecules is not so much in their solubility or *cmc* values but in the ability of amphiphiles to assemble into structures in which μ_N^0 reaches a minimum or constant value at some finite value of N, whereas in the case of alkanes μ_N^0 shows a monotonic decrease as N increases, therefore aggregates of infinite size are formed.

The forces governing self-assembly into well-defined structures such as micelles and bilayers are a consequence of several competing interactions: (1) hydrophobic attraction at the hydrocarbon-water interface which induces molecules to aggregate, (2) hydrophilic attraction at the headgroup-water interface which imposes that headgroups remain in contact with water, (3) ionic or steric repulsion of the headgroups. The balance between these opposing interactions determines the stability range of a given micellar architecture. By simple considerations and mathematical calculations, it is possibile to obtain a formula that gives the interfa-
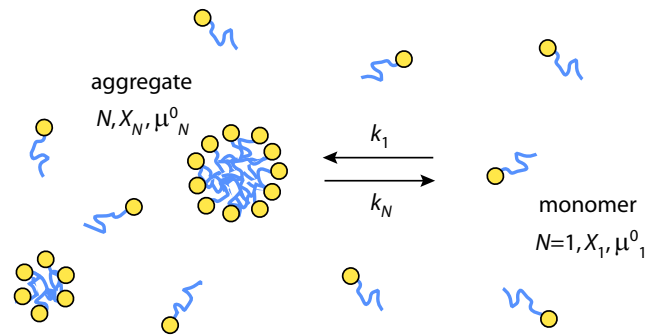
Figure 1.11. *Association of N monomers into an aggregate (e.g. a micelle). The mean lifetime of an amphiphilic molecule in a small micelle is very short, typically 10^{-5}–10^{-3} seconds.*

cial free energy per molecule in an aggregate:

$$\mu_N^0 = \gamma a + \frac{K}{a},$$ (1.7)

where N is the average number of molecules in a micelle, γ is the surface energy of the hydrophobic chain, a is the surface area per molecule and K is a constant. The minimum energy can therefore be obtained by letting $\partial \mu_N^0 / \partial a = 0$, that is $a_0 = \sqrt{K/\gamma}$. The term a_0 is referred to as the optimal surface area per molecule, defined at the hydrocarbon-water interface. It follows that the interfacial energy per molecule may now be expressed as:

$$\mu_N^0 = 2\gamma a_0 + \frac{\gamma}{a}(a - a_0)^2.$$ (1.8)

We see therefore how the concept of opposing forces leads to the notion of an optimal area per headgroup at which the total interaction energy per molecule has a minimum (Figure 1.12).

Once the existence of an optimum surface that leads to micellar aggregates is justified, we can derive the parameters that determine its shape. Simple geometric parameters provide a description of the shape of the aggregates: optimal area of the hydrophilic head a_0, volume of the hydrophobic tail v (considered incompressible for simplicity) and maximum length of the hydrophobic tail l_c (Figure 1.13). The latter represents the critical length whose further increase causes a net increment in energy, and can be thought as slightly shorter than a completely extended chain. Once the three parameters a_0, v, l_c are known (by means of calculation or measurement) it is possibile to predict which structure will form. This can be done by calculating a packing factor (g), which correlates the structure of the surfactant with the resulting aggregate morphology, defined as:[47–49]

$$g = \frac{v}{l_c a_0}.$$ (1.9)

One can also experimentally conclude that amphiphilic molecules with large polar headgroups tend to form high-curvature spherical aggregates, which will pack according to a cubic symmetry, whereas molecules with longer hydrocarbon tails or smaller polar headgroups will give cylindrical structures packed in a 2d-hex fashion, or lamellae. Surfactants with two hydrocarbon tails have a larger volume
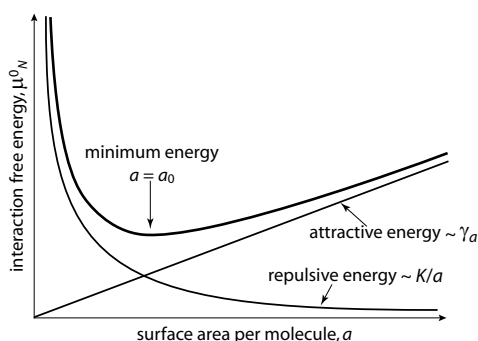
Figure 1.12. *Optimal headgroup area a_0 at which the opposing forces of headgroup repulsion and interfacial (hydrophobic) attraction are balanced.*

$g < 1/3$	$g = 1/3 - 1/2$	$g = 1$
single-chained with large headgroup areas	single-chained with small headgroup areas	double-chained with small headgroup areas
cone	truncated cone	cylinder
spherical micelles	cylindrical micelles	planar bilayers
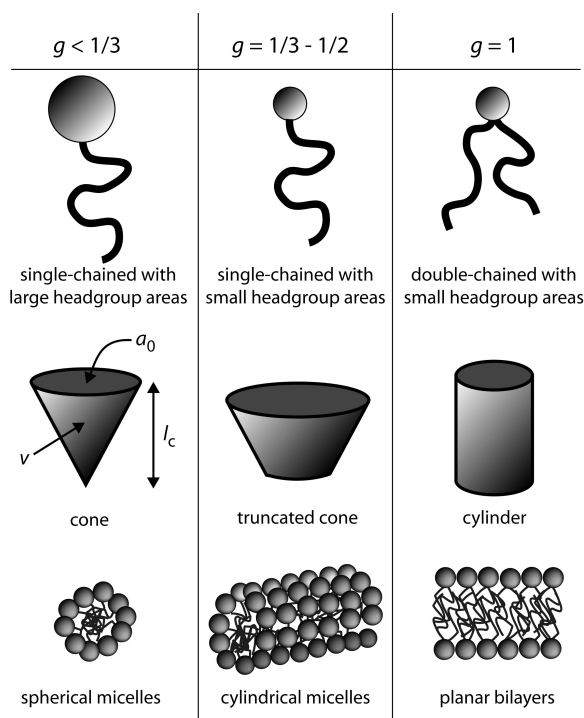
Figure 1.13. *Examples of packing shapes and micellar aggregates formed by surfactants (adapted from Israelachvili [21]).*

(*v*), therefore they will tend to form bilayers or vescicles (e.g. cell membranes are natural examples formed by the self-assembly of phospholipids, which have two hydrophobic tails). Finally, for $g > 1$ inverse micelles are favoured, where the hydrophilic headgroups point inwards. Table 1.2 gives a guideline for the correlation between the packing factor g and the resulting mesophase symmetry, whereas Figure 1.13 shows three examples of common packing shapes and micellar aggregates.

These considerations on surfactant-solvent systems come in handy when one has to design a synthesis for a mesoporous material: it is evident that such factors as size, shape, charge of surfactant, have a key role in the formation of the mesostructure. The packing factor has been shown to be a useful tool not only to rationalise experimental data, but also to tailor the desired mesostructure, either by selecting a suitable surfactant or even by synthesising molecules engineered *ad hoc* with a given g.

The first appearance of the g parameter in the field of mesoporous materials appeared in a work by Huo et al., where it was used to rationalise the symmetry of the mesophase obtained.[50,51] It has also been demonstrated that other synthesis parameters, such as chemical nature of the surfactant, pH, co-solvent and co-template, have an impact on the packing factor.[52,53] For example, in a work by Kim et al. this approach permitted to synthesise mesoporous silica with different mesophase symmetries (2d-hex *p6mm*, 3d-hex *P6₃/mmc* and cubic *Im3̄m*) by systematically varying g by suitable mixtures of nonionic surfactants.[54]

Table 1.2. *Ordered mesophases corresponding to different packing factor values.*

g	Symmetry
1/3	cubic *Pm3n*
1/2	2d-hex *p6mm*
1/2 – 2/3	cubic *Ia$\bar{3}$d*
1	lamellar

1.5.3 Types of hybrid interfaces

Since the synthesis of M41S is performed in alkaline conditions, the surface of the inorganic particles (denoted as I) bears a negative charge, which interacts with the cationic surfactant (denoted as S) and gives a hybrid interface (HI), denoted as S^+I^-.[§]

It is also possible to obtain mesoporous silica working in acidic conditions, below the isoelectric point (pH<2), for example by adding a hydrogen halide such as HCl or HBr: in these conditions silica acquires a positive charge because the silanols become protonated as $\equiv Si(OH_2)^+$.[23] Because the surfactant's cationic headgroup is surrounded by halogenide ions, the hybrid interface that forms is of type $S^+X^-I^+$, where the halogenide ions X^- form a negatively charged layer around the surfactant's headgroups S^+, and the protonated silica I^+ hydrogen bonds to halogenide anions. Therefore, the latter serve as the mediating agents that connect the inorganic and the organic cations. As inorganic condensation proceeds, protons are expelled from the interface, together with halogenide ions, in order to maintain electroneutrality. This process is underpinned by the following evidence: (1) the pH does not vary during synthesis, (2) the surfactant/halogenide molar ratio is equal to 1 in the final product, (3) the surfactant can be removed easily with ethanol, (4) TEOS and $SiCl_4$ give mesostructured products in acidic conditions, whereas non-hydrolysable precursors (e.g. fumed silica) do not. Mesophase symmetries that can be obtained in acidic conditions are essentially the same as those found in M41S. A well-known example is the SBA family (named after University of California at Santa Barbara). SBA materials are strikingly similar to M41S in their mesophase symmetries, but whereas the latter are obtained in alkaline media, the former are obtained in acidic media according to the proposed mechanism via a $S^+X^-I^+$ hybrid interface. The symmetries range from cubic *Pm3n* (SBA-1) to 3d hexagonal *P6$_3$/mmc* (SBA-2) to 2d hexagonal *p6mm* (SBA-3)[50,51]

The advantage provided by this type of HI is outstanding if one considers the formation of inorganic non-silica frameworks, where precursors are typically polyvalent cations (e.g. salts and ionic metal compounds): in this case the formation of a HI would be impossible without the use of mediating anions with bridging function between the inorganic phase and the surfactant. For example, mesoporous $ZnPO_4$ was prepared by this approach starting from cationic precursors.[45]

In another strategy for the synthesis of mesoporous materials starting from cationic precursors, a reverse HI is built up, where the inorganic building blocks I^+ are connected to the anionic headgroups of the surfactant S^-. For example,

---

[§]This notation was introduced in Huo et al.[45] to classify the interactions between inorganic phase and surfactant. The signs + and − refer to the sign of the electric charge. X^- and M^+ indicate anions (typically halogenide) and cations (typically metallic), respectively.

sulphonate surfactants such as $C_{16}H_{33}SO_3H$ have been successfully used in the synthesis of mesostructured Fe and Pb with hexagonal and lamellar phases. A fourth pathway is also possible: a HI is set up where inorganic precursor and surfactant are both anionic, and a cation mediates their interaction; this HI has a $S^-M^+I^-$ structure. However, this route leads typically to unstable lamellar phases. Table 1.3 reports a few examples of ionic surfactants.

1.5.4 Non-ionic surfactants

Although the combination of different anionic or cationic precursors allows building up different hybrid interfaces, permitting the synthesis of mesoporous materials of virtually any chemical composition, the products obtained using ionic surfactants have several drawbacks. First, the thickness of the inorganic wall (i.e. the distance between two adjacent pores) is so small (typically 8 to 13 Å) that it poses a serious limitation in terms of mechanical stability, especially for uses in catalysis. Second, ionic surfactants allow obtaining limited porosity (roughly 15 to 100 Å); furthermore, the use of swelling agents is associated with irreproducible results and poor quality, probably due to the formation of emulsion and phase separation. Third, the strong electrostatic interactions between the surfactant and the inorganic framework render surfactant extraction difficult: high calcination temperatures are needed, which may cause chemical degradation or collapse of the mesostructure; moreover, the counterions (e.g. Na^+, K^+, Br^-, Cl^-) are not completely removed and remain as impurities in the final product.

In 1995 Pinnavaia et al. presented a new synthesis of mesoporous silica using a non-ionic surfactant.[55] A mixture of TEOS and an alkylamine ($C_nH_{2n+1}NH_2$) in water and ethanol is aged for 18 hours, the product is dried, and the surfactant is removed by extraction with ethanol. This approach is based on the formation of a HI through hydrogen bonds between the amino groups in the surfactant and the silanols in partially hydrolysed TEOS. This HI is denoted as S^0I^0 because there is no net electrostatic charge on the two phases constituting the HI. The mesoporous silica thus obtained is characterised by larger inorganic walls (around 1.7 nm), which give better mechanical stability. Moreover, removal of surfactant is a less critical step because hydrogen bonds are more easily cleaved than electrostatic bonds. A major drawback of this first attempt is that the mesophase is not highly ordered, but rather made of disordered tubular cavities, a structure called "worm-like".

Because amines are easily absorbed by skin, they are regarded as highly toxic compounds. A family of more "green" surfactants are the alkyl-polyethylene oxides (C_nEO_m). The ethylene oxide group EO (OCH_2CH_2) is partially hydrophilic due to the electronic doublets in the oxygen atoms which can interact with polar or electron-attracting groups. Typical examples of this type of surfactants are octaethylene glycol monodecyl ether, $CH_3(CH_2)_9(OCH_2CH_2)_8OH$, and octaethylene glycol monohexadecyl ether, $CH_3(CH_2)_{15}(OCH_2CH_2)_8OH$.[56,57]

To date, amphiphilic block copolymers are the most important class of non-ionic surfactants used in the synthesis of mesoporous materials. Amphiphilic block copolymers are macromolecules constituted by two or more blocks having different chemical compositions and hydrophilic-hydrophobic properties. Their main advantages are: (1) they permit controlling the mesophase morphology easily, (2) pore size may be extended up to several tens of nanometres due to the large di-

mensions of macromolecules, (3) a wide variety of mesophase symmetries can be obtained. Because the surfactants used in the experimental work presented in this thesis are amphiphilic block copolymers, they will be addressed more thoroughly in Section 1.6.

Table 1.3. *Ionic surfactants used in the synthesis of mesoporous materials.*

Surfactant	*Chemical formula*
Alkyl ammonium salts (e.g. CTAB)	$C_nH_{2n+1}(C_2H_3)_3N^+X^-$, $C_nH_{2n+1}(C_2H_5)_3N$ (n=8,9,10,12,14,16,18,20,22, X=OH, Cl, Br)
Geminal surfactants	$[C_mH_{2m+1}(CH_3)_2N\text{-}C_sH_{2s}\text{-}N(CH_3)_2C_mH_{2m+1}]Br_2$ (m=16, s=2-12)
Sulphates	$C_nH_{2n+1}OSO_3$ (n=12,14,16,18)
Sulphonates	$C_{16}H_{33}SO_3H$, $C_{12}H_{25}C_4H_4SO_3^-Na^+$
Phosphates	$C_{12}H_{25}OPO_3H_2$, $C_{14}H_{29}OPO_3^-K^+$
Carboxylic acids	$C_{17}H_{35}COOH$ (stearic acid), $C_{14}H_{29}COOH$

1.5.5 Other structure-directing agents

The range of structure-directing agents employed in the synthesis of mesostructured materials are not limited to the templating units we have encountered so far (ionic and non-ionic surfactants, block copolymers). Other types of templates are dendrimers, colloidal crystals and certain biological systems.

Dendrimers   Dendrimers are macromolecules made of monomers that are linked in a branched structure around a central core. Contrary to structure-directing agents, in this case there is no self-assembly of molecules into aggregated structures, but the dendrimer templates the polycondensation of the inorganic phase with its structure. The high structural definition and the low polydispersity make dendrimers good candidates in the synthesis of mesoporous materials.[58] Functional groups can be covalently grafted onto the branched organic chains in order to produce mesostructured materials for given applications: for example, the typically low packing density of hydrocarbon chains can be suitably functionalised and serve as a host for metal clusters, as in decontamination of heavy metal-polluted water, while the inorganic framework ensures mechanical stability.

Colloidal crystals   Colloidal suspensions of polymeric (e.g. PS, PMMA) or inorganic (e.g. silica) spheres on a micron or sub-micron scale can sediment upon slow solvent evaporation, obtaining an ordered structure. These systems, known as colloidal crystals, are widely studied for example as photonic crystals[59] and templates for the fabrication of macroporous materials.[60,61] In this case, the interstices between the spheres are impregnated with inorganic precursors that polycondense into an interconnected phase. Next, the spheres are removed, either chemically (e.g. utilising a specific solvent for polymer colloids, HF for silica) or thermally. Colloidal spheres can be used as co-templates together with more conventional

surfactants for the synthesis of porous materials with hierarchical macro-meso-porosity.

Biological systems   Proteins and other biological units showing self-assembly behaviour, such as viruses and bacteria, may be used as templating agents. As the different combinations of biological units are virtually unlimited, the complexity of the structures that can be obtained is very high.[22]

Self-assembly with no templating agents   The idea of obtaining a mesostructure with no structure-directing agent seems counterintuitive. However, in this case the templating agents are directly incorporated into the inorganic units, by covalent bonds.[62] The advantage is that no use of templates other than the inorganic NBBs themselves is required and no extraction of the structure-directing agent is performed on the final product. On the other hand, given the typical instability of transition metal-carbon bonds, this is a method which can be applied almost exclusively to siliceous systems.

1.5.6 Synthetic approaches

So far, we have described the synthetic pathways based on cooperative mechanisms, where the formation of an ordered mesophase occurs via a hybrid interface where inorganic and organic NBBs are linked by electrostatic interactions or hydrogen bonds, typically in hydrothermal conditions. Electroneutrality at this interface accounts for its curvature and thus enables prediction of mesophase symmetry. We have also considered this problem from thermodynamic and kinetic viewpoints, concluding that a thermodynamically stable mesophase may be hindered by kinetic factors, typically fast inorganic condensation. However, other synthetic techniques that permit a more thermodynamic control are possible, in particular: true liquid crystal templating (TLCT) and evaporation-induced self-assembly (EISA).

True liquid crystal templating (TLCT)

In cooperative pathways, self-assembly occurs at surfactant concentrations much lower than those predicted for a surfactant-water mixture (*cmc*): this finds a justification assuming a charge-matching model in the formation of the hybrid interface. However, one could carry out the synthesis at concentrations higher than *cmc*, in this case with a different mechanism: the mesophase is already formed and constitutes a liquid crystal phase; next, the inorganic precursors are infiltrated between the micelles, and inorganic condensation takes place via sol-gel or redox reactions—hence the name, *true liquid crystal templating* (TLCT). This synthetic technique is also known as *nanocasting*, in that it is similar to the macroscopic process of shaping a material by casting a liquid phase into a mold. The most important advantage of TLCT is the possibility to obtain the desired mesophase symmetry based on the surfactant's phase diagram: because the influence of the synthetic parameters is not so crucial as in cooperative pathways, a higher thermodynamic control can be ensured. On the other hand, a major disadvantage of this technique is the inhomogeneity that may result as a consequence of the poor infiltration of the inorganic precursors into the liquid crystal phase. Moreover, the introduction of the inorganic phase into the lyotropic phase may lead to uncon-

trolled phase separation. Mesostructured materials can be obtained in the shape of monoliths by the TLCT technique, whereas powders and films are more difficult to prepare.

Attard's research group was among the first to introduce the TLCT technique in 1995[57,63] obtaining mesoporous silica from tetramethoxysilane (TMOS) and an alkyl-polyethylene oxide surfactant. This technique has shown to be effective also in the synthesis of mesoporous metals and semiconductors.[64,65] As a matter of fact, during this type of synthesis small quantities of methanol are formed as a product of TMOS hydrolysis. Methanol temporarily disrupts the liquid crystal phase, which forms again only after alcohol evaporation under vacuum conditions.[66] Besides, variations in water quantity during synthesis are neglected, which makes the proposed mechanisms questionable.

Evaporation-induced self assembly (EISA)

In methods based on precipitation, the self-assembly is *chemically* triggered during inorganic polycondensation, whereas in TLCT the liquid crystal phase is already formed in solution and inorganic polycondensation takes place around the organic domains after or during impregnation. Contrary to these approaches, in evaporation-induced self-assembly (EISA) the alcoholic solution contains the surfactant at very low concentration ($c \ll cmc$). Such a high dilution inhibits formation of a lyotropic phase as well as inorganic condensation. However, solvent evaporation triggers the self-assembly of the NBBs into an ordered mesophase and at the same time causes inorganic condensation. Thus self-assembly is induced by the *spatial gathering* occurring during evaporation. The interplay between such different factors as pH, precursor reactivity, time, etc. determines whether the synthesis is displaced towards a more thermodynamic or kinetic control.

There is no doubt that the most important advantage brought about by EISA is to enable the synthesis of mesoporous materials in the form of films. With precipitation based on cooperative pathways, almost exclusively powders could be obtained, useful for applications like catalysis and sorption but mostly useless for advanced applications (e.g. optics, sensing) where homogeneous films with optical quality are required. Self-assembled mesoporous films can be obtained by TLCT, but their quality cannot quite compare to that of films prepared by EISA. It is clear that this opportunity resulted in a boost in the research on mesoporous materials. In addition, EISA turns out to be very valuable in syntheses where highly reactive precursors are used (e.g. transition metal alkoxides, important in advanced applications), because inorganic condensation can be more easily controlled by controlling the evaporation process. As a consequence, not only films, but also powders, monoliths, nano- or microparticles (e.g. by aerosol) can be prepared. Since EISA was used in this research work to prepare mesoporous films, it will be described in detail in Section 1.7.

1.6 Mesostructures templated by amphiphilic block copolymers

1.6.1 Introduction

In a copolymer (or heteropolymer), two or more chemically different monomers are covalently linked in the same macromolecule, as opposed to a homopolymer, where only one type of monomer is used. In block copolymers (BC) the chemically dif-

ferent monomers are grouped in blocks, thus monomers within one block are alike and differ from the monomers belonging to the adjacent blocks (Figure 1.14).[67] Block copolymers whose blocks have different hydrophilic-hydrophobic properties are called *amphiphilic block copolymers* (ABCs). These belong to a family of macromolecular surfactants widely employed in industrial and households products, e.g. as foaming and dispersing agents, coatings, detergents. Beside these traditional applications, ABCs encompass uses in functional materials. Examples include the synthesis of nanoparticles and nanorods, hierarchical porous structures, biomaterials, drug release.[19] There are well-established synthetic techniques that permit preparing ABCs tailored with *ad hoc* architectures, chemical nature, functionality, polymerisation degree and polydispersity.[68]

Regarding their use in the synthesis of mesoporous materials, ABCs present several advantages as compared to low molecular weight surfactants.[69] A notable benefit is that micelles are bigger and permit obtaining porous structures with pore sizes up to several tens of nanometres. Another advantage is that mesophase symmetry can be controlled by such parameters as nature of copolymer, solvent and cosolvent composition. In particular, many ABCs with different chemical compositions, molecular weights and architectures are commercially available, or alternatively can be synthesised for specific purposes.[70] Table 1.4 shows three examples of ABCs used in the synthesis of mesoporous films, while Table 1.5 summarises the main aspects of ABCs, as well as the main differences with low molecular weight surfactants.

Considerations can be made on thermodynamic and kinetic factors on the synthesis of mesoporous materials using ABCs, similar to those discussed previously. Therefore, in this section we will respect the conceptual division between thermodynamic and kinetic factors that concur in creating a mesostructured material, first tackling the phenomenology and modelling of aggregated structures from ABCs in an aqueous solvent (thermodynamic parameters) in Section 1.6.2, and then introducing kinetic factors such as inorganic polycondensation and copolymer-inorganic interactions in Sections 1.6.3 and 1.6.4.
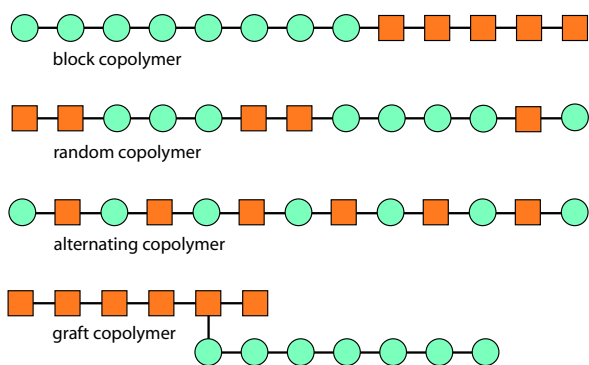

Figure 1.14. *Scheme representing four typical structures in copolymers (in this case a diblock copolymer): block, random, alternating and graft. The two chemically different monomers are represented by circles and squares.*

Table 1.4. *Examples of the main families of amphiphilic block copolymers commercially available used in the synthesis of mesoporous materials.*

Name	*Chemical formula*
Brij	C_xEO_y $H-(CH_2)_x-(CH_2CH_2O)_y-H$ $x = 12, 16, 18$ $y = 2, 4, 10, 20$
Pluronic	$EO_xPO_yEO_x$ $HO-(CH_2CH_2O)_x-(CH(CH_3)CH_2O)_y-(CH_2CH_2O)_x-H$ x and $y = 20 - 100$

$$HO(CH_2CH_2O)_w \qquad (OCH_2CH_2)_xOH$$

$$CH(OCH_2CH_2)_yOH$$

$$CH_2O(CH_2CH_2O)_{z-1}CH_2CH_2COOR$$
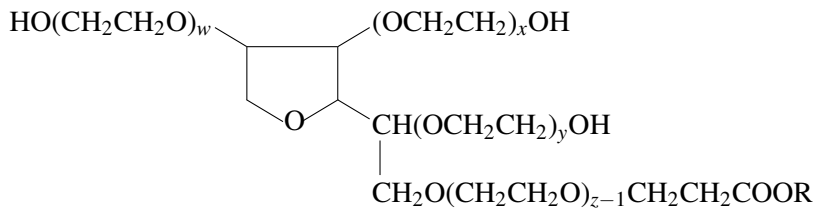
Tween

with $x + y + z + w = 20$.
Tween 80:
$R = (CH_2)_7CH=CH(CH_2)_7CH_3$

1.6.2 Self-assembling block copolymers

The formation of aggregates from amphiphilic block copolymers in solution can be understood using a simple model that takes into account thermodynamic parameters related to the solubility of the different blocks, such as entropy of mixing, and structural parameters, such as polymerisation degree.[71] Self-assembly can be regarded as a phase separation whose driving force lies in the chemical incompatibility between the chemically different blocks (Figure 1.2).[¶] Contrary to mixtures of low molecular weight homopolymers, the entropy of mixing per unit volume of chemically different high molecular weight A_n and B_n homopolymers is generally small, and it scales inversely with molecular weight. In other words, even small structural differences between A and B contribute to increasing the free energy and result in phase separation. An extreme example is a mixture of polystyrene and deuterated polystyrene, which are immiscible for sufficiently high molecular weights. The parameter used to estimate immiscibility is the so-called Flory-Huggins interaction parameter,

$$\chi_{AB} = \left(\frac{Z}{k_BT}\right)\left[\varepsilon_{AB} - \frac{1}{2}\left(\varepsilon_{AA} + \varepsilon_{BB}\right)\right], \qquad (1.10)$$

[¶]Amphiphilic block copolymers, unlike conventional nonionic surfactants, do not micellise at a critical micelle concentration (*cmc*). Instead, aggregation occurs over a broad concentration range that we refer to as the ACR (aggregation concentration range). The limiting aggregation concentration (LAC) is the point at which the surfactant reaches saturation, which would correspond to the more conventional *cmc*.[72] However, in all of the papers consulted for this thesis, *cmc* is reported instead of ACR or LAC, therefore we will refer to *cmc* in block copolymers, in keeping with low molecular weight surfactants.

Table 1.5. *Key aspects of low molecular weight surfactants and block copolymers. Reproduced from Soler-Illia et al.[69]*

Low MW surfactant	*Amphiphilic block copolymer*
Solution and mesophase behaviour	
Molecular / monodisperse	Polymeric / can be polydisperse
Head + chain structure object shape controlled by the g packing parameter	Enormous range of architectures: linear, branched, star,... Shape controlled by χ_{ij}, N, f_{ij} $(i, j = 1..n)$
Simple micelle-like or bicontinuous mesostructure	Possibility of complex multiscale mesostructures
Micellisation driven by hydrophilic-hydrophobic character	Micellisation driven by hydrophilic-hydrophobic character, block size and conformation
Cosolvent swelling modifies curvature	Differential swelling of domains by cosolvents
Use in the design of mesostructured materials	
"Hard" well-defined hybrid interfaces	"Blurry" interfaces, possibly swollen by the inorganic phase
Thin walls ($\sim$ 1 nm)	Thick walls (2–10 nm)
Walls not entangled with the template	Walls entangled with the template ("multiphase")
Pore size limited by micelle shape	Pore size tailorable modifying polymerisation degree, monomer nature, polymer fraction

which gives an indication on the increase in the Gibbs free energy when two A and B monomers are in contact, expressed in thermal energy units, $k_B T$. In Equation 1.10, Z is the number of nearest neighbour monomers and ε_{AB} is the interaction energy between A and B monomers. Positive χ_{AB} values indicate a repulsion between A and B, thus contributing to phase separation, whereas a negative χ_{AB} indicates a favourable entropic term towards miscibility. When there are no significant A–B interactions (as in the case of hydrogen or electrostatic interactions) χ_{AB} is positive (a typical value is 0.1). χ_{AB} also scales inversely with temperature, therefore higher temperatures favour mixing.

In amphiphilic block copolymers, the different A and B units are covalently linked, therefore long-range hydrophobic-hydrophilic repulsion and short-range covalent attraction coexist. Indeed, these are competitive forces that are the basis of the formation of aggregated self-assembled structures, as we have mentioned previously (see page 8). Microphase separation theories make large use of a simple parameter in order to quantify the driving force leading to ordered phases, that is $N\chi$, where N is the polymerisation degree and χ is the sum of χ_{AB} over all A and B monomers. $N\chi$ gives an estimate of the segregation degree of the block copolymer: when $N\chi \leq 10$ the system is governed by entropic terms and a disordered phase is formed; when $N\chi > 10$, enthalpic terms prevail and a disorder-to-order transition is observed.[73]

We also need a parameter to take into account geometric factors: for a diblock A–B copolymer, the parameters f_A and f_B describe the copolymer's composition, where $f_A = N_A/N$, $f_B = N_B/N$, $f_A + f_B = 1$. Perfectly symmetric architectures (i.e. A and B blocks have the same molecular weight) will give alternate A and B layers, that is to say a lamellar structure (lam). Slightly off-symmetric structures will form layered structures where the low molecular weight components are interrupted by channels, through which the high molecular weight components are interconnected (perforated layer, pl). Further asymmetries will lead to bicontinuous phases, where both blocks form interconnected phases with cubic $Ia\bar{3}d$ symmetry group (gyroid phase, gyr), whereas copolymers characterised by a very low block symmetry form 2d hexagonal ($p6mm$) and cubic ($Im\bar{3}m$) phases, associated with cylindrical and spherical micelles, respectively.

Note that this description of self-assembly is consistent with the geometric considerations that were discussed in Section 1.5.2, where geometric factors that account for the resulting mesophase symmetry are contained in the packing factor g. Strictly speaking, in block copolymer-based systems the self-assembled mesophase symmetry is not predictable on purely geometric grounds, in that one has to take into account also chemical and structural factors, expressed by the terms χ_{ij}, N, f_{ij}, where i and j vary with the number of blocks (for a diblock copolymer i=A, j=B). Nevertheless, as we will see in the experimental part of this thesis, the geometric prediction by g is a good rule of thumb to decide whether a block copolymer will favour the formation of cylindrical or spherical micelles. For example, block copolymers with large hydrophilic headgroups (large a_0) tend to form spherical micelles, whereas copolymers with small headgroups tend to give cylindrical micelles or lamellar phases (the term v prevails).

Other effects must be considered in order to formulate a comprehensive predictive theory. For example, the driving force that leads to phase segregation is countered by entropic forces within each single macromolecule: in order to maximise the distance between incompatible blocks, the organic chains adopt stretched configurations, which generate a restoring force (analogous to Hooke's law but entropic in origin). For a block constituted by N monomers in a stretched configuration and spaced by R, this force can be expressed as:

$$F_e = \frac{3k_{\mathrm{B}}TR^2}{2Na^2},$$
(1.11)

where a is a characteristic length of the monomer which depends on the local chain structure.

Finally, the aggregation number Z can be defined as the number of macromolecules that concur in micelle formation. Experimental results yield an empirical law:

$$Z = Z_0 N_A^{\alpha} N_B^{-\beta},$$
(1.12)

where Z_0 is a constant depending on the type of copolymer, N_A e N_B are the polymerisation degrees for blocks A and B, α and β are equal to 2 e 0.8 (with slight variations according to the system). This equation describes the aggregation number in systems containing di- and triblock, graft and star copolymers. Besides, it holds also for ionic and nonionic small molecular weight surfactants.

To summarise, the stability of different morphologies in a block copolymer solution is the result of multiple enthalpic (interaction of incompatible blocks) and

entropic (chain stretching, spatial frustration) contributions to the Gibbs free energy. It can be described by the parameters χN (tendency towards block segregation) and f (chemical composition). Simulations obtained by self-consistent field theory allow calculating the free energy of block copolymer solutions according to their composition, and they are generally in good agreement with experimental data. Nevertheless, to a first approximation, simpler geometric parameters like the packing factor g can be used in order to get a rough indication about which micelle shape the system will preferentially form.

The degree of complexity of the structures formed by block copolymers increases dramatically as the number of different blocks N increases. In diblock copolymers, χ_{AB}, N and f are generally sufficient to univocally determine the phase diagram, whereas in triblock copolymers a larger number of parameters must be known: at least three interaction parameters (χ_{AB}, χ_{BC}, χ_{AC}) and two compositional parameters (f_A, f_B). Moreover, other factors are introduced, which depend on the copolymer architecture, for example branching, side groups, etc. As a consequence, whereas in diblock copolymers only hexagonal, cubic, lamellar structures are typically observed, in triblock copolymers diverse and more exotic symmetries are experimentally found. As N is increased, the complexity of the structure increases exponentially. Examples of this exquisite diversity can be found in nature, where one can observe the rich variety of biological systems such as proteins, oligonucleotides, DNA and cell components, which can be described as large-N block copolymer systems (proteins) assembled from biological monomers (aminoacids). Synthetically, the wide range of block copolymers commercially available is reflected by a large number of architectures that can be obtained.[73]

The effect of solvent and cosolvent

The structures obtained by self-assembly depend on micelle curvature, which can be predicted from the copolymer's architecture and chemical composition through N, χ and f. Therefore, in order to obtain different structures, one should in principle vary at least one of these three parameters. As a matter of fact, experimental data show that a variety of structures that are not predicted by this model can be obtained from the same copolymer. This observation requires the introduction of a further parameter to account for the degree of freedom associated with the formation of these unpredicted structures. Experimentally, a solvent having affinity for one block can vary the range of stability of the predicted structures, or produce new ones. This can be explained by the selective volume increase of one block and the subsequent change in micelle curvature. For example, if we consider a triblock copolymer like polyethylene oxide-polypropylene oxide-polyethylene oxide (PEO-PPO-PEO) and a polar solvent like water, we can note that increasing solvent concentration leads to phase transitions following the order lam → hex → cub → disordered. This fact can be explained by the selective solvation of the hydrophilic PEO blocks by solvent molecules, whereas the hydrophobic PPO blocks remain practically unaltered: thus the observed phase transitions can be explained in terms of changes in micelle curvature.

Ivanova et al.[74] present the study of Pluronic P105 block copolymer (EO_{37}-PO_{58}-EO_{37}) in the presence of selective solvents. This copolymer should give lamellar structures, as the PEO:PPO weight ratio is 1:1. However, as water concentration is raised, PEO blocks are selectively swelled, therefore a planar in-

Table 1.6. *Name, mesophase symmetry, structure-directing agent and pore size relative to four typical SBA materials.*

Sample	Symmetry	Block copolymer	Pore size
SBA-11	$Pm3n$	$C_{16}EO_{10}$ (Brij)	25 Å
SBA-12	$P6_3/mmc$	$C_{18}EO_{10}$ (Brij)	24 Å
SBA-15	$p6mm$	$EO_{20}PO_{70}EO_{20}$ (Pluronic P123)	46–300 Å
SBA-16	$Im\bar{3}m$	$EO_{106}PO_{70}EO_{106}$ (Pluronic F127)	54 Å

terface becomes unfavoured and micelles with finite curvature form: the system responds to progressively higher water concentration by forming cylindrical micelles with 2d-hex packing (49–68 wt% P105), and spherical micelles with cubic symmetry (25–46 wt% P105). A further degree of freedom can be provided by a selective co-solvent. In the work cited, three cosolvents are chosen according to their different polarity: ethanol (CH_3CH_2OH), propylene glycol (CH_2OH-$CHOH$-CH_3) and glycerol (CH_2OH-$CHOH$-CH_2OH). Small-angle X-ray scattering (SAXS) measurements point out that, although all three cosolvents are polar and are miscible with water, they are localised in different domains in the mesophase: glycerol is localised in polar microdomains far from the PEO-PPO interface, whereas propylene glycol and ethanol partially swell the PEO or PPO blocks. This causes a decrease in lattice constant and a different micelle curvature.

Another example is provided by a study on a system of PEO-PPO-PEO in water and xylene, where liquid crystal phases with nine different symmetries are observed, seven of which are ordered and two disordered.[75] Another interesting case is reported by Holmqvist et al., regarding the effect of molecules like butanol, xylene and butyl acetate that selectively swell the hydrophobic PPO micelle core in systems based on block copolymer Pluronic F127 (EO_{106}-PO_{70}-EO_{106}).[76]

1.6.3 The formation of a hybrid interface

Stucky's research group at Santa Barbara, CA, was the first to report on the use of nonionic triblock copolymers of poly(ethylene oxide)-poly(propylene oxide)-poly(ethylene oxide) (PEO-PPO-PEO) as the templating agents in the synthesis of mesoporous silica:[77,78] in 1998, a new family of mesoporous silica was reported, among which the 2d-hexagonal ($p6mm$) SBA-15 and the cubic ($Im\bar{3}m$) SBA-16. Some of the amphiphilic block copolymers used in the syntheses are reported in Table 1.6. This was an important development due to the fact that these copolymers are inexpensive, environmentally benign, and commercially available with many choices of hydrophilic and hydrophobic block lengths. The SBA materials are synthesised in acidic conditions, as opposed to M41S which are obtained in alkaline media. Pore sizes are as high as 30 nm when Pluronic surfactants are employed. Since the pH is below the isoelectric point of silica (pH<2) the silica precursors are positively charged, and the hybrid interface can be described as $(S^0H^+)(X^-I^+)$, where the water-surfactant interaction is due to hydrogen bonds between the oxygen atoms in PEO blocks and the hydrogen atoms in water.

The interactions between block copolymers and inorganic precursor have a central role in the formation of the hybrid NBBs that will self-assemble to form the

ordered mesostructure.[79] Hydrogen bonds between the polyether group -[CH$_2$-O-CH$_2$]$_n$- of the hydrophilic PEO blocks and the polar solvent molecules are responsible for the attractive interactions between the copolymer and the polar solvent. The hydrophobic character of PPO block can be explained by the presence of a methyl side group, which prevents the formation of a PEO-water hydrogen bond because of its steric hindrance. Thus, micelles have a central PPO hydrophobic core and a hydrophilic corona made of PEO and inorganic species.

Melosh et al. have determined that in silica monoliths templated by Pluronic F127 self-assembly occurs at F127 concentrations higher than 40 wt%. The lack of order at lower concentrations leads to the conclusion that strong, hydrogen bond-like interactions are formed between Si-O-Si oligomers and both PEO and PPO polyethers, as pointed out by NMR data. As long as F127 concentration is low, these interactions inhibit microphase separation and a nearly homogeneous mixture of block copolymer in the silica network is observed. When surfactant concentration is raised, the PPO-PPO interactions prevail over the hydrophobic PPO-SiO$_2$ interactions, resulting in phase separation and in the increase in the degree of order with increasing surfactant content.[80]

A well-defined hybrid interface can be designed by choosing a suitable copolymer, whose blocks have a marked difference in solubility. Simon et al.[73] report on the synthesis of an aluminosilicate obtained from glycidoxypropyl-trimethoxysilane (GLYMO) and aluminium butoxide templated by a polyethylene oxide-polyisoprene (PEO-PI) block copolymer. This copolymer shows a high tendency to form well defined mesostructures, because of the greater solubility difference between the PEO and PI blocks (i.e. high χN).

Besides playing a major role in determining the formation of the HI, the interaction between silica species and PEO blocks are responsible for the creation of microporosity in the final mesoporous material. In fact, when the silica-PEO interaction is strong, the hydrophilic blocks will be partially or totally interpenetrated with the inorganic phase. Thus, inorganic crosslinking and subsequent removal of surfactant give rise to a range of voids having a size reflecting that of the single macromolecules.[81] This single macromolecule-generated microporosity pervading all mesoporous materials templated by block copolymers helps one to rationalise the experimental finding that the specific surface area (SSA) of these materials is typically larger than that estimated from geometrical assumptions considering the mesopores as the only contributions to SSA.[82] Quantitative XRD measurements on mesoporous silica support a model where low density silica is localised on the region of the inorganic framework that is closer to the pore, which is consistent with a certain amount of microporosity surrounding each mesopore.[83]

Considering a PEO-PPO block copolymer, three scenarios can be discerned according to the entity of the interactions at the hybrid interface (Figure 1.15). (1) PEO blocks form a layer interposed between the inorganic phase and the PPO core (*three-phase model*). (2) PEO chains totally interpenetrate the inorganic phase (*two-phase model*), where each single PEO chain acts as a single-macromolecule template and yields a micropore upon calcination. (3) The PEO chains interpenetrate the inorganic network according to the three-phase model until saturation is reached, and phase separation occurs according to the two-phase model; in this case both microporosity and an increase in pore size are observed (*mixed model*).

De Paul et al. have performed NMR analyses on a mesostructured aluminosilicate templated by polyethylene oxide-polyisoprene (PEO-PI), which reveals an

intermediate situation (point 3 in the previous description) where the hydrophilic blocks interpenetrate the inorganic framework. Interpretation of NMR data shows that the PEO blocks have much lower mobility with respect to the PI blocks. On the other hand, the mobility of the PI blocks is comparable with that observed in the absence of an inorganic phase. This can be justified admitting that the PEO blocks are anchored to the inorganic structure, therefore a lower mobility is observed.[84]

Boissière et al. compare the data obtained by dynamic light scattering (DLS) and SAXS on mesostructured silica prepared with TEOS and diblock copolymer Tergitol $[C_{15}H_{31}(EO)_{12}]$.[85] The synthesis is carried out by a two-step mechanism: first, an acidic solution is prepared (pH$\approx$2), where silica is highly hydrolysed but no significant condensation occurs; second, a catalyst (NaF) is introduced into the solution, which causes extended silica polycondensation. DLS and SAXS measurements allow calculating the size of the organic micelles in the silica framework. Different results are obtained, according to the molar ratio r=[silica]/[surfactant]. In particular, for $r < 4$ both characterisation techniques yield the same micelle dimensions. For $r > 4$ the micelle sizes obtained with the two techniques differ: DLS indicates increasing micelle size in direct proportion with r, whereas SAXS shows that micelles do not vary in size when r is raised. This apparent contradiction between the DLS and the SAXS results can be explained by observing that the two techniques are based on different properties: DLS measures particle size based on diffusion of the incident light, i.e. the hydrodynamic radius is obtained, whereas SAXS is based on the electronic contrast of a material, which in this case is provided by the different electronic density of silica and surfactant. In conclusion, the silica oligomers that originate from TEOS condensation upon addition of NaF penetrate into the external PEO corona of the micelle: for $r < 4$ the silica oligomers can be accommodated in this region, whereas for $r > 4$ the PEO corona is saturated with inorganic species, and the silica oligomers must be positioned in the outer region, forming a layer surrounding the micelle (Figure 1.16). Therefore, DLS "sees" the micelles as composed of copolymer aggregate and external silica shell, whereas SAXS "sees" the micelles as composed of surfactant, regardless of the presence of small quantities of silica between the PEO chains.

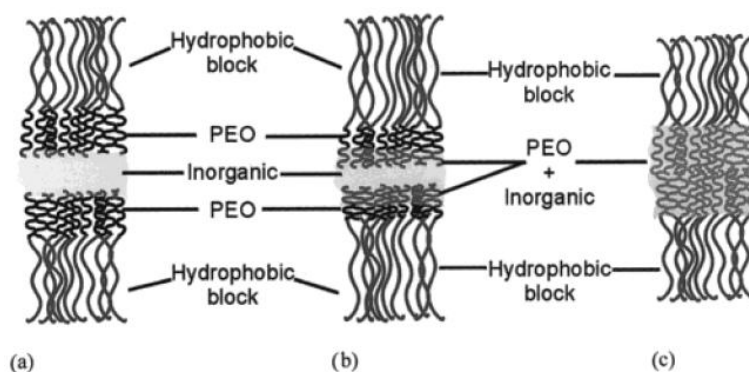**Figure 1.15.** *Three possible structures of the hybrid interface in a mesostructured material composed of an inorganic phase and a nonionic amphiphilic block copolymer with PEO as the hydrophilic block. (a) Three-phase system (i.e. inorganic, PEO, and hydrophobic block), (b) gradual transition from a two-phase to a three-phase system, and (c) two-phase system (PEO/inorganic and hydrophobic block). Reproduced from Göltner et al.* [82]

The block copolymer length and the resulting pore size can be related using a three-phase model. For example, Smarsly et al. have obtained mesoporous silica templated by C_nEO_m in the form of powder using the TLCT technique. The length of the hydrophobic and the hydrophilic blocks (N_A and N_B, respectively) can be used to determine the size of both micro- and mesopores through an empirical relation. In this way, both porosities can be controlled independently by choosing a suitable block copolymer.[86]

From these examples it is straightforward to infer that the entity of inorganic-organic interactions have a profound effect on the resulting mesophase, exerting a key influence in terms of critical concentration and microstructure. Nevertheless, it has been demonstrated that mesophase symmetry can be predicted basing on solvent-surfactant phase diagrams available in the literature. This offers an advantage in that the synthesis can be designed based upon surfactant/solvent rather than on much more complicated surfactant/silica/solvent phase diagrams. The idea behind this is surprisingly simple:[87] the copolymer volume fraction with respect to the non-volatile species (inorganic precursors and copolymer) is defined as:

$$\Phi = \frac{V_s}{V_s + V_i},$$

where V_s and V_i are the volumes of block copolymer and inorganic species, respectively. The definition of V_s is straightforward:

$$V_s = \frac{m_s}{\rho_s},$$

where m_s and ρ_s are the mass and density of the copolymer, respectively. The calculation of V_i involves some approximation, because the precise nature of the sol-gel precursors present when the mesostructure is formed is not known, therefore the volume of these species is assumed to be equal to that of the dense inorganic compounds plus the water that is released during condensation, and hydrochloric acid (especially if HCl is incorporated in the inorganic complexes as in the case of
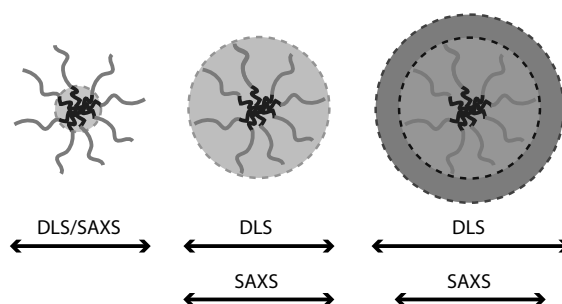
Figure 1.16. *Schematic drawing of the shape and evolution of the hybrid micellar objects, as probed by dynamic light scattering (DLS) and small-angle X-ray scattering (SAXS). Left: pure micelles, with hydrophobic core and hydrophilic shell. At a silica/surfactant ratio of 4 (middle picture) a coating of PEO-penetrated silica forms, whereas at silica/surfactant ratios larger than 4 an additional, loosely crosslinked silica shell is formed.*

titania). In the case of a tetravalent metal (or metalloid) like Ti or Si:

$$V_i = \frac{m_{M(OH_4)}}{\rho_{M(OH_4)}} + \frac{m_{HCl}}{\rho_{HCl}} \approx \frac{m_{MO_2}}{\rho_{MO_2}} + \frac{m_{H_2O}}{\rho_{H_2O}} + \frac{m_{HCl}}{\rho_{HCl}}.$$

For calculation purposes, the authors of this work have assumed that the stoichiometry of the silicate species in the coating solution was $Si(OH)_4$. However, because significant silica condensation may occur in solution prior to dip-coating, a better way to estimate che chemical nature of the silicate species would be to use ^{29}Si NMR data. This technique can give a quantitative estimate of the Q^x species, where Q^x indicates a Si atom connected to x Si atoms through siloxane (Si-O-Si) bridges.

The parameter Φ represents the volume fraction of block copolymer that should be looked up in the water-copolymer phase diagram in order to obtain the correct predicted mesophase (Φ can be regarded as a sort of "effective copolymer concentration" which takes into account the presence of the inorganic phase). To summarise, one can design the synthesis of a mesostructured film by locating the surfactant concentration for the desired mesophase in the surfactant/solvent phase diagram (Φ) and calculating the quantity of surfactant to introduce in the coating solution as

$$V_s = \frac{\Phi V_i}{1 - \Phi}.$$

Thus, V_s is the amount of surfactant to add to the precursor solution.

Experimental results are in good agreement with this predictive theory, both for mesoporous silica and titania. Many works on mesoporous materials make use of this simple calculation as a starting point in order to design a mesoporous material with a given mesophase symmetry.

The presence and type of solvent and cosolvent indeed influence the formation of the hybrid interface, affecting the resulting mesostructure. This has been previously described for surfactant-solvent systems, where selective swelling of one block is involved in the curvature change at the hybrid interface. The same happens in the synthesis of a mesostructured material: for example, cubic phases can be obtained whereas hexagonal or wormlike structures are predictable from the starting components. In silica-based systems, the presence of silanols (Si-OH) enhances the entity of the interactions at the hybrid interface, thus increasing its curvature.[69] Such an effect has been observed in mesoporous titania as well: in this case the introduction of an acidic solution contributes to building up a more defined hybrid interface, influencing both precursor hydrolysis and curvature. Table 1.7 summarises the main factors influencing the formation of a hybrid interface and determining the stability of a mesophase symmetry.

1.6.4 Inorganic condensation

As described previously, the formation of a mesostructure results from a delicate balance between two competitive processes: creation of a hybrid interface and inorganic polycondensation. As a consequence, the control of polycondensation kinetics is of primary importance in the achievement of a good degree of order. This can be accomplished in different ways: we have seen (page 28) how synthetic techniques can slow down inorganic polycondensation (EISA) or modify the processing conditions so that kinetics plays a less critical role (TLCT). Another pos-

Table 1.7. *Main factors influencing the formation of a hybrid interface and determining the stability of a mesophase symmetry.*

Parameter	Meaning
χN	Indicates the segregation degree between different blocks in an amphiphilic block copolymer. Gives an indication on the driving force that leads to the formation of ordered microphases. Indicatively, if $\chi N > 10$ an ordered mesophase is favoured
f	Polymer composition, indicates the ratio between the number of monomers in a block and the total number of monomers in a copolymer (degree of polymerisation). Concerns the copolymer architecture and determines the stable mesophase together with χN
g	Packing factor, describes the geometry of a surfactant considering the hydrophilic headgroup area, volume and length of hydrophobic tail. Small values determine a higher interfacial curvature (spherical micelles with cubic symmetry), larger values indicate a lower curvature (cylindrical micelles with hexagonal symmetry, lamellar micelles)
hydrophilic-inorganic	Determines the microporosity of the inorganic walls. The presence of hydrated inorganic species generally causes a higher interface curvature
hydrophilic-hydrophobic	Marked solubility difference between the blocks generate a well-defined HI
hydrophobic-hydrophobic	Hydrophobic-hydrophobic interactions prevail over hydrophilic-hydrophobic interactions for higher surfactant concentrations
Φ	Provides the range of stability of a given mesophase according to a surfactant-solvent phase diagram. Can be used in a predictive synthesis

sibility is to make use of ionic species that influence the reactivity of the inorganic precursors.

A study by Voegtlin et al.[88] presents the synthesis of highly-ordered mesoporous silica using amphiphilic block copolymers in the presence of F^- ions. In syntheses based on the use of ionic surfactants and pH>2, the role of fluoride ions is to stabilise the hybrid interface by restoring electroneutrality as the negative charge on the inorganic phase decreases upon polycondensation, with an interface of type $S^+(X^-I^0)$. The fluoride ions are also able to solubilise silica as SiF_6^{2-} and act as a catalyst in polycondensation reactions (in this hybrid interface, $X=SiF_6^{2-}$ or F^-). Using nonionic surfactants, fluoride ions are incorporated into the hybrid interface in a $S^0H^+(F^-I^0)$ hybrid interface. Essentially, the surfactant's hydrophilic headgroups hydrogen bond with protons, while on the other side of the interface, the F^- ions are electrostatically bound to silica and a hydrogen bond between F^- and H^- is formed. This allows for the construction of a well-defined interface, with the resulting mesostructure having a high degree of order (narrow Bragg X-ray diffraction peaks).

The role of fluoride ions in syntheses using amphiphilic block copolymers as the structure-directing agents is described also by Kim et al.,[89] who report on the synthesis of ordered mesostructures obtained at pH values 0 to 9 with an accurate control of hydrolysis and condensation kinetics of the silica precursors (tetram-

ethoxysilane) using fluoride ions. At pH>4 ordered structures are obtained exclusively upon addition of F^- ions, whereas at lower pH a good degree of order is attained even without fluoride. In fact, at pH<4 hydrolysis reactions occur much faster than condensation, therefore silica-surfactant structures are readily formed and act as the NBBs in mesostructure formation. At pH>4 hydrolysis and condensation start to have comparable kinetics and larger silica-surfactant aggregates are formed, which lead to an ill-defined hybrid interface and a disordered mesophase unless F^- is introduced into the precursor solution. This result suggests that small hydrolysed silica oligomers are needed to interact with the surfactant and create ordered mesostructures. Furthermore, the degree of order is higher in products obtained starting from tetramethoxysilane [Si-(O-Me)$_4$] rather than tetraethoxysilane [Si-(O-Et)$_4$]: this is because hydrolysis occurs much faster in the former than in the latter, as ethoxy group is more sterically hindering than methoxy.

1.7 Mesostructured films

1.7.1 Technological importance

The first mesoporous materials were synthesised in the form of powders through precipitation mechanisms. On the one hand, this was an adequate solution in such applications as catalysis and sorption. On the other hand, further studies rendered mesoporous materials a "solution looking for a problem": other applications were devised, such as sensors and low dielectric constant interlayers, owing to the ordered nanometric porosity and the high specific surface area of as much as $\sim$1000 m$^2 \cdot$g^{-1}. Thus, the synthesis of mesoporous films opened the way to such new advanced applications for which powders were unsuitable.

The first self-supporting mesoporous films appeared between 1994 and 1996. These first syntheses consisted in the precipitation of the precursors at the solution-air interface, involving transport of the precursors in the liquid phase towards the interface.[90,91] Supported mesoporous silica films were also grown on a substrate immersed in a solution with high surfactant concentration by a TLCT approach ($c_0 > cmc$).[92] Growth and coalescence of the solid phase on the substrate occurred on a time scale varying between few hours and several weeks. However, the films prepared according to these procedures are inhomogeneous even on a micron scale and have a low optical quality, which makes them unsuitable for advanced applications. Mesoporous films were also obtained by spin-coating a solution based on TMOS and an ionic surfactant, but the formation mechanisms are not clear.[93] In 1997, Lu et al. obtained 2d-hexagonal and cubic phases in silica films prepared by dip-coating.[94] Here, surfactant concentration is lower than cmc, and self-assembly occurs as a consequence of solvent evaporation which progressively increases the non-volatile species concentration.

The idea of using a very dilute solution, where $c_0 \ll cmc$, was developed in the same research group at the Sandia National Laboratories (US) and is the basis of the most widely employed technique, to date, in the synthesis of mesoporous films: *evaporation-induced self assembly* (EISA). This definition was coined by Brinker and coworkers in 1999 to indicate a new synthesis process where mesophase formation is triggered by solvent evaporation rather than precipitation reactions.[95]

If one considers the publications on mesoporous films, one can note that siliceous systems constitute the largest part. The reasons are manifold: first, there

is a historical reason, as many researchers come from the zeolite world and as such they are much more familiar with the silicon and the aluminium chemistry rather than, say, transition metal chemistry. Second, silica films obtained by sol-gel routes are less difficult to obtain with respect to other oxides, because the self-assembly process can be controlled more easily due to low hydrolysis-condensation rates of silicon alkoxides. Transition metal precursors are more prone to hydrolysis, redox reactions or phase transitions involving thermal breakdown of the structure, which makes it much more difficult to remove the template and create an ordered mesoporosity maintaining the optical quality of the film.[96] Third, the stability of the Si-C bond opens several perspectives on hybrid organic-inorganic materials, as well as on the possibility of grafting a number of chemical functionalities on the mesopore surface due to the presence of Si-OH groups. The other side is that transition metal oxides find interesting applications due to their optical, electronic and magnetic properties (e.g. high refractive index, semiconductivity, photocatalytic properties).[97]

1.7.2 Fundamentals of EISA

The starting point in the EISA technique is the preparation of a dilute solution containing the inorganic precursors (generally a metal/metalloid alkoxide or salt) and the organic templating agents (surfactant or macromolecular amphiphilic block copolymers). The solvent is an alcohol (generally ethanol or methanol) and small amounts of water may be added.

EISA is most often used in combination with the *dip-coating* deposition technique (or, less frequently, with *spin-coating*). In dip-coating, a substrate is dipped into the solution and extracted at a constant speed (typically, few mm·s^{-1}). Due to the solution-substrate wettability, a liquid layer is formed on the substrate, whose thickness depends on the extraction speed (*pulling rate*) and the viscosity of the solution. As the solvent evaporates from the liquid layer, the inorganic precursors undergo condensation and crosslinking processes, thus forming a gel, which can be defined as a phase constituted by a more or less condensed inorganic network within which residual solvent molecules form an interconnected liquid phase. In spin-coating, few drops of the precursor solution are placed on a substrate, which is then spinned at a constant angular speed (typical values: few thousands of rpm). Thus, a homogeneous film is spread on the substrate due to the centrifugal force. Because films are prepared exclusively by dip-coating in this doctorate work—as in most works in the literature—we will refer to this deposition technique.

In EISA (see Figure 1.17), solvent evaporation occurring in the first seconds after deposition causes an increase in the concentration of non-volatile (organic and inorganic) species in the film. This triggers both self-assembly and inorganic crosslinking, which therefore act concurrently. Thus, evaporation is not the driving force for self-assembly as such, but rather keeps the system on a pathway where self-assembly can occur during film formation. As we have seen, a more thermodynamic synthetic control allows for the formation of well-orderer mesostructures, whereas an increasing kinetic control leads to the formation of ill-defined or disordered mesostructures. The complexity and the rapidity of the concurring phenomena during solvent evaporation justify what is commonly known as *race towards order*: indeed, it is a sort of challenge in that the organic phase must form an or-

dered self-assembled mesophase before inorganic polycondensation stops it. (And of course, to win this race is the researcher's goal.)

That is why one needs to decrease inorganic reactivity, for example adjusting the pH near to the isoelectric point (e.g. in the case of silica alkoxide precursors) or using complexing agents (e.g. in the case of titania) and working in dilute conditions. EISA is a technique that can be readily adapted to perform these tasks: the chemical composition and the processing parameters can be adjusted in order to form well-ordered mesostructures, as well as to obtain the properties that are required for functional applications (i.e. homogeneity, transparency, etc.). Besides, EISA can be used in such different preparation processes based on solvent evaporation (e.g. dip- and spin-coating,[95] inkjet printing,[98] aerosol[99]) and self-assembly can be tuned by a careful control of the solvent evaporation process.[100] In this way, mesoporous materials in forms other than films can be prepared (e.g. mesoporous micro- and nano-spheres[101,102], monolayers[103,104], nanoscale islands[105]). Thermal treatments can follow the deposition step in order to promote further condensation, mechanically stabilise the mesostructure and remove the surfactant. Further operations that may be performed on films include chemical grafting of functional groups or molecules on the mesopore surface in order to change the physicochemical properties (e.g. grafting of organic groups in order to increase hydrophobicity) or the functional properties (e.g. inclusion of metallic[106] or semiconductor[107,108] nanoparticles within the mesopores for photocatalysis and sensing).

To summarise, mesoporous materials prepared by EISA require an adequate *composition of the initial solution* (inorganic precursors, templating agents, volatile media), the shape can be decided by selecting an *evaporation method* and the physicochemical and functional properties can be created or tuned by a thermal or chemical *post-synthesis modification*. As a consequence, a reproducible synthesis of mesoporous materials via EISA requires control on three levels: (1) chemical composition of the precursor solution, (2) deposition process, (3) post-treatments performed on the film. The remainder of this section tackles these synthetic and processing parameters.

1.7.3 Precursor solution

Solvent   The choice of solvent must meet at least three requirements: the solution must completely wet the substrate in order to ensure good film homogeneity; furthermore, the solvent must be volatile to promote a fast increase in concentration of the non-volatile species; and it must be a good solvent for the organic and inorganic precursors. Generally, ethanol is the preferred choice, as it can wet both hydrophilic and hydrophobic substrates, it is volatile, and it can easily dissolve amphiphilic block copolymers as well as inorganic alkoxides and metal salts.

An organic additive can selectively swell a region of the block copolymer causing a change in micelle shape and volume. Mesoporous silica films with a rhombohedral $R\bar{3}m$ symmetry have been obtained from a solution containing TEOS and CTAB to which 1,3,5-triisopropylbenzene (TIPB) was added.[109] Notably, the rhombohedral mesophase does not exist in the surfactant phase diagram and occurs as a distortion of a hexagonal *p6mm* mesophase via an intermediate cubic $Im\bar{3}m$ mesophase. The transition from cylindrical micelles to spheroids that yields the three-dimensional open mesostructure is driven by the requirement to cover an increased volume of TIPB with CTAB. TIPB swells out the hydrocarbon chains
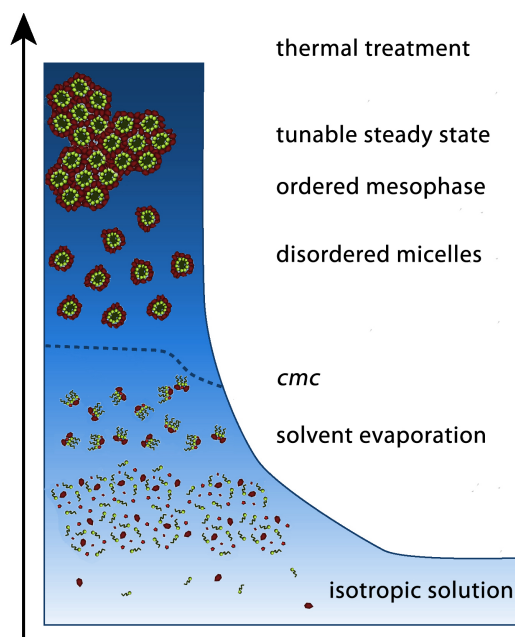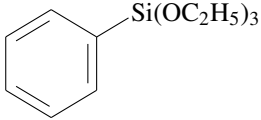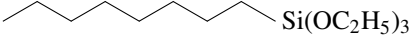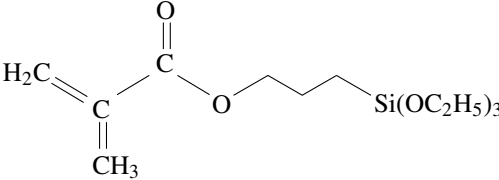
Figure 1.17. *Scheme of the formation of a mesostructured film by evaporation-induced self-assembly. The arrow indicates the time line. Step 1: In the isotropic solution condensation is slowed down and the nonvolatile precursors are free surfactant molecules and inorganic oligomers. Step 2: Solvent evaporation triggers the formation of surfactant-inorganic units. Step 3: Evaporation is complete and the film equilibrates its water content with the environment (tunable steady state, TSS). Step 4: The thermal treatment stabilises the mesostructure.*

of the surfactant until saturation, then pure TIPB core is formed at the centre of the micelle. To cover the TIPB molecules with CTAB the micelles become more spherical, inducing the formation of three-dimensional open mesostructure.

Inorganic precursors   In the synthesis of mesoporous silica, alkoxysilanes such as TEOS are widely employed. Small quantities of an organically-substituted alkoxysilane, called organo-alkoxysilane, may be added to TEOS. In organo-alkoxysilanes one or more hydrolysable groups are substituted by organic groups which are not hydrolysed due to the high stability of the Si-C bond. Therefore, these organic groups eventually end up covalently linked to the final inorganic framework, and a wide variety of mesoporous or mesostructured hybrid *organosilica* products can be obtained.[110]

Inorganic reactivity can be controlled by varying the pH. In silicon alkoxides, less ordered mesophases are obtained at high pH values (5–7), where condensation is fast and prevails over mesostructure formation (i.e. $k_{\text{inorg}} > k_{\text{org}}, k_{\text{inter}}$). A pH close to the isoelectric point (pH≈2) allows obtaining a better mesostructure organisation. Working in high dilution conditions, silica condensation is further inhibited and the solution is very stable in time (up to several months). Transition metal alkoxides are much more reactive, according to the series: $Si(OR)_4 \ll Sn(OR)_4 \sim Ti(OR)_4 < Zr(OR)_4 \sim Ce(OR)_4$.[111] This is because the reactivity of transition metal precursors is strongly dependent on the electrophilicity of the metal centre (hydrolysis and condensation proceed through nucleophilic attack by water molecules), therefore the reactivity trend is Si<Ti<Zr<Hf.[112] Condensation

Table 1.8. *Examples of organically modified Si alkoxides used in one-pot syntheses of hybrid films.*

Name	Chemical formula
Methyl-triethoxysilane (MTES)	$CH_3-Si(OCH_2CH_3)_3$
Dimethyl-diethoxysilane (DMDES)	$(CH_3)_2-Si(OCH_2CH_3)_2$
Phenyl-triethoxysilane (PhTES)	$\text{C}_6\text{H}_5-Si(OC_2H_5)_3$ (phenyl ring with $Si(OC_2H_5)_3$)
Octadecyl-triethoxysilane (OTES)	$CH_3(CH_2)_{17}-Si(OC_2H_5)_3$
3-Aminopropyl-triethoxysilane (APS)	$NH_2-CH_2CH_2CH_2-Si(OC_2H_5)_3$
Methacryloxypropyl-triethoxysilane	$CH_2{=}C(CH_3)-C(=O)-O-CH_2CH_2CH_2-Si(OC_2H_5)_3$

can be inhibited by introducing complexing agents, such as acetyl acetone, which are effective in sequestering the transition metal ion.

Water This is truly a multipurpose component of the precursor solution. In silica-based systems it takes part in alkoxide hydrolysis and condensation. For small values of $h =$ [H_2O]/[Si], no mesostructure or a wormlike mesophase forms, whereas too high h values may lead to uncontrolled condensation and poor order. A typical value found in the synthesis of silica is $h = 5\text{--}10$, which is relatively independent of the type of inorganic precursor (a silicon alkoxide or a salt). Water molecules are adsorbed on the hydrophilic crown of the micelles, increasing the hydrophilic headgroup area a_0 and thus decreasing the geometric packing factor g. In this way an increase in hybrid interface curvature is observed and the formation of spherical micelles rather than cylindrical is favoured. Besides, water favours the formation of silanols at the hybrid interface which contribute to strengthening the interactions between the inorganic precursors and the surfactant. In general, the role of water at the hybrid interface is of key importance in the synthesis of all mesostructured films.

A notable example is mesostructured TiO_2 obtained from $TiCl_4$, where the presence of significant amounts of water is essential in order to form an ordered mesostructure. Here, water is supplied either in the precursor solution or treating the as-deposited films with high relative humidity for a couple of seconds within a short time since solvent evaporation.[30,113] At least three effects can be discerned: (1) water promotes Ti(IV) hydrolysis and favours the formation of hy-

drophilic species such as $TiCl_{4-x}(OEt)_x$.[114] (2) Water favours phase separation by increasing the entity of the interactions at the interface, swelling the hydrophilic corona, thus increasing its curvature. (3) Water lowers viscosity acting as a lubricant by forming a layer around each micelle, permitting structural rearrangements in the mesophase which lead to a better degree of order.[26,114]

Structure-directing agent   The choice of type and quantity of surfactant has been shown to be a key parameter in order to obtain a final mesostructure with a given symmetry. Regarding the copolymer type, we have summarised in Sections 1.6.2 and 1.6.3 that size, architecture and chemical composition of the amphiphilic block copolymers deeply affect the final mesostructure. In particular, for simple estimates one can use the geometric packing factor g to predict whether high-curvature cubic or low-curvature 2d-hex mesostructures will form.

A calculation of the quantity to be introduced into the precursor solution can be made by inspection of the surfactant/water phase diagram, considering the surfactant volume fraction $\Phi = \frac{V_{surf}}{V_{surf}+V_{inorg}}$). As we have shown in Section 1.6.3, this is a good predictive model that allows calculating the quantities of inorganic and organic precursors to introduce into the precursor solution in order to attain a given mesophase symmetry, similar to the phase diagram approach of TLCT.

However, a work on oriented silica membranes templated by Pluronic F127[115] has revealed that wormlike or hexagonal phases can be obtained in conditions where cubic phases are expected ($\Phi < 70\%$). In these "silicatropic" hybrids, the final mesostructure can be tailored by the water content in solution (h), keeping Φ constant. The crucial role of h can be rationalised in this way: Φ is not the only parameter that directs mesophase formation, as the extent of the silica-template interface should be taken into account. Water helps to fold the hybrid interface with a higher curvature radius,[114] and also generates more hydrophilic silanol ends; a more hydrophilic hybrid interface tends to maximise interactions with the hydrophilic block and enhancing curvature. Therefore, the final mesophase symmetry cannot be predicted only on the grounds of the inorganic-template fraction (Φ), thus predictions made purely with phase diagrams may be misleading and care should be exerted when using this model.

It has been demonstrated[26] that in the case of films V_{inorg} should take into account also the presence of water as relative humidity in the deposition chamber, beside water contained in the precursor solution. In fact, as we describe in Section 1.7.4, the amount of relative humidity is crucial in determining mesostructure formation, in that it can diffuse from the environment into the film, affecting the interactions at the hybrid interface and exerting a critical role on micelle curvature.

Furthermore, the presence of solvents other than those reported in the phase diagrams can influence the chemistry of these systems, and mesophase symmetries different than those reported in the phase diagram have been reported. For example, $R\bar{3}m$ structures in mesoporous TiO_2 have been obtained using 1-butanol as the solvent: this enhances microphase segregation increasing the curvature at the hybrid interface, because the polar end of 1-butanol is localised at the hydrophilic/hydrophobic interface between the poly(ethylene oxide) and poly(propylene oxide) blocks, thereby helping to stabilise the mesophase with the required surface curvature.[116] Another factor that must be kept in mind is that the EISA synthesis conditions are dramatically affected by kinetic factors, whereas a phase diagram refers to a system in its thermodynamic equilibrium. Polycondensa-

tion increases film viscosity and reduces micelle mobility, therefore the mesophase in a film is typically in a metastable state, out of thermodynamic equilibrium.

To summarise, the synthesis parameters that are used to predict mesophase symmetry can be overwhelmed by other factors (e.g. water content in solution, relative humidity, evaporation rate, presence of a solvent with different polarity) that force the structure into an unpredicted phase.[117] In practice, the *molar* ratio $s =$[surfactant]/[inorganic] is generally reported in research works rather than the surfactant/inorganic *volume* fraction. In fact, s is considered more as a heuristic parameter, often determined through educated guesses in a trial-and-error fashion, where different quantities of surfactant are systematically varied, and the characterisation of the films thus obtained are used as a feedback to formulate a "working recipe". The s values are on the order of magnitude of 0.01 for ionic surfactants (e.g. CTAB), whereas for high MW block copolymers (e.g. Pluronic type) they can be as low as 10^{-3} or 10^{-4}.

Catalyst When an alkoxide is used as the inorganic precursor, a catalyst increases the kinetics of hydrolysis and condensation. There is a fundamental difference between basic and acid catalysts, in that the former favour hydrolysis and inhibit condensation, whereas the latter favour condensation and inhibit hydrolysis.[23] In the synthesis of mesoporous films, an acid catalyst is generally used, as it ensures good quality and homogeneity of the film. In particular, HCl is the choice in most cases as its high volatility ensures full evaporation once its function is not required any more and therefore it does not remain in the film as impurity. Furthermore, its evaporation causes the pH inside the film to increase, which favours condensation reactions, stiffening the mesostructure. When transition metal salts are used as the inorganic precursors (e.g. $TiCl_4$), the presence of Cl^- ions in the solution controls condensation kinetics by forming coordinated species $TiCl_{4-x}(OEt)_x$. After deposition, hydrolysis and condensation are accelerated by HCl evaporation.[114,118] In the case of silica, the pH is generally set near the isoelectric point, which is defined as the pH of a solution or dispersion at which the net charge on the macromolecules or colloidal particles is zero ($pH_{iep} \approx 2$ for silica, $pH_{iep} \approx 6$ for titania): in this way, the inorganic colloids in the solution do not aggregate, and the solution can be stable even for several months.

Ageing Hydrolysis and polycondensation reactions of inorganic precursors in the coating solution cause the formation and growth of oligomeric species (nano-building blocks, NBBs). In the case of silica, these can be constituted by cyclic, linear or branched structures, depending on the composition and the pH. The size of these oligomers increases as a function of time. Because the size of these NBBs is critical in mesostructure formation, it is of crucial importance to control ageing of the coating solution (at a first approximation, ageing can be identified as the time interval between the preparation of the solution and its use in the dip-coating).

Experimental results have demonstrated that ageing is a critical parameter which can affect deeply the degree of order of the final mesostructure. Structural information on silica oligomers can be inferred from ^{29}Si NMR measurements on solutions containing the EISA precursors aged for different times, by relating the observed chemical shift to the number of O atoms to which a Si atom is bonded. The notation Q_i is generally adopted, where i represents the number of O atoms bonded to a single Si atom and $0 \leq i \leq 4$. Grosso et al. have observed a trend in
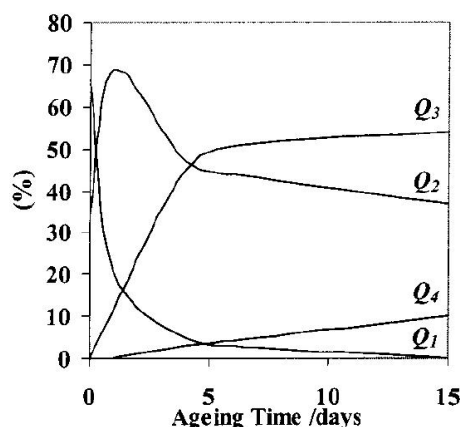
Figure 1.18. *Ageing time dependence of the relative amounts of Q_1, Q_2, Q_3 and Q_4 silica species in a solution containing CTAB/TEOS = 0.10. These evolutions were deduced from the ^{29}Si liquid-phase NMR spectra by integrating and adding Q_i peaks. Reproduced from Grosso et al.* [119]

Q_i concentration depending on the solution (TEOS, CTAB, HCl, H_2O in EtOH) ageing time (Figure 1.18). This trend was compared to the degree of order of the final mesostructure in films obtained by dip-coating with the aged solutions, which was estimated by the intensity of the main small-angle diffraction peak. The most ordered mesostructures are observed when the concentration of Q_2 and Q_3 is highest, corresponding to an ageing time of 6–7 days.[119] If ageing is either shortened or protracted, the resulting mesostructure is less ordered or absent. Too long an ageing leads to the formation of large silica oligomers that are not capable of accommodating the curvature at the hybrid interface during mesophase formation, whereas too short an ageing does not result in the formation of well-defined NBBs, which again leads to poor order. Most likely, the NBBs cannot exceed the feature size of a mesostructure, typically 1–20 nm. Optimal ageing times depend strongly on solution composition as well as its temperature. For a similar TEOS/ CTAB/ EtOH system but with a higher $[H_2O]/[Si]$ ratio and a lower $[EtOH]/[Si]$ ratio, Klotz et al. estimate an optimum ageing time of 200 minutes, which is lower of a factor of 50 than that reported by Grosso.[120]

In summary, controlling ageing permits controlling the size of the NBBs that build up a hybrid interface, thus it turns out to be a key requisite in the design of a synthesis process. For each system, an optimum ageing time must be determined, depending on the type and concentration of surfactant, water and inorganic precursor.

1.7.4   Film deposition

Whereas control of the precursor solution requires understanding the chemistry of the inorganic precursors and the self-assembly properties of the surfactant, in the deposition process control is transferred to the external conditions. The deposition step is no less critical than the preparation of the precursor solution, because in this stage inorganic condensation and self-assembly take place, driven by the local thermodynamic and kinetic conditions and ultimately triggered by the fast evaporation of the solvent.

Solvent evaporation It has been suggested that the departure of solvent from the film-air interface causes an increase in concentration of the inorganic and the organic nonvolatile species, which undergo self-assembly and condensation reactions and form a mesostructure. As the evaporation rate is faster at the film-air than at the film-substrate interface, nonvolatile species become more concentrated in the former than in the latter regions, triggering diffusive processes due to the concentration gradient within the film. Therefore, while solvent evaporates, the composition of the film is not univocally determined, but rather there exist several compositions in different regions, which constantly evolve with time until most solvent is evaporated (typically within 10–30 seconds).‖

Though it is practically impossible to calculate the exact composition as a function of space and time, there is one phenomenon that can give insight on what occurs within the film during the evaporation process: mesophase transition. Performing in situ SAXS measurements during dip-coating, one can obtain a time-resolved sequence of diffraction patterns which informs us on the structural evolution of the forming mesophase. The sequence: lamellar phase → 3d hexagonal → cubic is typically observed, corresponding to the sequence: isotropic → spherical micelles → cylindrical micelles → lamellar phase observed in the surfactant-solvent phase diagram for increasing concentrations.[121]

Different mesophases can be obtained by varying solvent evaporation rate: in an interesting study, a vacuum pump is connected to a cylindrical pipe sitting at given distances from a substrate covered with the desired solution, which is let to evaporate. By varying the pipe-to-sample distance, it is possible to adjust the evaporation rate of the liquid film (this procedure is called "vacuum-assisted evaporation", VAE).[122] For high evaporation rates, the simultaneous presence of different mesophases can be observed, an effect that can be ascribed to different compositions at different depths caused by high concentration gradient: since evaporation occurs at the film-air interface, nonvolatile concentration is higher in this region, thus giving an ordered phase sooner than in the region close to the substrate. As different compositions generally correspond to different stable symmetries in the phase diagram, different or overlapped diffraction patterns are observed. Where solvent is less present (close to the film-air interface) inorganic condensation may form a solid barrier that prevents further evaporation, thus multiple mesostructures are likely to be "frozen" in their metastable states. This can explain an aspect that is sometimes observed in TEM cross-sectional images of mesoporous films, that is an ordered structure near the surface and a wormlike or totally disordered region within the film (see Figure 1.19).

Relative humidity and tunable steady state There is evidence for structural rearrangements in the mesophase occurring even long after the solvent evaporation step. Experimentally, in situ SAXS measurements point out that mesophase transitions can be induced by the external environment well after solvent evaporation, most typically by a variation in relative humidity. Mesophase transitions reflect structural rearrangements in mesophase architecture, which are observed to be reversible as long as the film viscosity is low (i.e. as long as the inorganic network has a low degree of crosslinking). Therefore, we can identify a time inter-

---

‖Solvent evaporation may be considered finished when the film thickness stops decreasing. This can be measured, for example, by in situ optical interferometry.
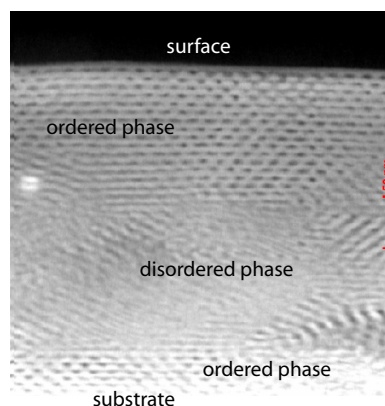
Figure 1.19. *TEM cross-sectional image of a mesoporous silica film obtained from TEOS and block copolymer Pluronic F127, showing a disordered region sandwiched between the two ordered regions at the film-air and film-substrate interfaces. Scale bar, 50 nm.*

val between film deposition and when inorganic condensation hinders mesophase rearrangements—this latter represents a broad time interval itself since inorganic condensation is a continuous process, in which kinetics varies according to the system in question. One of the most notable examples where this effect is reported is a work by the research group led by David Grosso, who first demonstrated the very important role of water originating from external humidity (relative humidity, RH) in the texturation of the hybrid mesostructure.[123] In this work, the effect of relative humidity during dip-coating is observed and mesostructure organisation is demonstrated to be affected by the diffusion of volatile molecules equilibrating between the environment and the film media. More precisely, high RH (70%) favours the formation of a *Pm3n* cubic phase, whereas low RH (20%) leads to lower quantity of water inside the film, which promotes the two-dimensional *p6mm* mesostructure. Too low RH may lead to poorly-defined structures.

If RH is sufficiently high, water is encouraged to stay inside the film, or a diffusive motion occurs from the environment into the coating. As we have said, water is preferentially localised in the hydrophilic part of the film, i.e. on the hydrophilic coronas of micelles and in between. During this dynamic equilibrium state, condensation progressively takes place, stabilising the inorganic framework around the spherical micelles and avoiding further phase transitions when the viscosity is too high. This state of as-deposited mesostructured films is called *tunable steady state* (TSS).** This time interval depends on the chemical composition of the film and may last up to few hours.

To sum up, we can identify a threefold role of RH. (1) It acts as a swelling agent with respect to the hydrophilic headgroups, thus increasing the micelle curvature and creating a well-defined hybrid interface. (2) It contributes to lowering the film viscosity, acting as a lubricant and favouring mobility of NBBs and mesophase rearrangements. This ultimately leads to a better degree of order and sometimes to mesophase symmetries not immediately predicted by phase diagrams: different symmetries can be obtained with different RH values, in particular cubic structures

---

**In the original work[123] it is "modulable steady state". However, because the term "modulable" does not exist in English language, this term has been replaced with "tunable".

are favoured for high RH. (3) In films obtained from inorganic salts (e.g. TiO_2 from $TiCl_4$, the departure of water from the film allows for HCl evaporation through diffusive motion, thus increasing inorganic polycondensation.

Because the amount of water in a film depends critically on RH, it is useful to derive a relation between them, especially if an estimate of V_{inorg} is needed in order to calculate the copolymer volume fraction Φ (page 46). This is often accomplished by resorting to experimental techniques; unfortunately, the quantity of matter in films is too low, so determining the total volume fraction of water is a difficult task and other systems than thin films are used. For example, Karl-Fischer titration measurements have been performed on a small amount of solution let to evaporate in the presence of an air flux with a preset RH.[123] Indicatively (and for the system studied by the authors) a correspondence between RH and water content expressed as $h =[H_2O]/[Si]$ can be found, corresponding to $h = 0.5, 4, 7$ for RH = 20%, 40%, 70%, respectively. Another way is to measure the film thickness by ellipsometric spectroscopy at different RH values: the variation in thickness is related to different concentrations of water in the film.[100] Based on these considerations, it is straightforward to conclude that one major key issue is to determine the temporal extent of the TSS in order to understand and direct the physicochemical phenomena occurring in this time frame. This is why dip-coaters are generally enclosed in a cabinet or in a glove box, in which air with controlled RH can be fluxed.

Dip-coating pulling rate   The film thickness bears a direct proportion with the speed at which the substrate is extracted from the solution (pulling rate) in the dip-coating process (in spin-coating this parameter is rotation speed, usually expressed in rpm). This well-known effect is due to surface tension effects occurring at the solution-film-air interface, which become less critical when the pulling rate is increased.[23] In terms of mesostructure order, a lower degree of order is generally observed when the pulling rate is increased. This can be explained considering that condensation is fastest at the film-air interface (*vide supra*): a high concentration gradient is set up and further evaporation from the bottom of the film is inhibited if the topmost layer is too crosslinked.[119]

1.7.5 Post-treatments

Thermal treatment   It has the double purpose of promoting inorganic condensation and decomposing the organic phase in order to free the mesopores (calcination). Generally, mild treatments with thermal ramps and steps are preferred: abrupt treatments at high temperatures may cause mechanical stress in the sample which can damage the mesostructure and lead to macroscopic cracking. A phenomenon that is always observed is thermal shrinkage: because the film is pinned to the substrate, the contraction occurs exclusively along the direction perpendicular to the substrate (out of plane), whereas the contraction parallel to the substrate (in plane) is negligible. As a consequence, calcination somewhat alters the shape of mesopores: this is evident in spherical pores, which become oblate spheroids. Furthermore, the thermal treatment may lead to the fusion of pores along those crystallographic directions where packing is most dense (e.g. [111] in cubic structures) forming structures that may resemble cylindrical pores when observed by TEM (see for example Chapter 2, page 78).

In transition metal oxides, thermal treatments may lead to phenomena related to inorganic crystallisation. This is often a very critical step, in that crystallisation and phase transitions can cause mesostructure collapse, especially if the surfactant decomposes at a temperature below the temperature of crystallisation. In this case the surfactant's role as a "supramolecular scaffold", ensuring stability while inorganic condensation/crystallization are in progress, ceases. These phenomena can be controlled by performing suitable thermal treatments, and mesoporous oxides can be obtained with nanocrystalline inorganic walls,[26] combining the physico-chemical properties of crystalline metal oxides with a high specific surface area.

In situ simultaneous small- and wide- angle X-ray scattering (SAXS/WAXS) experiments using synchrotron radiation have been performed on as-deposited mesostructured titania films.[124] In this way, the mechanisms involved during the thermal crystallisation of mesoporous TiO_2 films have been elucidated casting light on mesostructure formation and inorganic crystallisation. The growth of anatase particles was shown to be controllable to prevent mesostructure collapse. In particular, a fast and short treatment at elevated temperature applied to the cubic initial mesostructure allows rapid growing of the anatase particles up to the limit imposed by the mesostructure. Furthermore, the disappearing of the in-plane reflections and the simultaneous reinforcement of the out-of-plane reflection suggests that pores merge along the directions where the mesopore density is highest, i.e. [111] and [11$\bar{1}$], and large single crystallised particles are formed through epitaxial fusion/nucleation.

Ageing at controlled RH Recent studies have emphasised the importance of keeping the as-deposited mesostructured films (especially based on transition metal oxides) in controlled humidity conditions for a few days before performing thermal treatment.[26] For example, mesoporous yttria-zirconia and ceria-zirconia films with 2d-hexagonal and cubic structures show a relation between mesostructure order and humidity post-treatment.[125] Mesoporous tin oxide films with an orthorhombic *Fmmm* symmetry have been prepared by the Hillhouse research group.[126] The as-deposited samples show no long-range order. However, if the films are aged at high RH ($\approx$80%) for a time interval between 30 minutes and 48 hours, an ordered mesophase appears (a treatment called delayed humidity treatment (DHT) by the authors). The mechanisms leading to self-assembly have not been fully elucidated. What is sure, is that in this case we cannot speak of EISA, in that solvent evaporation is considered to have ceased when DHT begins, and self-assembly appears to be triggered by some unclear process during DHT itself.

Post-functionalisation The mesopores can be used to chemically graft functional (typically organic) groups on the inorganic walls, as well as to physically adsorb ions. The functional properties of grafted chemical groups can be exploited for particular applications and are enhanced by the high specific surface area exhibited by mesoporous films. The natural candidate for chemical grafting is silica, due to the high stability of the Si-C bond and the presence of reactive silanols, whereas transition metal oxides are somewhat more difficult to functionalise. For example, sensors with high sensitivity and selectivity towards uranyl cations have been produced by grafting sylilated β-diketone compounds in mesoporous silica.[127] Mesopores can also be exploited for the controlled growth of nanoclusters: this subject

will be covered in Chapter 4, where the experimental results on this topic will be presented.

1.7.6 Examples of prospected applications

The synthesis of mesoporous materials in the form of films enables us to devise new functional applications. Many patents, aimed at protecting synthesis methods and compositions of matter, have been deposited. As we have mentioned, the interest in mesoporous film is motivated essentially by (1) the high specific surface area, which may or may not be interconnected, (2) the possibility to introduce grafted or co-condensed functional groups on the mesopore surface, (3) the particular physicochemical properties, especially in transition metal oxides. We will now briefly examine three selected examples in order to clarify the potentials of mesoporous films in advanced applications: low-k interlayers, solar cells and sensors.

Low-k interlayers

A signal travelling in an integrated circuit is subject to a delay caused by resistance-capacitance (RC) coupling between two adjacent conductors, related to power dissipation as heat, and creates interference between the two adjacent circuits (crosstalk). These negative effects become more intense as the feature size is decreased. Therefore, as smaller and smaller integrated circuits are built, new solutions have to be looked for: one possibility is to insert a low dielectric constant (k) layer between two conductors, thus decreasing C.[128–130] A further decrease in k can be obtained by choosing a material with low polarisability, and mesoporous silica seems to be a good choice since it contains a high volumetric fraction of air. By substituting the Si-O bonds on the mesopore surface with species containing Si-C or Si-F bonds, low dielectric constant values are obtained, due to the low polarisability of such bonds and because the hydrophobic environment inhibits water (high k) uptake. This can be accomplished by the chemical modification of the mesopore surface by a post-synthetic grafting or by co-condensing hybrid organic-inorganic precursors during film synthesis.[131–133]

Solar cells

Titania is one of the most studied systems in photovoltaic applications, in particular in dye-sensitised solar cells (DSSC), commonly known as Grätzel cells. DSSC are made of nanocrystalline titania impregnated with an electrolyte and a suitable dye. The mechanism of current photogeneration is: (1) the dye absorbs a photon and creates an exciton, (2) the exciton is separated at the titania-dye interface, (3) charge transport occurs in TiO_2 (electrons) and electrolytic solution (holes). The formation of the exciton represents a critical step: because it can travel to a distance of $d \sim 20$ nm before radiative recombination, it is essential to have a nanoarchitecture with features smaller than d, so that the exciton can reach the interface and yield the opposite charges before recombination occurs. Such a structure can be obtained maximising the interfacial area, typically mixing the two phases on a nanometric level. A marked increase in interfacial area can be obtained with mesoporous titania with an accurate control on pore size and mesophase symmetry; the interconnected inorganic structure ensures electron transport towards the electrodes

and the interconnected mesopores are filled with a continuous electrolyte solution that permits hole transport. [134,135]

Hybrid organic-inorganic DSSC can be obtained by impregnating mesoporous titania with a semiconducting polymer (e.g. polythiophene) which acts both as the light absorber and as the hole-transporting medium. [136,137]

Humidity sensors

In this case, the principle is physisorption of H_2O molecules by the OH groups present on the mesopore surface. If a water molecule forms two hydrogen bonds with two hydroxyls, a proton can be transferred to water and form an hydronium ion. Thus, a H_3O^+ layer is formed on the mesopore surface, whose electrical conductivity depends on relative humidity according to Grotthus' model. Mesoporous silica films have been shown to have sensing properties selective towards water and ethanol, due to the high specific surface area that enhances protonic conduction. [138,139]

References

[1] G. Stix. Little big science. *Scientific American*, **2001**, *285*(3), 32–38.

[2] G. A. Ozin, A. C. Arsenault. *Nanochemistry. A chemical approach to nanomaterials*. The Royal Society of Chemistry, Cambridge, UK, 2005.

[3] D. M. Eigler, E. K. Schweizer. Positioning single atoms with a scanning tunnelling microscope. *Nature*, **1990**, *344*, 524–526.

[4] Avaliable online at http://www.zyvex.com/nanotech/feynman.html (accessed December 2007).

[5] http://www.foresight.org/nanodot/?p=1188 (December 2007).

[6] N. M. Pugno. Space elevator: out of order? *Nano Today*, **2007**, *2*, 44–47.

[7] C. A. Haberzettl. Nanomedicine: destination or journey? *Nanotechnology*, **2002**, *13*, R9–R13.

[8] http://www.nanotech-now.com/predictions.htm (accessed December 2007).

[9] Nanoscience and nanotechnologies: opportunities and uncertainties. Technical report, Royal Society and Royal Academy of Engineering, **2004**. URL: http://www.nanotec.org.uk/finalReport.htm (accessed December 2007).

[10] J. Y. Cheng, C. A. Ross, H. I. Smith, E. L. Thomas. Templated self-assembly of block copolymers: Top-down helps bottom-up. *Adv. Mater.*, **2006**, *18*, 2505–2521.

[11] G. A. Ozin, S. M. Yang. The race for the photonic chip: colloidal crystal assembly in silicon wafers. *Adv. Funct. Mater.*, **2001**, *11*, 95–104.

[12] http://en.wikipedia.org/wiki/Self-assembly (contributed by the Author, accessed December 2007).

[13] Special issue on self-assembly. *Proc. Natl. Acad. Sci U.S.A.*, **2002**, *99*(8).

[14] G. M. Whitesides, B. Grzybowski. Self-assembly at all scales. *Science*, **2005**, *295*, 2418–2421.

[15] G. M. Whitesides, M. Boncheva. Beyond molecules: Self-assembly of mesoscopic and macroscopic components. *Proc. Natl. Acad. Sci U.S.A.*, **2002**, *99*, 4769–4774.

[16] H. R. Horton, L. A. Moran, R. S. Ochs, J. D. Rawn, K. G. Scrimgeour. *Principles of biochemistry*. Prentice-Hall, Englewood Cliffs, NJ, 1993.

[17] P. A. Kralchevsky, K. Nagayama. Capillary forces between colloidal particles. *Langmuir*, **1994**, *10*, 23–36.

[18] J.-M. Lehn. Toward self-organization and complex matter. *Science*, **2005**, *295*, 2400–2403.

[19] S. Förster, T. Plantenberg. From self-organizing polymers to nanohybrid and bio-materials. *Angew. Chem. Int. Ed. Engl.*, **2002**, *41*, 688–714.

[20] S. Mann. *Biomineralization. Principles and concepts in bioinorganic materials chemistry*. Oxford University Press, Oxford, 2001.

[21] J. N. Israelachvili. *Intermolecular and surface forces*. Academic Press Ltd, London, 2nd edition, 1998.

[22] G. Soler-Illia, C. Sanchez, B. Lebeau, J. Patarin. Chemical strategies to design textured materials: From microporous and mesoporous oxides to nanonetworks and hierarchical structures. *Chem. Rev.*, **2002**, *102*, 4093–4138.

[23] C. J. Brinker, G. W. Scherer. *Sol-gel science: The physics and chemistry of sol-gel processing*. Academic Press, San Diego, 1992.

[24] J. D. Wright, N. A. J. M. Sommerdijk. *Sol-gel materials: Chemistry and applications*. CRC Press, Boca Raton, 2001.

[25] W. Stober, A. Fink, E. Bohn. Controlled growth of monodisperse silica spheres in the micron size range. *J. Colloid Interface Sci.*, **1968**, *26*, 62–69.

[26] E. L. Crepaldi, G. Soler-Illia, D. Grosso, F. Cagnol, F. Ribot, C. Sanchez. Controlled formation of highly organized mesoporous titania thin films: from mesostructured hybrids to mesoporous anatase TiO_2. *J. Am. Chem. Soc.*, **2003**, *125*, 9770–9786.

[27] A. Vioux. Nonhydrolytic sol-gel routes to oxides. *Chem. Mater.*, **1997**, *9*, 2292–2299.

[28] T. Cassagneau, F. Caruso. Oligosilsesquioxanes as versatile building blocks for the preparation of self-assembled thin films. *J. Am. Chem. Soc.*, **2002**, *124*, 8172–8180.

[29] S. Lücke, K. Stoppek-Langner, J. S. Murday, R. E. Palmer, R. B. Jackman, M. Petty. Polyhedral oligosilsesquioxanes (POSS)-building blocks for the development of nano-structured materials. *Appl. Surf. Sci.*, **1999**, *144-145*, 713–715.

[30] G. Soler-Illia, E. Scolan, A. Louis, P.-A. Albouy, C. Sanchez. Design of meso-structured titanium oxo based hybrid organic-inorganic networks. *New J. Chem.*, **2001**, *25*, 156–165.

[31] L. L. Hench, J. K. West. The sol-gel process. *Chem. Rev.*, **1990**, *90*, 33–72.

[32] F. Schüth, K. S. W. Sing, J. Weitkamp, editors. *Handbook of porous solids*. Wiley-VCH Verlag GmbH, Weinheim, Germany, 2002.

[33] A. Sayari, P. Liu. Non-silica periodic mesostructured materials: recent progress. *Microp. Mater.*, **1997**, *12*, 149–177.

[34] J. Roquerol, D. Avnir, C. W. Fairbridge, D. H. Everett, J. H. Haynes, N. Pernicone, J. D. F. Ramsay, K. S. W. Sing, K. K. Unger. Recommendations for the characterization of porous solids. *Pure and Appl. Chem.*, **1994**, *66*, 1739–1758.

[35] P. Behrens, G. D. Stucky. Ordered molecular arrays as templates: A new approach to the synthesis of mesoporous materials. *Angew. Chem. Int. Ed. Engl.*, **1993**, *32*, 696–699.

[36] S. Beck, J, J. C. Vartuli, W. J. Roth, M. E. Leonowicz, C. T. Kresge, K. D. Schmitt, C. T.-W. Chu, D. H. Olson, E. W. Sheppard, S. B. McCullen, J. B. Higgins, J. L. Schlenker. A new family of mesoporous molecular sieves prepared with liquid crystal templates. *J. Am. Chem. Soc.*, **1992**, *114*, 10834–10843.

[37] C. T. Kresge, M. E. Leonowicz, W. J. Roth, J. C. Vartuli, S. Beck, J. Ordered mesoporous molecular sieves synthesized by a liquid-crystal template mechanism. *Nature*, **1992**, *359*, 710–711.

[38] J. C. Vartuli, K. D. Schmitt, C. T. Kresge, W. J. Roth, M. E. Leonowicz, S. B. McCullen, S. D. Hellring, S. Beck, J, J. L. Schlenker. Effect of surfactant/silica molar ratios on the formation of mesoporous molecular sieves: Inorganic mimicry of

surfactant liquid-crystal phases and mechanistic implications. *Chem. Mater.*, **1994**, *6*, 2317–2316.

[39] J. C. Vartuli, C. T. Kresge, M. E. Leonowicz, A. S. Chu, S. B. McCullen, I. D. Johnson, E. W. Sheppard. Synthesis of mesoporous materials: Liquid-crystal templating versus intercalation of layered silicates. *Chem. Mater.*, **1994**, *6*, 2070–2077.

[40] A. Firouzi, D. Kumar, L. M. Bull, T. Besier, R. Sieger, Q. Huo, S. A. Walker, J. A. Zasadzinski, C. Glinka, J. Nicol, D. I. Margolese, G. D. Stucky, B. F. Chmelka. Cooperative organization of inorganic surfactant and biomimetic assemblies. *Science*, **1995**, *267*, 1138–1143.

[41] A. Monnier, F. Schüth, Q. Huo, D. Kumar, D. I. Margolese, R. S. Maxwell, G. D. Stucky, M. Krishnamurti, P. M. Petroff, A. Firouzi, M. Janicke, B. F. Chmelka. Cooperative formation of inorganic-organic interfaces in the synthesis of silicate mesostructures. *Science*, **1993**, *261*, 1299–1303.

[42] G. D. Stucky, A. Monnier, F. Schüth, Q. Huo, D. I. Margolese, D. Kumar, M. Krishnamurti, P. M. Petroff, A. Firouzi, M. Janicke, B. F. Chmelka. Molecular and atomic arrays in nano-and mesoporous materials synthesis. *Mol. Cryst. Liq. Cryst.*, **1994**, *240*, 187–200.

[43] O. Regev. Nucleation events during the synthesis of mesoporous materials using liquid crystalline templating. *Langmuir*, **1996**, *12*, 4940–4944.

[44] S. Mann, S. L. Burkett, S. A. Davis, C. E. Fowler, N. H. Mendelson, S. D. Sims, D. Walsh, N. T. Whilton. Sol-gel synthesis of organized matter. *Chem. Mater.*, **1997**, *9*, 2300–2310.

[45] Q. Huo, D. I. Margolese, U. Ciesla, D. G. Demuth, P. Feng, T. E. Gier, P. Sieger, A. Firouzi, B. F. Chmelka, F. Schüth, G. D. Stucky. Organization of organic molecules with inorganic molecular species into nanocomposite biphase arrays. *Chem. Mater.*, **1994**, *6*, 1176–1191.

[46] A. Firouzi, F. Atef, A. G. Oertli, G. D. Stucky, B. F. Chmelka. Alkaline lyotropic silicate-surfactant liquid crystals. *J. Am. Chem. Soc.*, **1997**, *119*, 3596–3610.

[47] J. N. Israelachvili, D. J. Mitchell, B. W. Ninham. Theory of self-assembly of hydrocarbon amphiphiles into micelles and bilayers. *J. Chem. Soc. Faraday Trans.*, **1976**, *72*, 1525–1568.

[48] U. Hendriksson, E. S. Blackmore, G. J. T. Tiddy, O. Soderman. Intermediate liquid crystalline phases in the binary system C_{16}TACl-H_2O: An NMR and low-angle X-ray diffraction study. *J. Phys. Chem.*, **1992**, *96*, 3894–3902.

[49] G. J. T. Tiddy. Surfactant-water liquid crystal phases. *Phys. Rep.*, **1980**, *57*, 1–46.

[50] Q. Huo, R. Leon, P. M. Petroff, G. D. Stucky. Mesostructure design with gemini surfactants: supercage formation in a three-dimensional hexagonal array. *Science*, **1995**, *268*, 1324–1327.

[51] Q. Huo, D. I. Margolese, G. D. Stucky. Surfactant control of phases in the synthesis of mesoporous silica-based materials. *Chem. Mater.*, **1996**, *8*, 1147–1160.

[52] C. C. Landry, S. H. Tolbert, K. W. Gallis, A. Monnier, G. D. Stucky, P. Norby, H. J. C. Phase transformations in mesostructured silica/surfactant composites. Mechanisms for change and applications to materials synthesis. *Chem. Mater.*, **2001**, *13*, 1600–1608.

[53] S. H. Tolbert, C. C. Landry, G. D. Stucky, B. F. Chmelka, P. Norby, J. C. Hanson, A. Monnier. Phase transitions in mesostructured silica/surfactant composites: Surfactant packing and the role of charge density matching. *Chem. Mater.*, **2001**, *13*, 2247–2256.

[54] J. M. Kim, Y. Sakamoto, Y. K. Hwang, Y.-U. Kwon, O. Terasaki, S.-E. Park, G. D. Stucky. Structural design of mesoporous silica by micelle-packing control using blends of amphiphilic block copolymers. *J. Phys. Chem. B*, **2002**, *106*, 2252–2258.

[55] P. T. Tanev, T. J. Pinnavaia. A neutral templating route to mesoporous molecular sieves. *Science*, **1995**, *267*, 865–867.

[56] S. A. Bagshaw, E. Prouzet, T. J. Pinnavaia. Templating of mesoporous molecular sieves by nonionic polyethylene oxide surfactants. *Science*, **1995**, *269*, 1242–1244.

[57] G. S. Attard, J. C. Glyde, C. G. Göltner. Liquid-crystalline phases as templates for the synthesis of mesoporous silica. *Nature*, **1995**, *378*, 366–368.

[58] G. Larsen, G. Lotero, M. Marquez. Amine dendrimers as templates for amorphous silica. *J. Phys. Chem. B*, **2000**, *104*, 4840–4843.

[59] V. L. Colvin. From opals to optics: Colloidal photonic crystals. *MRS Bulletin*, **2001**, 637–641.

[60] A. Imhof, D. J. Pine. Ordered macroporous materials by emulsion templating. *Nature*, **1997**, *389*, 948–951.

[61] J. E. G. J. Wijnhoven, W. L. Vos. Preparation of photonic crystals made of air spheres in titania. *Science*, **1998**, *281*, 802–804.

[62] A. Shimojima, N. Umeda, K. Kuroda. Synthesis of layered inorganic-organic nanocomposite films from mono-, di-, and trimethoxy(alkyl)silane-tetramethoxysilane systems. *Chem. Mater.*, **2001**, *13*, 3610–3616.

[63] G. S. Attard, C. G. Göltner, J. M. Corker, S. Henke, R. H. Templer. Liquid-crystal templates for nanostructured metals. *Angew. Chem. Int. Ed. Engl.*, **1997**, *36*, 1315–1317.

[64] G. S. Attard, P. N. Bartlett, N. R. B. Coleman, J. M. Elliott, J. R. Owen, J. Wang. Mesoporous platinum films from lyotropic liquid crystalline phases. *Science*, **1997**, *278*, 838–840.

[65] P. V. Braun, P. Osenar, V. Tohver, S. B. Kennedy, S. I. Stupp. Nanostructure templating in inorganic solids with organic lyotropic liquid crystals. *J. Am. Chem. Soc.*, **1999**, *121*, 7302–7309.

[66] C. G. Göltner, M. Antonietti. Mesoporous materials by templating of liquid crystalline phases. *Adv. Mater.*, **1997**, *9*, 431–436.

[67] A.-V. Ruzette, A. L. Leibler. Block copolymers in tomorrow's plastics. *Nature Materials*, **2005**, *4*, 19–31.

[68] R. Jerome, J. Tong. Recent developments in anionic polymerization. *Curr. Opinion Solid State Mater. Sci*, **1998**, *3*, 573–578.

[69] G. Soler-Illia, E. L. Crepaldi, D. Grosso, C. Sanchez. Block copolymer-templated mesoporous oxides. *Curr. Opinion Colloid Interf. Sci.*, **2003**, *8*, 109–126.

[70] A. Thomas, H. Schlaad, B. Smarsly, M. Antonietti. Replication of lyotropic block copolymer mesophases into porous silica by nanocasting: Learning about finer details of polymer self-assembly. *Langmuir*, **2003**, *19*, 4455–4459.

[71] F. S. Bates, G. H. Fredrickson. Block copolymers-designer soft materials. *Physics Today*, **1999**, 32–38.

[72] http://www.basf.com/performancechemical/bcperfphysical_chemistry.html (accessed December 2007).

[73] P. F. W. Simon, R. Ulrich, H. W. Spiess, U. Wiesner. Block copolymer-ceramic hybrid materials from organically modified ceramic precursors. *Chem. Mater.*, **2001**, *13*, 3464–3486.

[74] R. Ivanova, B. Lindman, P. Alexandridis. Modification of the lyotropic liquid crystalline microstructure of amphiphilic block copolymers in the presence of cosolvents. *Adv. Colloid Interf. Sci.*, **2001**, *89-90*, 351–382.

[75] P. Alexandridis, U. Olsson, B. Lindman. A record nine different phases (four cubic, two hexagonal, and one lamellar lyotropic liquid crystalline and two micellar solutions) in a ternary isothermal system of an amphiphilic block copolymer and selective solvents (water and oil). *Langmuir*, **1998**, *14*, 2627–2638.

[76] P. Holmqvist, P. Alexandridis, B. Lindman. Modification of the microstructure in poloxamer block copolymer-water-"oil" systems by varying the "oil" type. *Macromolecules*, **1997**, *30*, 6788–6797.

[77] D. Zhao, J. Feng, Q. Huo, N. A. Melosh, G. H. Fredrickson, B. F. Chmelka, G. D. Stucky. Triblock copolymer syntheses of mesoporous silica with periodic 50 to 300 angstrom pores. *Science*, **1998**, *279*, 548–552.

[78] D. Zhao, Q. Huo, J. Feng, B. F. Chmelka, G. D. Stucky. Nonionic triblock and star diblock copolymer and oligomeric surfactant syntheses of highly ordered, hydrothermally stable, mesoporous silica structures. *J. Am. Chem. Soc.*, **1998**, *120*, 6024–6036.

[79] F. Tiberg, J. Brinck, L. Grant. Adsorption and surface-induced self-assembly of surfactants at the solid-aqueous interface. *Curr. Opinion Colloid Interf. Sci.*, **2000**, *4*, 411–419.

[80] N. A. Melosh, P. Lipic, F. S. Bates, F. Wudl, G. D. Stucky, G. H. Fredrickson, B. F. Chmelka. Molecular and mesoscopic structures of transparent block copolymer-silica monoliths. *Macromolecules*, **1999**, *32*, 4332–4342.

[81] C. G. Göltner. Non-ionic templating of silica: Formation mechanism and structure. *Curr. Opinion Colloid Interf. Sci.*, **2002**, *7*, 173–178.

[82] C. G. Göltner, B. Smarsly, B. Berton, M. Antonietti. On the microporous nature of mesoporous molecular sieves. *Chem. Mater.*, **2001**, *13*, 1617–1624.

[83] M. Imperor-Clerc, P. Davidson, A. Davidson. Existence of a corona around of the mesopores of silica-based SBA-15 materials templated by triblock copolymers. *J. Am. Chem. Soc.*, **2000**, *122*, 11925–11933.

[84] S. M. De Paul, J. W. Zwanziger, R. Ulrich, U. Wiesner, H. W. Spiess. Structure, mobility, and interface characterization of self-organized organic-inorganic hybrid materials by solid-state NMR. *J. Am. Chem. Soc.*, **1999**, *121*, 5727–5736.

[85] C. Boissiâ"re, A. Larbot, C. Bourgaux, E. Prouzet, C. A. Bunton. A study of the assembly mechanism of the mesoporous MSU-X silica two-step mechanism. *Chem. Mater.*, **2001**, *13*(3580-3586).

[86] B. Smarsly, S. Polarz, M. Antonietti. Preparation of porous silica materials via sol-gel nanocasting of nonionic surfactants: A mechanicistic study on the self-aggregation of amphiphilies for the precise prediction of the mesopore size. *J. Phys. Chem. B*, **2001**, *105*, 10473–10483.

[87] P. C. A. Alberius, K. L. Frindell, R. C. Hayward, E. J. Kramer, G. D. Stucky, B. F. Chmelka. General predictive syntheses of cubic, hexagonal, and lamellar silica and titania mesostructured thin films. *Chem. Mater.*, **2002**, *14*, 3284–3294.

[88] A. C. Voegtlin, F. Ruch, J. L. Guth, J. Patarin, L. Huve. F- mediated synthesis of mesoporous silica with ionic- and non-ionic surfactants. A new templating pathway. *Microp. Mater.*, **1997**, *9*, 95–105.

[89] J. M. Kim, Y.-J. Han, B. F. Chmelka, G. D. Stucky. One-step synthesis of ordered mesocomposites with non-ionic amphiphilic block copolymers: implications of iso-electric point, hydrolisis rate and fluoride. *Chem. Commun.*, **2000**, 2437–2438.

[90] A. S. Brown, S. A. Holt, T. Dam, M. Trau, J. W. White. Mesoporous silicate film growth at the air-water interface – Direct observation by X-ray reflectivity. *Langmuir*, **1997**, *13*, 6363–6365.

[91] S. H. Tolbert, T. E. Schaffer, J. Feng, P. K. Hansma, G. D. Stucky. A new phase of oriented mesoporous silicate thin films. *Chem. Mater.*, **1997**, *9*, 1962–1967.

[92] P. Yang, A. Kuperman, N. Coombs, S. Mamiche-Afara, G. A. Ozin. Synthesis of oriented films of mesoporous silica on mica. *Nature*, **1996**, *379*, 703–705.

[93] M. Ogawa. Formation of novel oriented transparent films of layered silica-surfactant nanocomposites. *J. Am. Chem. Soc.*, **1994**, *116*, 7941–7942.

[94] Y. Lu, R. Ganguli, C. A. Drewien, M. T. Anderson, C. J. Brinker, W. Gong, Y. Guo, H. Soyez, B. Dunn, M. H. Huang, J. I. Zink. Continuous formation of supported cubic and hexagonal mesoporous films by sol-gel dip-coating. *Nature*, **1997**, *389*, 364–368.

[95] C. J. Brinker, Y. Lu, A. Sellinger, H. Fan. Evaporation-induced self-assembly: Nanostructures made easy. *Adv. Mater.*, **1999**, *11*, 579–585.

[96] F. Schüth. Non-siliceous mesostructured and mesoporous materials. *Chem. Mater.*, **2001**, *13*, 3184–3195.

[97] C. J. Brinker, D. R. Dunphy. Morphological control of surfactant-templated metal oxide films. *Curr. Opinion Colloid Interf. Sci.*, **2006**, *11*, 126–132.

[98] H. Fan, Y. Lu, A. Stump, S. T. Reed, T. Baer, R. Schunk, V. Perez-Luna, G. P. López, C. J. Brinker. Rapid prototyping of patterned functional nanostructures. *Nature*, **2000**, *405*, 56–60.

[99] E. Ruiz-Hernández, A. López-Noriega, D. Arcos, I. Izquierdo-Barba, O. Terasaki, M. Vallet-Regí. Aerosol-assisted synthesis of magnetic mesoporous silica spheres for drug targeting. *Chem. Mater.*, **2007**, *ASAP*.

[100] D. Grosso, F. Cagnol, G. Soler-Illia, E. L. Crepaldi, H. Amenitsch, A. Brunet-Bruneau, A. Bourgeois, C. Sanchez. Fundamentals of mesostructuring through evaporation-induced self-assembly. *Adv. Funct. Mater.*, **2004**, *14*, 309–322.

[101] N. Baccile, D. Grosso, C. Sanchez. Aerosol generated mesoporous silica particles. *J. Mater. Chem.*, **2003**, *13*, 3011–3016.

[102] D. Grosso, G. Soler-Illia, E. L. Crepaldi, B. Charleux, C. Sanchez. Nanocrystalline transition-metal oxide spheres with controlled multi-scale porosity. *Adv. Funct. Mater.*, **2003**, *13*, 37–42.

[103] D. Grosso, C. Boissiãre, L. Nicole, C. Sanchez. Preparation, treatment and characterisation of nanocrystalline mesoporous ordered layers. *J. Sol-Gel. Sci. Technol.*, **2006**, *40*, 141–154.

[104] T. Brezesinski, M. Groenewolt, A. Gibaud, N. Pinna, M. Antonietti, B. Smarsly. Evaporation-induced self-assembly (EISA) at its limit: ultrathin, crystalline patterns by templating of micellar monolayers. *Adv. Mater.*, **2006**, *18*, 2260–2263.

[105] D. Grosso, C. Boissiãre, B. Smarsly, T. Brezesinski, N. Pinna, P.-A. Albouy, H. Amenitsch, M. Antonietti, C. Sanchez. Periodically ordered nanoscale islands and mesoporous films composed of nanocrystalline multimetallic oxides. *Nature Materials*, **2004**, *3*, 787–792.

[106] G. Cortial, M. Siutkowski, F. Goettmann, A. Moores, C. Boissiãre, D. Grosso, P. Le Floch, C. Sanchez. Metallic nanoparticles hosted in mesoporous oxide thin films for catalytic applications. *Small*, **2006**, *2*, 1042–1045.

[107] S. Besson, T. Gacoin, C. Jacquiod, C. Ricolleau, J.-P. Boilot. 3D periodic arrays of nanoparticles inside mesoporous silica films. *Mat. Res. Soc. Symp. Proc.*, **2002**, *707*.

[108] S. Besson, T. Gacoin, C. Ricolleau, C. Jacquiod, J.-P. Boilot. 3D quantum dot lattice inside mesoporous silica films. *Nano Lett.*, **2002**, *2*, 409–414.

[109] S. P. Naik, T. Yokoi, W. Fan, Y. Sasaki, T.-C. Wei, H. W. Hillhouse, T. Okubo. Versatile fabrication of distorted cubic mesoporous silica films using CTAB together with a hydrophilic organic additive. *J. Phys. Chem. B*, **2006**, *110*, 9751–9754.

[110] L. Nicole, C. Boissiãre, D. Grosso, A. Quach, C. Sanchez. Mesostructured hybrid organic-inorganic thin films. *J. Mater. Chem.*, **2005**, *15*, 3598–3627.

[111] L. G. Hubert-Pfalzgraf. Toward molecular design of oxide precursors for advanced materials.

[112] J. Livage, M. Henry, C. Sanchez. Sol-gel chemistry of transition metal oxides. *Prog. Solid State Chem.*, **1988**, *18*, 259–341.

[113] E. L. Crepaldi, G. Soler-Illia, D. Grosso, C. Sanchez. Nanocrystallised titania and zirconia mesoporous thin films exhibiting enhanced thermal stability. *New J. Chem.*, **2003**, *27*, 9–13.

[114] G. Soler-Illia, C. Sanchez. Interactions between poly(ethylene oxide)-based surfactants and transition metal alkoxides: their role in the templated construction of mesostructured hybrid organic-inorganic composites. *New J. Chem.*, **2000**, *24*, 493–499.

[115] G. Soler-Illia, E. L. Crepaldi, D. Grosso, D. Durand, C. Sanchez. Structural control in self-standing mesostructured silica oriented membranes and xerogels. *Chem. Commun.*, **2002**, 2298–2299.

[116] S. Y. Choi, B. Lee, D. B. Carew, M. Mamak, F. C. Peiris, S. Speakman, N. Chopra, G. A. Ozin. 3D hexagonal (R-3m) mesostructured nanocrystalline titania thin films: Synthesis and characterization. *Adv. Funct. Mater.*, **2006**, *16*, 1731–1738.

[117] M. P. Tate, B. W. Eggiman, J. D. Kowalski, H. W. Hillhouse. Order and orientation control of mesoporous silica films on conducting gold substrates formed by dip-coating and self-assembly: A grazing angle of incidence small-angle X-ray scattering and field emission scanning electron microscopy study. *Langmuir*, **2005**, *21*, 10112–10118.

[118] P. Yang, D. Zhao, D. I. Margolese, B. F. Chmelka, G. D. Stucky. Block copolymer templating syntheses of mesoporous metal oxides with large ordering lengths and semicrystalline framework. *Chem. Mater.*, **1999**, *11*, 2813–2826.

[119] D. Grosso, F. Babonneau, P.-A. Albouy, H. Amenitsch, A. R. Balkenende, A. Brunet-Bruneau, J. Rivory. An in situ study of mesostructured CTAB-silica film formation during dip coating using time-resolved SAXS and interferometry measurements. *Chem. Mater.*, **2002**, *14*, 931–939.

[120] M. Klotz, A. Ayral, C. Guizard, L. Cot. Synthesis conditions for hexagonal mesoporous silica layers. *J. Mater. Chem.*, **2000**, *10*, 663–669.

[121] D. Grosso, F. Babonneau, G. Soler-Illia, P.-A. Albouy, H. Amenitsch. Phase transformation during cubic mesostructured silica film formation. *Chem. Commun.*, **2002**, 748–749.

[122] A. Gibaud, D. Grosso, B. Smarsly, A. Baptiste, J. F. Bardeau, F. Babonneau, D. A. Doshi, Z. Chen, C. J. Brinker, C. Sanchez. Evaporation-controlled self-assembly of silica surfactant mesophases. *J. Phys. Chem. B*, **2003**, *107*, 6114–6118.

[123] F. Cagnol, D. Grosso, G. Soler-Illia, E. L. Crepaldi, F. Babonneau, H. Amenitsch, C. Sanchez. Humidity-controlled mesostructuration in CTAB-templated silica thin film processing. The existence of a modulable steady state. *J. Mater. Chem.*, **2003**, *13*, 61–66.

[124] D. Grosso, G. Soler-Illia, E. L. Crepaldi, F. Cagnol, C. Sinturel, A. Bourgeois, A. Brunet-Bruneau, H. Amenitsch, P.-A. Albouy, C. Sanchez. Highly porous TiO_2 anatase optical thin films with cubic mesostructure stabilized at 700Â°C. *Chem. Mater.*, **2003**, *15*, 4562–4570.

[125] E. L. Crepaldi, G. Soler-Illia, A. Bouchara, D. Grosso, D. Durand, C. Sanchez. Controlled formation of highly ordered cubic and hexagonal mesoporous nanocrystalline yttria-zirconia and ceria-zirconia thin films exhibiting high thermal stability. *Angew. Chem. Int. Ed. Engl.*, **2003**, *42*, 347–351.

[126] C. N. Urade, H. W. Hillhouse. Synthesis of thermally stable highly ordered nanoporous tin oxide thin films with a 3D face-centered orthorhombic nanostructure. *J. Phys. Chem. B*, **2005**, *109*, 10538–10541.

[127] L. Nicole, C. BoissiÃ¨re, D. Grosso, P. Hesemann, J. Moreau, C. Sanchez. Advanced selective optical sensors based on periodically organized mesoporous hybrid silica thin films. *Chem. Commun.*, **2004**, 2312–2313.

[128] D. Shamiryan, T. Abell, F. Iacopi, K. Maex. Low-k dielectric materials. *Materials*

Today, **2004**, *7*, 34–39.

[129] S. Baskaran, J. Liu, K. Domansky, N. Kohler, X. Li, C. Coyle, G. E. Fryxell, S. Thevuthasan, R. E. Williford. Low dielectric constant mesoporous silica films through molecularly templated synthesis. *Adv. Mater.*, **2000**, *12*, 291–294.

[130] K. Maex, M. R. Baklanov, D. Shamiryan, F. Iacopi, S. H. Brongersma, Z. S. Yanovitskaya. Low dielectric constant materials for microelectronics. *Appl. Phys. Lett.*, **2003**, *93*, 8793–8841.

[131] S. Yu, T. K. S. Wong, K. Pita. Surface modified silica mesoporous films as a low dielectric constant intermetal dielectric. *J. Appl. Phys*, **2002**, *92*, 3338–3344.

[132] B. D. Hatton, K. Landskron, W. Whitnall, D. D. Perovic, G. A. Ozin. Spin-coated periodic mesoporous organosilica thin films - Towards a new generation of low-dielectric-constant materials. *Adv. Funct. Mater.*, **2005**, *15*, 823–829.

[133] W. Cho, R. Saxena, O. Rodriguez, R. Achanta, J. L. Plawski, W. N. Gill. Effects of sintering on dielectric constants of mesoporous silica. *J. Non-Cryst. Solids*, **2004**, *350*, 336–344.

[134] L. Malfatti, P. Falcaro, H. Amenitsch, S. Caramori, R. Argazzi, C. A. Bignozzi, S. Enzo, M. Maggini, P. Innocenzi. Mesostructured self-assembled titania films for photovoltaic applications. *Microp. Mesop. Materials*, **2006**, *88*, 304–311.

[135] E. Lancelle-Beltran, P. Prene, C. Boscher, P. Belleville, P. Buvat, S. Lambert, G. F., C. Boissiàˆre, D. Grosso, C. Sanchez. Nanostructured hybrid solar cells based on self-assembled mesoporous titania thin films. *Chem. Mater.*, **2006**, *18*, 6152–6156.

[136] K. M. Coakley, Y. Liu, M. D. McGehee, K. L. Frindell, G. D. Stucky. Infiltrating semiconducting polymers into self-assembled mesoporous titania films for photovoltaic applications. *Adv. Funct. Mater.*, **2003**, *13*, 301–306.

[137] K. M. Coakley, M. D. McGehee. Photovoltaic cells made from conjugated polymers infiltrated into mesoporous titania. *Appl. Phys. Lett.*, **2003**, *83*, 3380–3382.

[138] J. Mio Bertolo, A. Bearzotti, P. Falcaro, E. Traversa, P. Innocenzi. Sensoristic applications of self-assembled mesostructured silica films. *Sensor Letters*, **2003**, *1*, 64–70.

[139] A. Bearzotti, J. Mio Bertolo, P. Innocenzi, P. Falcaro, E. Traversa. Humidity sensors based on mesoporous silica thin films synthesized by block copolymers. *J. Eur. Ceramic Soc.*, **2004**, *24*, 1969–1974.

Chapter 2

Characterisation techniques

Abstract

The study of mesostructured films requires powerful characterisation techniques able to detect multiple aspects such as mesostructure symmetry and degree of order, inorganic crosslinking and presence of specific molecular species. The primary experimental technique that can provide structural information on mesostructure is small-angle X-ray scattering (SAXS). It is based on the diffraction of X-rays by the ordered disposition of matter in a mesostructure and provides information regarding symmetry group, degree of order, cell parameter, micelle size. Because mesostructure formation occurs during dip-coating in a short time, *in situ* experiments are required, usually at synchrotron facilities utilising high-flux radiation. Another powerful tool for investigating mesostructured materials is the transmission electron microscope (TEM), which provides direct images of the mesostructure with nanometric resolution. TEM can be regarded as a structural technique complementary to SAXS, in that it describes the structure on a very local scale. Fourier-transform infrared spectroscopy (FTIR) is related to the interaction of infrared radiation with matter and provides information on the presence of specific chemical species within the film, as well as on the degree of inorganic crosslinking and the chemical environment. Other techniques utilised in the experimental work of this thesis, such as atomic force microscopy and nitrogen sorption, are outlined in the present chapter.

2.1 Introduction

The physics and the chemistry underlying templated self-assembly in mesostructured films have been understood in detail. Some characterisation techniques, such as transmission electron microscopy and infrared spectroscopy, have been applied to the study of mesoporous materials; other techniques, such as small-angle X-ray scattering, were borrowed from other disciplines and successfully adapted to the investigation of mesostructured films. These characterisation techniques have been coupled in order to overcome the intrinsic complexity of mesostructured systems: self-assembly and inorganic polycondensation occur at the same time, furthermore the interactions between the organic and the inorganic species are highly cooperative and the synthesis is very sensitive to initial conditions and external perturbations.

The phenomena leading to the formation of a mesostructured film can be divided into (1) chemical reactions and physical processes in the precursor solution, (2) intermediate liquid-solid state at the onset of polycondensation and self-assembly, (3) tunable steady state, thermal treatment and final product. It is evident that discontinuous *ex situ* techniques can be used to sample only a part of the global self-assembly process. For example, dynamic light scattering can give information on the size of the aggregates present in the precursor solution, transmission electron microscopy gives structural information on thermally treated and mechanically stable samples. However, because mesostructure formation occurs during dip-coating and is often a matter of seconds rather than minutes or hours, the study of this part—which has obviously a central role—requires the use of *in situ* techniques with special configurations, for example a high incident flux (e.g. synchrotron radiation) and a specific dip-coating apparatus. As we will see, the primary in situ experimental technique that can give highly instructive structural information on mesostructure is small-angle X-ray diffraction utilising synchrotron radiation. This can be coupled with other in situ techniques in order to get complementary information, for example with interferometry in order to calculate film thickness. In Chapter 3 we present the development of a new coupled structural-spectroscopic technique providing simultaneous structural and spectroscopic information on the self-assembly of mesostructured films.

Because a description of all characterisation techniques utilised in the research on mesostructured materials falls outside the scope of this thesis, the present chapter provides information on the techniques employed in the experimental work of this doctorate. These can be classified into *structural* techniques, giving information on the mesostructure (e.g. symmetry, degree of order, cell parameter, micelle size), and *spectroscopic* techniques, yielding physicochemical information on the film (e.g. presence of specific chemical species, degree of inorganic crosslinking). Other techniques, such as ellipsometry, atomic force microscopy and nitrogen sorption, provide physical information on the films such as refractive index, thickness and surface topology.

2.2 Small-angle X-ray scattering (SAXS)

2.2.1 Physics of X-ray diffraction

One of the most used techniques to carry out structural characterisation of solid materials is X-ray diffraction (XRD). This technique is based on the interaction between an incident electromagnetic wave in the X-ray range and the sample. When an electromagnetic wave impinges on the sample, it interacts with the electron cloud and undergoes elastic scattering phenomena. If the electron density is arranged periodically, as in a crystal lattice, the scattered waves add up and give constructive and destructive interference, and their intensity is recorded by a detector as a function of the exit angle. These processes of scattering and interference usually go under the name of *diffraction*. Diffraction occurs with any type of wave other than electromagnetic waves, including sound and water waves, and also with matter displaying wave-like properties such as electrons. Its effects are generally only noticeable for waves whose wavelength is on the order of the feature size of the diffracting objects or apertures, thus for crystal lattices with periodicity on the order of the Å, X-rays are used.

A visual way to rationalise X-ray diffraction by an ordered crystal lattice is provided by the so-called Bragg's interpretation. A given crystal is constituted by regular arrays of atoms spaced with fixed distances d. The crystal can be decomposed into any number of different planes, due to the periodicity of crystal lattice (Figure 2.1 a). As the wave enters the crystal, some portion of the wave is reflected by the first layer, while the rest continues through to the second layer, and so on. By the definition of constructing interference, the separately reflected waves remain in phase if the difference in the path length of each wave is equal to an integer multiple of the wavelength. This happens only if $2x = n\lambda$, which gives the well-known formula for Bragg diffraction conditions, or Bragg's law (Figure 2.1 b):

$$2d_{hkl} \sin\theta = n\lambda, \tag{2.1}$$

where d_{hkl} is the periodicity of a given family hkl of planes (d-spacing), θ is the incidence and exit angle, n is an integer and λ is the wavelength. Waves that satisfy this condition interfere constructively and result in a reflected wave of significant intensity. Therefore, according to Bragg's interpretation one can imagine diffraction as a reflection of the incident wave by a family of atomic planes, which happens selectively for a finite number of incident angles θ.

Bragg's interpretation of X-ray diffraction is an effective way of interpreting diffraction. However, the physics of diffraction involves scattering of electromagnetic waves and has nothing to do with "traditional" reflection of light on a surface. Let us now examine in detail the physics of X-ray diffraction by a crystal.[1] The electron density in a periodic lattice $\rho(\mathbf{r})$ is invariant under lattice translation, so that $\rho(\mathbf{r}) = \rho(\mathbf{r} + \mathbf{R})$, where $\mathbf{R} = u_1\mathbf{a}_1 + u_2\mathbf{a}_2 + u_3\mathbf{a}_3$ is a vector of the crystal lattice which indicates the periodicity of crystallographic planes, $\mathbf{a}_1, \mathbf{a}_2, \mathbf{a}_3$ are the base vectors in the direction of the three crystal axes, and u_1, u_2, u_3 are integers. The density function $\rho(\mathbf{r})$ can be represented as a Fourier series:

$$n(\mathbf{r}) = \sum_{\mathbf{G}} n_{\mathbf{G}} \exp(i\mathbf{G} \cdot \mathbf{R}). \tag{2.2}$$
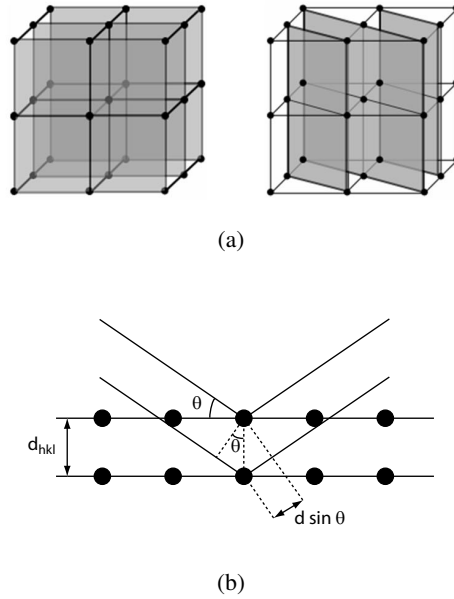
(a)

(b)

Figure 2.1. *Interpretation of diffraction according to Bragg: (a) the ordered arrangement of repeating units in a lattice can be pictured as sets of parallel planes, which (b) give diffraction when the scattered waves are in the condition of constructive interference, i.e. the difference in their optical path is a multiple of the wavelength.*

It can be demonstrated that the set of Fourier coefficients $n_{\mathbf{G}}$ is

$$n_{\mathbf{G}} = V_c^{-1} \int_{\text{cell}} dV\, n(\mathbf{r})\, \exp(-i\mathbf{G} \cdot \mathbf{r}), \tag{2.3}$$

where V_c is the volume of a cell of the crystal. The vectors $\mathbf{G}$ of the Fourier sum in Equation 2.2 are described by $\mathbf{G} = v_1\mathbf{b}_1 + v_2\mathbf{b}_2 + v_3\mathbf{b}_3$, where v_1, v_2, v_3 are integers and the axis vectors $\mathbf{b}_1$, $\mathbf{b}_2$, $\mathbf{b}_3$ are expressed by:

$$\mathbf{b}_1^* = 2\pi \frac{\mathbf{a}_2 \times \mathbf{a}_3}{\mathbf{a}_1 \cdot (\mathbf{a}_2 \times \mathbf{a}_3)}. \tag{2.4}$$

Each vector defined by Equation 2.4 is orthogonal to two axis vectors of the crystal lattice, thus $\mathbf{b}_i \cdot \mathbf{a}_j = 2\pi\delta_{ij}$ The vector $\mathbf{G}$ is the *reciprocal lattice vector*: every crystal structure has both a crystal lattice and a reciprocal lattice associated with it, which describes the periodicity of matter according to a Fourier sum (Equation 2.2). The reciprocal lattice, therefore, can be seen as the lattice in the Fourier space associated with the crystal, and each point in the reciprocal lattice corresponds to a set of lattice planes (*hkl*) in the real space lattice. The reciprocal lattice itself is a Bravais lattice: the direction of the reciprocal lattice vector corresponds to the normal to the real space planes, and the magnitude of the reciprocal lattice vector is equal to the reciprocal of the interplanar spacing of the real space planes. Vectors in the direct lattice have the dimensions of [length], whereas vectors in the reciprocal lattice have the dimensions of [1/length].

From Equation 2.2, and considering an invariant crystal translation $\mathbf{R} = u_1\mathbf{a}_1 +$

$u_2\mathbf{a}_2 + u_3\mathbf{a}_3$ it follows that

$$n(\mathbf{r}) = n(\mathbf{r} + \mathbf{R}) = \sum_{\mathbf{G}} \exp(i\mathbf{G} \cdot \mathbf{r}) \exp(i\mathbf{G} \cdot \mathbf{R}) \qquad (2.5)$$

The exponential can be expressed using vectors of the direct ($\mathbf{a}_i$) and the reciprocal lattice ($\mathbf{b}_i$):

$$\exp(i\mathbf{G} \cdot \mathbf{r}) = \exp[i(v_1\mathbf{b}_1 + v_2\mathbf{b}_2 + v_3\mathbf{b}_3) \cdot (u_1\mathbf{a}_1 + u_2\mathbf{a}_2 + u_3\mathbf{a}_3)] =$$
$$= \exp[2\pi i(v_1u_1 + v_2u_2 + v_3u_3)]. \qquad (2.6)$$

The argument of the exponential is $2\pi i$ times an integer, being the sum of products of integers, therefore:

$$\exp(i\mathbf{G} \cdot \mathbf{r}) = 1. \qquad (2.7)$$

An incident wave $\exp(i\mathbf{k}_i \cdot \mathbf{r})$ of wavevector $\mathbf{k}_i$ is coherently scattered by a diffusion centre (i.e. electron density) and the scattered wave $\exp(i\mathbf{k}_f \cdot \mathbf{r})$ emerges with a wavevector $\mathbf{k}_f$. The scattering vector, or momentum transfer, is defined as:

$$\mathbf{q} = \mathbf{k}_f - \mathbf{k}_i \qquad (2.8)$$

The amplitude F of the wave scattered from a volume element is proportional to the integral over the crystal of $n(\mathbf{r})d\mathrm{V}$ times the phase factor $\exp[i(\mathbf{k}_i - \mathbf{k}_f) \cdot \mathbf{r}]$, therefore:

$$F = \int d\mathrm{V}\, n(\mathbf{r}) \exp[i(\mathbf{k}_i - \mathbf{k}_f) \cdot \mathbf{r}] = \int d\mathrm{V}\, n(\mathbf{r}) \exp[-i\mathbf{q} \cdot \mathbf{r}]. \qquad (2.9)$$

We introduce the Fourier components of n($\mathbf{r}$) (Equation 2.2) into Equation 2.9 to obtain:

$$n(\mathbf{r}) \sum_{\mathbf{G}} \int d\mathrm{V}\, n_{\mathbf{G}} \exp[i(\mathbf{G} - \mathbf{q}) \cdot \mathbf{r}]. \qquad (2.10)$$

From Equation 2.10 it follows that the scattering amplitude is maximum when $\mathbf{q} = \mathbf{G}$, in other words *there is diffraction when the momentum transfer vector is a vector of the reciprocal lattice*. Therefore, a diffraction pattern of a crystal is a map of the reciprocal lattice of the crystal, and by recording the diffracted intensity as a function of the exit angle, we sample a region of the reciprocal lattice.

In elastic scattering the energy of the incident wave is conserved, so that the magnitudes k_i and k_f are equal, thus $k_i^2 = k_f^2$. From this and from Equation 2.10 it follows that $(\mathbf{k} + \mathbf{G})^2 = k^2$, or

$$2\mathbf{k} \cdot \mathbf{G} = G^2, \qquad (2.11)$$

which is called the *von Laue diffraction condition*.

It can be demonstrated[2] that the vector $\mathbf{G} = h\mathbf{b}_1 + k\mathbf{b}_2 + l\mathbf{b}_3$ is perpendicular to (*hkl*) planes, and that $d_{hkl} = 2\pi/|\mathbf{G}|$. As a consequence, and because $k = 2\pi/\lambda$, Equation 2.11 may be written as:

$$2|\mathbf{k}||\mathbf{G}|\cos(\pi - \theta) = 2kG\sin\theta = G^2 \Rightarrow 2\frac{2\pi}{\lambda}\sin\theta = \frac{2\pi}{d_{hkl}}, \qquad (2.12)$$

which is the Bragg condition for diffraction (Equation 2.1): $\lambda = 2d_{hkl}\sin\theta$. This can be considered an approach different from Bragg's, in that no particular sec-
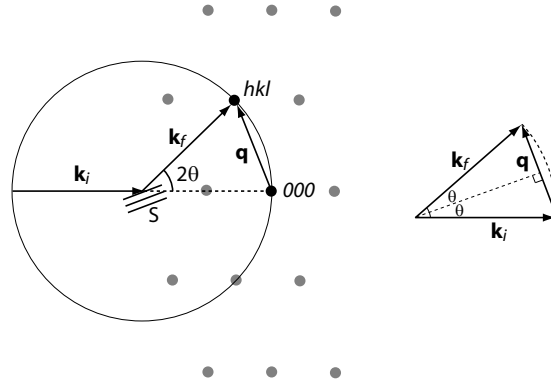
Figure 2.2. *Interpretation of diffraction according to Ewald: a sphere of radius equal to the incident wavevector $\mathbf{k}_i$ is built (Ewald sphere), such that the tip of $\mathbf{k}_i$ is centred on the sample, and $\mathbf{k}_i$ and the origin of the reciprocal space lie on the same line. Diffraction conditions are fulfilled when the Ewald sphere intersects a point of the reciprocal lattice, thus the scattering vector $\mathbf{q} = \mathbf{k}_f - \mathbf{k}_i$ is a vector of the reciprocal lattice.*

tioning of the crystal is singled out, and no assumption of specular reflection is imposed. However, both approaches are based on the assumption that X-rays scattered from individual scattering centres interfere constructively, therefore a mathematical equivalence descending from the common physical assumption was not unexpected.

Let us now consider a sphere drawn in the reciprocal space, centred on the origin of the incident wavevector $\mathbf{k}_i$ of radius $k = 2\pi/\lambda$, so that it passes through the origin O of the reciprocal space (Figure 2.2). According to Equation 2.11, there will be some wave vector $\mathbf{k}_f$ satisfying the von Laue condition ($\mathbf{q} = \mathbf{k}_f - \mathbf{k}_i = \mathbf{G}$) if and only if some reciprocal lattice point (other than the origin O) lies on the surface of the sphere. In this case we have diffraction, and we observe a Bragg reflection from the family of direct lattice planes perpendicular to that reciprocal lattice vector $\mathbf{G}$. The sphere construction is called the *Ewald construction*, and the sphere is called the Ewald sphere. It can be noted (Figure 2.2 b) that $q/2 = k \sin\theta$, therefore $q/2 = 2\pi/\lambda \sin\theta$, which, considering Equation 2.1, becomes $q = 2\pi/d$. The factor 2π is often dropped in the *crystallographer's notation*, so that $\exp(2\pi i \mathbf{G} \cdot \mathbf{R}) = 1$, and we have:

$$q = \frac{1}{d}. \tag{2.13}$$

This is a simple relation between the scattering vector and the d-spacing of reflection *hkl*. As we will see in the experimental part of this thesis, the Ewald construction will be of great use.

2.2.2 Diffraction on mesostructured films

The periodicity considered so far, described by the electron density function $\rho(\mathbf{r})$, was assumed to be due to the ordered disposition of atoms in a crystal lattice. However, in principle nothing prohibits us from considering $\rho(\mathbf{r})$ as *any* electron density periodicity, invariant under a given lattice translation $\rho(\mathbf{r}) = \rho(\mathbf{r} + \mathbf{R})$. Mesostructured materials are no exception, in that the ordered arrangement of the

mesophase provides an electron density contrast between the inorganic and the organic phase which can be described by $\rho(\mathbf{r})$. The same holds for mesoporosity, where $\rho(\mathbf{r})$ describes the periodicity of the inorganic walls. As a consequence, the interaction of an electromagnetic wave with mesostructured and mesoporous materials gives diffraction.

As we have seen, a diffraction experiment can be regarded as the sampling of the reciprocal lattice, therefore information on the symmetry of the ordered mesophase can be inferred by diffraction data. Since the feature size of a mesostructure is typically $\sim$10 nm, using incident X-rays of wavelength $\sim$1 Å will typically give diffraction at 2θ angles in the range 0.5–2°. Because of these small diffraction angles, the diffracted beams are only slightly separated from the incident beam, therefore the detector must be suitably shielded in order to avoid being damaged by the direct beam.

On this principle are based small-angle X-ray scattering (SAXS) techniques. The "small-angle" refers to the angular range of the scattered beams, containing information on the structure in the reciprocal space in the nanometre range. Deviations from average electron density must be present in the sample, therefore many applications of small-angle X-ray scattering technique are found in structural biology, polymer science, colloid chemistry and materials science.[3] In structural biology this technique is used for crystallographic structural analysis and is one of a few non-destructive structural techniques: it can be used also in situ for studying proteins in solution, such as those in unfolded states or those whose crystallisation conditions have not been determined. Biological fibers such as skeletal muscle are quasi-crystalline but not as well ordered as crystals, thus giving relatively broad diffraction peaks mostly at small angles. Many biological lipids exist as vesicles or liquid crystals, physical states that are rather poorly ordered; micellar structures and synthetic polymer materials are often studied with this technique.[4]

SAXS has been adapted to the study of mesoporous materials, mostly powders and films, becoming one of the most useful tools to investigate the ordered mesostructure. The importance of real-time SAXS analysis has been fully understood when the existence of a tunable condition in mesostructured materials, the so-called "tunable steady state", was observed: here, changes in the deposition variables (e.g. relative humidity during dip-coating) can induce variations in the mesophase even after solvent evaporation. Specially-designed dip-coaters for deposition of films from liquid phase have been built by different groups to be used at synchrotron facilities for time-resolved in situ SAXS analyses.

2.2.3   SAXS at synchrotron facilities

A synchrotron is a particular type of cyclic electron accelerator in which the magnetic and the electric fields are carefully synchronised with the travelling particle beam. As the electrons, travelling at relativistic speed in the electron storage ring, are deflected by devices such as undulators and wigglers, electromagnetic radiation is emitted in a narrow cone in the forward direction at a tangent to the particle's orbit. This light is channelled through beamlines to experimental workstations where it is used for research (Figure 2.3). Electron storage rings provide radiation from the infrared through the visible, near-ultraviolet, vacuum-ultraviolet, soft X-ray, and hard X-ray parts of the electromagnetic spectrum, extending to 100 keV and beyond.
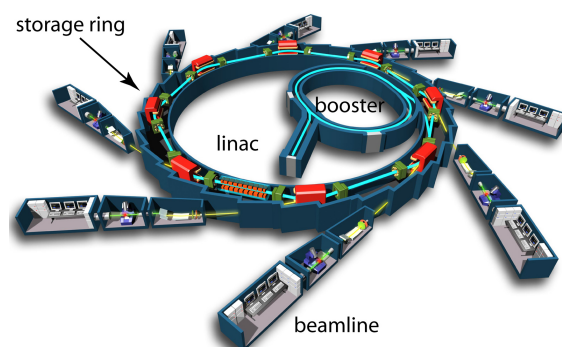
Figure 2.3. *Scheme of a synchrotron: electrons are accelerated by a linear accelerator (linac) and a booster, and injected into the circular storage ring, off which the beamlines branch.*

Synchrotron radiation thus emitted has many unique features that make it ideal for a wide variety of applications in experimental science and technology. These include: high flux [photons/(second, unit bandwidth)], high brightness [flux/(unit source size, unit solid angle)], wide energy spectrum (from IR to hard X-rays), tunability of wavelength with insertion devices, high polarisation, emission in short pulses (typically ∼1 ns). Synchrotron light is used in such diverse research fields as biosciences (protein crystallography and cell biology), medical research (microbiology, disease mechanisms, high resolution imaging and cancer radiation therapy), environmental sciences (toxicology, atmospheric research, clean combustion and cleaner industrial production technologies), minerals exploration (rapid analysis of drill core samples, comprehensive characterisation of ores for ease of mineral processing), advanced materials (nanostructured materials, intelligent polymers, ceramics, light metals and alloys, electronic and magnetic materials), engineering (imaging of industrial processes in real time, high resolution imaging of cracks and defects in structures, the operation of catalysts in large chemical engineering processes) and forensics (identification of suspects from extremely small and dilute samples).

Regarding mesostructured films, there are a few aspects of synchrotron radiation that have made small-angle scattering studies at synchrotron facilities very effective. These are: very small beam divergence, high beam flux, and in some cases energy tunability. It is crucial to have small beam divergence in order to isolate weak scattering at very small angles from the direct beam which is orders of magnitude stronger. The flux of a synchrotron source is usually several orders of magnitude higher than those from conventional X-ray sources, therefore a diffraction pattern can be acquired in short times, typically on the order of 500 ms, making it possible to perform time-resolved in situ experiments during dip-coating. When beam energy is tunable, it is possible to conduct anomalous small-angle X-ray scattering. All SAXS experiments (in situ and ex situ) presented in this thesis were conducted at the Austrian beamline at Elettra synchrotron facility in Trieste, Italy.[5,6] A more detailed description of Elettra synchrotron facility can be found at Elettra's website (http://www.elettra.trieste.it). The experimental setup at the SAXS beamline at Elettra is the subject of the next subsection.
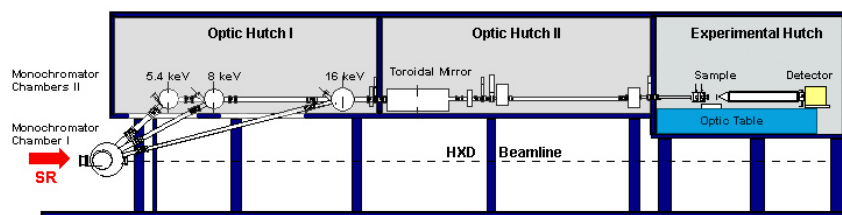
Figure 2.4. *Scheme of the Austrian SAXS beamline at Elettra: synchrotron radiation is monochromated by a flat double crystal in optics hutch 1 and focused by a toroidal mirror in optics hutch 2. Downstream of the optics hutches is the experimental hutch.*

2.2.4   SAXS measurements on mesostructured films at Elettra

The SAXS beamline at Elettra was built by the Institute of Biophysics and Nanosystems Research (IBN), Austrian Academy of Sciences, Graz, and is operative since September 1996. The photon source is the 57-pole NdFeB hybrid wiggler, whose beam is shared with a macromolecular crystallography beamline. The wiggler delivers a very intense radiation between 4 and 25 keV, of which 3 discrete energies (5.4, 8 and 16 keV) can be selected by a flat double crystal (111 Si) monochromator in optics hutch 1 and focused by a double focusing toroidal mirror in optics hutch 2 (Figure 2.4). These can be controlled via a software interface developed with LabView. The LabView software procedures also control sample manipulation, beamline shutter control, gate valves, etc. Typically, for an electron energy in the storage ring of 2 GeV, an intensity of 200 mA and a selected energy of 8 keV, the flux density at the sample is $2.5 \cdot 10^{11}$ photons $\cdot$ s^{-1} $\cdot$ mm^{-2}. The optical table in the experimental hutch allows optimisation of the sample-to-detector distance with respect to SAXS resolution and sample size setup, as well as installation of specialised sample equipment, such as a dip-coater or a liquid flow cell for in situ experiments (Figure 2.5 a). A two-dimensional CCD detector (Photonic Science, UK) is used for data acquisition. Optionally, an additional one-dimensional wide angle X-ray scattering (WAXS) detector can be inserted for acquiring diffraction data in the d-spacing range of 1 to 9 Å.

Before a measurement session, the equipment is set up, in particular the sample-to-detector distance is adjusted in order to ensure that the diffracted beams be well-separated from the direct beam, and a sufficiently large area of the reciprocal space be sampled by the CCD detector. The beam stop must be correctly positioned in order to prevent the direct beam from hitting the detector, as this may cause irreversible damage to the CCD array. In a typical collection of a SAXS pattern, the sample is placed on a sample holder, which can be rotated via a servo motor from the control room, so that the angle of incidence can be varied (Figure 2.5 b). After interlocking the experimental hutch prior to each measurement, the main shutter is opened. Then, diffraction patterns are acquired using the CCD detector provided with a software-triggered fast shutter positioned upstream of the sample. Image-Pro® Plus is used as the CCD control software. At first, a low acquisition time is selected (e.g. 100 ms) in order to avoid saturation which could damage the detector. In the following measurements the acquisition time can be increased so that less intense diffraction signal is acquired (e.g. from higher diffraction orders).
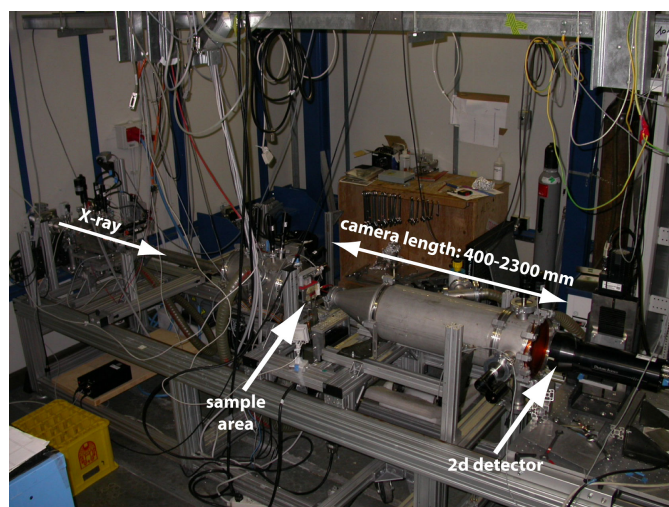
(a)
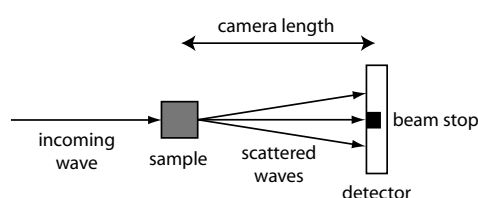
(b)

Figure 2.5. *(a) Experimental hutch with optical table: the incident and scattered waves propagate in vacuum tubes with kapton windows; the camera length (sample-to-detector distance) can be varied by moving the CCD detector and using vacuum tubes with different length. (b) Side view of the optical table.*

It is of utmost importance that a diffraction pattern of a calibration standard be acquired for each setup of the optics. Diffraction standards provide a tool to determine accurately the beam centre position and the sample-to-detector distance. Without such a calibration it is not possible to perform quantitative data analysis such as cell constant calculation. Calibration is done prior to each measurement session, or in any case before modifying the beamline setup. We used a silver behenate powder standard $(CH_3(CH_2)_{20}COOAg$, d-spacing: 58.38 Å$)$[7] in a capillary glass: the ring-like diffraction pattern is used in the data analysis software as will described later.

2.2.5 Grazing and transmission incidence

The diffraction pattern of a mesostructured film depends not only on the mesostructure's symmetry and orientation, but also on the experimental measurement conditions, such as the angle of incidence. Let us first examine the diffraction of an X-ray beam by an "ideal" monocrystal-like mesostructure, following Ewald's interpretation (Figure 2.6). Since the reciprocal lattice is a collection of points in the reciprocal space, its intersection with the Ewald sphere is a set of points, and we have a diffraction pattern made of spots (Figure 2.6).

In general, the model of the monocrystal-like mesostructure is not true for "real" films. These are almost always composed of micron-sized mesostructured
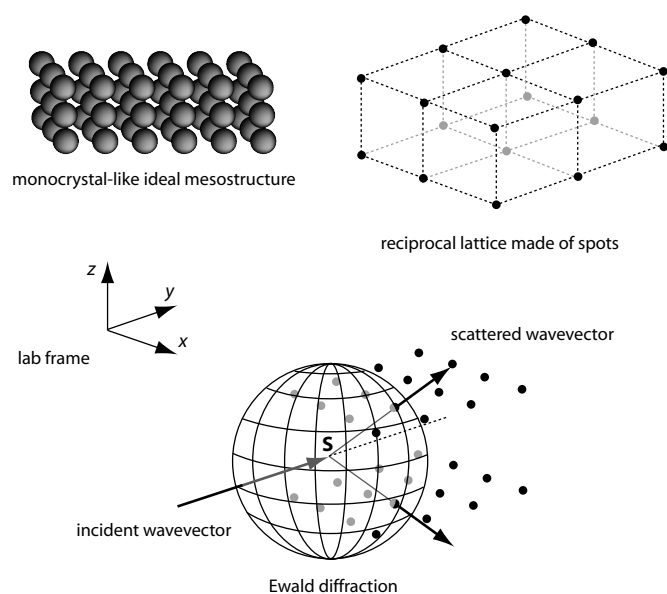
monocrystal-like ideal mesostructure

reciprocal lattice made of spots

z

y

x

lab frame

scattered wavevector

S

incident wavevector

Ewald diffraction

Figure 2.6. *Ideal mesostructure with mesopores placed at the nodes of a "single-crystal" lattice, and its reciprocal lattice. The intersection of the reciprocal lattice with the Ewald sphere gives the directions of the diffracted beams.*

domains which possess an orientational disorder around the axis perpendicular to the substrate—this is a feature common to nearly all mesostructured films that is also called *planar disorder*. Thus, mesostructured films typically have *out-of-plane* order (i.e. related to diffraction planes parallel to the substrate) but lack *in-plane* order (i.e. related to diffraction planes perpendicular to the substrate). This is true if we consider a sufficiently large region investigated by the impinging beam: at the SAXS beamline at Elettra this is typically on the order of the millimetre, therefore $\sim 10^3$ mesostructured domains are sampled.

There are essentially two configurations used in the acquisition of SAXS patterns of mesostructured films: the angle of incidence of the X-ray beam impinging on the sample may be set to either small angle (slightly above the critical angle, i.e. 0.2–0.3°) or perpendicular to the film surface (90°). These two configurations are referred to as *grazing* and *transmission* incidence, respectively, and yield information on the out-of-plane and in-plane mesostructure order. When the sample is in grazing incidence (GISAXS) the detector acquires out-of-plane reflections that are not accessible by transmission mode, whereas in transmission mode in-plane reflections are sampled which cannot be recorded in grazing incidence.

This can be understood by visualising the structure of the reciprocal lattice and its intersection with the Ewald sphere (Figure 2.7). Due to the lack of global in-plane order, the reciprocal lattice is a collection of concentric rings, centred on the axis perpendicular to the substrate. These rings can be thought as the infinite replication of the spots around the axis perpendicular to the substrate and intersecting the origin. Alternatively, one can visualise it as a breakdown of symmetry in the direction perpendicular to the substrate, thus any *n*-fold rotation axis in the reciprocal space perpendicular to the substrate is lost, and circular symmetry is obtained.

When the Ewald sphere slices the ring-like reciprocal lattice in grazing incidence, the intersection is constituted by spots, whereas in transmission mode the

intersection is constituted by rings (central part of Figure 2.7), thus the detectors records spots in the former case and rings in the latter case. As a consequence, grazing incidence patterns still give spots, but patterns in transmission incidence are made of rings. Combined measurements in grazing and transmission incidence help understand the symmetry of the ordered mesophase as well as the extent of planar disorder.

The choice of the substrate depends on whether we are working in grazing incidence or transmission mode. In transmission mode the diffracted beams must travel through the substrate and towards the detector, therefore a *thick* substrate (e.g. 400 µm Si wafer, soda-lime glass) cannot be used and *thin* substrates must be resorted to (e.g. 50 µm Si wafer). In fact, the transmitted intensity fraction of a 8 keV radiation (corresponding to a wavelength of 1.54 Å) on a 400 µm Si wafer is only $\approx 10^{-3}$.[*][8] Using a 50 µm Si wafer however the transmitted intensity fraction increases to 0.5. Alternatively, one can increase the incident energy: for example a 16 keV radiation impinging on a 400 µm Si wafer has a transmitted intensity fraction of 0.47. However, a major disadvantage is that the scattering yield at 16 keV is much lower than at 8 keV for the elements typically used in mesostructured films (e.g. Si, Ti), therefore the diffracted signal is too weak than at 8 keV. Furthermore, fluorescence effects at 16 keV contribute to increasing the noise. In grazing incidence, substrate thickness is not an issue, as the diffracted beams do not traverse the substrate, therefore either thick or thin substrates can be used.

A third measurement mode can be set up by using a mixed grazing-transmission configuration: the incoming X-ray beam is set to impinge on the sample in grazing incidence, but a thin substrate is used instead of a thick one, therefore part of the incoming radiation is transmitted. This configuration has a few advantages with respect to grazing incidence using a thick substrate, especially if thin microscope cover slides are used as the substrates, as they can be handled more easily than thin Si wafers.

2.2.6 In situ measurements

One major advantage of using synchrotron light as the X-ray source is high brightness, which is hundreds of thousands of times higher than a conventional X-ray tube. Thus a diffraction pattern of a mesostructured film can be taken in a very short time, typically less than 1 second, whereas in a conventional instrument this would require hours of exposition. Together with the non-destructiveness of this technique, this feature makes SAXS with synchrotron light the most important tool for structural characterization of mesostructured films.

A dip-coater was specifically built by our research team in order to conduct in situ experiments at the SAXS beamline of Elettra (Figure 2.8). The goal was to investigate mesostructure formation upon solvent evaporation during dip-coating and in the first seconds after film deposition. In standard laboratory dip-coaters, the solution vessel is fixed and the substrate is dipped into and extracted from the solution by a moveable sample holder. In our dip-coater it is the other way round: the solution is moved by a linear guide and the sample is fixed. This is to ensure that the probed region of the sample remains fixed during the whole ex-

---

[*]The transmitted intensity is given by $T = I_0 \exp(-n\mu_a d)$, where n is the number of atoms per unit volume, μ_a is the atomic photoabsorption cross section and d is the thickness of the substrate.

in-plane disorder

out-of-plane order

real mesostructure with planar disorder

000

reciprocal lattice made of concentrical rings

z
y
x

lab frame

S: sample

scattered
wavevectors

incident
wavevector

S

000

beam
stop

grazing incidence:
diffraction along specific directions

beam
stop

000

S

transmission mode:
diffraction along cones

out-of-plane
spots

in-plane and
out-of-plane
rings

in-plane
spots
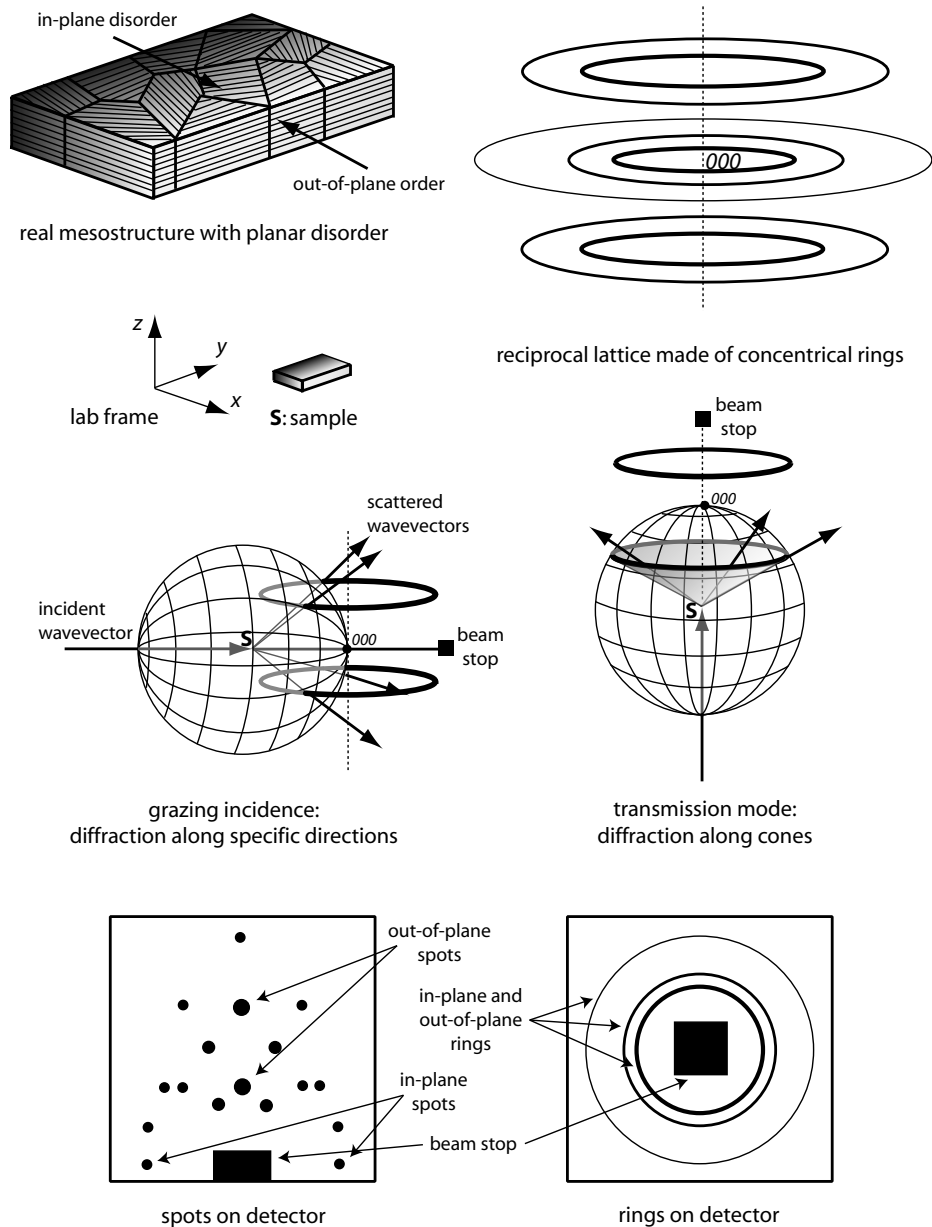
beam stop

spots on detector

rings on detector

Figure 2.7. *Real mesostructure with in-plane misorientation of ordered mesostructured do-
mains: the reciprocal lattice can be pictured as a collection of concentric rings,
whose intersection with the Ewald sphere gives either spots or rings depending
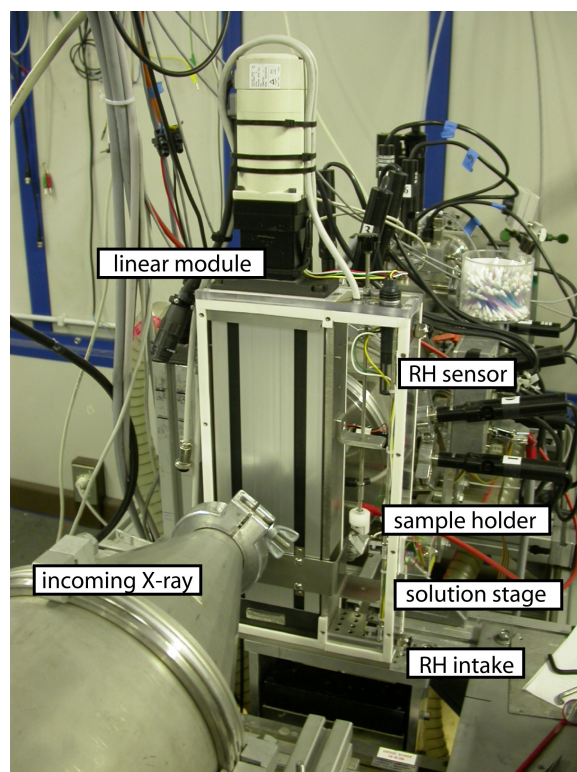on whether the measurement is in grazing incidence or in transmission mode.*

Figure 2.8. *Dip-coater in its in situ configuration at the SAXS beamline, Elettra.*

periment. The linear guide is moved by a direct current motor which is remotely controlled through a controller interfaced with a PC. A set of connector cables ensures communication between the dip-coater in the optics hutch and the hardware in the experimental hutch, so that it is possible to operate from the control room, as entry in the experimental hutch is strictly forbidden when shutters are open for obvious safety reasons. The linear guide provides micrometric control on the movement and speed when raising and lowering the solution vessel, as well as vibration damping. The dip-coater is enclosed in an airtight cabinet into which dry or wet air can be pumped in order to control relative humidity (see Chapter 1, page 48).

2.2.7 Data analysis

Diffraction patterns are stored in 12-bit TIFF files[9] which can readily manipulated with software Fit2d. This is a general purpose and specialist data analysis programme developed at the European Synchrotron Research Facility (ESRF), used on most beamlines at ESRF and other synchrotron facilities, as well as by many other crystallography groups throughout the world.[10] Fit2d is used for both interactive and batch data processing, and includes important image analysis tools such as intensity scaling, one-click d-spacing calculation, 1-d integration, calibration and correction for detector distortions.

The finite curvature of the CCD detector introduces a distortion on the image, therefore it is necessary to recalculate the pixel matrix on the basis of a standard correction grid (previously determined by the Austrian SAXS group and valid for all measurements with that CCD detector). Upon loading a diffraction im-

age on the graphical interface, a macro corrects for space distortion. Other image manipulations, such as dark current correction and background correction, were not performed, as they did not result in a significant improve in image quality. Furthermore, they were not strictly required in our data analysis which is based on qualitative (e.g. distance between diffraction maxima) rather than quantitative (e.g. absolute intensity) calculations.

The sample-to-detector distance and the beam centre position are calculated using the silver behenate diffraction pattern. This pattern is loaded into the Fit2d graphical interface, and the ring coordinates are input by clicking on the diffraction ring. A calibration routine fits the coordinates with the equation of a circle and yields the beam centre position (in pixels) and the sample-to-detector distance (in mm), as well as other parameters such as detector tilt angle (Figure 2.9). Subsequently, TIFF files of diffraction patterns of samples can be loaded into Fit2d for analysis (Figure 2.10).

Diffraction patterns taken in grazing incidence and transmission mode give a first indication on the presence of an ordered mesostructure and its planar disorder. A first visual inspection may suggest the mesostructure symmetry group if this is known from the literature or from previous data, especially for a trained eye: for example, $Im\bar{3}m$, $p6mm$, $R\bar{3}m$ patterns are very easily recognisable as they are very recurrent in mesostructured films. The operation of associating a diffraction pattern with a space group is often called *attribution*. A major advantage in using a two-dimensional detector instead of a linear detector is that attribution is much less ambiguous. With a linear detector, space group identification is often ambiguous, since attribution is based on a small number of reflections. Conversely, a two-dimensional detector can acquire a higher number of spots which can be used for a more reliable attribution.

A more accurate attribution of the pattern to a space group can be performed by software simulations, for example with CMPR, or with Nanocell. CMPR[11] is a multipurpose program that can be used for displaying diffraction data, as well as manual auto-indexing and peak fitting. Nanocell[12] is an interesting code written for Mathematica® by Prof. Hillhouse's research group specifically for mesostructured films, and which takes into account dynamical effects involving multiple reflection-refraction effects in the film.

The diffraction pattern is then indexed according to its space group: *indexation* is the process of assigning *hkl* indices to each spot in the pattern. After that, the d-spacings of each spot are measured so that cell parameters can be calculated. The cell parameter calculation can be automated: in the case of this doctorate work, mathematical procedures have been implemented in Mathematica® 5.1. These calculation methods will be addressed to in more detail in the experimental chapters.

2.3 Transmission Electron Microscopy (TEM)

2.3.1 Introduction

One of the most powerful instruments for investigating the microstructure of materials is transmission electron microscope (TEM). TEM enables the fine-scale microstructure to be examined in specimens sufficiently thin to facilitate transmission of a beam of electrons without a great loss of intensity. The schematic diagram of a TEM is presented in Figure 2.11. Electrons are accelerated by a tungsten
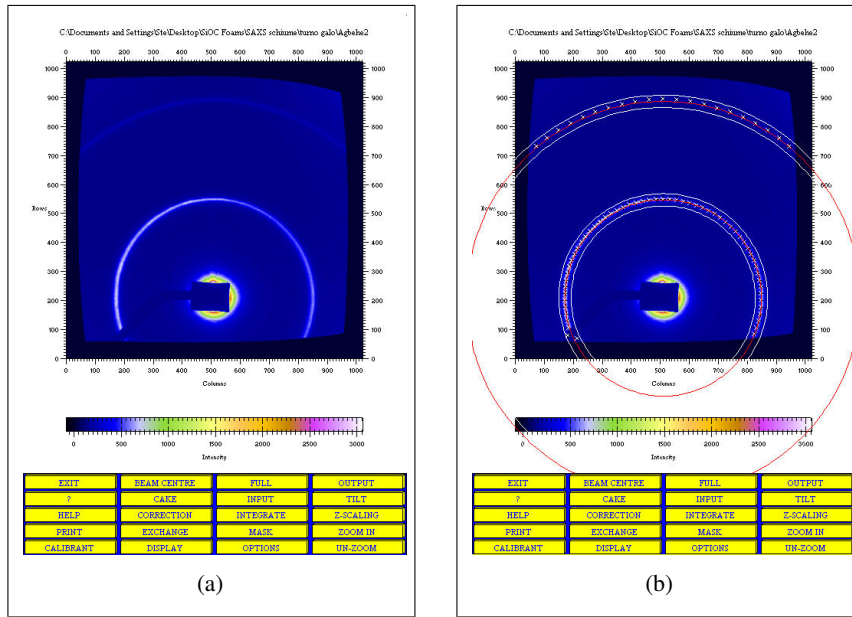
Figure 2.9. *Fit2d graphical interface: (a) the silver behenate diffraction pattern is loaded for calibration; (b) the calibration routine fits the rings and yields the calibration parameters, such as sample-to-detector distance and beam centre position.*

filament or a LaB_6 crystal through an evacuated column containing an assembly of condenser, objective and projector lenses.[13] Alternatively, in high resolution instruments a field emission (FE) electron source is used instead of conventional sources based on the thermionic effect. The interaction of the electron beam with the sample and the subsequent formation of an image can be treated with Abbe's theory of image formation. According to this theory, the incident electromagnetic wave impinges on the grating object and is diffracted, a diffraction pattern then forms in the back focal plane, which corresponds to the object's Fourier transform. The diffraction pattern is then reconverted into a real image in the image plane by the objective lens through an inverse Fourier transform. The intermediate lens then produces a second intermediate image which is magnified at the viewing screen by the final projector lens.

The incident radiation is not an electromagnetic wave, but rather the particle wave associated with the accelerated electrons:

$$\lambda = \frac{h}{\sqrt{2m_0 E \left(1 + \frac{E}{2E_0}\right)}}, \tag{2.14}$$

where m_0 is the mass electron at rest, $E = eV$ is the energy of the electron accelerated by the potential V, and the term $E_0 = m_0 c^2$ accounts for the relativistic correction. For example, an electron of energy 100 keV has a wavelength of 3.7 pm.

Theoretically, very high resolution can be attained, but in practice this is limited by strong aberration effects, and resolutions on the order of the Å are obtained in high resolution instruments. Because electron are used instead of electromagnetic radiation, electrostatic lenses are used, which deflect the electron trajectory. Furthermore, the wavelength of the incident electron beam can be tuned by varying the accelerating voltage.
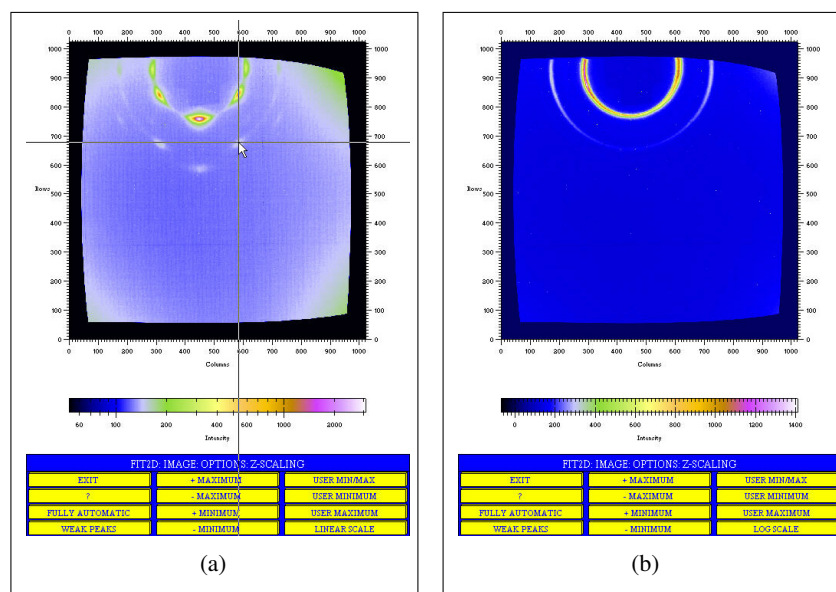
Figure 2.10. *Examples of SAXS patterns of a mesoporous silica films loaded into Fit2d, showing spots in grazing incidence (a) and rings in transmission mode (b). The d-spacing value of a spot can be obtained by clicking on that spot with the practical crosshair cursor visible in (a).*

The resolution of the image depends on the number of grating orders that are transmitted through the optical system. Interchangeable objective apertures, typically ∼50 µm to ∼200 µm are positioned close to the back focal plane of the objective lens to enhance image contrast. If an objective aperture intercepts all the diffracted beams and allows only the direct beam to pass, deficiency contrast occurs and a *bright field* image is formed. Alternatively, the objective aperture can be used to select a single diffracted beam to produce a *dark field* image.

2.3.2   *Applications of TEM in mesoporous films*

TEM in mesoporous films can give direct high quality images of the mesostructure. Typically, the film is cut into µm-thick slices by a microtome, and further thinned by Ar^+ ion beam milling, until a hole is dug at the centre of the sample. Measurements are then carried out close to the edge of the hole, so that a region of the sample with the desired thickness can be observed by moving the sample stage. A more rapid but less effective method is to scratch a film from its substrate and disperse the fragments in an organic solvent. Mesoporous films which have undergone full removal of the template generally give better quality images than samples where the organic mesophase is still present within the film: this is because the former has a high electronic contrast (inorganic-void), whereas the latter provides a lower electronic contrast (inorganic-organic). Furthermore, a mesostructured film that has not undergone thermal treatment is mechanically unstable, and can collapse when the film is cut and drilled before TEM measurements.

TEM can be regarded as a structural technique complementary to SAXS. In fact, in SAXS the probed region extends on the volume of matter interested by the interaction with the impinging X-ray beam, of characteristic length ranging from 500 µm to several mm. Conversely, TEM describes the structure on a very local
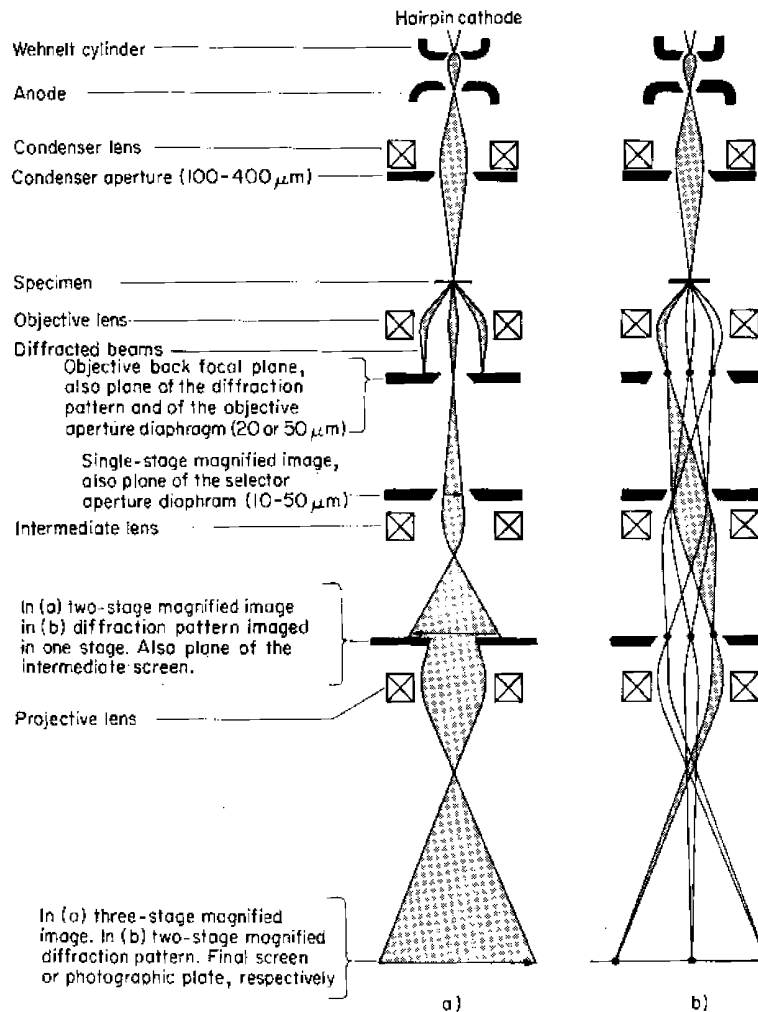
Hairpin cathode

Wehnelt cylinder

Anode

Condenser lens

Condenser aperture (100-400 µm)

Specimen

Objective lens

Diffracted beams

Objective back focal plane, also plane of the diffraction pattern and of the objective aperture diaphragm (20 or 50 µm)

Single-stage magnified image, also plane of the selector aperture diaphram (10-50 µm)

Intermediate lens

In (a) two-stage magnified image in (b) diffraction pattern imaged in one stage. Also plane of the intermediate screen.

Projective lens

In (a) three-stage magnified image. In (b) two-stage magnified diffraction pattern. Final screen or photographic plate, respectively

a)   b)

Figure 2.11. *Schematic diagram of a transmission electron microscope.*

scale, typically few tens of nm to ∼1 µm. When determining the mesostructure symmetry, TEM measurements may be misleading, in that only a localised area of the specimen is sampled: this can be the case when the film is not homogeneous (i.e. one can find a "lucky" ordered area when the rest of the sample is more or less disordered, or the other way round). Furthermore, different planes merge due to the depth of field of the electron microscope, so that three-dimensional structures are necessarily collapsed into two-dimensional images, and this can lead to wrong conclusions: for instance, cylindrical pores may be observed when in fact this is the superposition of planes where the pores are most densely packed. This latter case is exemplified in Figure 2.12, which shows the 100 and 110 projections of a cubic $Im\bar{3}m$ structure: along the [110] direction the pores seem to fuse together into parallel cylinders. However, SAXS measurements of the observed sample were compatible only with an $Im\bar{3}m$ structure so we could get to the conclusion that the cylinders are an artifact.

In order to have reliable information on mesostructure symmetry, different projection planes are accessed by multiple TEM observations, such as cross-section and in-plane views. Thus, the right mesophase symmetry can be sorted out by care-
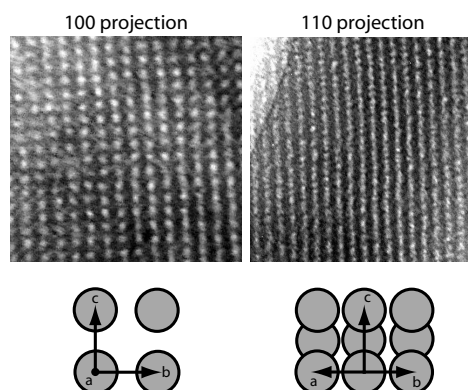
Figure 2.12. *TEM images may be misleading: a cubic mesostructure with spherical pores may look like a two-dimensional hexagonal stack of cylindrical pores (top right), and only SAXS (not shown in figure) can sort out the discrepancy. Top: TEM images along the [100] (left) and [110] (right) directions. Bottom: simulations of the respective projection planes with CaRIne crystallography software.*[14]

ful inspection or software simulation. For example, if 6-fold symmetry axes are observed in one image, a two-dimensional hexagonal symmetry is the first guess, with ordered stacks of cylindrical pores. But if a 4-fold symmetry axis is observed in the same sample, one has to call into question the previous guess and suppose the presence of a cubic unit cell—unless we are in the presence of multiple phases, in which case we may be observing different domains having different mesostructures. These observations underline, once again, the key importance of having the support of SAXS measurements.

Mesoporous films can be investigated by acquiring TEM images in scanning mode (Scanning Transmission Electron Microscopy, STEM) in which a small electron probe (about 1 nm FWHM) is rastered over the sample. In STEM, a bright field detector is placed in a conjugate plane to the back focal plane to intercept the direct beam while a concentric annular dark field detector intercepts the diffracted electrons. In STEM images the image contrast is proportional to the local atomic number, therefore the contrast between pores and inorganic framework is highly enhanced with respect to conventional bright-field mode. Furthermore, this technique causes a lower radiation damage to the investigated sample, therefore systems that require special care can be studied (STEM is routinely used for biological research). For example, TEM measurements performed on mesoporous films containing Au nanoparticles led to aggregation of nanoparticles to large clusters, this was avoided when TEM was performed in scanning mode. An important requisite of STEM is that the electron spot be small (1 nm FWHM), therefore field emission guns (FEG) must be employed as the electron sources.

2.4   Fourier Transform Infrared spectroscopy (FTIR)

Spectroscopic techniques are based on the interaction of electromagnetic waves (most typically UV, visible, IR, MW, X-rays) with matter. The nature of the interaction depends upon the properties of the substance. When radiation passes through a sample (solid, liquid or gas), certain frequencies of the radiation are ab-

sorbed, thus from the measurement of the intensity absorbed by the sample under investigation at different incident energies it is possible to perform qualitative and quantitative analysis.

The infrared (IR) portion of the electromagnetic spectrum ranges from 12800 to 10 cm^{-1}, corresponding to wavelengths 0.78 to 1000 μm.[†] The IR portion is divided into three regions: the near-, mid- and far- infrared, named for their relation to the visible spectrum. The far-infrared, (400–10 cm^{-1}) lying adjacent to the microwave region, has low energy and may be used for rotational spectroscopy. The mid-IR region (4000–400 cm^{-1}) may be used to study the fundamental vibrations and associated rotational-vibrational structure. The higher energy near-IR (14000–4000 cm^{-1}) can excite overtone or harmonic vibrations. The majority of applications is restricted to the mid-IR region, especially in organic compounds identification: in many cases the IR spectrum of an organic compound gives a specific fingerprint which can be used to detect that particular substance.

2.4.1 Theoretical model for IR spectroscopy

Infrared spectroscopy is related to the interaction of IR radiation with matter. More specifically, it is based on the coupling between the electromagnetic radiation and the resonance frequencies of vibration of chemical bonds (*vibrational modes*). For a molecule to show infrared absorption (*IR active*), its electric dipole moment must change during the vibration (selection rule). For example, charge distribution in a HCl molecule is not symmetric, in that Cl has a higher electronic density than H, thus the molecule is said to be polar. As the HCl molecule starts to vibrate, the dipole momentum changes and a restoring electric field is set up. If there is a match between the incident electromagnetic radiation and the resonance frequency of the HCl molecule, energy is transferred to the HCl molecule and a decrease in the transmitted intensity is observed. By varying the incident energy in small steps and recording the intensity transmitted through the sample, a wavenumber vs. absorbed intensity spectrum can thus be obtained.

Let us consider a simple mechanical model where two masses m_1 and m_2 are linked by a spring. A perturbation of one mass along the spring axis, such as a movement of y from its equilibrium position, causes a restoring force $F = -ky$ which is proportional to the mass displacement, the proportionality constant being the spring constant k. Thus a vibration is set up, called *simple harmonic movement*. The vibrational energy can be expressed in classical mechanics as $E = \frac{1}{2}ky^2$. However, since we are dealing with atoms and chemical bonds instead of masses and springs, we need to resort to quantum mechanics: here, the molecular Hamiltonian corresponding to the electronic ground state can be approximated by a harmonic oscillator in the neighborhood of the equilibrium molecular geometry (Figure 2.13). Solving the Schrödinger equation for this system with the harmonic potential $V = \frac{1}{2}ky^2$ leads to the well-known effect of energy quantisation, which can be expressed as:

$$E = \hbar \left(n + \frac{1}{2} \right) \sqrt{\frac{k}{\mu}}, \tag{2.15}$$

where n is the *vibrational quantum number*, which is a positive integer, and μ is

---

[†]The wavenumber, unit length cm^{-1}, is defined as the reciprocal of the wavelength expressed in cm, and is traditionally employed in infrared spectroscopies.

the reduced mass $\mu = \frac{m_1 m_2}{m_1 + m_2}$. For $n = 0$ we have the zero-point energy $E = \frac{h}{2\nu_m}$, where ν_m is the molecule's resonance frequency. As a consequence, the allowed vibrational transitions are quantised according to selection rule $\Delta n = \pm 1$:

$$\Delta E = h\nu_m = \hbar \sqrt{\frac{k}{\mu}}, \tag{2.16}$$

and we have a set of allowed energies:

$$E_0 = \frac{1}{2} h\nu_m, \; E_0 = \frac{3}{2} h\nu_m, \; E_0 = \frac{5}{2} h\nu_m, \ldots \tag{2.17}$$

It is useful to express the transition energy as a wavenumber:

$$\overline{\nu} = \frac{1}{2}\pi c \sqrt{\frac{k}{\mu}} = 5.3 \cdot 10^{12} \sqrt{\frac{k}{\mu}} \tag{2.18}$$

According to the harmonic model, the transition energy from level 1 to level 2 is equal to the transition energy from level 2 to level 3, and so on (Equations 2.17 and 2.18). Thus, according to the selection rule $\Delta \nu = \pm 1$ only one absorption band should be observed for each molecular vibration, but this is in contrast with experimental data. Therefore, we have to make some correction to the harmonic model, introducing *anharmonic* terms: in particular, when the displacement of the two atoms is not so small to be considered a perturbation, the harmonic approximation does not hold. For example, when the atoms get too close, the potential energy increases dramatically because of electrostatic repulsion; on the other hand, when the atoms are too far away, the interatomic distance is so large that dissociation can occur. This can be solved analytically, however the solutions are quite complicated and fall outside the scope of this description. In practice, there are several factors increasing the number of absorption bands, such as: overtone bands (absorption at frequencies representing the fundamental frequencies at the multiples of the fundamentals), combination bands (two fundamental vibrations interact and are influenced by radiation at the combined frequency), vibrational-rotational bands (the single vibrational band is accompanied by a series of smaller bands at lower and higher frequencies, especially in gas phase), and harmonic coupling bands (interaction from adjacent groups of nearly identical oscillation frequencies produces a series of bands quite apart from those normally expected).

The frequency of the vibrations can be associated with a particular bond type. Simple diatomic molecules have only one bond, which may stretch. For example, in a carboxyl group C=O, $m_C = 2 \cdot 10^{-26}$ kg and $m_O = 2.7 \cdot 10^{-26}$ kg, so the approximate wavenumber is $\overline{\nu} = 1600$ cm^{-1} and the wavenumber is experimentally found to be between 1600 and 1800 cm^{-1}. More complex molecules may have many bonds, and vibrations can be conjugated, leading to infrared absorptions at characteristic frequencies that are related to chemical groups.

Vibrational motions fall into two categories: *stretching* when there is a change in the interatomic distance along the bond axis, and *bending* when there is a change in the angle between two bonds. Stretching and bending modes can be further divided into six types of vibration: symmetric and asymmetric stretching, scissoring, rocking, wagging and twisting, as shown in Figure 2.14. In general, a molecule consisting of n atoms has a total of $3n$ degrees of freedom, corresponding to the
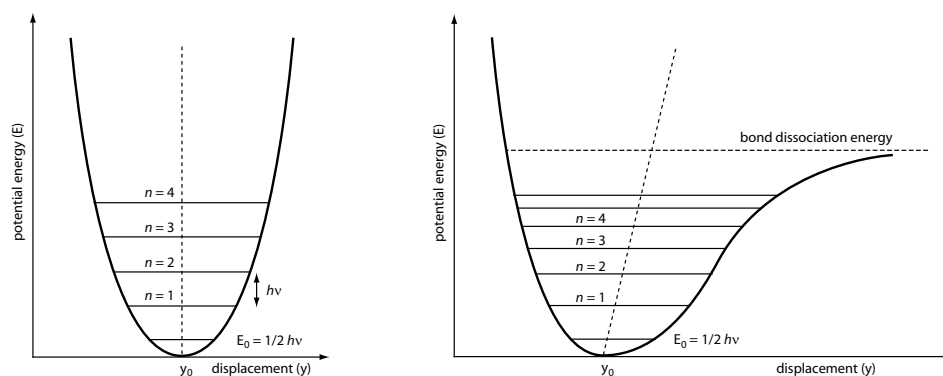
Figure 2.13. *Left: Energy curve for a vibrating spring with quantum mechanical behaviour. Right: energy curve for an anharmonic oscillator, showing the vibrational levels for a vibrating bond.*

Cartesian coordinates of each atom in the molecule. In a nonlinear molecule, 3 of these degrees are rotational and 3 are translational and the remaining correspond to fundamental vibrations; in a linear molecule, 2 degrees are rotational and 3 are translational. The net number of fundamental vibrations is therefore $3n - 6$ for nonlinear molecules and $3n - 5$ for linear molecules. For example, propane has 27 fundamental vibrations, therefore one can predict 27 absorption bands in an IR spectrum. Water, which is a nonlinear molecule, has 3 fundamental vibrations: symmetric stretching, asymmetric stretching and scissoring.

2.4.2 Fourier transform

In Fourier transform spectroscopy, spectra are collected based on measurements of the temporal coherence of a radiative source, using time-domain measurements of the electromagnetic radiation or other type of radiation. In other words, instead of varying the energy of the electromagnetic radiation, Fourier transform spectroscopy exposes the sample to a single pulse of broad bandwidth radiation and measures the response. The resulting signal, called a free induction decay, is a direct measurement of the temporal coherence of the light and contains a rapidly decaying composite of all possible frequencies. Using a Fourier transform of this, the spectrum of the light can be calculated. In this way the Fourier transform spectrometer can produce the same kind of spectrum as a conventional spectrometer, but in a much shorter time.

The principles of the Fourier transform approach can be compared to the behaviour of a musical tuning fork: if a tuning fork is exposed to sound waves of many frequencies, it will vibrate only when the incident sound wave frequency is in tune, i.e. equal to the characteristic vibration frequency of the tuning fork. This is similar to conventional spectroscopic techniques, where the radiation frequency is varied and absorption is detected at those frequencies where the sample is in tune with the incoming radiation. However, if we strike the tuning fork or expose it to many sound waves with broad bandwidth, the tuning fork will tend to vibrate at the fork's own characteristic resonance frequency. This is similar to Fourier transform spectroscopy, where a broadband pulse of radiation excites the sample and a signal consisting primarily of the characteristic frequencies for that sample is generated.

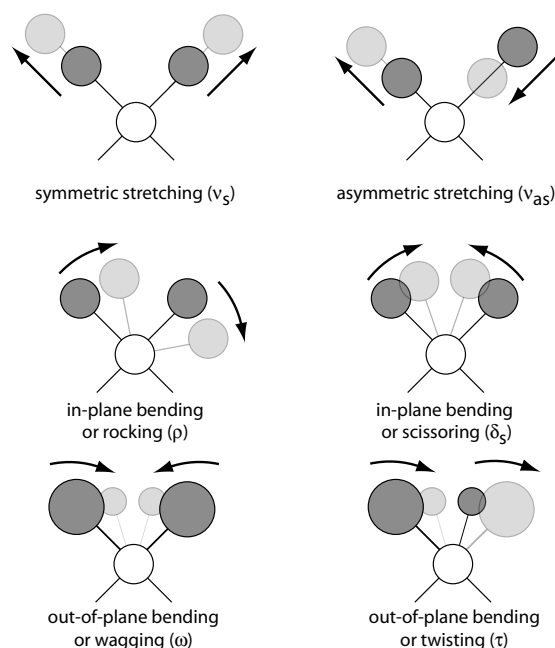A conventional IR spectrometer records the amount of energy absorbed when

symmetric stretching (ν_s)   asymmetric stretching (ν_{as})

in-plane bending
or rocking (ρ)   in-plane bending
or scissoring (δ_s)

out-of-plane bending
or wagging (ω)   out-of-plane bending
or twisting (τ)

Figure 2.14. *Examples of vibrational modes: the first two are stretching modes (symmetric and asymmetric), the others can be classified as bending modes (rocking, scissoring, wagging, twisting).*

the frequency of the IR light is varied by a monochromator. Conversely, in a Fourier transform spectrometer a broadband IR light illuminates the sample, and the radiation transmitted is guided through an interferometer. Performing a mathematical Fourier transform on this signal (*interferogram*) results in a spectrum identical to that which would be obtained by conventional energy-dispersive infrared spectroscopy. FTIR spectrometers are cheaper than conventional spectrometers because the fabrication of an interferometer is cheaper than a monochromator. In addition, measurement of a single spectrum is faster for the FTIR technique because information at all frequencies is collected simultaneously. This allows multiple samples to be collected and averaged resulting in an improvement in sensitivity. Because of its various advantages, virtually all modern infrared spectrometers are FTIR instruments.

The FTIR equipment used for the experimental work of this thesis was a Thermo Nicolet Nexus FTIR spectrophotometer. We used a KBr-DTGS detector and a KBr beamsplitter working in the mid-IR range (7400–350 cm^{-1}). Spectra were acquired with 4 cm^{-1} resolution, averaging 256 scans (which gives 16 times more sensitivity with respect to 1 scan).

2.5   Nitrogen sorption

Adsorption-desorption of gas molecules (typically N_2) on surfaces of solid materials is a commonly used method for characterization of porous materials.[15,16] The techniques based on gas sorption output adsorption-desorption isotherms obtained from multiple gas adsorption and desorption cycles, from which information about
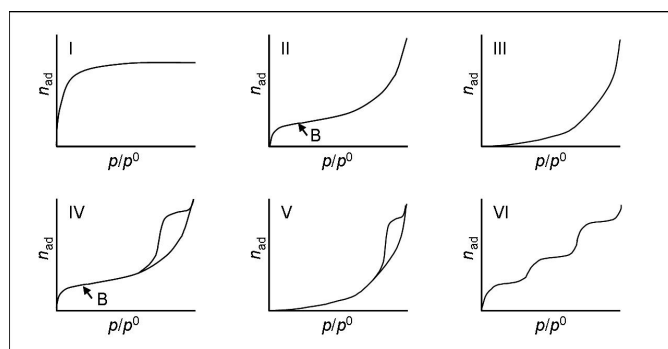
Figure 2.15. *The six adsorption-desorption isotherm types according to the IUPAC classi-fication.*

the porosity of the materials can be calculated, e.g. specific surface area of the sample, size and shape of pores.

According to IUPAC, isotherms are classified into six types according to the different shapes, and the different types of hysteresis loops are classified into four types (Figure 2.15). Type I isotherms are typical for microporous materials such as zeolites, where the steep slope of the curve at low partial pressures indicates a high surface area. Type II isotherms are typical for aggregated powders such as clays, pigments and cements, which have no ordered pore structure. Type III and Type V isotherms are very rare, but may be seen in water/graphite systems. Type IV isotherms are typical of materials containing mesopores. The distinctive form of Type VI isotherms is due to a stepwise layer-by-layer adsorption process, usually by non-polar molecules such as argon, krypton or xenon on uniform surfaces.

The specific surface area of porous materials may be estimated from the theory by Brunauer, Emmett and Teller, which is expressed by the BET equation:

$$\frac{p/p_0}{n(1-p/p_0)} = \frac{1}{n_m C} + \frac{C-1}{n_m C}(p/p_0),\qquad(2.19)$$

where p/p_0 is the relative pressure, n is the amount absorbed, n_m is the mono-layer capacity, i.e. the maximum amount adsorbed, and C is a constant. The plot of $(p/p_0)/[n(1-p/p_0)]$ versus p/p_0 gives a straight line with the slope $s = (C-1)/n_m C$. The specific surface area $a(\text{BET})$ may then be calculated from the relation: $a(\text{BET}) = n_m N_A \sigma$, where N_A is Avogadro's constant and σ is the average area occupied by one molecule.

2.6 Atomic Force Microscopy (AFM)

The atomic force microscope is based on the possibility of performing a surface scan of the sample using a nanometre-sized tip positioned on a microscale can-tilever. A laser light is shone onto the cantilever, off which it is reflected towards a position-sensitive detector (typically an array of photodiodes), which gives a mea-sure of the cantilever deflection. Therefore, the measure of the cantilever height variation with the scan can be used to reconstruct the sample's surface morphol-ogy.

Forces that are measured in AFM include mechanical contact force, Van der Waals forces, capillary forces, chemical bonding, electrostatic forces, magnetic

forces. The modes of operation are contact and non-contact, depending on whether the interatomic repulsion or attraction forces are measured. In dynamic mode, the cantilever is oscillated at or close to its resonance frequency; the oscillation amplitude, phase and resonance frequency are modified by tip-sample interaction forces and provide information about the sample's surface characteristics.

References

[1] C. Kittel. *Introduction to solid state physics*. John Wiley & sons, Inc., New York, 7th edition, 1996.

[2] N. W. Ashcroft, N. D. Mermin. *Solid state physics*. Harcourt College Publishers, 1976.

[3] P. Dubček. Nanostructure as seen by the SAXS. *Vacuum*, **2005**, *80*, 92–97.

[4] M. Rappolt, H. Amenitsch, J. Strancar, C. V. Teixeira, M. Kriechbaum, G. Pabst, M. Majerowicz, P. Laggner. Phospholipid mesophases at solid interfaces: in situ X-ray diffraction and spin-label study. *Adv. Colloid Interf. Sci.*, **2004**, *111*, 63–77.

[5] H. Amenitsch, M. Rappolt, M. Kriechbaum, H. Mio, P. Laggner, S. Bernstoff. First performance assessment of the small-angle X-ray scattering beamline at ELETTRA. *J. Synchrotron Rad.*, **1998**, *5*, 506–508.

[6] http://www.ibr.oeaw.ac.at/beamline/saxs_group.html (accessed December 2007).

[7] T. N. Blanton, T. C. Huang, H. Toraya, C. R. Hubbard, S. B. Robie, D. Louer, H. E. Gobel, G. Will, R. Gilles, T. Raftery. JCPDS-International center for diffraction data round robin study of silver behenate. A possible low-angle X-ray diffraction calibration standard. *Powder Diffr.*, **1995**, *10*, 91–95.

[8] http://henke.lbl.gov/optical_constants/filter2.html (accessed December 2007).

[9] http://www.ibr.oeaw.ac.at/beamline/software/tiff_doc_6_0.pdf (accessed December 2007).

[10] http://www.esrf.eu/computing/scientific/FIT2D/ (accessed December 2007).

[11] http://www.ncnr.nist.gov/programs/crystallography/software/cmpr/ (accessed December 2007).

[12] http://cobweb.ecn.purdue.edu/~hgroup/Research/Nanocell/NANOCELL.html (accessed December 2007).

[13] P. E. J. Flewitt, R. K. Wild. *Physical methods for materials characterization*. Institute of Physics Publishing, Bristol, 1994.

[14] http://pros.orange.fr/carine.crystallography/ (accessed December 2007).

[15] S. J. Gregg, K. S. W. Sing. *Adsorption, surface area and porosity*. Academic Press, London, 1982.

[16] F. Rouquerol, J. Rouquerol, K. Sing. *Adsorption by powders and porous solids*. Academic Press, San Diego, USA, 1999.

Chapter 3

Mesoporous silica films

Abstract

This chapter presents the development of the research on mesoporous silica films. As an introduction, we present the previous findings upon which the experimental work of this thesis is based on. The remainder of the chapter deals with the physicochemical tuning of mesoporous silica films. In particular, different block copolymers were used as the templating agents with the aim of tailoring pore size. The inorganic framework was modified by a co-condensation synthesis employing organo-substituted silicon alkoxides, leading to the inclusion of organic moieties and a higher degree of order. Different hybrid precursors (organo-alkoxysilanes) were also tested for the preparation of mesoporous materials in the form of membranes. Eventually, a separate study on mesoporous silica and organosilica membranes is presented, focusing on the mechanisms of water adsorption-desorption at the mesopore surface.

3.1   Introduction to experimental chapters

The following three chapters focus on the most significative experimental findings of this doctorate work. Chapter 3 presents the research on mesoporous silica films, which has been conducted with the twofold purpose of acquiring insight into the basic self-assembly mechanisms and tuning the physicochemical properties of such systems (e.g. pore size, inorganic framework composition). Chapter 4 revolves around the integration of mesoporous silica coatings in the fabrication of other types of materials, with the purpose of exploring the possibilities and the advantages offered by mesoporosity in functional materials (e.g. high specific surface area, nanometric pore size). In particular, in Chapter 4 three applications of mesoporous silica are presented: (1) as *nanoreactors* for the growth of nanoparticles inside the mesopores, (2) mesoporous coatings in macroporous ceramic foams for the fabrication of ceramic bodies with hierarchical meso-macro-porosity, (3) patterning with synchrotron radiation as an integration of nano- and micro-fabrication techniques. Chapter 5 focuses on two studies on mesostructured materials using advanced in situ characterisation techniques, with the aim of acquiring a better understanding of the synthetic parameters and the physicochemical processes occurring during film deposition. A novel in situ FTIR-SAXS combined technique for the simultaneous detection of physicochemical-structural changes in a mesostructured film is also presented.

This sectioning into three chapters does not strictly reflect the chronological development of research, but rather constitutes a logical division according to different subjects. Temporally, the doctorate activity started with the study of mesoporous silica films, extending the framework composition to organosilicas (hybrid organic-inorganic) and varying the pore size utilising different block copolymers as the structure-directing agents. Based on these findings, other applications were developed involving the integration of mesoporous silica coatings into other systems of interest, such as the synthesis of ceramic bodies with hierarchical macro-meso-porosity and the patterning of mesoporous films using X-ray lithography. At the same time, the periodic SAXS beamtime shifts available at the Elettra synchrotron throughout the doctorate were exploited for acquisition of experience on the analysis of mesoporous films. On these occasions new analytical techniques were developed in the framework of a collaboration with the beamline scientific staff. These improvements supplied feedback which led to the discovery of new applications and new synthesis protocols.

In the next section we outline the synthesis of mesoporous silica films and their characterisation applying the concepts described in Chapters 1 and 2. The developments in mesoporous silica constitute the pathway towards the application of mesoporous films in functional materials. Functional properties can be enhanced or created in mesoporous silica films, for example by the modification of the framework including chemical species exhibiting a functional property. Mesoporous films can be integrated with other types of materials or other technologies and find a place in advanced applications.

3.1.1   Mesoporous silica films

The synthesis protocol of mesoporous silica films was the subject of a previous work, consisting in the optimisation of a precursor solution and the processing

parameters for the synthesis of inorganic mesoporous films. This protocol was obtained after optimisation of the type and quantity of precursors in the initial sol (quantity and type of solvent, organic and inorganic precursors, quantity of water, ageing), as well as processing parameters (relative humidity, dip-coating pulling rate, thermal treatment).[1,2]

The inorganic precursor is tetraethoxysilane (TEOS), which was chosen because of its low kinetics of hydrolysis and condensation. Ethanol was selected as the solvent because of good wettability with the substrates (either Si wafers or glass slides) and compatibility with TEOS. Hydrochloric acid was selected as the catalyst in a concentration such that the solution's pH was set near to the isoelectric point of SiO_2 ($pH_{iep} \approx 2$) in order to ensure stability of the sol increasing shelf life. A poly(ethylene oxide)-*block*-poly(propylene oxide)-*block*-poly(ethylene oxide) amphiphilic block copolymer, commercially available from Sigma-Aldrich as Pluronic™ F127 (BASF) was selected as the templating agent (or *porogen agent*) due to its optimal self-assembly properties.

The precursor solution is prepared in two step: a first solution (*mother solution*) is prepared mixing 3.08 mL of EtOH and 4.26 mL of TEOS, and adding 0.355 mL of a 0.768 M HCl solution. This sol is stirred for 60 minutes, then a *templating solution* is added, which is obtained by mixing 15 mL of EtOH, 1.3 g of Pluronic F127 and 1.5 mL of a 0.057 M HCl solution. The molar ratios are reported in Table 3.1.

This solution is aged for ≈ 7 days to allow for a slight pre-condensation of the silane units (formation of the inorganic nano building blocks, NBBs), after which it is ready to be deposited. This period of time was chosen after films obtained from precursor solutions aged at different times were tested by SAXS experiments, which showed that the degree of order has a maximum when the precursor solution is aged for one week at room temperature. This phenomenon can be explained with the formation of NBBs with suitable size (see Chapter 1, page 47).

The common choice for the substrates is Si wafers (typically 100-oriented, p-type B-doped, thickness 400 μm) because they are suitable for SAXS, TEM and FTIR measurements. Regarding the use of the substrates for SAXS measurements, either thick or thin Si substrates may be chosen (page 75); in TEM measurements, Si ensure thermal dispersion and mechanical robustness; when FTIR spectra are acquired, a crystalline Si substrate allows transmission of the incident radiation due to its transparency in the mid-IR region.

Dip-coating at low relative humidity (RH$\approx$20%) yields mesostructured films with optical quality. This was determined by in situ SAXS experiments on mesostructured silica films: in particular, faster pulling rates yield thicker and less ordered films, and vice versa (see page 51). Therefore, in order to maximise the

Table 3.1. *Molar ratios of the mother, templating and final solutions used in the preparation of mesoporous silica.*

	TEOS	EtOH	H_2O	HCl	F127
Mother	1	2.78	1.04	$1.43 \cdot 10^{-2}$	-
Templating	-	1	0.32	$3.32 \cdot 10^{-4}$	$3.76 \cdot 10^{-4}$
Final	1	16.32	5.42	0.019	$5 \cdot 10^{-3}$

degree of order a low pulling rate is selected, in this case the minimum speed allowed by the dip-coater: 2.3 mm·s^{-1}.

Two structural characterisation techniques are usually employed for the study of the ordered mesostructure, SAXS and TEM. Whereas SAXS yields a more averaged information, extending to several domains in the millimetre range, TEM provides localised information. In addition, by SAXS measurements one can univocally determine the symmetry group to which a mesostructure belongs (see Chapter 2).

SAXS experiments showed that the as-deposited films are well organised into a cubic phase with spherical micelles when deposition is carried out at RH around 20%, whereas a two-dimensional hexagonal symmetry with cylindrical micelles is formed at higher RH. For RH values different than these, wormlike (disordered) phases are formed. SAXS measurements in both grazing incidence (GISAXS, Figure 3.1) and transmission (not shown in figure) were interpreted in order to obtain an unambiguous attribution of the ordered mesophase.

Crystallography software CMPR[3] was employed to analyse the SAXS patterns in transmission mode. The SAXS pattern of a sample treated at 60°C, acquired in transmission mode, presented diffraction rings (not shown in figure). This pattern was integrated radially from the beam centre in order to obtain a 1-dimensional plot of intensity vs. 2 theta. We used the "HKLGEN" function of CMPR which generates a list of the allowed reflections for a given set of unit cell constants and extinction conditions. It is possible to specify symmetry by space group and specify preferential orientation with respect to a substrate. A sample treated at 60°C was chosen because the structure at this temperature is assumed to be undistorted. Inspection of the intensity vs. 2 theta plot obtained by radial integration of the SAXS pattern revealed that the interplanar distances d_{002} and d_{202} were representative of a cubic cell, because the ratio between the two d-spacings was found to be d_{002}:d_{202}=1:$\sqrt{3}$.

Next, the patterns taken in grazing incidence were taken into consideration for simulations using CMPR, analysing the samples treated at different thermal treatments. The best fit for the undistorted structure observed at 60°C corresponded to a body-centred cubic lattice having $Im\bar{3}m$ symmetry group oriented with the (110) plane parallel to the substrate, i.e. the direction [110] of the unit cells is normal to the film surface (Figure 3.2 a). The $Im\bar{3}m$ unit cells form domains which are randomly oriented around the axis perpendicular to the substrate. This common feature of mesostructured films is commonly known as *planar disorder* and consists in the presence of out of plane order (i.e. order in the directions perpendicular to the film surface) and absence of in plane order (i.e. lack of order in the direction parallel to the film surface).

The GISAXS patterns of samples treated at increasing temperatures show the increase of the out of plane spots, whereas the in plane spots remain substantially unaltered. This corresponds to the uniaxial contraction of the mesostructure in the out of plane direction. This feature is commonly observed in mesostructured films[4,5] and is also known as *thermal shrinkage*. In this case, a "distorted $Im\bar{3}m$" mesophase symmetry can be detected. This smooth transition to a distorted mesostructure is generally reflected in a loss of symmetry, so the mesostructure symmetry at high temperature can be classified according to a symmetry group having lower symmetry. In the present case, two different symmetries that can originate from the uniaxial distortion of an $Im\bar{3}m$ structure along [110], namely *Fmmm* and
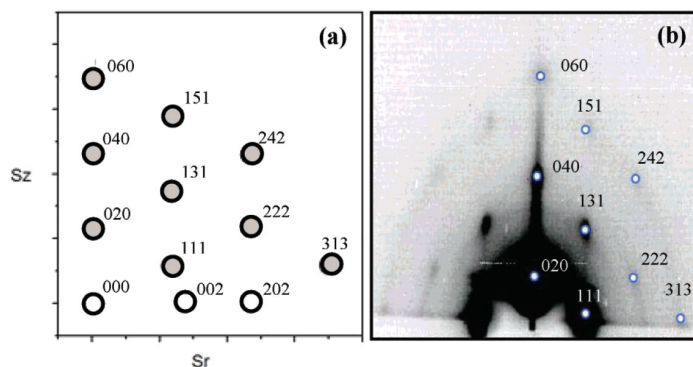
Figure 3.1. *Comparison between a computer-simulated image utilising the CMPR programme, of an Fmmm structure (a), and the GISAXS pattern of a mesoporous silica film synthesised at RH=20% and treated at 250°C with the Fmmm indexing (b).*

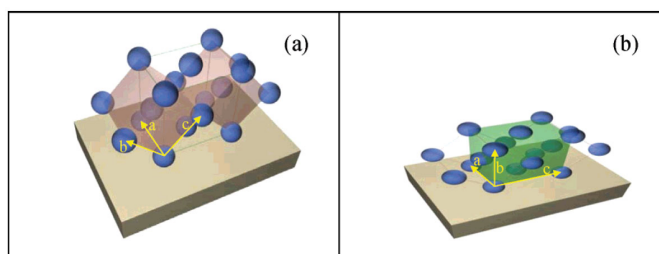**Figure 3.2.** *(a) Body-centred cubic unit cell (Im$\bar{3}$m symmetry) with the (110) face oriented parallel to the substrate ([110] direction normal to the substrate). (b) The shrinkage occurring upon thermal treatment causes a phase transition from cubic Im$\bar{3}$m to face centred orthorhombic Fmmm.*

Fddd which are both orthorhombic structures. These were taken into consideration for simulations utilising CMPR using the same procedure described above. The only symmetry that gave results matching the experimental SAXS patterns corresponded to the *Fmmm* symmetry group oriented with the (100) face parallel to the substrate.

A list of the allowed *hkl* Miller indices and the corresponding coordinates (d-space and 2-theta) were obtained as the best fit for the *Fmmm* cell. These reflection coordinates were transferred to the cylindrical coordinates observed in the GISAXS diffraction experiments (s_x and s_y). This was done by preparing a worksheet with the coordinates given by the *hkl* values and the relative s_x and s_y values (scattering vectors in the reciprocal space) according tho the cell parameters which gave the best fit:

$$s_x = \sqrt{\frac{h^2}{a^2} + \frac{l^2}{c^2}}, \quad s_y = \frac{k}{b}, \tag{3.1}$$

with the constraint $c = a\sqrt{2}$. Two-dimensional plots of s_x and s_y were thus obtained from the worksheet for each pattern. Figure 3.1 shows the experimental GISAXS pattern superimposed with the simulation output by CMPR referring to a film treated at 200°C.

Considering the SAXS patterns at 200°C, it can be noted that the *Im$\bar{3}$m* to *Fmmm* transition is not yet marked, likely because the surfactant has not been re-

moved (*vide infra*) and hinders shrinkage acting as a scaffold for the inorganic framework. The calculated cell parameters are a=13 nm for the $Im\bar{3}m$ cell and $a = 21$ nm, $b = 18$ nm and $c = 29.7$ nm. Simple geometric considerations and inspection of Figure 3.2 allow establishing the correspondence between the distorted $Im\bar{3}m$ and the orthorhombic $Fmmm$ structures: in the $Fmmm$ cell the c parameter corresponds to $\sqrt{a}$, this clearly indicates that the c parameter of the orthorhombic $Fmmm$ cell corresponds to the diagonal of the cubic $Im\bar{3}m$ face. This can be explained admitting that a is unaltered in both symmetries (in plane cell parameter).

Transmission electron microscopy (TEM) cross-sectional pictures reveal the ordered arrays of mesopores in the films. In Figure 3.3 it is possible to discern the 100 projection of the cubic $Im\bar{3}m$ structure and the 4-fold symmetry axis. It can be noted that two ordered zones are located at the film-air and film-substrate interfaces, but at the centre of the film the mesopores become less defined and give rise to a wormlike or disordered region. As described in Chapter 1, this is due to inorganic condensation which may form a solid barrier that prevents further evaporation at the film-air interface, thus multiple mesostructures are likely to be "frozen" in their metastable states. The disordered central region does not affect deeply the GISAXS patterns (only a diffuse ring passing through the spots is visible, indicating a disordered region) because of the small penetration depth of X-rays in this configuration (the angle of incidence is slightly above the critical angle of the film). Due to the reason that only the first arrays of mesopores are probed, disordered regions or mesophases with different symmetries that might be embedded in the bulk of the film are difficult to detect. On the other hand, TEM images of different mesoporous silica samples often give the same results, which rules out the statistical case of sampling a disordered zone.

A line profile analysis was conducted on the ordered region of the film (cubic region at the film-air interface). A representative TEM image was loaded in the image manipulation software (open source software "ImageJ" was used)[6] and the "plot profile" tool was used to display a two-dimensional graph of the intensities of pixels along a line passing through the centres of 10 pores, where the x axis represents distance along the line and the y axis is the pixel intensity (see Figure 3.4 for an example). The pore width was calculated as the FWHM of the curves in the plot and the pixel width was converted into nm using the scale bar. This analysis gave an estimated pore size of 5×3 nm (the pores have an elliptical cross section due to uniaxial shrinkage), with an error of 0.7 nm

The mesoporous silica films thus obtained exhibit an excellent thermal stability in a wide range of temperatures and it has been shown that the mesostructure remains ordered up to the temperature of 950°C.[2] Fourier transform infrared spectroscopy (FTIR) showed that this high thermal stability is correlated with a progressive strengthening of the SiO_2 framework during thermally-induced polycondensation reactions and structural rearrangements of 4-fold rings present in the silica walls. The mesostructure after annealing at 850°C is free from silanols and maintains a high degree of order. Refractive index, volume porosity, and shrinkage have also been studied by ellipsometry, as a function of the thermal treatment up to 1050°C (Figure 3.5). The refractive index shows an interesting variation with the thermal treatment: a decrease in refractive index from 1.37 to 1.32 is observed upon full removal of the organic template; after this decrease n remains constant in the 350–750 °C range and increases again from 850°C because of pore shrinkage and inorganic framework collapse. At 1050°C the refractive index is 1.46, corre-

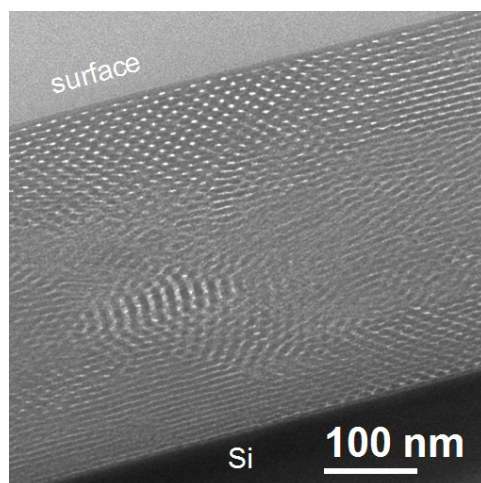**Figure 3.3.** *Transmission electron microscopy image in cross-section of a mesoporous silica film calcined at 350°C. Note the presence of a well-ordered phase at the film-air interface, a wormlike region at the centre of the film and a layered zone at the film-substrate interface.*
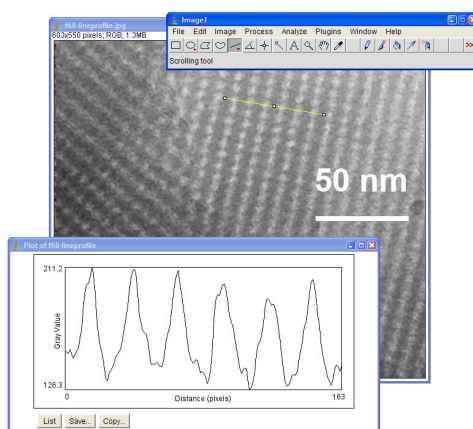

Figure 3.4. *Example of a line profile analysis using ImageJ.*

sponding to the value of dense silica: this is an indication of pore collapse and complete densification of the film.

The synthesis protocol of mesoporous silica films described above allows obtaining mesoporous films with framework composition of silica or hydrated silica, possessing a content of hydroxyl groups which can be roughly tuned with the thermal treatment. However, one can see from the TEM image reported in Figure 3.3 that the film is not well ordered: a wormlike zone is sandwiched between the two ordered interface regions. Therefore, an important step in the research work of this doctorate was to increase the degree of order. The choice was between working on synthesis parameters (e.g. pH, ageing, type of precursor) and working on deposition parameters (e.g. RH, thermal treatment). Because the deposition parameters had already been optimised in previous work, we chose to tackle this problem at a molecular level, working on the precursor solution and aiming at obtaining different NBBs with which to build up a more defined mesostructure.
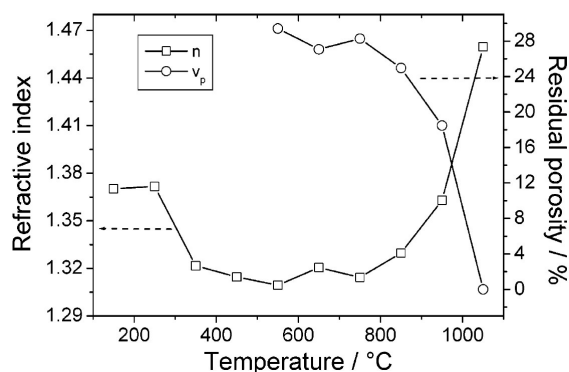
Figure 3.5. *Volume fraction of residual pores, V_p, and refractive index, n, at λ =632.8 nm, as a function of the calcination temperature.*

3.2 Hybrid organosilica mesoporous films

3.2.1 Methyl-functionalised mesoporous silica films

In order to improve the quality of the films by increasing the degree of order, we decided to modify the precursor solution by replacing part of TEOS with a hybrid precursor, that is methyl-triethoxysilane (MTES). MTES has three hydrolysable ethoxy (OCH_2CH_3) groups and a non-hydrolysable CH_3 group which is covalently bonded to the central Si atom. The synthetic strategy that led us to use organically-modified alkoxysilanes in the synthesis of mesoporous silica films was the hypothesis that such precursor would allow for a better compatibility with the organic surfactant by lowering the interfacial energy at the silica-surfactant interface. MTES was chosen instead of other precursors because methyl groups are the smallest modifying organic chemical unit: this provides the advantage of keeping the perturbation to the initial (non-hybrid) system to the minimum extent possible.

Samples with variable MTES:TEOS volume ratios were synthesised, using the protocol described in the previous paragraph. The volume ratios were chosen in order to cover a range of values around what was considered the optimum molar ratio according to an educated guess: on the one hand a larger quantity of MTES would result in a high degree of order; on the other hand, because MTES contains a non-hydrolysable methyl group, the resulting silica network would be less interlinked, therefore mechanically more unstable. In the remainder of this section we present a detailed study on the MTES:TEOS=0.56:1 volume ratio, which gave the best results in terms of mesostructural degree of order.

3.2.2 Synthesis protocol

The precursor solution is similar to the one reported for silica mesoporous films (TEOS-Pluronic F127 system), except that a part of TEOS is replaced by the same volume of MTES. The mother solution is prepared mixing 3.08 mL of EtOH, 2.84 mL of TEOS, 1.42 mL of MTES and 0.355 mL of a 0.768 M HCl solution. This sol is stirred for 60 minutes, then a templating solution with 15 mL of EtOH, 1.3 g of Pluronic F127 and 1.5 mL of a 0.057 M HCl solution, is added. The final molar ratios are: TEOS : MTES : EtOH : H_2O : HCl : Pluronic F127 = 1: 0.56 : 15.56 : 5.20 : 0.018 : $5 \cdot 10^{-3}$. Mesoporous organosilica films were synthesised
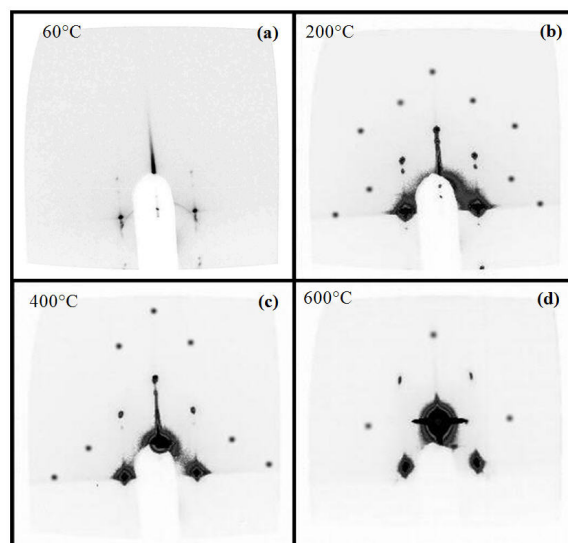
Figure 3.6. *GISAXS images of the mesostructured films upon thermal calcination at (a) 60 °C, (b) 200 °C, (c) 400 °C and (d) 600 °C*

by dip-coating and treated at 60°C for 1 hour. Subsequently, they were treated at temperatures ranging from 60 to 1000°C, with 1 hour dwell time at the final temperature, in order to study the evolution of mesophase symmetry and framework chemistry with temperature.

3.2.3 Structural characterisation (mesophase symmetry)

All of the SAXS experiments reported here were conducted at the Austrian SAXS beamline of Elettra synchrotron facility, using an incident energy of 8 keV (corresponding to a wavelength of λ=1.54 Å) in grazing incidence mode (GISAXS).

The GISAXS data of films treated at 60, 200, 400, 600°C are reported in Figure 3.6. A large number of spots is clearly visible in the thermally treated films, extending to the second and third order, while no diffuse ring (as that observed in TEOS-Pluronic F127 films) is present. This is an indication that the films possess a high degree of order. The film treated at 60°C shows only spots belonging to the first order, probably because the electron contrast between the framework and the block copolymer phase is not large enough, whereas at 200°C part of the templating agent has already been removed thus increasing contrast and diffraction signal.

In order to identify the mesostructure we used the GISAXS pattern of the film treated at 200°C because the presence of a large number of diffraction spots allows an accurate attribution of the mesophase. The spots were obtained from images taken with different exposure times (from 200 ms to 2 s), which were merged into a low-saturation level diffraction image keeping their original positions in the detector. A support to start the identification of the mesophase was given by the TEM cross-sectional images of a film thermally treated at 200°C, which shows a 2-fold symmetry axis, probably originating from a 4-fold axis in the as-deposited film which is then broken by the thermal shrinkage (Figure 3.7 a and d). This observation suggested a cubic, tetragonal or orthorhombic symmetry. We then analysed the fast-Fourier transforms (FFT) of the cross-sectional STEM images of the sample
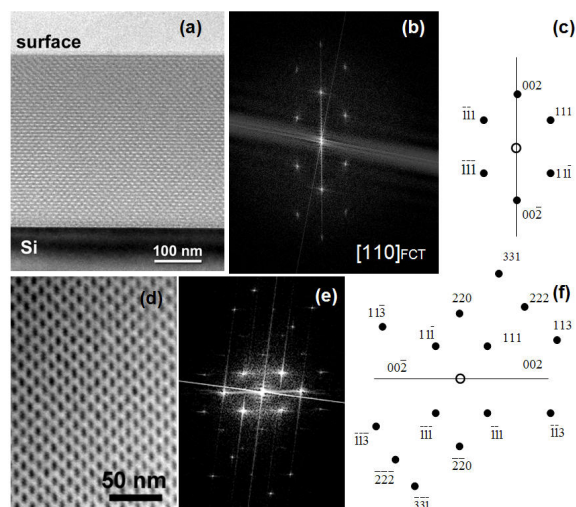
Figure 3.7. *(a) Bright-field cross-section TEM image, (b) its Fourier transform, and (c) the correspondent indexation along the [110] direction. (d) Dark-field cross-section TEM image that is rotated 90° with respect to the image in subfigure a, (e) its Fourier transform, and (f) the correspondent indexation along the [110] direction.*

calcined at 200°C, finding that the patterns are compatible with a $I4/mmm$ body-centred tetragonal (BCT) structure (Figure 3.7 b, c, e and f). The next step was to perform a simulation of the GISAXS diffraction spots by constructing a data sheet which output the s_x and s_y positions of the spots according to the input cell parameters of the $I4/mmm$ symmetry, X-ray wavelength and sample-to-detector distance. This was done with an electronic worksheet (MS Excel), by which a graph could be output and superimposed to the experimental GISAXS pattern (Figure 3.8). The details of pattern simulation using the $I4/mmm$ space group are reported in Appendix A.

Figure 3.8 a shows that there is good agreement between the simulated (yellow circles) and the experimental data. Some spots appear to match precisely with the simulated data (red hollow circles) whereas other spots appear shifted with respect to the predicted positions (green hollow circles). It can be noted that this discrepancy affects the spots which are closer to the s_x axis, i.e. spots generated by small-angle reflections. At first we attributed this discrepancy to a secondary phase in a region of the film, however TEM micrographs reveal a homogeneous mesophase symmetry, therefore we concluded that these shifts are caused by the impinging X-ray and outgoing diffracted beam which undergo multiple refraction-reflection events inside the film. This causes an alteration in the exit angle α_f which appears to be closer to the s_x axis (green hollow circle in Figure 3.8 a) than it actually is (red hollow circle). These so-called *dynamical effects* are attributed to multiple reflection events at the film-air and film-substrate interfaces and refraction inside the film, resulting in the appearance of double or triple spots in the GISAXS pattern, shifted with respect to the "real" value. The position in the detector of these spurious spots can be calculated according to the distorted wave Born approximation (DWBA) theory. Here we will not discuss about these dynamical effects, which are described in full detail elsewhere.[7]

A more accurate method for the evaluation of the experimental data and the comparison with simulated data was performed using a code for Mathematica, which calculates the spot positions on the detector for a given $I4/mmm$ mesophase
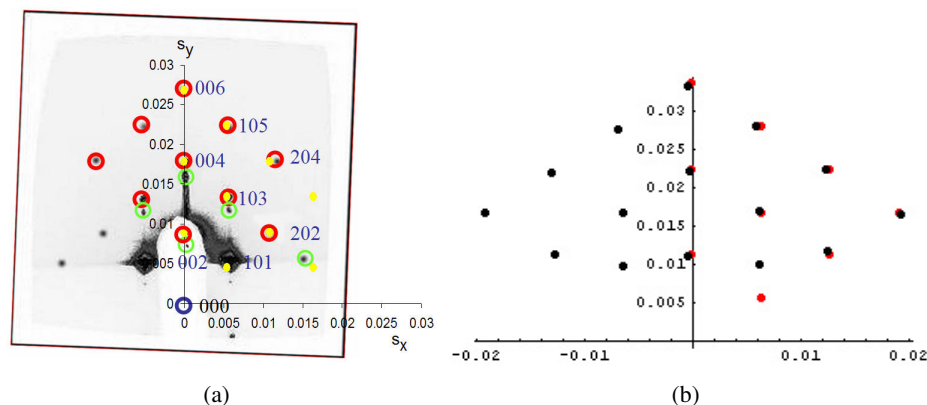
Figure 3.8. *(a) GISAXS image of a sample calcined at 200 °C and superimposed simulated spots obtained by an Excel worksheet. (b) Output of the Mathematica code that calculates the cell parameters by a best-fit function.*

symmetry and given cell constants. The experimental data was loaded from a .csv (comma-separated values) file and superimposed to the simulated data. In order to calculate the cell parameters, an error function was defined as the standard deviation of the difference between the calculated and the experimental s_x, s_y values divided by the number of spots; this error function was minimised varying the cell parameters, which were eventually output together with the estimated errors. An output image is given as an example in Figure 3.8 b, while the Mathematica code used for this calculation is reported in Appendix A.

The GISAXS data of the films treated at temperatures higher than 200°C present similar patterns, with a decrease in the d-spacing values of the out-of-plane spots (i.e. along the s_y axis) and no variation in the in-plane spot positions (i.e. along the s_x axis). All of the patterns (60, 200, 400 and 600°C) were analysed with the Mathematica code presented above, and the cell parameters were calculated for the corresponding $I4/mmm$ structures. Plotting the cell constants as a function of temperature (Figure 3.9) we noted that the in-plane a cell parameter did not vary significantly upon thermal treatment, whereas the out-of-plane c parameter decreased markedly. More in detail, the c cell parameter varied from 23 to 14 nm, whereas $a = 19$ nm was unaffected within the error bar. Therefore, we concluded that a phase transition occurred during thermal treatment between two tetragonal $I4/mmm$ symmetries, that is $a < c$ to $a > c$, the transition temperature being around 450°C (Figure 3.10).

This BCT structure can also be described by a distorted face-centred cubic (FCC) cell oriented with its (100) face parallel to the substrate, the in-plane cell constant being a diagonal of the BCT (001) face and the out-of-plane cell constant shrunk by thermal treatment (Figure 3.11). From a simple analysis of the BCT cell parameters of the films treated at 60°C ($a = 18$ nm, $c = 23$ nm) we concluded that the out-of-plane cell constant of the distorted FCC cell was $\sqrt{2} \cdot 18 = 25.5$ nm, slightly greater than the c parameter of the BCT cell. Therefore the tetragonal structure of the sample treated at 60°C appears to be already slightly shrunk if we assume that it originates from an FCC cell, i.e. the symmetry is already broken from cubic to tetragonal when the film has been treated at 60°C.

The thermal shrinkage perpendicular to the film surface can be observed in
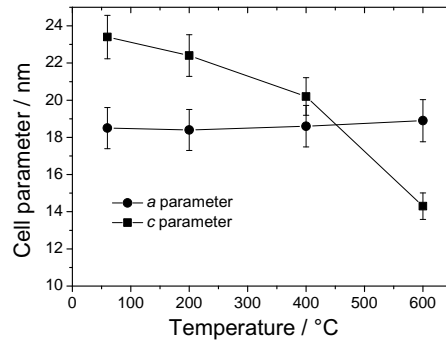
Figure 3.9. *Variation of a (circles) and c (squares) cell parameters in mesoporous organosilica films as a function of the thermal treatment.*
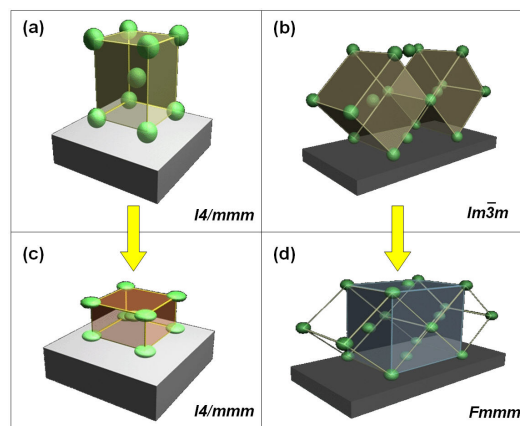

Figure 3.10. *Symmetry transition due to thermal shrinkage. Left: tetragonal I4/mmm space group with the out of plane cell constant changing from c > a to c < a in hybrid organosilica mesoporous films (the c axis is normal to the substrate). Right: body-centred cubic Im3̄m space group becomes orthorhombic Fmmm in mesoporous silica films.*
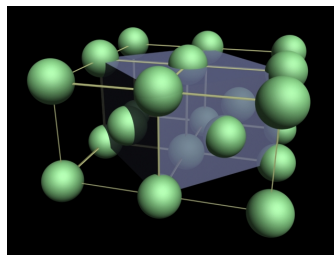

Figure 3.11. *Alternative description of the BCT ordered mesostructure as a vertically-shrunk FCC cell, whose in-plane cell parameter is represented by a diagonal of the (001) BCT face, whereas the out-of-plane cell constant is the BCT c constant along the [001] direction.*

TEM images: a deformation of the spherical pores is clearly visible, and the shape of mesopores in calcined samples becomes ellipsoidal. With reference to Figure 3.7, the major axis (parallel to the substrate) is (8.2±0.8) nm, the minor axis (perpendicular to the substrate) is (4.8±0.5) nm, with a ratio between the two axes of 1.8±0.3.

3.2.4 Spectroscopic characterisation

Information on the presence of specific chemical species in the films was provided by Fourier-transform infrared (FTIR) spectroscopy. This technique gives important insight on the chemical nature of the film and on the self-assembly process. FTIR spectra have been analysed according to the main vibrational modes of interest, reported in Table 3.2.

Table 3.2. *Assignments of the IR vibrational modes belonging to different chemical species in mesostructured and mesoporous thin films. WN=wavenumber.*

$WN\ (cm^{-1})$	Vibrational mode
	SiO_2
460	TO_1 (transverse-optical) rocking motion of the O atoms perpendicular to the Si-O-Si plane
800	TO_2 symmetric stretching of Si-O-Si
1070	TO_3 asymmetric stretching of Si-O-Si
1250	LO_3 (longitudinal-optical) higher-frequency shoulder of TO_3
930	Si-OH stretching
550–640	Broad band associated with residual cyclic structures, mainly 4-fold and 6-fold siloxane rings
	Alkoxide
2976	Asymmetric stretching $\nu_a(CH_3)$
2929	Asymmetric stretching $\nu_a(CH_2)$
2890	Symmetric stretching $\nu_s(CH_3)$
1365	Rocking $\rho(HCH)$
1296	Twisting $\tau(CH_2)$
1168	Rocking $\rho(CH_3)$
1106, 1103	Asymmetric stretching $\nu_a(C\text{-}C + C\text{-}O)$
1082, 1080	Asymmetric stretching $\nu_a(SiO\text{-}CO)$
965	Rocking $\rho(H_3CO + COC)$
793	Stretching $\nu(Si\text{-}O + C\text{-}O)$
670	Symmetric stretching $\nu_s(SiO_4)$
481	Rocking $\rho(CCO)$
	EtOH
3380	Stretching $\nu(OH)$ of H-bonded hydroxyls
2975	Asymmetric stretching $\nu_a(CH_3)$
2894	Symmetric stretching $\nu_s(CH_3)$
1457	Rocking $\rho(HCH)$
1274	Twisting $\tau(CH_2)$
1090	Asymmetric stretching $\nu_a(C\text{-}C + C\text{-}O)$, rocking $\rho(COH)$

(Continued on next page)

(Table 3.2 – Continued from previous page)

WN (cm^{-1})	Vibrational mode
1049	Rocking ρ(CCH$_3$ + COH)
880	Symmetric stretching v_s(C-C + C-O)
442	Rocking ρ(CCO)
OH	
3600–3300	H-bonded OH vibrations of alcohol (O-H stretching)
3500–3300	H-bonded H$_2$O (O-H stretching)
3800–3650	Stretching modes of OH groups not involved in H bonding (isolated and terminal OH)
3750	Isolated surface OH
3690	Terminal OH, or partially involved in H bonding
3650–3200	H-bonded silanols in chain (OH stretching)
1640	Scissor bending of molecular H$_2$O v_b(H$_2$O) or δ(H$_2$O)
3250	First overtone, bending of molecular H$_2$O $2v_b$(H$_2$O)
Organic template	
3000–2800	Stretching C-H
2971	Asymmetric stretching C-H in CH$_3$
2930	Asymmetric stretching C-H in CH$_2$ groups, symmetric stretching C-H in CH$_3$ groups
2930–2900	CH$_2$ (methylene) chain symmetric stretching
2871	Symmetric stretching v_s(C-H) in CH$_2$
1710	stretching v(C=O)
1500-1300	C-H bending
1374	Symmetric stretching v_s(CH$_3$)
1350	Wagging ω(CH$_2$), stretching v(C-C) in PEO chains
1343	Wagging ω(CH$_2$)
1281, 1242	Twisting τ(CH$_2$)
1160	Rocking δ(CH$_3$)
1149	Stretching v(C-C)
1113	Stretching v(C-O-C)
1060	Stretching v(C-O-C), rocking ρ(CH$_2$)
963	Rocking ρ(CH$_2$)
947	Rocking ρ(CH$_2$), stretching v(C-O-C)

FTIR absorption spectra of films treated at 60, 200, 400 and 600°C are shown in Figure 3.12. The presence of methyl groups is revealed by the absorption peaks at 1276 cm^{-1} attributed to the C-H symmetric stretching in CH$_3$, and 2977 cm^{-1} attributed to asymmetric stretching.[8] The intensity of these bands decreases at higher temperatures, indicating a removal of methyl groups from the mesostructure, at 600°C only $\approx$20% of the methyl groups remain in the films due to Si-C cleavage.[9] The calcination of the films is accompanied by a decrease in intensity of the Si-OH stretching band around 950 cm^{-1} and the shift to lower wavenumbers of the Si-O-Si asymmetric stretching mode around 1070 cm^{-1}, indicating strengthening of the silica network due to polycondensation.[10] The latter band is composed of
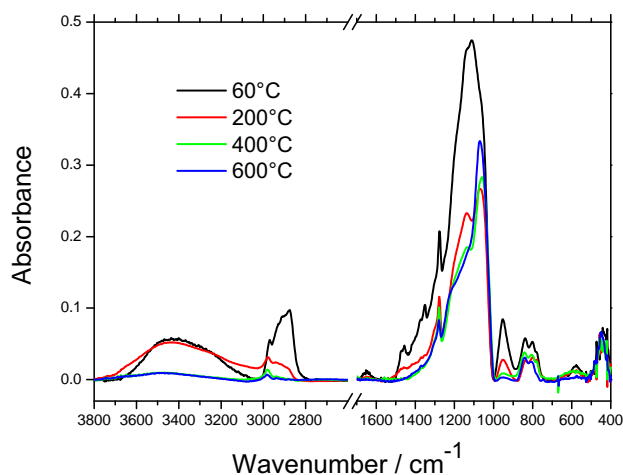
Figure 3.12. *FTIR absorption spectra, collected in air, of films treated at 60, 200, 400 and 600 °C.*

several overlapped contributions and is generally very difficult to deconvolute.[11] In the present case a clear attribution is more complicated by the overlapping with the absorption bands in the 1050–1175 cm^{-1} interval, which are the most intense modes observed in a pure Pluronic F127 spectrum,[12] (in particular, C-O-C stretching at 1110 cm^{-1}, C-C stretching at 1150 cm^{-1}, CH$_2$ rocking at 1160 cm^{-1}, see Figure 3.13).

The presence of a weak and broad absorption band around 600 cm^{-1}, which is assigned to vibrations of four-member rings within the ring plane (Si-O stretching vibrations coupled with O-Si-O and Si-O-Si bending vibrations),[13] indicates that fourfold cyclic species are present in the silica framework. We suppose that the vibrational mode at 1135 cm^{-1} is mostly due to asymmetric stretching (Si-O-Si) in strained 4-fold siloxane rings[14] because Pluronic is nearly completely removed upon calcination at 400°C, as shown by the disappearing C-H stretching bands in the 2700–3000 cm^{-1} region. The formation of 4-fold rings in gels prepared in acidic conditions from MTES is well documented both for powders[15] and films[9] and has been also observed in silica mesostructured films prepared from CTAB[11] and block copolymers.[2]

Calcination of the films causes dehydroxylation and a change in the amount of methyl groups present in the mesopores. These two processes are simultaneous and affect the hydrophobicity of the system and, hence, the ability to absorb water. To evaluate how the calcination is affecting this process we have performed a deconvolution of the FTIR spectra in the range ≈3000–3800 cm^{-1} (Figure 3.14). To deconvolute the FTIR spectrum of the sample treated at 60°C we selected three components: (1) at the highest wavenumber assigned to terminal silanols, (2) at ≈3350 cm^{-1} due to hydrogen-bonded silanols in chains that contain more than one pair of mutually H-bonded OH groups, and (3) at ≈3250 cm^{-1} attributed to the first overtone of the 1640 cm^{-1} bending mode of molecular water $2\nu_b(H_2O)$.[10,16–18] In the fit of the samples treated at higher temperatures (200, 400 and 600°C) we introduced another component due to the isolated silanols that are formed during
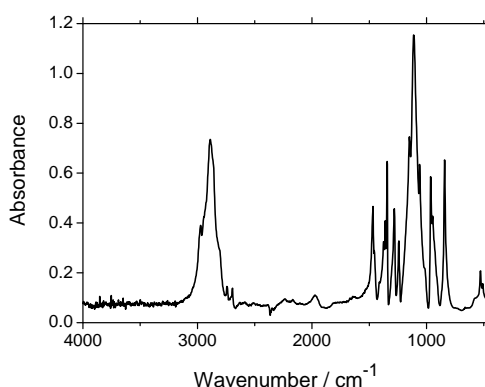
Figure 3.13. *FTIR absorption spectrum of block copolymer Pluronic F127 in a KBr pellet.*

dehydroxylation (≈ 3650 cm^{-1}). The deconvolution shows a decrease in intensity of all the components after calcination at 200°C. The dehydroxylation is practically complete at 400°C, because only weak traces of terminal and isolated silanols are observed, without residual water. If the sample is treated at higher temperatures new silanols are formed and a small amount of water is absorbed (600°C).

This trend can be explained as follows. At 60°C the pores are filled with the block copolymer whose hydrophilic chains are able to absorb and retain water, at the same time the pore walls are covered with hydrophilic silanols. In these conditions, the hydrophobicity of methyl groups is largely shadowed. When the surfactant is completely removed upon calcination at 400°C, the pores are covered only by methyl groups and the absorption of water is inhibited. At 600°C the methyl groups are removed forming silanols.[19]

The curve obtained from the deconvolution that is assigned to the $2\nu_b(H_2O)$ contribution (overtone of the bending mode of molecular water at ≈ 3200 cm^{-1}) was used to qualitatively investigate the change in water absorption during calcination. A plot of the peak area vs. temperature shows that the presence of H_2O has a minimum at 400°C (Figure 3.15). The data obtained from the $\nu_b(H_2O)$ at 1640 cm^{-1} are in agreement with those calculated from the deconvolution, supporting the choice done for the fit.

The transversal vibrational TO$_3$ mode (Si-O-Si asymmetric stretching) at ≈ 1070 cm^{-1} has a shoulder at ≈ 1200 cm^{-1} (longitudinal LO$_3$ mode). With increasing temperature, the intensity of TO$_3$ shifts towards higher wavenumbers, indicating higher degree of silica polycondensation. This shift can be observed also in films obtained without MTES (i.e. where TEOS is the only silica source). However, the two shifts have a different trend, which can give insight into the polycondensation process.

Figure 3.16 shows the wavenumber peak of the TO$_3$ mode for mesostructured silica (TEOS) and organosilica (TEOS-MTES) films. The slope of the organosilica films is steeper for temperatures below 700°C with respect to the silica films, whereas for temperatures above 700°C the two wavenumbers become similar. The shift of the TO$_3$ mode towards higher wavenumbers is related to the higher degree of crosslinking of the inorganic network. The central force model by Galeener[20]
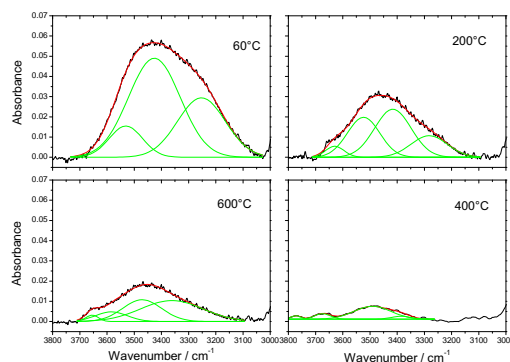
Figure 3.14. *Deconvolution of the FTIR spectra in the range 3000–3800 cm^{-1} for films treated at 60, 200, 400 and 600°C.*

(Figure 3.17) describes the frequency ω of the TO$_3$ mode as:

$$\omega^2 = \frac{k}{m_O}\left(1 - \cos\theta\right) + \frac{4}{3}\frac{k}{m_{Si}},$$

where m_O and m_{Si} are the O and Si masses, k is the constant of the stretching in Si-O-Si and θ is the angle formed by the Si-O-Si bond. Increasing polycondensation degree, the average Si-O bond distance decreases and k increases; at the same time, the average θ increases. This causes ω to increase, thus explaining the shift observed in the TO$_3$ peaks for increasing temperatures.

This observation suggests that the presence of non-hydrolysable methyl groups in the organosilica films is associated with a lower polycondensation degree than in silica films (for the same thermal treatment). The methyl groups inhibit further polycondensation until they are fully removed between 600 and 700°C: then the Si atoms can bond to 4 bridging oxygens thus increasing the overall polycondensation degree. The peak positions shift to a limit value of 1085 cm^{-1} (at 950–1000°C), when silica densification is complete and the mesopores collapse due to silica viscous flow. Note that temperatures below 400°C (removal of organic template) were not considered in this analysis, as the overlap of the bands arising from the copolymer are superimposed to the TO$_3$ mode causing the wavenumber shift to be uncorrelated to the polycondensation degree.

Methyl groups perform an important role to help self-assembly, in that they affect the micelle-silica interface and the kinetics of the reactions of the species involved in EISA. The strong electrostatic and hydrophilic interactions between the silica and the PEO blocks are reduced by the presence of CH$_3$ in the silica oligomers. At the same time, k_{inorg} results smaller due to the presence of the non-hydrolysable Si-CH$_3$ groups, allowing for a high degree of organisation. In these conditions, organisation of the micelles is not hindered by a more condensed inorganic network and a faster organisation occurs. In other words, we observe a twofold effect in mesostructured organosilica films: (1) the inorganic condensation rate and condensation degree are lowered by the presence of non-hydrolysable units, so that only 3 bridging oxygens per Si atom can form a network instead of 4 as in TEOS; (2) the hydrophobic methyl units act as a "cosurfactant" between the inorganic units and the organic micelles. These two factors explain why a higher
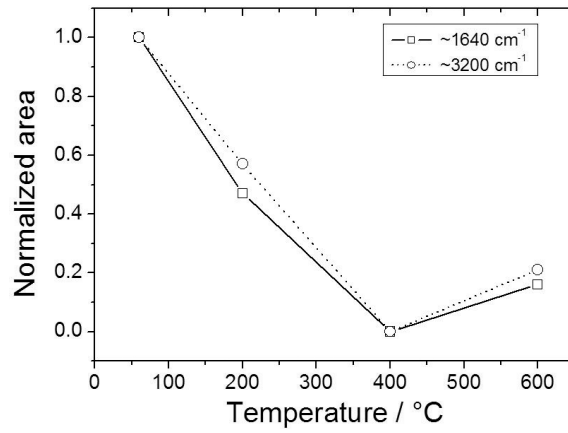
Figure 3.15. *Area variation of peaks attributed to $\nu_b(H_2O)$ at 1640 cm^{-1} (hollow squares) and $2\nu_b(H_2O)$ at 3200 cm^{-1} (hollow circles) as a function of film thermal treatment.*
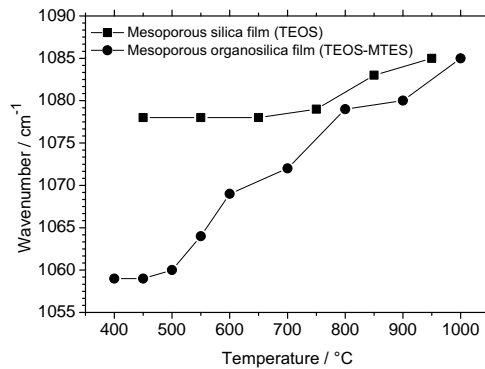

Figure 3.16. *Trend of the TO_3 peak position as a function of temperature for mesoporous silica (TEOS) and organosilica (TEOS-MTES) films.*
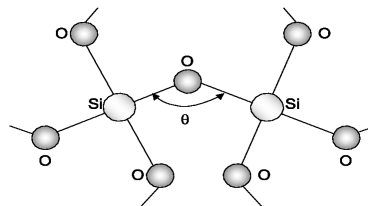

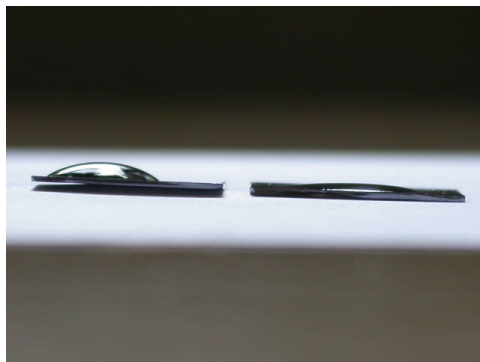**Figure 3.17.** *Scheme of local order in Galeener's model.*

Figure 3.18. *Different hydrophobicity of an organosilica (left) and an inorganic silica mesoporous film (right). Note the different contact angle, higher in the hybrid film and lower in the inorganic one.*

degree of order (virtually "defect-free" at least in the micrometre range) is obtained in this new class of hybrid mesoporous films.

These films are highly hygroscopic due to the high amount of hydroxyl groups and extremely high surface area. Contact angle measurements have not been performed, however Figure 3.18 gives a hint about the hydrophobicity of a hybrid (TEOS-MTES) mesoporous silica film (left) compared to a silica (TEOS) mesoporous film (right).

In mesoporous films with silica framework, we expect that the presence of hydroxyl groups causes a dramatic increase of the dielectric constant because of both the presence of highly polarisable O-H bonds and the presence of physisorbed water on the pore surface.[19,21] One way to decrease the dielectric constant is the substitution of highly polarisable and hydrophilic Si-O and O-H groups with less polarisable and more hydrophobic Si-C and C-H groups in a strategy similar to this one-pot synthesis of mesoporous hybrid films. Therefore, we expect that important properties such as the dielectric constant k can be controlled, possibly bringing these materials into the field of such applications as low-k dielectrics in microelectronic packaging. In addition, the introduction of organic methyl groups into the inorganic framework decreases mechanical stress in the silica gel during solvent evaporation and densification: this reduces the probability of cracking and increases the critical thickness of the film (i.e. the maximum thickness that can be obtained without crack formation) to thicknesses grater than 1 μm.

3.2.5 Preliminary study on different hybrid mesoporous films

This co-condensation synthetic approach was extended to other systems: different hybrid precursors were employed as the silicon source together with TEOS, and different [hybrid]/[TEOS] molar ratios were used in order to evaluate the degree of order of the mesostructure, whereas the [surfactant]/[Si] molar ratio was kept constant. The organo-alkoxysilanes co-hydrolysed with TEOS in the precursor solutions are listed in Table 3.3.

Since DMDES has two hydrolysable groups, the network formed by a TEOS-DMDES system is less condensed than one formed by an ETES-TEOS system (at constant [TEOS]/[hybrid] molar ratios), which in turn forms a less condensed network than a TEOS-only system. While a lower degree of crosslinking favours me-

Table 3.3. *Hybrid precursors (organo-alkoxysilanes) used in the co-condensation synthesis of mesostructured films.*

Hybrid precursor	Full name	Chemical formula
ETES	ethyltrimethoxysilane	$CH_3CH_2Si(OCH_2CH_3)_3$
DMDES	dimethyldiethoxysilane	$(CH_3)_2Si(OCH_2CH_3)_2$
OTES	octadecyltriethoxysilane	$C_{18}H_{37}Si(OCH_2CH_3)_3$
APTES	(3-aminopropyl) triethoxysilane	$H_2N(CH_2)_3Si(OC_2H_5)_3$

sostructure formation, too low a condensation degree could cause the mesostructure to collapse during thermal treatment after deposition. Therefore, an optimum concentration of the hybrid species constitutes a balance between mesostructural degree of order and stiffness of inorganic network. OTES has a long hydrophobic chain (18 carbon atoms), therefore it was chosen to study whether a more hydrophobic nature of the sol-gel precursor could influence the self-assembly process. The amine-functionalised precursor (APTES) is an interesting precursor because it bears a functional amino group which can be exploited for example in biosensors, due to the affinity of NH_2 groups for biological species such as proteins. Furthermore, amino groups can form strong bonds with heavy metal cations, so they can be used in gas filters, pollutant removal and nanoreactors.

ETES and DMDES The organo-alkoxysilane concentration in the solution was varied in the range e=[ETES]/[TEOS]=(0–2) for ETES and d=[DMDES]/[TEOS]=(0.04–0.19) for DMDES. The two different concentration ranges are justified by the different chemistry of inorganic network formation, given by the different condensation conditions of these two precursors. Since a DMDES-TEOS system forms a less condensed structure than an ETES-TEOS system, the optimum concentration of organo-substituted alkoxysilane in the former case must be somewhat smaller than in the latter case.

Selected GISAXS diffraction patterns of films obtained from solutions containing different precursor compositions and treated at 150°C can be seen in Figure 3.19, the complete indexation is given in Figure 3.20. The degree of order can be estimated examining the number of diffraction spots in the GISAXS patterns at constant experimental parameters (exposition time, glancing angle, etc.). In Figure 3.19 it can clearly be seen that the highest degree of order is obtained for concentrations $e = 0.2$ in ETES-TEOS films and $d = 0.11$ in DMDES-TEOS films. The films with the highest degree of order were found to have a body centred tetragonal unit cell belonging to the $I4/mmm$ space group, which is the same as that found in hybrid mesostructured silica films obtained from TEOS-MTES precursor solutions. The cell parameters are $a = (15.7 \pm 0.9)$ nm, $c = (17.8 \pm 1.1)$ nm for ETES-TEOS films and $a = (13.9 \pm 0.8)$ nm $c = (20.2 \pm 1.2)$ nm for DMDES-TEOS films.

OTES Films prepared using OTES and TEOS as the silicon source appeared opaque soon after dip-coating. Optical microscope observations revealed the pres-
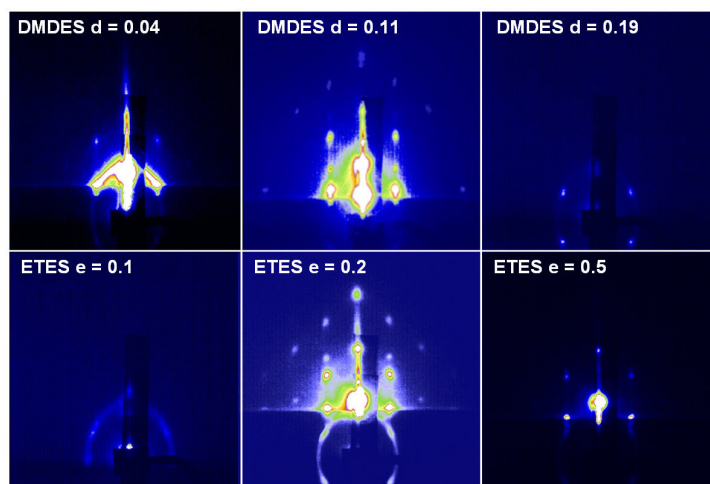
Figure 3.19. *Selected GISAXS diffraction patterns of films obtained from solutions containing different precursor compositions and treated at 150°C. Top: films obtained with DMDES-TEOS as the Si source, bottom: films obtained with ETES-TEOS as the Si source.*
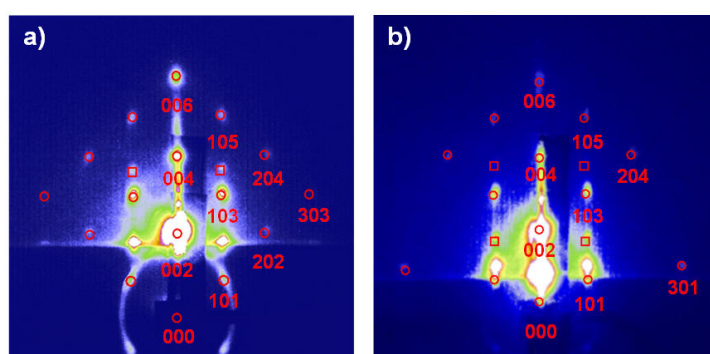

Figure 3.20. *Indexation of GISAXS patterns of films obtained with ETES (a) and DMDES (b).*

ence of phase separation. As a consequence, the films were not submitted for further characterisation.

APTES The main issue in films obtained from an APTES-TEOS mixture was to obtain a precursor sol in acidic conditions: the amino group in APTES is weakly basic ($pK_a \approx 10$), therefore addition of water to the mixture causes uncontrolled hydrolysis and polycondensation (self-catalysis by the amino groups) leading to branched structures, unsuitable for coating. In order to protonate the amino groups, concentrated HCl was added to the precursor sol, therefore the standard synthesis was adjusted to meet this requirement. TEOS (3.24 mL) and APTES (0.55 mL) were added to ethanol (15 mL). Next, 0.4 mL of 12M HCl were added under stirring and a clear solution was obtained with pH$\approx$2. Eventually, Pluronic F127 (1.3 g) was added as the templating agent. GISAXS measurements showed the presence of an ordered mesostructure with a tetragonal symmetry (not shown in figure).

3.3 Tailoring pore size

Mesopores size can be increased by adding co-solvents which selectively swell a portion of the surfactant, so as to tailor pore size and residual microporosity. Alternatively, a range of surfactants or amphiphilic block copolymers can be explored in order to obtain larger or smaller mesopore size. We followed this latter path, using four amphiphilic block copolymers for the synthesis of films with cubic phases: this strategy is known to have the advantage of getting more ordered mesostructures and more reproducible syntheses if compared with the use of swelling agents. Three templating agents other than Pluronic F127 were tested in order to get pores with different size: Pluronic F68, Pluronic P123 and Brij-58. Pluronic F68 and P123 are three-block copolymers of the PEO_x-PPO_y-PEO_x type, similar to F127 but with different x and y values, whereas Brij-58 is a two-block copolymer containing a PEO block and an alkyl chain.[22] Table 3.4 shows the chemical formula and the molecular weights of these templating agents.

The nomenclature for Pluronic surfactants gives information on the physical state and the composition of the macromolecule. The first letter refers to the physical state of the product: F is for solid, P is for paste, L is for liquid (e.g. F127 is a powder, P123 is a paste, L121 is a liquid). The first or first two num-

Table 3.4. *Block copolymers used as templating agents in the synthesis of mesoporous silica films. The out-of-plane cell parameters at 100°C (GISAXS) and the pore sizes obtained at 300°C (TEM) are reported.*

Block copolymer	Chemical formula	MW (g/mol)	Cell param (100°C)	Pore size (300°C)
Pluronic F127	EO_{106}-PO_{70}-EO_{106}	12600	18 nm	7 nm
Pluronic F68	EO_{80}-PO_{30}-EO_{80}	8400	14 nm	4 nm
Pluronic P123	EO_{20}-PO_{70}-EO_{20}	5800	14 nm	4 nm
Brij-58	$C_{16}H_{33}EO_{20}OH$	1125	8 nm	2 nm

(a) F68, *s*=0.003, partially assembled

(b) F68, *s*=0.006, cubic mesophase

(c) Brij-58, *s*=0.02, not assembled

(d) Brij-58, *s*=0.06, cubic mesophase

(e) P123, RH=10%, wormlike
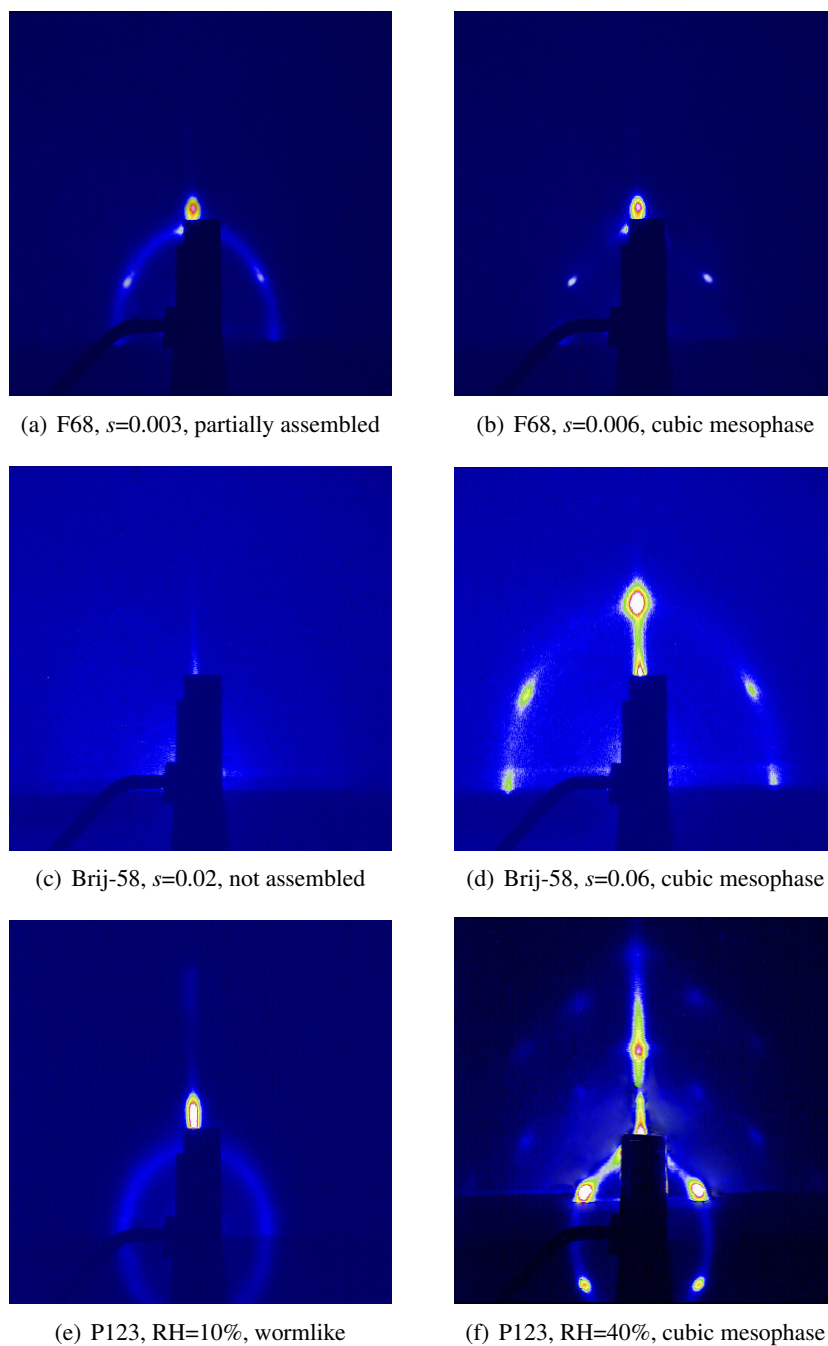
(f) P123, RH=40%, cubic mesophase

Figure 3.21. *GISAXS patterns of Pluronic F68-templated mesostructured silica films synthesised with different s=[surfactant]/[silica] ratios, treated at 100°C.*

bers must be multiplied by 300 to get the PPO molecular weight (e.g. in F68, MW(PPO)=6·300=1200 g·mol^{-1}). The last numbers refer to the PEO percentage with respect to the entire polymer chain (e.g. in F68 8·10=80%). Note that F68 has a structure similar to F127 in that the PEO chain is much larger than the PPO chain (70% in weight in F127 and 80% in F68). On the contrary, P123 has a much smaller PPO chain (30% in weight). This can be readily inferred also from Table 3.4, where the ratio between EO and PO constituents x and y is larger than 1 in F127 and F68, whereas it is smaller than 1 in P123. We can draw some conclusions regarding the packing factor g (see Chapter 1, page 23): both F127 and F68 are expected to form high-curvature spherical micelles, whereas P123 is expected to form low-curvature cylindrical micelles or lamellar structures. Regarding Brij-58, the MW of the PEO chain is 900 g·mol^{-1}, whereas the alkyl chain has a molecular weight of 225 g·mol^{-1}, which means that the percent weight of the hydrophilic alkyl chain with respect to the total weight of the molecule is 80%, the same value found in Pluronic F127. Therefore, films templated by Brij-58 are expected to show high-curvatures micelles.

The preparation of the coating sols with these templating agents is similar to that reported previously. Different [surfactant]/[Si] ratios were tested in order to investigate the optimum surfactant concentration to have the maximum degree of order. The s=[surfactant]/[Si] molar ratios ranges were 3–15 · 10^{-3} with 3 · 10^{-3} steps for Pluronic F68 and P123, and 2–10 · 10^{-2} with 2 · 10^{-2} steps for Brij-58. The films were deposited at different RH (10, 40, 70%) in order to assess the influence of water vapour on self-assembly. In films templated by Pluronic F68 and Brij-58, ordered mesostructures were found to form at low RH (around 10%), whereas higher RH led to hexagonal (40% RH, not shown in figure) or no mesophases. Figure 3.21 a and b shows the GISAXS pattern of a Pluronic F68-templated mesostructured film, thermally treated at 100°C for 2 hours in order to stabilise the inorganic framework. Films templated by Brij-58 gave cubic phases in accordance with our expectation, as shown in Figure 3.21 c and d. In both Pluronic F68- and Brij-58-templated films, the scattering angles were found to be higher than in films templated by Pluronic F127, associated with smaller cell constant parameters. This is not unexpected, because both block copolymers have shorter chains with respect to Pluronic F127 and form smaller micelles. The cell parameter a for films templated by Pluronic F68 and thermally treated at 100°C was found to be a=14 nm, whereas films templated with Brij-58 gave a=8 nm. Films templated by Pluronic F127 yielded a=18 nm at 100°C.

When Pluronic P123 was used as the templating agent, the mesostructure was found to respond to RH in a different way than in Pluronic- and Brij-templated films. Dip-coating at low RH (10%) resulted in no mesostructure formation (Figure 3.21 e), whereas higher RH (40%) favoured ordered cubic structures (Figure 3.21 f). This is likely due to swelling of the copolymer's hydrophilic end blocks by water molecules, which increases the volume of the hydrophilic headgroup increasing the packing parameter g and forming a well-defined hybrid interface between the organic and the inorganic phases. In this way, spherical micelles packing in cubic symmetries are favoured.[23] The cell parameter for mesostructured films templated by Pluronic P123 was a=14 nm.

3.4 Hybrid mesoporous membranes

3.4.1 Mesoporous membranes

Membranes are defined as thin physical barriers allowing selective transport of mass species. Thin films can be deposited on any support (substrate), whereas membranes must be prepared either on a porous support allowing transport of mass species, or as self-standing objects. Mesoporous and macroporous films and membranes have been studied extensively in the past decades and many of them have found commercial applications. Examples include a large number of inorganic membranes for microfiltration and ultrafiltration processes used in industry, for example in drinking water purification and wastewater treatment. The majority of these materials are made by compacting nano- or micron-sized dense crystallites (such as γ- or α-alumina crystals).[24]

Whereas there are many publications on mesoporous films and powders, only a small number of papers deal with mesoporous membranes, foams and bulk monoliths. Soler-Illia et al.[25] report on the preparation of membranes synthesised starting from an acidic solution of alkoxysilane and an amphiphilic block copolymer (Pluronic F127 or P123). After slow evaporation of the solvent in the containers, disks of 0.1–0.2 mm thickness and 2–3 cm diameter are obtained. The mesostructure presents $Im\bar{3}m$ cubic or $p6mm$ hexagonal domains, extending up to the centimetre scale. Recently, the possibility of synthesising hierarchically structured transparent hybrid membranes by in situ growth of mesostructured organosilica in a host polymer has been demonstrated by Vallé et al.[26]

In this section we describe the study on silica and hybrid organosilica self-standing mesostructured and mesoporous membranes. We have concentrated on structural characterisation by SAXS and on the study of physicochemical properties of the pore surface and the mechanism of water adsorption-desorption by Fourier-transform infrared spectroscopy analysis in vacuum at different partial pressures. As the membrane is not supported by any substrate, it can be studied by SAXS in grazing and transmission mode, as well as any other angle of incidence, permitting a whole sampling of the reciprocal lattice.

Self-standing mesoporous silica membranes are synthesised by the EISA route. In a typical preparation, a precursor solution containing the silicon source and the templating agent (the same used in the preparation of silica and hybrid films) is poured into a container (e.g. a Petri dish) and the solvent is allowed to evaporate slowly in a controlled RH environment (RH$\approx$30%) for approximately 60 days. After drying, the membranes can be detached from the bottom of the container using tweezers, then they are submitted to thermal treatment for surfactant removal. The membranes are calcined in a furnace, which must be located under a chemical hood in order to remove the vapours originating from template decomposition, with a heating ramp of 1°C·min^{-1} from room temperature to 350°C with a dwell time at 350°C of 12 hours. After calcination, the membranes become brittle and prone to breaking into fragments of several cm, partially losing their transparency.

3.4.2 Structural characterisation of hybrid mesostructured membranes

GISAXS

As-prepared and thermally treated silica and hybrid organosilica membranes were broken into fragments so that they could be investigated by grazing incidence and
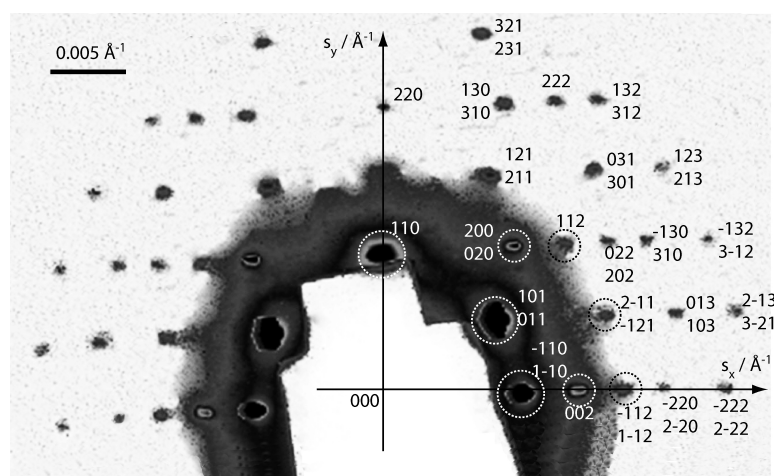
Figure 3.22. *GISAXS diffraction pattern of the as-prepared organosilica membrane obtained from a solution containing TEOS and MTES as the Si source, and its full indexation according to the cubic Im$\overline{3}$m symmetry.*

transmission SAXS. Figure 3.22 shows a representative GISAXS pattern of an uncalcined organosilica membrane. This GISAXS pattern was attributed to the cubic *Im$\overline{3}$m* symmetry group as the result of simulations using the Nanocell software for Mathematica (see page 2.2.7) and the indexation was done according to the *Im$\overline{3}$m* symmetry. Inorganic silica membranes yield the same diffraction pattern, with a slight difference in the cell constant values.

The cell constants of the ordered mesostructure were calculated using a Mathematica code developed for the *Im$\overline{3}$m* cubic cell, which is reported in Appendix A. They are $a = (16.3 \pm 1.1)$ nm for the as-prepared hybrid membrane and $a = (11.8 \pm 1.0)$ nm for the calcined hybrid membrane. This corresponds to a contraction in the cell parameter of 28% upon calcination. In the silica membranes the cell constants are $a = (18.0 \pm 1.0)$ nm and $a = (14.2 \pm 1.0)$ nm for the as prepared and the calcined membranes, respectively, with a contraction of 22% induced by calcination. Note that the shrinkage is isotropic, contrary to films, where uniaxial contraction perpendicular to the substrate is always observed.

In another experiment we have tried to increase the evaporation rate by placing the Petri dishes containing the precursor solutions under a chemical hood. In a few days the membranes dried, however they gave no appreciable signal in GISAXS measurements. This indicates that there is no ordered mesostructure in the membrane (in this case a diffuse ring should be visible in the pattern, corresponding to a wormlike mesophase), suggesting that evaporation must be slow in order for self-assembly to occur and create an ordered pore array, and that objects thicker than films require slower solvent evaporation.

It should also be noted that both the inorganic silica and the organosilica membranes show the same mesophase symmetry with a high degree of order and only a slight difference in the cell parameters. On the other hand, it has previously been shown that hybrid films prepared from a mixture of TEOS and MTES are more ordered with respect to films prepared from TEOS. In the corresponding membranes the role of the methyl groups does not seem to be so critical to affect the final structure. This is probably due to the particular synthesis conditions: in particu-
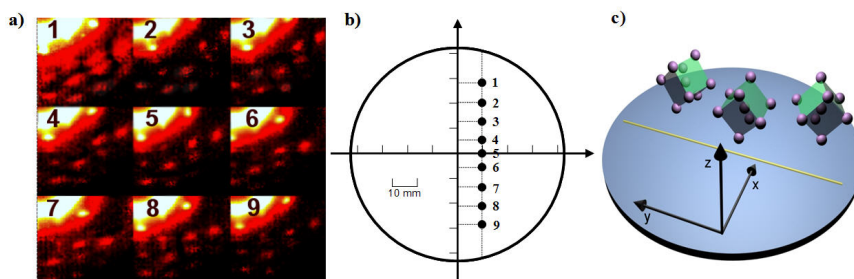
Figure 3.23. *SAXS sampling (transmission mode) of the inorganic mesostructured membrane with steps of 10 mm (a) and drawing of the corresponding positions along the membrane diameter (b). Picture of the rotation of the mesostructure from the centre of the membranes (snapshot 5) towards the outer regions (c).*

lar, a slow solvent evaporation may favour a more thermodynamic and less kinetic control on the formation of the mesostructure.

SAXS membrane mapping

The use of a sample holder equipped with an *x-y* stage system (parallel to the membrane surface) allowed the sampling of the T membrane along two orthogonal directions with steps of 10 mm (see Figure 3.23). With this system different portions of the membranes were sampled by SAXS to probe the extension of the ordered mesophase in the membrane. Nine different SAXS diffraction patterns, recorded in *transmission* mode, are shown in Figure 3.23 a, and the corresponding positions in the membrane are reported in Figure 3.23 b. Comparing the SAXS patterns taken starting from the centre of the membranes towards the outer region, it is possible to detect the presence of the ordered mesophase in the central region of the membrane within a radius of 30 mm Figure 3.23 b. The presence of spots both in the transmission and grazing diffraction patterns relative to this inner region shows that the mesostructure has both in-plane and out-of-plane order. This is a feature not commonly observed in mesoporous materials, which are characterised by planar disorder. The SAXS patterns show only a small rotation (around 3–4°) from the centre of the membranes (snapshot 5) to the external areas, corresponding to an in-plane rotation of the mesostructure (see Figure 3.23 c). In the outer region of the membrane (indicatively beyond the zone delimited by the 30 mm radius), the in-plane order is lost but the out-of-plane order of the mesostructure is retained, as confirmed by the presence of diffraction rings in transmission mode (not shown in figure). This phenomenon is probably caused by an increase in the radius of curvature of the membrane surface, affecting the peripheral regions of the samples. Because the precursor sol wets the container's walls creating a meniscus, the final membrane thickness rises from 30 μm in the membrane centre to 48 μm at the edges and the radius of curvature of the air-sample interface is smaller in the region closer to the edge of the container than in the central region. As already reported,[27] the self-assembly of micelles starts from the interfaces, therefore the smaller radius of curvature can determine a gradient in the evaporation rate of solvent and, in turn, the loss of order.
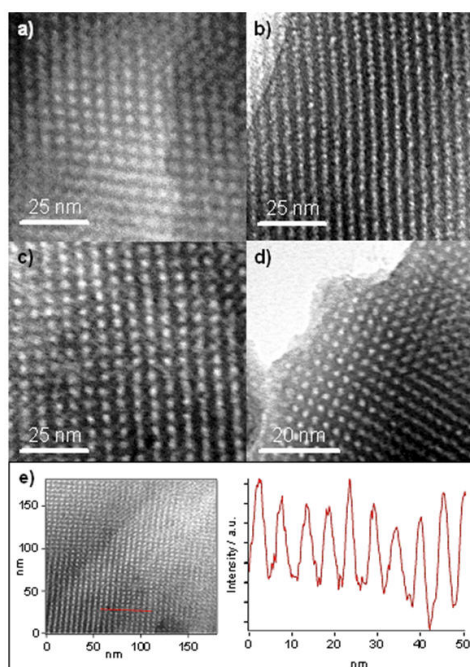
Figure 3.24. *Bright field TEM images for samples calcined at 350°C. Four different images of inorganic (a and b) and hybrid (c and d) membranes are shown. In particular (a), (c) and (d) show the {100} faces, (b) shows the {110} face. (e) represents the line profile analysis (right side) to evaluate pore and walls dimensions. The TEM image on the bottom left refers to a hybrid membrane.*

Transmission electron microscopy

TEM images were collected to support the information provided by SAXS data. Bright field TEM images for mesoporous silica and organosilica membranes thermally treated at 350°C are reported in Figure 3.24, whereas the uncalcined samples did not give significant images due to the small electronic contrast between the framework and the templating phase, and due to electron beam damage on the weakly condensed membrane framework during observation. Figure 3.24 shows four representative images of the silica (a and b) and organosilica (c and d) membranes. The presence of 4-fold symmetry axes suggests that the structure is cubic. In both membranes an $Im\bar{3}m$ body-centred cubic mesostructure is compatible with the TEM images, which refer to different sample orientations corresponding to different projection planes of the mesostructure. In particular, Figure 3.24 a, c and d show the (100) face and Figure 3.24 b shows the (110) face. The (110) face appears as a sequence of channels because the depth of field of the electron microscopy merges different mesopores located on different levels.

By a line profile analysis on a representative TEM image showing the (100) projection plane (Figure 3.24 e) we estimated pore diameter and wall thickness as the average FWHM of the intensity distribution along a line passing through the pore centres (red line in figure). Pore diameter in organosilica membranes is (6 ± 1) nm and wall thickness is (3.3 ± 0.5) nm. Thus the average centre-to-centre distance of two adjacent pores is ≈ 4.5 nm. Due to the merging of planes, the (100) projection plane shows the pores both at the cube vertices and at the centre of the unit cell. Therefore, the interpore distance represents half the diagonal of a face of

the cubic unit cell and must be multiplied by $2\sqrt{2}$ in order to get the cell parameter a, which gives $a \approx 12$ nm, a value in agreement with SAXS data. Similar results were obtained for the inorganic silica membranes.

3.4.3 Spectroscopic analysis at low pressure

Fourier-transform infrared analysis was performed at the synchrotron infrared beamline SINBAD at the INFN Laboratori Nazionali at Frascati (Rome). The equipment used was a Bruker Equinox 55 spectrophotometer with a conventional Globar source. To investigate the desorption kinetics of chemical moieties physically adsorbed on the pore surface, the spectrophotometer was equipped to work in vacuum down to 10^{-2} mbar. Measurements were carried out at different pressures in transmission mode using the interferometer working in the 500–6000 cm^{-1} range at a resolution of 4 cm^{-1}. A nitrogen-cooled MCT detector cooled with liquid nitrogen and a KBr beam splitter were used.

Figure 3.25 shows the 2800–3800 cm^{-1} portion of a FTIR absorption spectra of the inorganic membrane calcined at 350°C, as a function of the pressure within the vacuum chamber. At atmospheric pressure the spectra are saturated, so the first significant spectrum was collected at 0.5 mbar. The relative intensities of the main vibrational modes[10,16] observed around 3500, 3650 and 3750 cm^{-1} appear to be affected by pressure.

The broad band peaking around 3500 cm^{-1} decreases in intensity and shifts to higher wavenumbers as pressure decreases. In particular, the maximum shifts from 3494 cm^{-1} in the spectrum recorded at 0.5 mbar to 3547 cm^{-1} in the spectrum measured at 0.001 mbar. Moreover, the shape of this band and its changes versus pressure suggest that different contributions are responsible for these variations. At $\sim$3500 cm^{-1} there is a contribution from OH stretching of silanols that are hydrogen bonded to the oxygen of neighbouring silanols (ν_s (OH$\cdots^H$OSi)),[16] whereas the presence of adsorbed atmospheric water vapors gives rise to two contributions in the 3000–3500 cm^{-1} region, overlapping with the ν_s(OH) band of silanols.

A first water band falls at higher energies around 3450 cm^{-1} and is assigned to molecular water that is chemically bonded to the silica network (ν_{as}(H$_2$O)) or hydrogen-bonded to the silanol groups (ν_s(H$_2$O)). The second contribution due to molecular water that is assigned to the first overtone of the bending mode of H-bonded water ($2\nu_b$), falls at lower energy, around 3200 cm^{-1}. The changes observed in the low-wavenumber tail of the 3500 cm^{-1} band (the band shrinks and the tail disappears in the spectra from 0.5 to 0.06 mbar) indicate water removal at lower pressures (Figure 3.25). In accordance, the intensity decrease and shift of the 3500 cm^{-1} band is also attributed to removal of residual H-bonded water.

We used the band at 1628 cm^{-1} (ν_b, water bending)[28] to follow the desorption of water induced by the pressure changes (Figure 3.26 a). This band is not overlapped to other species and can give a direct semiquantitative indication of water desorption. The asymmetric shape of the band suggests that different types of water are present within the membrane pores at ambient pressure. Following the literature, three different vibrational components due to molecular water can be observed: water molecules that aggregate with strong hydrogen bonding ($\approx$1676 cm^{-1}) (type I), water molecule clusters with moderate intensity of hydrogen bonding ($\approx$1654 cm^{-1}) (type II) and water molecules that interact with each other with weak hydrogen bonding ($\approx$1592 cm^{-1}) (type III).[29] Generally, a lower
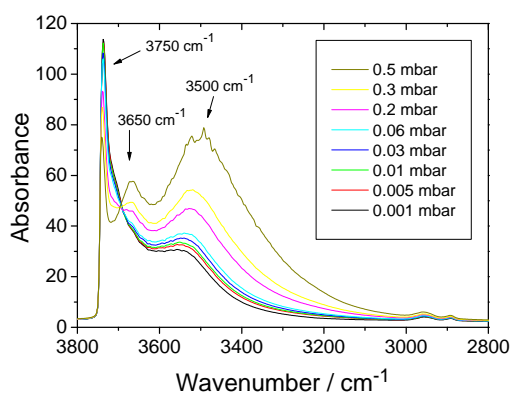
Figure 3.25. *FTIR absorption spectra of the inorganic silica membranes after calcination at 350°C, in the 2800–3800 cm^{-1} range, taken at decreasing pressures within the experimental chamber.*
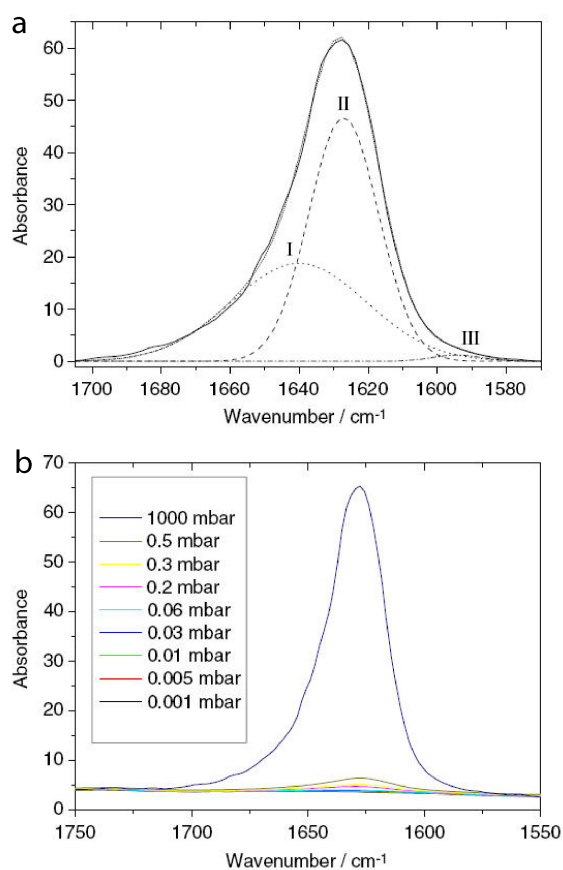

Figure 3.26. *(a): Deconvolution of the water band, the three components (I (dot line), II (dash line) and III (dash-dot line)) of water bending modes were resolved by Gaussian curves. The short dot line represents the three components Gaussian fit of the experimental data. (b): 1628 cm^{-1} (ν_b, water bending) as a function of the pressure changes in the experimental chamber.*
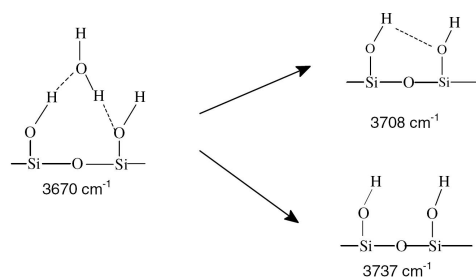
Figure 3.27. *Surface species detected by FTIR: water molecules bridge two adjacent silanols, which become either isolated silanols or geminal silanols upon water departure and condensation.*

wavenumber is an indication of a decrease in the strength of the hydrogen bonding, and type-III hydrogen bond is so weak that the water involved can be considered as "free" water. Figure 3.26 b shows a deconvolution of the water band and the three components of water bending modes were resolved by Gaussian curves. Only two components are resolved with a significant intensity (I and II). The component III is very weak, which is an indication that almost no "free" water is present within the pores. Whereas at ambient pressure the sample adsorbs water that is hydrogen bonded on the pore surface through the silanols, at 0.06 mbar the water is completely removed, in accordance with the spectra in Figure 3.25 ($3200\,\mathrm{cm}^{-1}$ component). Furthermore, because most water is easily desorbed at 0.5 mbar (Figure 3.25), the amount of water directly bonded to the silica network is negligible.

At higher wavenumbers, in the 3800–2800 cm^{-1} region, the FTIR spectra show three other vibrational modes, which change in intensity with the variation of the pressure: at 3670, at 3708 (shoulder) and at 3737 cm^{-1} (Figure 3.25). The 3670 cm^{-1} band is assigned to OH stretching of SiOH with a contribution from asymmetric stretching of hydrogen bonded molecular water ($\nu_{as}(\mathrm{H_2O})$).[16] The decrease in intensity of this band at higher vacuum pressures indicates that the contribution from molecular water is predominant. On the other hand, the intensity decrease of this mode is accompanied by a simultaneous increase of the 3708 and 3737 cm^{-1} bands. We attribute the 3708 cm^{-1} band to geminal silanols and the 3737 cm^{-1} to isolated silanols.[11] The removal of the bridging water can induce a condensation between adjacent silanols that will form twin species or will give new isolated silanols. Figure 3.27 shows the picture of the different silanol species and their changes activated by water desorption, as previously described.

The FTIR measurements performed in vacuum vs. pressure confirm that the pores of the membranes are fully accessible from the external environment, as shown by the full removal of the adsorbed atmospheric water. The process of adsorption-desorption is also reversible and it appears related to the nature of the pore surface. On the basis of FTIR data it should be noted that at ambient pressure the pore surface, in silica-based mesoporous materials, is in any case covered by at least one layer of hydrogen-bonded atmospheric water linked to the residual silanols. Such layer is responsible for the high protonic conductivity of silica mesoporous materials and their application as electrochemical sensors.[30,31]

References

[1] P. Falcaro. *Film mesostrutturati inorganici ed ibridi ottenuti attraverso l'impiego di copolimeri a blocchi come agenti stampanti.* Phd thesis, Università degli studi di Bologna, 2006.

[2] P. Falcaro, D. Grosso, H. Amenitsch, P. Innocenzi. Silica orthorhombic mesostructured films with low refractive index and high thermal stability. *J. Phys. Chem. B*, **2004**, *108*, 10942–10948.

[3] http://www.ncnr.nist.gov/programs/crystallography/software/cmpr/ (accessed December 2007).

[4] E. L. Crepaldi, G. Soler-Illia, D. Grosso, F. Cagnol, F. Ribot, C. Sanchez. Controlled formation of highly organized mesoporous titania thin films: from mesostructured hybrids to mesoporous anatase TiO_2. *J. Am. Chem. Soc.*, **2003**, *125*, 9770–9786.

[5] E. L. Crepaldi, G. Soler-Illia, A. Bouchara, D. Grosso, D. Durand, C. Sanchez. Controlled formation of highly ordered cubic and hexagonal mesoporous nanocrystalline yttria-zirconia and ceria-zirconia thin films exhibiting high thermal stability. *Angew. Chem. Int. Ed. Engl.*, **2003**, *42*, 347–351.

[6] http://rsb.info.nih.gov/ij/ (accessed December 2007).

[7] M. P. Tate, C. N. Urade, J. D. Kowalski, T.-C. Wei, B. D. Hamilton, B. W. Eggiman, H. W. Hillhouse. Simulation and interpretation of 2D diffraction patterns from self-assembled nanostructured films at arbitrary angles of incidence: From grazing incidence (above the critical angle) to transmission perpendicular to the substrate. *J. Phys. Chem. B*, **2006**, *110*, 9882–9892.

[8] R. N. Ward, D. C. Duffy, P. B. Davies, C. D. Bain. Sum-frequency spectroscopy of surfactants adsorbed at a flat hydrophobic surface. *J. Phys. Chem.*, **1994**, *98*, 8536–8542.

[9] J. Gallardo, A. Duran, D. Di Martino, R. Almeida. Structure of inorganic and hybrid SiO_2 sol-gel coatings studied by variable incidence infrared spectroscopy. *J. Non-Cryst. Solids*, **2002**, *298*, 219–225.

[10] P. Innocenzi. Infrared spectroscopy of sol-gel derived silica-based films: a spectra-microstructure overview. *J. Non-Cryst. Solids*, **2003**, *316*, 309–319.

[11] P. Innocenzi, P. Falcaro, D. Grosso, F. Babonneau. Order-disorder transitions and evolution of silica structure in self-assembled mesostructured silica films studied through FTIR spectroscopy. *J. Phys. Chem. B*, **2003**, *107*, 4711–4717.

[12] Y. Su, J. Wang, H. Liu. FTIR spectroscopic investigation of effects of temperature and concentration on PEO-PPO-PEO block copolymer properties in aqueous solutions. *Macromolecules*, **2002**, *35*, 6426–6431.

[13] H. Yoshino, K. Kamiya, H. Nasu. IR study on the structural evolution of sol-gel derived SiO_2 gels in the early stage of conversion to glasses. *J. Non-Cryst. Solids*, **1990**, *126*, 68–78.

[14] A. Fidalgo, L. M. Ilharco. The defect structure of sol-gel-derived silica/polytetrahydrofuran hybrid films by FTIR. *J. Non-Cryst. Solids*, **2001**, *283*, 144–154.

[15] K. Kamiya, T. Yoko, K. Tanaka, M. J. Takeuchi. Thermal evolution of gels derived from $CH_3Si(OC_2H_5)_3$ by the sol-gel method. *J. Non-Cryst. Solids*, **1990**, *121*, 182–187.

[16] K. Davis, M. J. Tomozawa. An infrared spectroscopic study of water-related species in silica glasses. *J. Non-Cryst. Solids*, **1996**, *201*, 177–198.

[17] X. S. Zhao, G. Q. Lu, A. K. Whittaker, G. J. Millar, H. Y. Zhu. Comprehensive study of surface chemistry of MCM-41 using CP/MA NMR, FTIR, pyridine-TPD, and TGA. *J. Phys. Chem. B*, **1997**, *101*, 6525–6531.

[18] J. Chen, Q. Li, R. Xu, F. Xiao. Distinguishing the silanol groups in the mesoporous molecular sieve MCM-41. *Angew. Chem. Int. Ed. Engl.*, **1995**, *34*, 2694–2696.

[19] S. Sugahara, T. Kadoya, K.-I. Usami, T. Hattori, M. Matsumura. Preparation and characterization of low-k silica film incorporated with methylene groups. *J. Electrochem. Soc.*, **2001**, *148*(148), F120.

[20] F. L. Galeneer. Band limits and the vibrational spectra of tetrahedral glasses. *Phys. Rev. B*, **1979**, *19*, 4292–4297.

[21] D. Shamiryan, T. Abell, F. Iacopi, K. Maex. Low-k dielectric materials. *Materials Today*, **2004**, *7*, 34–39.

[22] D. Zhao, Q. Huo, J. Feng, B. F. Chmelka, G. D. Stucky. Nonionic triblock and star diblock copolymer and oligomeric surfactant syntheses of highly ordered, hydrothermally stable, mesoporous silica structures. *J. Am. Chem. Soc.*, **1998**, *120*, 6024–6036.

[23] B. W. Eggiman, M. P. Tate, H. W. Hillhouse. Rhombohedral structure of highly ordered and oriented self-assembled nanoporous silica films. *Chem. Mater.*, **2006**, *18*, 723–730.

[24] V. V. Guliants, M. A. Carreon, Y. S. Lin. Ordered mesoporous and macroporous inoragnic films and membranes. *J. Membr. Sci.*, **2005**, *235*, 53–72.

[25] G. Soler-Illia, E. L. Crepaldi, D. Grosso, D. Durand, C. Sanchez. Structural control in self-standing mesostructured silica oriented membranes and xerogels. *Chem. Commun.*, **2002**, 2298–2299.

[26] K. Vallé, P. Belleville, F. Pereira, C. Sanchez. Hierarchically structured transparent hybrid membranes by in situ growth of mesostructured organosilica in host polymer. *Nature Materials*, **2006**, *5*, 107–111.

[27] S. Besson, T. Gacoin, C. Jacquiod, C. Ricolleau, D. Babonneau, J.-P. Boilot. Structural study of 3D-hexagonal mesoporous spin-coated sol-gel films. *J. Mater. Chem.*, **2000**, *10*, 1331.

[28] J. G. Bayly, V. B. Kartha, W. H. Stevens. Absorption spectra of liquid phase H_2O, HDO, and D_2O from 0.7 to 10 μ. *Infrared Phys.*, **1963**, *3*, 211–222.

[29] Y. Shen, P. Wu. Two-dimensional ATR-FTIR spectroscopic investigation on water diffusion in polypropylene film: water bending vibration. *J. Phys. Chem. B*, **2003**, *107*, 4224–4226.

[30] A. Bearzotti, J. Mio Bertolo, P. Innocenzi, P. Falcaro, E. Traversa. Humidity sensors based on mesoporous silica thin films synthesized by block copolymers. *J. Eur. Ceramic Soc.*, **2004**, *24*, 1969–1974.

[31] J. Mio Bertolo, A. Bearzotti, P. Falcaro, E. Traversa, P. Innocenzi. Sensoristic applications of self-assembled mesostructured silica films. *Sensor Letters*, **2003**, *1*, 64–70.

Chapter 4

Applications of mesoporous silica films

Abstract

In this chapter three applications of mesoporous silica films are presented. The first application revolves around the deposition of a mesoporous coating on macroporous silicon oxycarbide foams. In this way, ceramic bodies with hierarchical meso-macro-porosity can be obtained, which can be used for example in removal of pollutants and organic compounds. The second application consists in the patterning of mesoporous thin films by deep X-rays using synchrotron radiation. Mesoporous structures with feature size of around 30 μm can be fabricated using this lithographic technique, prospecting a possibile use in microarray spotting. The third application makes use of mesoporous silica films as nanoreactors: the mesopores are used for the in situ growth of magnetic FeCo nanoparticles by an impregnation technique followed by a reduction treatment. The FeCo-SiO$_2$ nanocomposites thus obtained can be used for the preparation of nanoparticles, for example for magnetic resonance imaging.

4.1   Hierarchical porosity by infiltration of a ceramic foam

4.1.1   Introduction

Porous materials containing cavities in the nanometre to millimetre size range (e.g. zeolites, M41S, honeycombs, foams) hold a significant position in industry owing to their widespread use in several industrial processes and household products. Applications include catalysis, filtration (of liquids or gases), extraction, separation, sorption, thermal management, scaffolds for biological applications and low-specific gravity components for structural applications.[1] In all these cases, the synthesis procedure of a porous material must allow for the control of both pore dimension and pore size distribution, which are generally required to be narrowly centred on a specific value. Advanced applications may require pores that are either interconnected and open to the external environment in order to allow for diffusing species to flow through the porous material, or isolated and not accessible from the outside, e.g. in low dielectric constant materials in microelectronics. Graded or oriented porosity is also sometimes required for specialised applications.[1] As we have seen, according to IUPAC classification[2] porous solids fall into three categories according to pore size (d): microporous ($d < 2$ nm), mesoporous (2 nm $< d < 50$ nm) and macroporous ($d > 50$ nm).

A special category of macroporous solids is that of cellular materials (foams, honeycombs, fiber mats), which are defined as materials possessing high porosity (typically >70 vol%), in which the morphology of the pores is mostly regular and the overall three-dimensional architecture of the body derives from the superposition of polyhedral voids (cells), packed to efficiently fill space. Roughly speaking, cell size typically varies from ~1 to ~50 μm for the so-called *microcellular* materials, while it ranges from ~50 μm to a few mm for *macrocellular* materials. In particular, ceramic foams possess a unique combination of different properties, such as low density, thermal conductivity, dielectric constant, thermal mass and high geometric surface area, thermal shock resistance, permeability (if open cells), dimensional stability, resistance to wear and chemical corrosion, and tortuosity of flow paths, which permits them to satisfy specific functional purposes of significant industrial interest.[3]

A porous material containing porosity on two or more length scales is referred to as a material with hierarchical porosity. Here, the term "hierarchical" refers to n length scales which are arranged according to a relationship of subordination. Different types of hierarchical porosity may exist according to the pore sizes d that are involved in the porous structure, i.e. bimodal size distribution micro-meso, meso-macro, micro-macro, or trimodal micro-meso-macro. When porous materials are required to perform multiple functions (multifunctional materials), hierarchical porosity is a way to accomplish these multiple tasks. For example, micro-macro-porosity can highly improve the performance of microporous materials in applications where a material with both catalytic function and high mechanical strength is required.[4,5] In this case the catalytic function is performed by the microporous material such as a zeolite, which contains cavities at the molecular scale acting as the catalytic sites. Zeolites can be fabricated in packed beds and inserted on the flow path of a fluid, but a significant improvement is attained by either supporting the zeolitic material on a macroporous material or using a macroporous material with micropores embedded in its structure. In this way, a

higher mechanical strength is ensured by the macroporous structure (e.g. a ceramic foam); moreover, the resistance to the flow provided by the macroporous material is lower than the zeolitic packed bed, thus increasing efficiency. In general, the macroporous framework ensures chemical and mechanical stability, as well as mass transport properties due to interconnections between the macropores, while the microporous system provides the functionality for a given application. When adsorption of larger molecules is involved, meso-macro-porous materials come into play, for example in the case of catalysis of large hydrocarbon macromolecules or devices for biosensing of large-molecular weight biomolecules such as proteins.

One-pot strategies for the synthesis of materials with this type of hierarchical porosity have been devised: for instance, Danumah et al. obtained silica powders showing high surface area with a bimodal meso- and macro-porosity by a dual templating approach,[6] while the synthesis of trimodal (micro-meso-macro-porous) silica using an ionic liquid, KLE block copolymer[*] and polystyrene (PS) spheres as the templating agents was reported. Another interesting approach is to infiltrate a template made of colloidal PS spheres with a gel containing the silica source and a block copolymer: thus, a macroporous material with mesoporous walls is obtained after calcination.[7] Moreover, if suitable precursors are used in the infiltration step, other chemical compositions of the walls can be obtained, such as TiO_2, ZrO_2 and aluminophosphates.[8]

The use of one-pot synthetic strategies leads to the presence of porosity in the whole macroporous framework, which may impair the mechanical strength of the final material. An alternative is the separate synthesis of the porous components according to pore size. This modular approach involves the synthesis of the macroporous scaffold and its functionalisation with the mesoporous or microporous system, for example by impregnation. The synthetic strategy of depositing a meso- or micro-porous coating on the macroporous structure is best suited when the function involves either chemical reactions at the very surface of the macropores such as in catalysis, or rapid adsorption-desorption of analytes such as in sensing. Another advantage of this modular approach is that the materials constituting the macroporous scaffold and the coating can be selected independently, therefore a wide range of chemical compositions (e.g. oxides, aluminophosphates, carbides, nitrides) enables flexible design of multifunctional porous materials.

Ceramic foams are optimal candidates as the substrates for the development of porous bodies with hierarchical porosity. Their very large geometric surface area (on the order of a few $m \cdot cm^{-3}$ for micro-cellular foams) provides a large area for the deposition of coatings of suitable materials possessing micro-/meso-porosity. The complete interconnection of the porosity provides easy access to the precursors for obtaining such coatings and their chemical inertness allows processing and use in harsh environments. Furthermore, in comparison to the conventional packed beds used as catalyst support in chemical engineering applications, these cellular macro-porous materials afford a lower pressure drop, a higher external mass transfer rate, greater turbulence and increased convective heat transfer.[9–12]

---

[*]KLE is a [poly(ethylene-*co*-butylene)-*block*-poly(ethylene oxide)] block copolymer, with the chemical formula $[H(CH_2CH_2)_{0.67}(CH_2(CH)CH_2CH_3)_{0.33}]_{100}(OCH_2CH_2)_{86}$-OH.

4.1.2 *Preparation of a meso-/macro-porous foam*

In the recent past, the research group led by prof. Paolo Colombo at the University of Padova has been pursuing the development of ceramic bodies possessing hierarchical porosity either by a controlled thermal treatment and/or the addition of suitable fillers[5] or by depositing zeolites onto the cell walls of SiOC microcellular foams.[4] We decided to follow this approach to prepare a silicon oxycarbide (SiOC) macroporous (microcellular) foam, which has good mechanical properties and high chemical durability,[13] and deposit a mesoporous SiO_2 coating on the cell walls through impregnation.

SiOC ceramic foams belong to the class of materials called *cellular solids*. The properties of this class of materials are deeply influenced by the morphology (porosity percentage, cell size, cell size distribution, degree of interconnectivity) and by the relative density of the foam, defined as the ratio between the apparent density (given by the ratio between the weight and the size of the sample) of the foam and that of the solid from which it is made.[3] It is possible to produce SiOC microcellular ceramics possessing a high degree of interconnectivity and a wide range of cell sizes, just by varying the size and amount of the PMMA sacrificial microbeads.[13,14]

Since the goal of the present work was to verify the feasibility of the proposed method, foams with the largest cell and cell-window size ((135 ± 57) µm and (20 ± 8) µm, respectively) were chosen in order to favour the impregnation step, because smaller macropores could lead to a more difficult uptake of the mesoporous silica precursor solution. On the other hand, mechanical strength scales with the inverse of pore size; therefore the choice of a PMMA size of 185 µm (measured compression strength: $\sigma = (1.8 \pm 0.2)$ MPa, for a bulk density $\rho = 0.24$ g·cm^{-3}) is a trade-off between the two issues. The SiOC foam was synthesised from preceramic polymers using PMMA spheres as the macropore formers, while the mesoporous silica coating was obtained by a templated self-assembly strategy using tetraethoxysilane as the silicon source and block copolymer Pluronic F127 as the structure-directing agent.

SiOC microcellular foams were prepared using a preceramic polymer (MK Wacker-Chemie GmbH, Germany) and poly-methylmetacrylate (PMMA) microbeads (Altuglas BS) of nominal size 185 µm acting as the sacrificial filler.[13] The powders were mixed at a constant weight ratio (20 wt% MK, 80 wt% PMMA) by ball milling for 1 hour and then warm pressed (130°C, 20 MPa). The warm pressing temperature was adjusted as a function of PMMA microbead size, in order to optimise the viscous flow of the molten polymer through the beads and the degree of crosslinking of the preceramic polymer. The green samples were then treated in air at 300°C for 2 h (heating rate = 0.5°C·min^{-1}) in order to burn out the PMMA microbeads and allow for further preceramic polymer crosslinking. The foams, still in their polymeric stage, were then pyrolysed under nitrogen flow at 1200°C for 2 hours (heating rate = 2°C·min^{-1}). During pyrolysis, the preceramic polymer samples were subjected to a large volume shrinkage ($\approx$50%; about 23% linear shrinkage) due to the polymer-to-ceramic transformation, occurring with the elimination of organic moieties and leading to the formation of an amorphous SiOC ceramic. Cylindrical samples of 30 mm diameter and 4 mm thickness (after pyrolysis) were prepared. The SiOC samples were then cut in smaller pieces for characterisation.
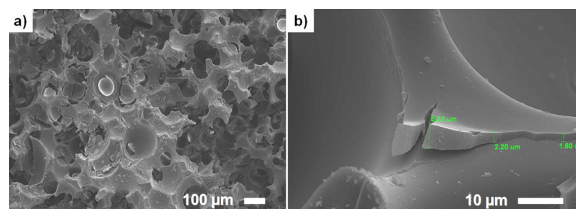
Figure 4.1. *a) Low magnification image of the S185 sample after calcination in air at 350°C. b) Detail of the film thickness on the strut surface.*

The mesoporous silica precursor solution was prepared as described on page 90. Several impregnation procedures were tested, in particular: (1) impregnation time was varied, (2) different thermal treatments were done, (3) drying was done either by spinning the sample at different rotation speeds, in air or in vacuum, (4) impregnation was carried out in a vessel with reduced atmospheric pressure by a water aspirator based on the Venturi effect. The procedure that gave the best results was the following: SiOC foams were soaked in the silica solution and withdrawn after 1 minute, excess solution was then removed from the samples with a paper towel. The impregnated samples were dried in air at ambient temperature for 20 days. A thermal treatment was then performed on the impregnated samples in order to remove the surfactant from the mesopores and promote further condensation of the silica framework. Calcination was carried out in air at 350°C for 1 hour (heating rate = $1°C \cdot min^{-1}$).

4.1.3 Results and discussion

SEM (Scanning Electron Microscopy) investigations reveal the presence of a coating on the foam surface (Figure 4.1). Few cracks can be detected at the surface curvatures, where stresses concentrate preferentially during drying. The coating appears to be delaminated in some areas; however, this could likely have been induced by sample cutting before SEM analysis. The film thickness ranges from 1 µm to 5 µm in correspondence of the struts (Figure 4.1 b). From TEM images, the coating appears to be ordered throughout the whole thickness, with less ordered regions located close to the coating-foam interface (Figure 4.2). In few cases, poor order is observed at the coating-foam interface. There is a good agreement between thickness values measured by TEM (thickness ≈700 nm, Figure 4.2) and SEM images (µm range, Figure 4.1), even though the latter gives more reliable information revealing that the film is somewhat inhomogeneous in thickness depending on the macropore region considered. TEM images of mesoporous coatings in samples treated at 350°C, taken at different projection planes, show 6-fold (Figure 4.3 a) and 4-fold (Figure 4.3 b) symmetry axes: this is compatible with a cubic lattice, based on the assumption that the symmetry of the mesostructure is constant in the whole material.

As TEM gives information about the ordered mesostructure on a strictly local scale (a few hundred of nanometres), SAXS measurements were performed in order to obtain structural information averaged on a larger volume of sample. SAXS was performed in transmission mode: a slice of the sample was placed in the beam path at a given distance from the CCD detector. The lateral dimension of the X-ray beam was ≈3 mm^2 so that the volume probed by SAXS was ≈10 mm^3. SAXS patterns of foams impregnated with the mesoporous silica solution display a ring,
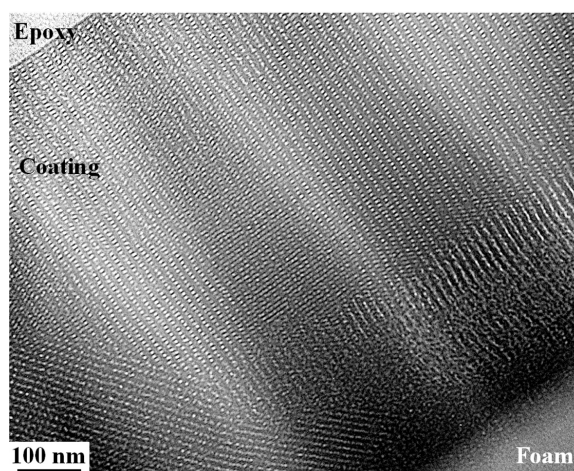
Figure 4.2. *Cross sectional TEM image showing a regular pore arrangement in the coating on the foam.*
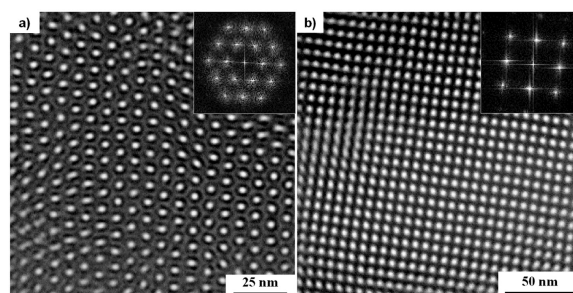

Figure 4.3. *TEM images of selected pore arrangements in the coating (inset: calculated FFT diffraction pattern demonstrating the well-arranged pores with individual lattice orientations).*

both for thermally treated and untreated samples (Figure 4.4 a). As a matter of fact, these SAXS patterns can be considered to be the intersection of the Ewald sphere with the reciprocal lattice, which describes the periodic modulations in the electronic density of matter (here, the periodicity of the silica mesoporous coating) in the reciprocal space (see Chapter 2). Since the structure is made of ordered domains lying on curved polyoriented surfaces, the reciprocal lattice appears as a set of concentric spheres, and its intersection with the Ewald sphere yields a set of concentric rings. On the other hand, SAXS patterns of foams that were not impregnated do not show any feature, which is a further confirmation that the ring is related to the ordered mesoporous silica coating.

The concentric rings in the SAXS patterns can be thought as the d-spacings relative to the *hkl* family planes in the mesostructure. Thus, a radial integration, which can be defined as the integration of the pattern intensity along a line passing through the beam centre coordinates, yields a 1-dimensional diffractogram. The radial integration of the SAXS patterns, starting from the beam centre towards the outer region, yields an intensity vs. 2-theta curve which is reported in Figure 4.4 b. This plot shows the presence of three additional peaks that are not immediately visible in the patterns. The d-spacings relative to these three smaller peaks can be related to the d-spacing of the most intense, with ratios $\sqrt{2}$, $\sqrt{3}$ and 2 (Figure 4.4.
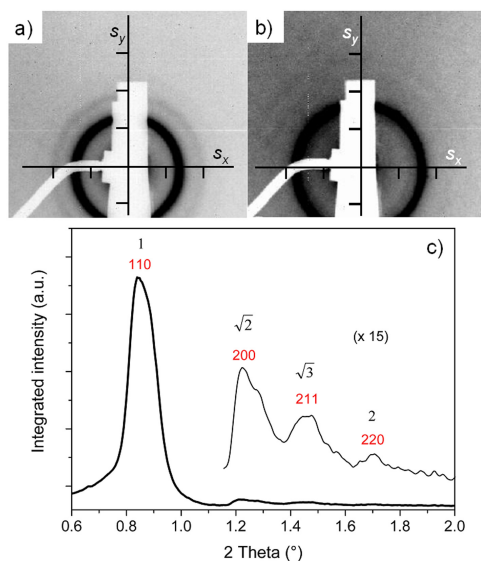
Figure 4.4. *Diffraction patterns of impregnated samples: with no thermal treatment (a) and after calcination (b); the scattering vector axes s_x and s_y are reported, with the scale bar corresponding to $0.007 \, \text{Å}^{-1}$. The radial integration of the diffraction pattern in (a) is reported in (c), where each peak shows its $Im\bar{3}m$ Miller index and its d-spacing relative to the main peak position.*

In the thermally-treated samples the d-spacings were found to be smaller than in the untreated samples, but the ratios between the 2-theta values remained constant. These ratios are consistent with a BCC unit cell with $Im\bar{3}m$ space group having no preferential orientation with respect to the laboratory frame ("powder-like"). Simulations were performed using the software CMPR (see page 92) to reproduce diffraction data, selecting different space groups according to those most often observed in mesoporous silica,[15] especially cubic phases because TEM images suggested a cubic symmetry. The best fit was obtained with a cubic $Im\bar{3}m$ unit cell with lattice parameter $a = 18$ nm in untreated samples, and $a = 14$ nm in thermally-treated samples. The peaks were thus assigned to the 110, 200, 211, 220 reflections.

Based on these results, TEM representative images relative to different projection planes were selected and the BCC cell parameter was calculated from their FFT by from simple geometric considerations, assuming that planes merge due to the depth of field of the electron microscopy (see Figure 4.3). Due to the merging of planes, the (111) and (100) projection planes (Figures 4.4 a and b, respectively) show the pores at the cube vertices as well as the pores located in the centre of the unit cell. Therefore, the (100) interpore distance represents half diagonal of a face of the cubic unit cell, and must be multiplied by $\sqrt{2}$ in order to get the cell parameter a, while the (111) interpore distance must be multiplied by $\sqrt{3/2}$. This calculation yields $a = (13 \pm 1)$ nm, which is in agreement with the present SAXS data, as well as with previously reported data relative to mesoporous silica films and membranes. The average diameter of mesopores was estimated with a line profile analysis of representative TEM images, as the average FWHM of the intensity distribution along a line passing through the centres of the pores, obtaining a value of (4.5 ± 0.8) nm.

The nitrogen adsorption-desorption isotherms for coated samples are reported in Figure 4.5 a. Specific surface area (SSA) was determined from a Brunauer-

Emmet-Teller (BET) analysis[16] in the P/P_0 range of 0.05–0.2 with a correlation coefficient of 0.999, using a molecular cross-sectional area for N_2 of 0.162 nm^2 and a minimum of 5 data points. The pore size distributions were obtained from the desorption branch of the isotherm through the Barret-Joyner-Halenda (BJH) analysis,[17] which takes into account the KJS equation for the calculation of the layer thickness and Faas correction.[18] The micropore size distribution was calculated using the improved Horvath-Kawazoe equation[19] for cylindrical pore geometry. The uncoated SiOC foams have a SSA of 3.4 m$^2 \cdot$g^{-1}, and pores having size <100 nm were not detected. Regarding the coated samples, the isotherm follows the typical behaviour of mesoporous materials. The fast rise at low relative pressure values reflects the presence of micropores (<2 nm). The hysteresis loop shape is typical for interconnected pores that give rise to a three-dimensional network.[20] BJH desorption cumulative pore volume as a function of the pore size is reported in Figure 4.5 b. The pore size distribution is narrow and the main pore diameter measures (3.2 ± 0.3) nm, in reasonable agreement with the data obtained using image analysis on the TEM micrographs $(4.5 \pm 0.8$ nm). The underestimation of pore size compared to the values measured from TEM investigations is a typical inconvenience of the method, even after the introduction of the Faas correction for layer thickness.[20] Micropores volume and median size were calculated using the Horwath-Kawazoe method. The volume of micropores and their median size were calculated using the Horwath-Kawazoe method, extended to cylindrical pores geometry by Saito and Foley, obtaining values of 0.01 cm$^3 \cdot$g^{-1} and 1.3 nm, respectively.

The SSA measured by the BET method gave a value of (60.2 ± 0.3) m$^2 \cdot$g^{-1}. However, considering that the effective weight of the mesoporous material is the weight of the mesoporous silica film coating the macroporous SiOC foam, the SSA value was recalculated considering the weight difference of the sample before and after impregnation and calcination. This gave a SSA value of (564.9 ± 2.5) m$^2 \cdot$g^{-1}, which is two orders of magnitude higher than that of SiOC foams with the same macropore size (3.4 m$^2 \cdot$g^{-1}), and is comparable to the typical SSA values of mesoporous silica powders found in the literature.[21]

Selected tests on the meso-macro-porous material demonstrated that the compression strength of the material was the same as that of the ceramic foam before impregnation, that is the deposition of a mesoporous coating does not affect the properties of the component.

To sum up, a ceramic component with hierarchical meso- and macro-porosity was obtained by depositing a mesoporous silica coating on the surface of an open-cell SiOC foam. The walls of the macropore substrate were found to be covered uniformly by a mesoporous silica layer having a thickness ranging from <1 to ~5 µm. The mesostructure has a high degree of order almost everywhere in the coating, and it can be described by a body-centred cubic cell ($Im\bar{3}m$ space group) having no preferential orientation with respect to the macropore curved surface. The mesopores exhibit a narrow size distribution and appear to be interconnected through micropores, giving rise to an interconnected three-dimensional porous network in the coating. The SSA of the component increased by one order of magnitude due to the presence of the meso-porosity in the coating. This material with a hierarchical porosity can be of use in applications where a high SSA as well as a high permeability are required, for examples in catalysis and sorption. The possibility of functionalising the pore surface with species bearing specific chemical
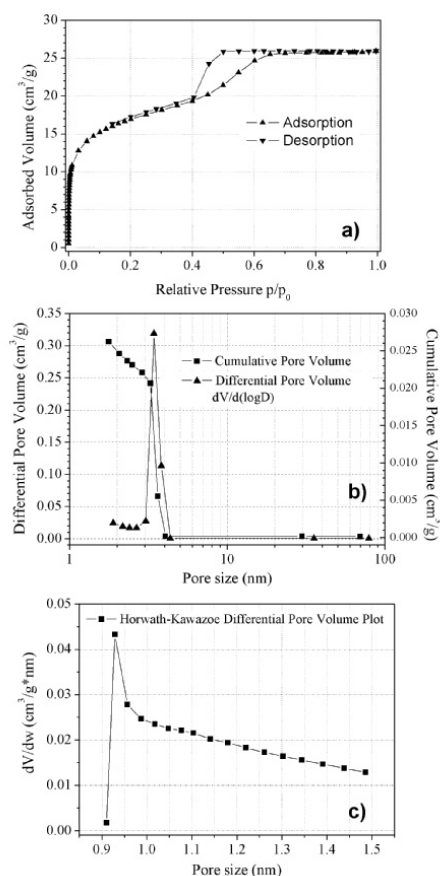
Figure 4.5. *Adsorption-desorption isotherm for the coated sample (measured after calcination in air at 350°C). b) BJH desorption cumulative pore volume and BJH desorption* $\mathrm{d}V/\mathrm{d}(\log D)$. *c) H-K micropore cumulative pore size.*

units opens the way to more functional applications, for example as sensors or selective filters for removing pollutants,[22] or as a scaffold for the immobilisation of biological species.

4.2 Patterning of mesoporous silica films with synchrotron radiation

4.2.1 Introduction

Combined bottom-up and top-down approaches to the synthesis of organised matter are attracting much interest due to the possibility of fabricating complex functional nano- and micro-structures for advanced applications.[23,24] Typically, the possibility of building structures defined at the atomic or molecular level is a prerogative of bottom-up syntheses, whereas complex structures such as micro- and nanoscopic interconnects and circuits can be obtained by top-down approaches, which also are suited for industrial scale-up. Therefore, the development of specific technologies based on combinations of both types of synthetic approaches is an important goal for basic and applied research.

Self-assembled mesoporous thin films are a notable example of materials synthesised by a bottom-up approach,[21,25] whose integration in devices requires, however, top-down processing. Specific patterning of mesoporous films aimed at ob-

taining circuits or dot arrays is a task that cannot be fulfilled by merely dip-coating or spin-coating the precursor solution on a substrate without further processing. In particular, the bottom-up EISA technique used in the synthesis of mesoporous films needs coupling with top-down processing such as substrate pre-patterning or film lithography.[25] In this way, hierarchically-structured porous materials can be obtained, where self-assembly is locally directed and organisation resides on multiple length scales: porosity (typically 2–10 nm), film thickness (50–500 nm) and pattern size (150 nm to 1.3 μm). The ordered mesopores constitute an ideal host for guest functional organic molecules or nanoparticles,[26] while the patterns, from the nano- to the micro-scale, allow designing devices for different advanced applications,[27] for example as DNA nanoarrays or lab-on-a-chip devices.

The possibility of patterning mesoporous films was first demonstrated by Brinker et al.,[28,29] who applied several lithographic techniques to fabricate patterned mesoporous films. These techniques are based either on mesophase change or on mesostructure disruption occurring upon irradiation with deep UV radiation (λ=256 nm). Thin (max thickness 360 nm) films were patterned with a lateral resolution of 10 μm. Using an excimer laser (wavelength λ=248 nm) coupled with a phase mask, a resolution of around 560 nm could be attained. However, the use of a phase mask is restricted to the patterning of periodic objects and is not suited for the fabrication of nonperiodic structures. Alternatively, DPN (dip-pen nanolithography) or ink-jet printing using a "self-assembling ink", dip-coating and selective de-wetting were used to obtain patterned mesoporous arrays with high resolution (150 nm) and microfluidic devices.[30] Photopatternable cyclic silsesquioxane compositions containing a photoacid generator were prepared, with the goal of achieving a photoresist-free porous low-dielectric constant (k) layer.[31] The films were patterned with a standard UV lamp (λ=350 nm), reaching a lateral resolution on the micrometre scale (≈ 2 μm) with the possibility of patterning thick (1.3 μm) films. A spatially-directed impingement of UV light (λ=187–254 nm) was demonstrated to be effective in selectively removing surfactant molecules from mesostructured thin films, generating patterns as small as 3 μm.[32] However, only thin (300 nm) films could be obtained. Immersion in a NaOH solution preferentially and completely etched the mesostructured material from the surface, leaving patterned mesoporous islands. This process was studied using optical microscopy, spatially resolved FTIR and spatially resolved ellipsometry.

The need for hi-tech integrated components requires more and more sophisticated lithographic techniques to achieve higher aspect-ratios, a higher definition, the capability to pattern thick structures, higher resolution (depending on film thickness, down to few tens of nanometres) and the capability to define patterns of complex non-periodic shapes. Several of the possible applications that are envisioned for mesoporous materials, such as nano-micro arrays and lab-on-a-chip devices, have exactly these stringent requirements. At the moment there is a gap between the material development and the available technologies. With the aim of providing knowledge to cover this gap we have developed an integrated fabrication patterning process which is based on deep X-ray lithography[33] and dip-pen writing[34,35] of the mesoporous patterned arrays.

Deep X-ray lithography (DXRL) has never been used to obtain patterned mesoporous films. This is surprising, because the development of a technology for patterning mesoporous coatings based on X-rays has several advantages compared to other techniques such as DPN and UV lithography: for example, integration with

the current fabrication techniques for electronic devices, high aspect ratio, better lateral resolution (depending on film thickness, down to few tens of nanometres), possibility of patterning thick coatings and complex non-periodic structures, or periodic objects using the phase mask technology.

It has been demonstrated that a peculiar property of mesoporous materials, the presence of a tunable steady state after film deposition, can be exploited for inducing reversible phase changes by X-rays (see Chapter 5). These experiments were conducted on mesostructured hafnia films, but this processing can be generalised to develop a technology based on X-ray lithography on mesoporous films of different compositions, for instance silica and titania. In the work presented in this section we have strived to develop a patterning technology based on this mesoporous response to X-ray radiation. We have used deep X-ray lithography (DXRL) to pattern mesostructured silica thin films. DXRL is a manufacturing process by which a material that is exposed to high-resolution, high-intensity and extremely collimated synchrotron radiation through an X-ray mask changes its dissolution rate in a liquid solvent (developer). By this lithographic method, the mask pattern is, therefore, transferred to the material.[36] In our case, this lithographic approach is based on selective template removal and silica polycondensation induced by synchrotron radiation. The areas of the film that are not exposed to radiation can be selectively etched due to a lower crosslinking degree of the inorganic network. An important advantage of this method is the possibility of simultaneously removing the surfactant and inducing condensation of the silica network in a single-step process. Several patterned objects, not limited to periodic structures, have been obtained. By this approach, we have patterned several objects with different sizes and shapes on mesostructured silica films.

4.2.2 Experimental

Mesostructured silica films were prepared as described on page 90, using block copolymer Pluronic F127 as the structure-directing agent and TEOS as the silicon source. An amount of 0.6 g of photoacid generator bis(4-*tert*-butylphenyl)iodonium *p*-toluenesulfonate (see Figure 4.6) was added to the final solution. The substrates chosen for deposition were p-type boron-doped, (100)-oriented, 400 μm-thick silicon wafers. The silicon substrates, previously cleaned with water, EtOH and rinsed with acetone, were dip-coated in the precursor sol at the pulling rate of 2.3 mm·s^{-1} at the relative humidity (RH) of 40%.

The as-deposited mesostructured silica films were patterned at the DXRL beamline at Elettra synchrotron[37] 3 hours after deposition. The samples were exposed through X-ray masks containing test patterns of different size, shape and geometry (5 to 500 μm). The masks had a gold absorber with thickness of 20 μm and a titanium transparent membrane with thickness of 2.2 μm. The deposited dose on the bottom of the film was 3 kJ·cm^{-3}. After 12–24 hours from X-ray exposure, the films were rinsed in a developing solution to remove the unirradiated parts of the mesostructure. The developing solution was optimised in order to obtain the etching in a time scale of seconds and the maximum aspect ratio for the patterened structures. This solution was prepared by mixing 35 mL of ethylene glycol with 10 mL of ethanol. The samples were sonicated for 20–30 seconds in the solution, then they were dried under an air flow. The films, after the lithographic process,
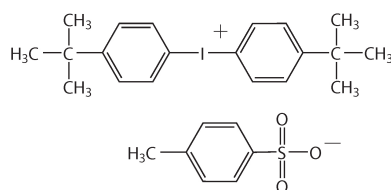
Figure 4.6. *Photoacid generator used in the fabrication of patterned mesostructured silica films: bis(4-tert-butylphenyl)iodonium p-toluenesulfonate.*

were thermally treated at 150°C for 1 hour in order to stabilise the inorganic network.

The mesostructure was investigated by GISAXS with an incident wavelength of 1.54 Å. TEM images were obtained in bright field mode on a JEOL 200CX microscope equipped with a tungsten cathode operating at 200 kV. Samples were prepared evaporating on a carbon-coated copper grid one drop of a suspension containing scratched fragments of the films in *n*-octane

FTIR microscopy was performed at the SISSI beamline of the synchrotron Elettra. IR spectra were collected using a Bruker Hyperion 3000 microscope attached to a Bruker Vertex 70 interferometer working in the mid-IR range with a conventional Globar source and a KBr beamsplitter. The microscope was equipped with a liquid nitrogen-cooled MCT (Mercury-Cadmium-Telluride) detector and a motorised sample stage that allowed mapping of the samples using a rectangular aperture of 15×30 μm^2. Each spectrum was obtained in transmission mode averaging 700 interferograms at a resolution of 8 cm^{-1}.

The samples were observed by an optical microscope Nikon Optiphot 500 both before and after the development. A white-light optical profiler (ADE-Shift MicroXAM) with a $50\times$ objective was employed for the three-dimensional mapping of different patterned zones.

An NT-MDT Ntegra Atomic Force Microscope (AFM) was used to analyse the topography of the samples. Surfaces were measured at 0.5–1 Hz scan speed in semicontact mode, using a silicon tip with nominal resonance frequency of 150 kHz, 5 N·m^{-1} force constant, and 10 nm typical curvature radius. The same AFM was used to perform a Dip Pen Nanolithography (DPN) experiment in the following way. We have prepared a solution containing Rhodamine 6G $8 \cdot 10^{-3}$ M and deposited a small volume (a droplet of 2 μL) on a Si surface. The AFM tip was then dipped into the droplet and subsequently moved above the patterned sample. The position was chosen by observation with the optical microscope and then the tip was approached onto the surface in contact mode. A square was drawn performing a 5×5 μm scan at 1 Hz. Another experiment was conducted leaving the whole sample in a diluted solution ($3 \cdot 10^{-5}$ wt% of Rhodamine 6G in ethanol) for 2 min. The sample was then extracted at controlled speed (140 mm·s^{-1}) and rinsed 3 times with pure ethanol. The result of the DPN and dipping experiments was investigated by a confocal fluorescence microscope (Witec CRM 200), equipped with an Ar-Ion Laser (514 nm excitation line) and with a 200×200 μm^2 piezoelectric scanner. The spatial distribution of Rhodamine 6G has been detected mapping the fluorescence excited on the surface after the deposition process.
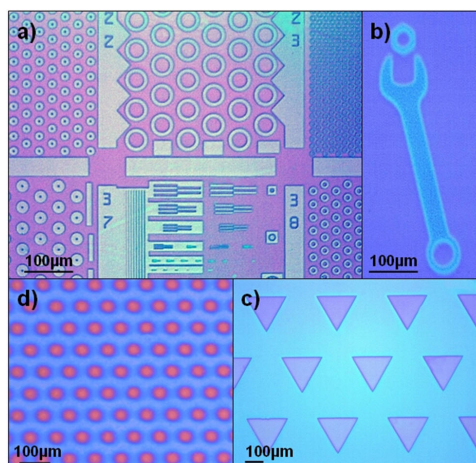
Figure 4.7. *Optical micrograph of a patterned mesostructured silica film. The patterned objects can be discerned by their colour, due to the difference in refractive index between the masked and the unmasked regions.*

4.2.3   Results and discussion

The patterned films were first observed by optical microscopy in order to assess the quality of the lithographic process. Figure 4.7 shows a few optical micrographs of a patterned sample, in which patterned objects are discernible due to the difference in refractive index between the masked and the unmasked regions: the patterned areas appear either white (Figure 4.7 a), light blue (Figure 4.7 b and c) or red (Figure 4.7 d). This observation suggested that physical or chemical changes took place in the unmasked areas of the films. Therefore we used GISAXS and TEM to detect the mesophase variations in the films upon X-ray irradiation, while infrared microscopy was employed to investigate the chemical changes induced on the mesoporous materials by the patterning process.

In order to perform GISAXS tests, as-deposited mesostructured films were exposed to DXRL synchrotron radiation through a mask that covered half of the film, so that a large area of the sample could be investigated by the probing beam. GISAXS experiments showed that in both the irradiated and the masked regions, the mesostructure has two-dimensional hexagonal symmetry (space group *p6mm*), which is composed by a stack of tubular micelles packed in structures with hexagonal cross section.[38] TEM measurements confirmed a *p6mm* mesostructure with cylindrical micelles: cross-sectional images revealed the presence of either hexagonal stacking (front view, Figure 4.8 a) or tubular structures (side view, Figure 4.8 b). A comparison between the masked and the unmasked GISAXS patterns showed that no substantial change in spot position and sharpness occurred, leading to conclude that no change in mesostructure symmetry took place upon deep X-ray patterning.

The exposure of the films to X-rays did not cause any change in the mesophase but the regions that were not exposed to X-rays could be easily etched as described in the Experimental section. This developing process is fast and effective: optical profilometry measurements revealed that the masked areas of the samples were completely removed by the etching. Figure 4.9 a and b show portions of a mesoporous film patterned with circular pillars 50 μm in diameter and subsequently etched, whereas Figure 4.9 c shows the results of a partial etching leading to low
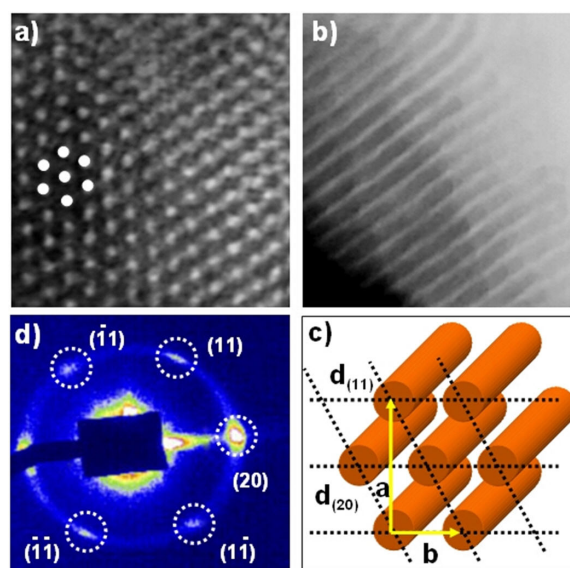
Figure 4.8. *Transmission electron microscopy images showing the shape of the cylindrical mesopores (a and b), which are disposed according to a two-dimensional hexagonal cross section (c). The grazing incidence small-angle X-ray scattering pattern reveals a p6mm symmetry group.*

aspect ratio. We also evaluated whether the etching process affects the mesostructure, because in the etching procedure the whole film is soaked in the solution: this could cause a partial degradation of the Si-O-Si network resulting in loss of order or collapse of the inorganic walls with mesostructure disruption. However, an etched film presenting a large exposed area was investigated by GISAXS and no change in the diffraction patterns of the etched film was detected (not shown in figure), indicating that the mesostructure was retained upon etching. Mesostructure preservation is very important from the viewpoint of applications, in that the properties associated with the ordered mesostructure (e.g. high specific surface area, pore accessibility) must be retained in order to ensure functionality.

Regarding the physicochemical phenomena occurring during the lithographic process, the most likely hypothesis, supported by the literature, is that silica polycondensation reactions are induced by the acid photocatalyst upon activation by the X-rays.[29] However, only indirect evidence has been reported on this point, therefore one of our goals was to elucidate this important aspect by infrared microscopy, which is a very useful tool to obtain a chemical mapping of an object on a micrometre scale. We have chosen this imaging technique to study the chemical changes induced by the synchrotron radiation on the samples because it readily correlates the distribution of the chemical species by a three-dimensional mapping of the sample, providing a "chemical picture" of a selected area. This picture is composed of a fixed number of pixels, each containing an interferogram associated with a FTIR spectrum. The integrated areas of the spectra in a selected wavenumber interval are associated with a colour according to an intensity scale, therefore an image is obtained showing the presence of the chemical species relative to that wavenumber interval.[39] The IR microscope used in this work can perform measurements in transmission mode if the substrate transmits IR radiation, Alternatively, measurements either in reflection or in ATR mode (attenuated total reflection) can overcome
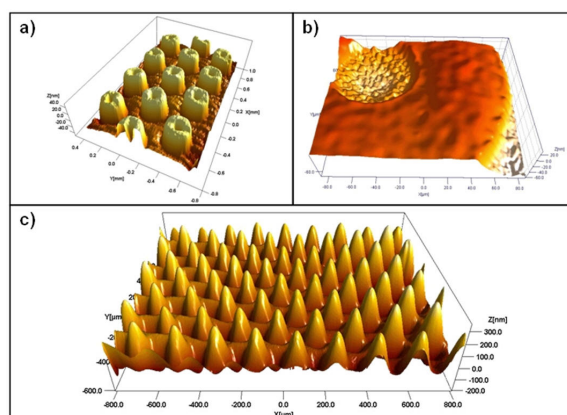
Figure 4.9. *Optical profilometry of etched patterned mesoporous silica films relative to different objects: hollow pillars (a and b) and partial etching leading to low aspect ratio (c).*

the limitation of a substrate opaque in the IR range. In this case we have conducted the experiments in transmission mode because Si substrates allow transmission of the incident IR radiation.

The visible image taken by the integrated optical microscope (Figure 4.10 a) refers to a 200×200 µm^2 portion of a sample which was patterned but not etched. It shows a purple-pink ring corresponding to the irradiated region, whereas the light-blue portion corresponds to the unirradiated region. The same area was observed by infrared microscopy, by which an image was obtained (Figure 4.10 b) by calculating the absorbance intensity of the FTIR spectrum at 2891 cm^{-1} (symmetric C-H stretching of CH$_2$ in Pluronic F127) after a baseline subtraction in the 3030–2840 cm^{-1} region. The different colours, corresponding to different intensities in a linear intensity scale, point out that a sharp decrease in intensity of the CH$_2$ stretching mode (2891 cm^{-1}) occurred in the ring area. This effect was induced by exposure to X-rays and can be quantified calculating the ratio between the maximum and the minimum band intensities along a diameter of the circular pillar reported in Figure 4.10 a. In this case the reduction of the CH$_2$ stretching band between the points A and B (see Figure 4.10 a) is around 38%. This indicates a partial removal of the surfactant by the incident radiation.

Another chemical map was obtained from the data collected in the same experiment by integrating the Si-OH stretching band around 930 cm^{-1} (Figure 4.10 c). These data show a strong decrease of silanols in the exposed areas, which is associated with higher silica degree of polycondensation. The mechanism, supported by other works, is the decrease of pH upon X-ray irradiation due to photodecomposition of the photoacid, which yields aryliodo radical-cation and aryl-radical species.[40] The decrease of pH from $\approx$2 to $\approx$0 leads to acid-catalysed inorganic polycondensation.[29] De-polymerisation in the organic phase is likely to be caused by the radicalic species generated upon irradiation from the photoacid molecules.[40] As reported in the literature, X-rays can induce a radicalic de-polymerisation in the organic phase which may be caused by OH**.** free radicals created from water molecules by high-flux radiation, either via direct homolysis or via photoelectric effect.[41,42] Because this phenomenon is not detected in films prepared without photoacid initiator, a leading role should be attributed to the photoinitiator molecules.
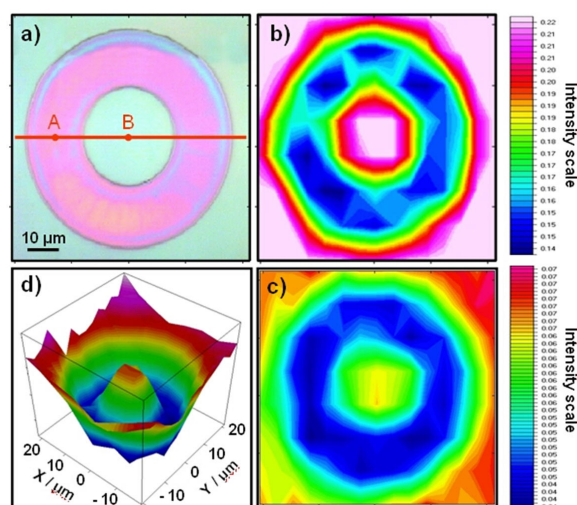
Figure 4.10. *Visible image (a) and infrared microscopy images relative to template (b and d) and silanols (c).*

As a crosscheck, we have exposed mesostructured silica films that did not contain the photoinitiator: no difference in silica condensation between the irradiated and the unirradiated regions of the film was detected as well as no difference in organic removal (not shown in figure). The observation that the irradiated areas of the patterned films containing the photoinitiator were preserved after the exposure and the developing process, whereas the unexposed areas were easily dissolved, confirms the increased degree of polycondensation of the silica network induced by the photoacid.

One of the aims of this work was to test integration of top-down techniques with the bottom-up self-assembly pathway leading to mesostructure formation. The lithographic approach by DXRL enabled the fabrication of isolated mesoporous pillars; another top-down technique was chosen to chemically functionalise the pillars by means of a controlled writing process using an atomic force microscope (AFM). In a proof-of-concept experiment, the AFM cantilever tip was used as a dip pen using rhodamine 6G as the ink in order to functionalise selected mesoporous pillars. The AFM cantilever tip was dipped into the rhodamine solution so that it took up a drop of solution, then it was approached to its destination pillar. When the cantilever landed on the pillar and the solution came into contact with the film, capillary forces drove the solution from the cantilever tip into the pillar, so that the mesopores became filled with the rhodamine solution.

The results of this controlled writing process were observed by confocal fluorescence microscopy. Figure 4.11 a shows the mapping of the fluorescence signal integrated in the spectral range 530–580 nm. The two regions where the dip-pen functionalisation was performed are characterised by a high fluorescence intensity and can be clearly distinguished on two separate pillars. Here, the signal due to rhodamine is two orders of magnitude higher than the background, which might be due to the slight fluorescence effect typically found in sol-gel derived materials. This experiment demonstrates that, using this method, it is possible to fabricate highly fluorescent mesoporous microstructures by the functionalisation of micrometric mesoporous objects with different guest molecules (for example, oligonucleotide strands can be attached to the pillars in the fabrication of microarrays for
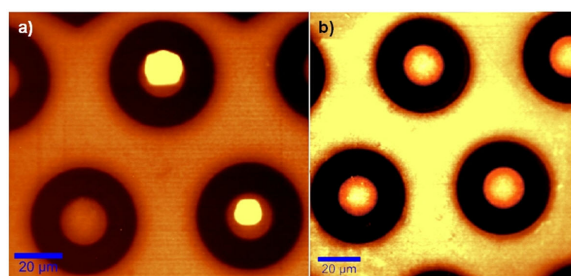
Figure 4.11. *Results of the dip-pen functionalisation process showing fluorescence integrated in the spectral range 530–580 nm (a).*

DNA spotting). The lateral feature size of the patterned pillars corresponds to the conditions for microarray deposition, which are typically around 30 μm.[43] The lateral resolution of AFM enables functionalisation of sub-micron mesoporous objects using small amounts of analytes; in addition, the patterned mesoporous support maximises the adsorption of guest molecules due to the high specific surface area of mesoporosity. Furthermore, the hexagonal *p6mm* mesostructure allows accessibility of the material from the outside and diffusion of analytical species into the material, opening the route for efficient immobilisation of biological species in analytical applications.

Another experiment was performed with the aim of testing the fluorescence efficiency of the patterned structure. A patterned mesoporous film was impregnated with a $3 \cdot 10^{-5}$ wt% rhodamine 6G solution in ethanol: the sample was soaked in this solution for 2 min, then it was rinsed with ethanol to ensure that no excess solution was left on the film surface. Confocal fluorescence microscopy (Figure 4.11 b) revealed the presence of rhodamine 6G on the mesoporous patterned areas, whereas the etched regions of the film showed no fluorescence, with around one order of magnitude between the fluorescence intensity in the etched (dark areas) and unetched (bright areas) regions. This also demonstrated that the etching process completely removes the unexposed region of the film, leaving no residue of the film on the substrate.

To summarise, ordered mesoporous silica films were patterned by means of deep X-ray lithography using synchrotron radiation, obtaining mesoporous objects with controlled size and shape. The mesostructure was investigated by GISAXS and TEM, revealing an ordered two-dimensional hexagonal *p6mm* structure. The patterning mechanism was studied by infrared imaging, which provided evidence for the selective increase of silica polycondensation and the partial removal of the templating agent. A dip-pen approach using an atomic force microscope enabled selective functionalisation of the mesoporous objects with rhodamine 6G. This experiment allows envisioning new fabrication technologies of functional materials for applications such as, for example, DNA nano-spotting or lab-on-a-chip devices.

4.3   FeCo-SiO$_2$ nanocomposites: working with nanoreactors

4.3.1   Introduction

Bulk FeCo alloys are soft ferromagnets whose magnetic properties have been widely investigated as a function of composition and temperature, owing to their technological importance. The major field of application of FeCo alloys is in the

technology of transformer cores and electrical generators because of their soft ferromagnetic behaviour combined with high Curie temperatures and large saturation inductions, about 15% larger than pure iron.[44] The preparation of iron-cobalt alloy nanoparticles is usually approached by the use of a coating in order to avoid agglomeration and coalescence between the nanoparticles. For example, radio frequency plasma torch was used to produce C-coated FeCo nanoparticles of about 50 nm.[45] Serna et al. made use of hydrolytic routes to produce anisotropic alloy nanoparticles in order to increase the magnetic coercivity: needle-like alumina- and yttria-coated FeCo nanoparticles were prepared by annealing of YCo-FeOOH nanoparticles obtained by oxidation-precipitation.[46] Recently, monodisperse 15-nm nanoparticles were obtained by co-decomposition in toluene at 150°C under H_2 of appropriate organometallic precursors.[47]

An alternative approach lies in embedding the iron-cobalt nanoparticles in an insulating matrix, which acts as a dispersing medium. Sol-gel processing is very suitable for the preparation of such nanocomposites as it offers unique advantages in terms of compositional homogeneity, dispersion of the nanophase within the matrix and purity of the resulting material.

Recently, co-gelation sol-gel routes have been successfully exploited for the preparation of FeCo-SiO_2 and FeCo-Al_2O_3 nanocomposite materials.[48,49] The main advantage of this method is the compositional control of the nanocomposite and the high distributional homogeneity of the nanoparticles within the matrix, because the mixing of the precursors occurs at the molecular level in the initial stages of sol preparation. A major drawback of this preparation route is that the microstructure—and, in turn, the magnetic properties—are related to many independent processing parameters. For example, an increase in the loading of the nanophase in the composite will increase the average size of the nanocrystals, broaden the size distribution and decrease the interparticle distance.

Alternatively, if the nanocrystals are grown within a pre-formed matrix with a controlled texture, the size, size distribution and dispersion of the nanocrystals will be dictated by the porous structure of the host matrix. In principle, the growth of magnetic nanoparticles in a host matrix with controlled pore architecture allows the fine-tuning of the nanocomposite microstructure. Ordered mesoporous matrices prepared by template-assisted sol-gel techniques are particularly suited to this end in that they exhibit narrow pore size distribution together with pore diameter tunability, well-defined porous structure and high specific surface areas. The major drawback of this approach is that the nanophase is added to the matrix by diffusion and therefore the overall composition and homogeneity are more difficult to control.

Mesoporous silicas have been shown to constitute a versatile material to produce nanocomposites with interesting properties. For example, nanocomposites prepared by introducing pre-formed Co nanocrystals of suitable diameter into the pore channels of SBA15 mesoporous matrix have been used to form Co chains within the pore channels; this resulted in magnetic coupling giving rise to a transition from soft to hard magnetic behaviour.[50] In this case, the magnetic behaviour of the Co-SBA15 nanocomposite is directed by the ordered porous structure of the host matrix despite the intrinsic magnetic properties of the individual nanoparticles. Moreover, dissolution of the silica matrix in FeCo-SiO_2 nanocomposites has been shown to be an effective way to fabricate FeCo graphitic nanoparticles to be used as MRI (magnetic resonance imaging) contrast agents.[51]

If we now turn to mesoporous films, the presence of an ordered porous structure that can be tailored through the control of the synthesis parameters suggests the employment of mesoporous films as *nanoreactors* for the controlled bottom-up synthesis of nanostructured materials. Basically, the mesopores can be filled with suitable liquid or gaseous precursors which subsequently form nucleation seeds, for example by precititation or oxidation reactions. The growth of the solid phase is controlled by the chemical and the physical properties of the mesostructure (pore size, hydrophobicity, etc.). With spherical mesopores of the order of few nm, one can obtain quantum dots or metal nanoparticles with controlled size and composition. There is a large number of publications revolving on this synthetic approach: just to cite a few examples, CdS,[52–54] CdSe,[55] and Cd$_{1-x}$Mn$_x$S[56] were grown in mesoporous silica. Techniques other than impregnation can be used to grow nanoparticles inside mesopores: for example, CdS and CuInS$_2$ were grown by CVD (chemical vapour deposition) inside mesoporous titania.[57]

In a previous study conducted by the Author, CdS nanoparticles were grown by precipitation through a two-step impregnation process by immersing mesoporous silica films in solutions containing Cd^{2+} and S^{2-} species.[58] The films thus obtained contain CdS nanoparticles with size roughly tunable by the immersion time in the Cd or S precursor solutions. Different particle sizes can be obtained, as revealed by photoluminescence at different wavelengths under a standard UV lamp (Figure 4.12) and XRD data (not shown in figure).

The inclusion of nanoparticles in mesoporous films presents at least three advantages in comparison with other systems (e.g. in a dense sol-gel silica film). First, the size of the nanostructure is controlled by the size of the mesopores, which in turn can be precisely controlled in the synthesis process of the mesoporous film; therefore, it is possible to obtain highly monodisperse particles. Second, the periodicity of the mesopores allows a more efficient packing, which results in a higher nanoparticle density assuming that (almost) every pore is filled. Third, the presence of micropores in the inorganic walls of the mesoporous films ensures interconnection between the mesopores, which is an essential condition for a complete impregnation of the film in the nanoparticle growth process, as well as for permeability in the application of the final product for example as a sensor. Previously, we have observed that in block copolymer-templated mesoporous silica films the ordered mesoporosity is maintained even at temperatures higher than 800°C (page 94). This property makes the mesoporous films an interesting host material for nanoparticles whose preparation requires high temperatures. Furthermore, mesoporous films ful-
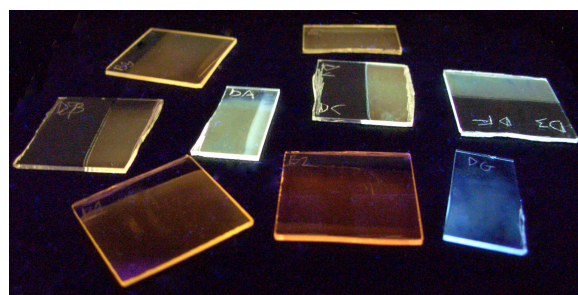

Figure 4.12. *Mesoporous silica films containing CdS nanoparticles with different sizes. A UV lamp (wavelength 365 nm) reveals photoluminescence effects due to particle size.*

fil the requirement of having good chemical stability to undergo an impregnation process.

Mesoporous silica films with different mesopore size have been used as the host and the template to prepare FeCo-SiO$_2$ nanocomposites through an impregnation process followed by a reduction treatment under H$_2$ flow. As we will see, FeCo nanocrystals grow inside the mesopores and their monodisperse size is dictated only by the size of the mesopores.

4.3.2   Experimental

Mesoporous silica thin films were prepared as described on page 90. Silicon substrates (thickness 400 µm) were dip-coated at constant relative humidity ($\approx$40%), the pulling rate was set to 2.5 mm·s^{-1}. The films were calcined at 350°C for 2 hours. The mesoporous silica films were impregnated with an aqueous solution of Fe(NO$_3$)$_3$·9H$_2$O (Aldrich, 98%) and Co(NO$_3$)$_2$·6H$_2$O (Carlo Erba, 95%) having an overall metal molar concentration of 0.4 M. The Co:Fe ratio was set to 1:2 in order to obtain a FeCo alloy with the desired composition in the final composite (Fe$_{67}$Co$_{33}$). Impregnation was carried out for 30 min under stirring. Afterwards the samples were treated at 450°C for 1 hour in air to remove residual nitrate ions and solvent. The samples were finally reduced at 600°C for 2 hours under a hydrogen flow (80 mL·min^{-1}) in a quartz tubular reactor in order to promote formation of the metal phase.

X-ray diffraction (XRD) patterns were recorded on a X3000 Seifert powder diffractometer equipped with Cu K$_\alpha$ radiation and with a graphite monochromator on the diffracted beam. XRD patterns at small 2θ values (0.5–3.0°) were acquired in Bragg-Brentano geometry in order to monitor the ordered mesostructure. Patterns at wide 2θ values (20–50°) were acquired to investigate the FeCo alloy formation; in this case a grazing incidence diffraction (GID) attachment was used in order to minimise the contribution of the substrate and the incident angle was set to 1°. TEM images were obtained on a JEOL 200CX microscope equipped with a tungsten cathode operating at 200 kV. Finely ground films scratched from the silicon substrate were dispersed in n-octane by sonication, then they were dropped on a carbon-coated copper grid and allowed to dry for TEM observations. The mesostructure of the films was investigated by GISAXS at the Austrian SAXS beamline of the Elettra synchrotron. The incident energy was set to 8 keV (wavelength 1.54 Å). The instrumental glancing angle between the incident radiation and the sample was set slightly above the critical angle (grazing incidence). Each measurement consisted typically in the average of 10 acquisitions with integration time of 500 ms.

4.3.3   Results and discussion

The mesoporous films were investigated after the thermal treatment at 600°C. This study was carried out both on films that had been previously impregnated with the Fe and Co precursor solution and on films that had not undergone impregnation. The effects induced by the impregnation process on the silica matrix were evaluated on the basis of XRD, TEM and GISAXS measurements.
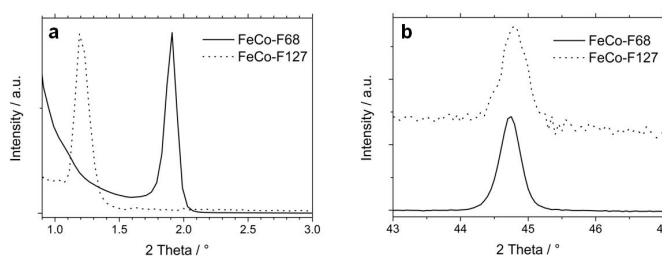
Figure 4.13. *Selected angular regions XRD patterns of the FeCo-F68 (solid line) and the FeCo-F127 (dotted line) nanocomposites, indicating the presence of the mesostructure at small angles (a) and of the FeCo alloy at high angles (b).*

X-ray diffraction A standard powder diffractometer was used to gather a first rough indication on the presence of an ordered mesostructure in the silica films and its modification with impregnation and reduction treatment by collecting patterns at small angles (0.5 to 3°, *SA-XRD*). X-ray diffraction experiments also provided evidence on the formation of FeCo nanocrystals by collecting patterns at wide angles (*WA-XRD*). In Figure 4.13 a the SA-XRD patterns of samples F68 and F127 after impregnation and reduction at 600°C show an intense peak around 2°, indicating the presence of an ordered mesostructure. The peak is centred around 1.9° in the F68-templated films and around 1.2° in the F127-templated films, indicating a larger cell constant in the latter case. In Figure 4.13 b the WA-XRD patterns are also shown, indicating that in both the F68-templated and the F127-templated films a peak around 44° is present, corresponding to the most intense peak of BCC FeCo due to the (110) reflection.

In Figure 4.14 a we compare the SA-XRD patterns of F68-templated unimpregnated and untreated films, the F68-templated film reduced at 600°C without impregnation and the F68-templated film reduced at 600°C after being impregnated. The position of the peak is centred around 1.7° in the unimpregnated and untreated film, 2.2° in the film reduced at 600°C without impregnation and around 1.9° in the film reduced at 600°C after impregnation. These results indicate that the mesoporous structure is affected by the thermal treatment, which induces a shrinkage of the mesoporous structure. However, the presence of the FeCo nanocrystals hinders the shrinkage, which is much less evident in the sample which has been reduced after impregnation. This suggests that the nanocrystals are inside the mesopores: the presence of nanocrystals inside the mesopores reduces the uniaxial shrinkage, most likely due to a steric effect: the mesopores are supported by the nanocrystals which act as a scaffold, therefore the mesostructure is less prone to contract upon thermal treatment. The same results were also obtained for the samples templated by F127. Figure 4.14 b shows that the porous structure of the FeCo-F127 sample is more shrunk with respect to the parent F127 silica matrix; however, the contraction of the pore structure is more pronounced when the pure silica film undergoes thermal treatment at the same temperature.

Grazing-incidence small-angle X-ray scattering The SA-XRD patterns gave a first indication on the presence of an ordered mesostructure and its behaviour upon impregnation and thermal treatment. However, the presence of a single peak indicates the existence of order in the out-of-plane direction, but it does not allow determining the symmetry group of the mesostructure. Therefore, a detailed
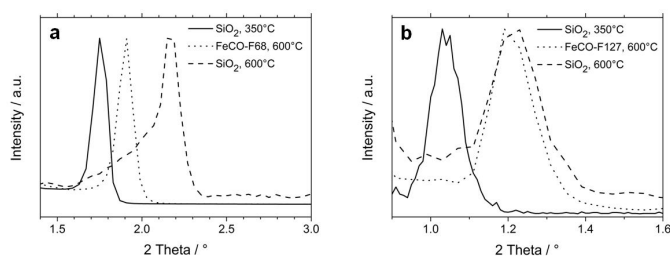
Figure 4.14. *XRD patterns in the low angular range of the F68-templated (a) and the F127-templated films (b). The data refer to mesoporous silica films treated at 350°C before impregnation (solid line), FeCo-SiO$_2$ nanocomposites treated at 600°C after impregnation (dotted line) and mesoporous silica films treated at 600°C with no impregnation (dashed line).*

characterisation of the ordered mesoporosity was performed by collecting two-dimensional GISAXS patterns. Silica films prepared utilising Pluronic F68 as the templating agent prior to impregnation and reduction gave GISAXS patterns presenting well-defined spots, which indicates high degree of order of the mesostructure (Figure 4.15 a and b). The patterns were assigned to a cubic symmetry mesostructure (body-centred cubic, space group $Im\bar{3}m$) with the (110) plane oriented perpendicular to the substrate (z direction), uniaxially distorted in the z axis.[59,60] The cell parameter a was calculated according to each single hkl reflection from its d-spacing d_{hkl} using the formula $a_{hkl} = d_{hkl}\sqrt{h^2+k^2+l^2}$. The distorted cubic mesostructure symmetry can also be described as an orthorhombic space group, as reported in Chapter 3. However, for practical purposes here we consider the observed mesostructure as a slightly z-distorted $Im\bar{3}m$ rather than a lower symmetry orthorhombic structure, and calculate the cell constants accordingly. The distortion is thus a contraction of the unit cell in the out-of-plane [110] direction (normal to the substrate), which is hereafter referred to as $d_{110,z}$, whereas the in-plane (parallel to the substrate) cell constant a is referred to as $d_{110,x}$.

The cell parameters of the distorted cubic $Im\bar{3}m$ structure in Pluronic F68-templated films treated at 350°C that did *not* undergo any impregnation and reduction treatment are $d_{110,x} = (14.0 \pm 1.4)$ nm and $d_{110,z} = (7.8 \pm 0.8)$ nm. The GISAXS patterns of the films templated by Pluronic F68 that were impregnated with the Fe/Co solution and subsequently reduced at 600°C, showed that no mesostructure symmetry change occurred upon impregnation; in this case the cell parameters are $d_{110,x} = (14.1 \pm 1.4)$ nm and $d_{110,z} = (7.1 \pm 0.7)$ nm. We can note that the in-plane cell constant is substantially unaltered, whereas the out-of-plane cell constant is smaller in impregnated films treated at 600°C.

Films templated by Pluronic F127 have a two-dimensional hexagonal *p6mm* symmetry composed of ordered arrays of tubular micelles with hexagonal cross section (Figure 4.15 c). The cell parameters of the 2d-hexagonal *p6mm* mesophase templated by Pluronic F127 are (11.0 ± 1.1) nm and (7.9 ± 0.8) nm in the in-plane (x) and out-of-plane (z) directions, respectively. The presence of a distorted ring intersecting the spots indicates that the mesophase is not well-ordered and reveals the presence of disordered or wormlike regions in the mesostructure. The cell constants of the nanocomposite (i.e. impregnated and reduced) films are (10.4 ± 1.0) nm and (7.2 ± 0.7) nm, in the x and z direction, respectively.
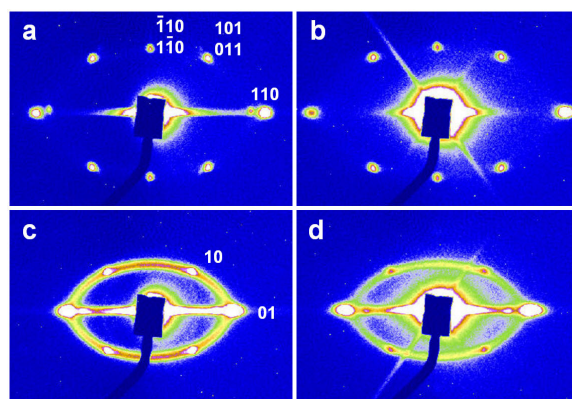
Figure 4.15. *GISAXS patterns of F68-templated mesoporous silica films treated at 350°C (a) and after impregnation and reduction at 600°C (b). F127-templated mesoporous silica films treated at 350°C (c) and after impregnation and reduction at 600°C (d).*

Transmission electron microscopy   Transmission electron microscopy images were acquired in order to evaluate local order as well as pore size and shape. The samples investigated by TEM were the starting mesoporous silica films and the final nanocomposite obtained by the impregnation process and annealing at 600°C. Figure 4.16 b shows the ordered arrays of pores in the 100 projection plane of the $Im\bar{3}m$ cubic structure. A line profile analysis was conducted on the image shown in Figure 4.16 c: the pore diameter and the wall thickness were calculated as the average FWHM of the intensity distribution along a line intersecting the pore centres. This analysis revealed that the pore-to-pore distance is different in the two orthogonal directions, which indicates the presence of a 2-fold symmetry axis, probably originating from the thermal contraction along the [110] direction of the $Im\bar{3}m$ cell (z axis). The average centre-to-centre distance between two adjacent pores is (8.6 ± 1.0) nm in the x (in-plane) direction and (6.3 ± 1.0) nm in the z (out-of-plane) direction, while the average pore diameter is (4.0 ± 1.0) nm and the inorganic pore wall thickness is (2.3 ± 1.0) nm.

Mesoporous films templated by Pluronic F127 show a short-range order, where the hexagonal packing extends only to the nearest neighbour pores, as shown in Figure 4.16 a. The line profile analysis showed that the average pore diameter is (7.4 ± 1.0) nm, which is almost double of a Pluronic F68-templated mesopore.

Figure 4.17 reports representative TEM images of the FeCo-F68 and FeCo-F127 samples obtained in bright field and dark field mode, which show the formation of the FeCo-SiO₂ nanocomposite. Due to small nanocrystal size, the alloy nanoparticles are barely detectable as darker spots in the bright field image FeCo-F68 nanocomposite (Figure 4.17 a), whereas they are more evident in the FeCo-F127 sample (Figure 4.17 d) where larger nanocrystals can be imaged.

This is even more evident in the dark field images, reported in Figure 4.17 b and e for the FeCo-F68 and FeCo-F127 samples respectively, which also show that the nanoparticles are single crystals. In fact, the dark spots in the bright field images correspond to the bright spots in the dark field images, indicating that the whole nanoparticle corresponds to a single crystalline domain. The size distribution as obtained from dark field images analysis shows that the nanocrystal size is monodisperse in both samples and is centred at 5 and 7 nm in the FeCo-F68 and FeCo-F127 samples, respectively. In both samples no aggregated nanoparticles or nanoparticles outside the mesopores of the silica matrix are observed.
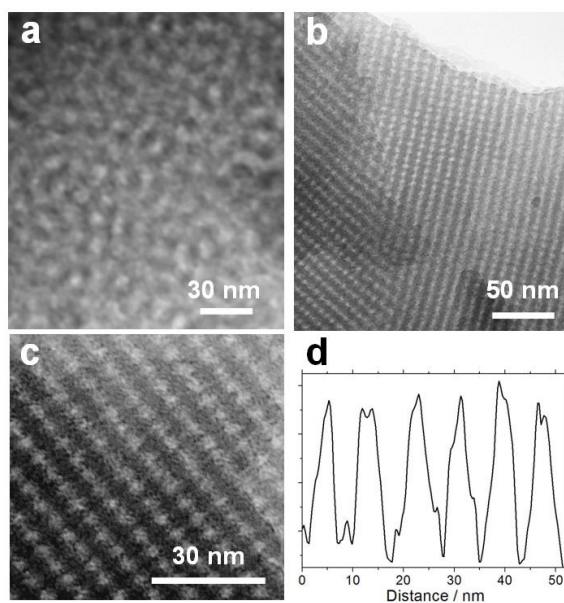
Figure 4.16. *Bright-field TEM images of mesoporous silica films templated by F127 (a) and F68 (b). Line profile analysis of a F68-templated film conducted on a representative area with higher magnification (c and d).*
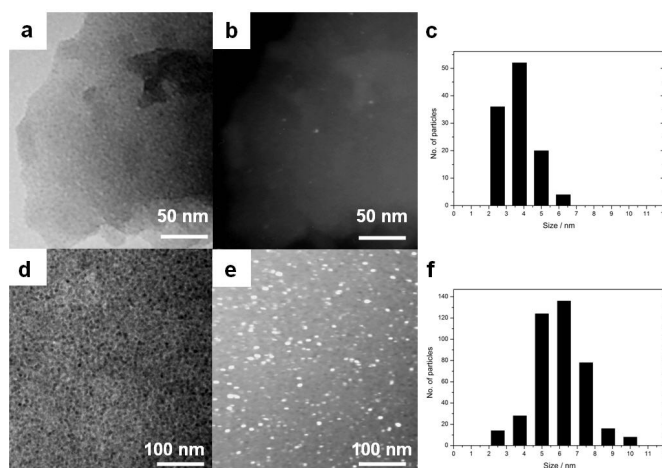

Figure 4.17. *TEM representative bright field and dark field images of the FeCo-F68 (a,b) and FeCo-F127 (d,e) nanocomposites. Nanoparticle size distribution analysis plot are shown in c and f for the FeCo-F68 and FeCo-F127 nanocomposites, respectively.*

4.3.4 Conclusions

We have shown the preparation of iron cobalt-mesoporous silica nanocomposites obtained by the impregnation of the silica mesoporous films with a precursor solution containing the Fe and Co precursors, followed by heat treatment at 600°C under a H_2 flow. Silica mesoporous films have shown to be an effective matrix for the preparation of nanoparticles requiring high crystallisation temperatures (>600°C). The films maintain their porosity even after thermal treatment at 600°C and show only a slight shrinkage after the impregnation process. The mesoporous silica films used as the matrix have either spherical or cylindrical pores, depending on the templating agent used in the synthesis, as determined by TEM and GISAXS. The growth of the FeCo nanocrystals in the silica films was confirmed by X-ray diffraction and transmission electron microscopy, showing that nanocrystal growth took place inside the mesopores. As the mesopores represent a spatial confinement for the growth of the nanocrystals, we have shown that the mesopore diameter constitutes an upper limit for the nanocrystal size, therefore nanocomposites with different FeCo sizes can be obtained by choosing the appropriate host matrix.

This synthetic approach represents a method for obtaining magnetic nanocomposites in the form of thin films, which is desirable for perspective integration in technological devices: tuning the magnetic properties of the nanocrystals can be accomplished by selecting the mesopore size of the host mesoporous matrix, which in turn can be accomplished by utilising a suitable templating agent. Our approach also represents a method for obtaining monodisperse FeCo nanocrystals: for example, dissolution of the silica matrix from a FeCo-SiO_2 nanocomposite has been shown to be an effective way to fabricate FeCo graphitic nanoparticles to be used as MRI (magnetic resonance imaging) contrast agents.

References

[1] F. Schüth, K. S. W. Sing, J. Weitkamp, editors. *Handbook of porous solids*. Wiley-VCH Verlag GmbH, Weinheim, Germany, 2002.

[2] J. Roquerol, D. Avnir, C. W. Fairbridge, D. H. Everett, J. H. Haynes, N. Pernicone, J. D. F. Ramsay, K. S. W. Sing, K. K. Unger. Recommendations for the characterization of porous solids. *Pure and Appl. Chem.*, **1994**, *66*, 1739–1758.

[3] M. Scheffler, P. Colombo, editors. *Cellular Ceramics: Structure, Manufacturing, Properties and Applications*. Wiley-VCH Verlag GmbH, Weinheim, Germany, 2004.

[4] A. Zampieri, P. Colombo, G. T. P. Mabande, T. Selvam, W. Schwieger, F. Scheffler. Zeolite coatings on microcellular ceramic foams: a novel route to microreactor and microseparator devices. *Adv. Mater.*, **2004**, *16*, 819–823.

[5] H. M. Schmidt, D. Koch, G. Grathwohl, P. Colombo. Micro-macro porous ceramics from preceramic precursors. *J. Am. Cer. Soc.*, **2001**, *84*, 2252–2255.

[6] C. Danumah, S. Vaudreuil, L. Bonneviot, M. Bousmina, S. Giasson, S. Kaliaguine. Synthesis of macrostructured MCM-48 molecular sieves. *Microp. Mesop. Materials*, **2001**, *44-45*, 241–247.

[7] T. Sen, G. J. T. Tiddy, J. L. Casci, M. T. Anderson. One-pot synthesis of hierarchically ordered porous-silica materials with three orders of length scale. *Angew. Chem. Int. Ed. Engl.*, **2003**, *42*, 4649–4653.

[8] B. T. Holland, C. F. Blanford, T. Do, A. Stein. Synthesis of highly ordered, three-dimensional, macroporous structures of amorphous or crystalline inorganic oxides, phosphates, and hybrid composites. *Chem. Mater.*, **1999**, *11*, 795–805.

[9] W. M. Carty, P. W. Lednor. Monolithic ceramics and heterogeneous catalysts: honeycombs and foams. *Curr. Opinion Solid State Mater. Sci*, **1996**, *1*, 88–95.

[10] J. T. Richardson, M. Garrait, J.-K. Hung. Carbon dioxide reforming with Rh and Pt-Re catalysts dispersed on ceramic foam supports. *Appl. Catal. A: General*, **2004**, *266*, 235–244.

[11] J. T. Richardson, Y. Peng, D. Remue. Properties of ceramic foam catalyst supports: pressure drop. *Appl. Catal. A: General*, **2000**, *204*, 19–32.

[12] B. Schimmoeller, H. Schulz, S. E. Pratsinis, A. Bareiss, A. Reitzmann, B. Kraushaar-Czarnetzki. Ceramic foams directly-coated with flame-made V_2O_5/TiO_2 for synthesis of phthalic anhydride. *J. Catal.*, **2006**, *243*, 82–92.

[13] P. Colombo, E. Bernardo, L. Biasetto. Novel microcellular ceramics from a silicone resin. *J. Am. Cer. Soc.*, **2004**, *87*, 152–154.

[14] P. Colombo, E. Bernardo. Macro- and micro-cellular porous ceramics from preceramic polymers. *Comp. Sci. Tech.*, **2003**, *63*, 2353–2359.

[15] B. W. Eggiman, M. P. Tate, H. W. Hillhouse. Rhombohedral structure of highly ordered and oriented self-assembled nanoporous silica films. *Chem. Mater.*, **2006**, *18*, 723–730.

[16] S. J. Gregg, K. S. W. Sing. *Adsorption, surface area and porosity*. Academic Press, London, 1982.

[17] E. P. Barret, L. G. Joyner, P. H. Halenda. The determination of pore volume and area distributions in porous substances. I. Computations from nitrogen isotherms. *J. Am. Chem. Soc.*, **1951**, *53*, 373–380.

[18] M. Kruk, M. Jaroniec, A. Sayari. Adsorption study of surface and structural properties of MCM-41 materials of different pore sizes. *J. Phys. Chem. B*, **1997**, *101*, 583–589.

[19] G. Hovarth, K. Kawazoe. Method for the calculation of effective pore size distribution in molecular sieve carbon. *J. Chem. Eng. Jpn.*, **1983**, *16*, 470–475.

[20] S. Lowell, J. E. Shields, M. A. Thomas, M. Thommes. *Characterization of orous solids and powders: surface area, pore size and density*. Kluwer Academic Publishers, 2004.

[21] G. Soler-Illia, C. Sanchez, B. Lebeau, J. Patarin. Chemical strategies to design textured materials: From microporous and mesoporous oxides to nanonetworks and hierarchical structures. *Chem. Rev.*, **2002**, *102*, 4093–4138.

[22] L. Nicole, C. Boissiãˇre, D. Grosso, P. Hesemann, J. Moreau, C. Sanchez. Advanced selective optical sensors based on periodically organized mesoporous hybrid silica thin films. *Chem. Commun.*, **2004**, 2312–2313.

[23] J. Y. Cheng, C. A. Ross, H. I. Smith, E. L. Thomas. Templated self-assembly of block copolymers: Top-down helps bottom-up. *Adv. Mater.*, **2006**, *18*, 2505–2521.

[24] G. A. Ozin, S. M. Yang. The race for the photonic chip: colloidal crystal assembly in silicon wafers. *Adv. Funct. Mater.*, **2001**, *11*, 95–104.

[25] D. Grosso, F. Cagnol, G. Soler-Illia, E. L. Crepaldi, H. Amenitsch, A. Brunet-Bruneau, A. Bourgeois, C. Sanchez. Fundamentals of mesostructuring through evaporation-induced self-assembly. *Adv. Funct. Mater.*, **2004**, *14*, 309–322.

[26] P. Innocenzi, P. Falcaro, S. Schergna, M. Maggini, E. Menna, H. Amenitsch, G. Soler-Illia, D. Grosso, C. Sanchez. One-pot self-assembly of mesostructured silica films and membranes functionalised with fullerene derivatives. *J. Mater. Chem.*, **2004**, *14*, 1838–1842.

[27] B. J. Scott, G. Wirnsberger, M. D. McGehee, B. F. Chmelka, G. D. Stucky. Dye-doped mesostructured silica as a distributed feedback laser fabricated by soft lithography. *Adv. Mater.*, **2001**, *13*, 1231–1234.

[28] H. Fan, Y. Lu, A. Stump, S. T. Reed, T. Baer, R. Schunk, V. Perez-Luna, G. P. López,

C. J. Brinker. Rapid prototyping of patterned functional nanostructures. *Nature*, **2000**, *405*, 56–60.

[29] D. A. Doshi, N. Huesing, M. Lu, H. Fan, Y. Lu, K. Simmons-Potter, B. G. Potter Jr., A. J. Hurd, C. J. Brinker. Optically defined multifunctional patterning of photosensitive thin-film silica mesophases. *Science*, **2000**, *290*, 107–111.

[30] Y. Lu, Y. Yang, A. Sellinger, M. Lu, J. Huang, H. Fan, R. Haddad, G. Lopez, A. R. Burns, D. Y. Sasaki, J. Shelnutt, C. J. Brinker. Self-assembly of mesoscopically ordered chromatic polydiacetylene/silica nanocomposites. *Nature*, **2001**, *410*, 913–917.

[31] Y. Y. Lyu, J. H. Yim, Y. Byun, J. M. Kim, J. K. Jeon. Photo patternable porous siloxane thin films using cyclodextrins as template materials. *Thin Solid Films*, **2006**, *496*, 526–532.

[32] A. M. Dattelbaum, M. L. Amweg, L. E. Ecke, C. K. Yee, A. P. Shreve, A. N. Parikh. Photochemical pattern transfer and enhancement of thin film silica mesophases. *Nano Lett.*, **2003**, *3*, 719–722.

[33] F. Cerrina. X-ray imaging: applications to patterning and lithography. *J. Phys. D: Appl. Phys.*, **2000**, *33*, R103–R116.

[34] K. Salaita, Y. H. Wang, C. A. Mirkin. Applications of dip-pen nanolithography. *Nature Nanotechnology*, **2007**, *2*, 145–155.

[35] M. Su, X. Liu, S.-Y. Li, V. P. Dravid, C. A. Mirkin. Moving beyond molecules: patterning solid-state features via dip-pen nanolithography with sol-based inks. *J. Am. Chem. Soc.*, **2002**, *124*, 1560–1561.

[36] E. W. Becker, W. Ehrfeld, P. Hagmann, A. Maner, D. Münchmeyer. Fabrication of microstructures with high aspect ratios and great structural heights by synchrotron radiation lithography, galvanoforming, and plastic moulding (LIGA process). *Microelectron. Eng.*, **1986**, *4*, 35–56.

[37] F. Pérennès, F. De Bona, F. J. Pantenburg. Deep X-ray lithography beamline at ELETTRA. *Nucl. Instrum. Methods Phys. Res. A*, **2001**, *467-468*, 1274–1278.

[38] D. Grosso, A. R. Balkenende, P.-A. Albouy, A. Ayral, H. Amenitsch, F. Babonneau. Two-dimensional hexagonal mesoporous silica thin films prepared from block copolymers: detailed characterization and formation mechanism. *Chem. Mater.*, **2001**, *13*, 1848–1856.

[39] http://www.brukeroptics.com/applications/microscopy.html (accessed December 2007).

[40] J. V. Crivello, J. H. W. Lam. Diaryliodonium salts. A new class of photoinitiators for cationic polymerization. *Macromolecules*, **1977**, *10*, 1307–1315.

[41] J. Murray, E. Garman. Investigation of possible free-radical scavengers and metrics for radiation damage in protein cryocrystallography. *J. Synchrotron Rad.*, **2002**, *9*, 347–354.

[42] A. Cheng, M. Caffrey. Free radical mediated X-ray damage of model membranes. *Biophys. J.*, **1996**, *70*, 2212–2222.

[43] M. Schena. *Microarray analysis*. Wiley-Liss, 2003.

[44] A. M. Saad, A. V. Mazanik, Y. E. Kalinin, J. A. Fedotova, A. K. Fedotov, S. Wrotek, A. V. Sitnikov, I. A. Svito. Structure and electrical properties of CoFeZr-aluminium oxide nanocomposite films. *Rev. Adv. Mater. Sci.*, **2004**, *8*, 152–157.

[45] Z. Turgut, J. H. Scott, M. Q. Huang, S. A. Majetich, M. E. McHenry. Magnetic properties and ordering in C-coated Fe_xCo_{1-x} alloy nanocrystals. *J. Appl. Phys*, **1998**, *83*, 6468–6470.

[46] N. O. Nunez, P. Tartaj, M. Puerto Morales, P. Bonville, C. J. Serna. Yttria-coated FeCo magnetic nanoneedles. *Chem. Mater.*, **2004**, *16*, 3119–3124.

[47] C. Desvaux, C. Amiens, P. Fejes, P. Renaud, M. Respaud, P. Lecante, E. Snoeck,

B. Chaudret. Multimillimetre-large superlattices of air-stable iron-cobalt nanoparticles. *Nature Materials*, **2005**, *4*, 750–753.

[48] M. F. Casula, G. Concas, F. Congiu, A. Corrias, A. Falqui, G. Spano. Near equiatomic FeCo nanocrystalline alloy embedded in an alumina aerogel matrix: microstructural features and related magnetic properties. *J. Phys. Chem. B*, **2005**, *109*, 23888–23895.

[49] M. F. Casula, A. Corrias, G. Paschina. FeCo-SiO$_2$ nanocomposite aerogels by high temperature supercritical drying. *J. Mater. Chem.*, **2002**, *12*, 1505–1510.

[50] A. F. Gross, M. R. Diehl, K. C. Beverly, E. K. Richman, S. H. Tolbert. Controlling magnetic coupling between cobalt nanoparticles through nanoscale confinement in hexagonal mesoporous silica. *J. Phys. Chem. B*, **2003**, *107*, 5475–5482.

[51] W. S. Seo, J. H. Lee, X. Sun, Y. Suzuki, D. Mann, Z. Liu, M. Terashima, P. C. Yang, M. V. McConnell, N. D. G., H. Dai. FeCo/graphitic-shell nanocrystals as advanced magnetic-resonance-imaging and near-infrared agents. *Nature Materials*, **2006**, *5*, 971–976.

[52] S. Besson, T. Gacoin, C. Jacquiod, C. Ricolleau, J.-P. Boilot. 3D periodic arrays of nanoparticles inside mesoporous silica films. *Mat. Res. Soc. Symp. Proc.*, **2002**, *707*.

[53] S. Besson, T. Gacoin, C. Ricolleau, C. Jacquiod, J.-P. Boilot. 3D quantum dot lattice inside mesoporous silica films. *Nano Lett.*, **2002**, *2*, 409–414.

[54] V. Della Savia, M. C. Marchi, E. H. Otal, B. Bozzano, G. Soler-Illia. Tuned photoluminescence emission of CdS dots embedded in mesoporous silica, EMRS Spring Meeting. **2005**.

[55] M. Wark, H. Wellmann, J. Rathousky. Homogeneously distributed CdS and CdSe nanoparticles in thin films of mesoporous silica. *Thin Solid Films*, **2004**, *458*, 20–25.

[56] A. V. Kouzema, M. Fröba. Cd$_{1-x}$Mn$_x$S diluted magnetic semiconductors as nanostructured guest species in mesoporous thin-film silica host media. *Adv. Funct. Mater.*, **2005**, *15*, 168–172.

[57] J. P. Waters, D. Smyth-Boyle, K. Govender, A. Green, J. Durrant, P. O'Brien. Simple CVD routes towards infiltration of mesoporous TiO$_2$. *Chem. Vap. Deposition*, **2005**, *11*, 254–260.

[58] D. Buso, P. Falcaro, S. Costacurta, M. Guglielmi, A. Martucci, P. Innocenzi, L. Malfatti, V. Bello, G. Mattei, C. Sada, H. Amenitsch, I. Gerdova, A. Haché. PbS-doped mesostructured silica films with high optical nonlinearity. *Chem. Mater.*, **2005**, *17*, 4965–4970.

[59] G. Soler-Illia, E. L. Crepaldi, D. Grosso, D. Durand, C. Sanchez. Structural control in self-standing mesostructured silica oriented membranes and xerogels. *Chem. Commun.*, **2002**, 2298–2299.

[60] P. Innocenzi, P. Falcaro, D. Grosso, F. Babonneau. Order-disorder transitions and evolution of silica structure in self-assembled mesostructured silica films studied through FTIR spectroscopy. *J. Phys. Chem. B*, **2003**, *107*, 4711–4717.

Chapter 5

Advanced characterisation by synchrotron radiation

Abstract

Synchrotron radiation is a powerful tool to investigate the ordered mesophase of mesostructured films, in particular when in situ small-angle X-ray scattering experiments are performed during dip-coating. The first part of this chapter deals with mesostructured hafnium oxide films, showing a tunable steady state which was very sensitive to relative humidity changes in the deposition chamber. Experiments on this tunable state allowed to draw important conclusions on the self-organisation process of micelles as an entropy-driven process towards order. Moreover, the synchrotron X-rays used for these experiments were used to selectively disrupt the mesostructure, providing a means to write a pattern on mesostructured hafnium oxide films. In the second part of the chapter an in situ experiment involving simultaneous small-angle X-ray scattering and infrared spectroscopy established a new technique capable of providing both structural (mesophase symmetry and degree of order) and spectroscopic (solvent evaporation, polycondensation) information on self-assembling mesostructured silica films. This technique can be adapted also to the study of biological systems involving simultaneous chemical and structural evolution.

5.1 Mesostructured hafnium oxide

The synthesis of mesoporous films is generally regarded as a combination of inorganic sol-gel and colloidal chemistry, consisting in the so-called templated self-assembly of organised matter. Due to the many factors cooperating during the short time of a typical synthesis (usually a few seconds or minutes by dip- or spin-coating), it is difficult to sort out the role of each synthesis and processing parameter. This requires characterisation techniques which are not always readily available, such as synchrotron facilities for in situ studies.[1] To date, the main phenomenology of the self-assembly process can be considered to be well understood, and the term "evaporation-induced self-assembly"[2] is now commonly used to describe the triggering of self-assembly by the process of solvent evaporation, eventually leading to the formation of organised porous materials.[3]

Nevertheless, how organic micelles self-organise into a periodical array and why some ordered structures are obtained instead of others within the same chemical system are still open questions to which a satisfying answer has not yet been provided. Different unit cells and symmetry groups are reported in the literature, the most common being cubic $Im\bar{3}m$, $Fm\bar{3}m$, $Pm3n$, $Ia\bar{3}d$, 2d-hexagonal $p6mm$, 3d-hexagonal $P6_3/mmc$ and rhombohedral $R\bar{3}m$. In our case, we obtained either orthorhombic $Fmmm$ or very ordered tetragonal $I4/mmm$ symmetries simply varying the chemical composition of the inorganic framework, adding methyl groups (Chapter 3), but no answer could be provided as to why one structure is obtained instead of other possible structures. Whereas the difference between cylindrical micelles packing into hexagonally-arranged bundles and spherical micelles packing into three-dimensional structures can be explained by simple geometric factors such as the packing factor g (see Chapter 1, from page 23 onwards), the factors influencing the final symmetry group of micelle packing remain largely unknown.

We found ourselves to cope with this issue when we endeavoured to synthesise mesoporous hafnium oxide (*hafnia*) films, due to the interesting findings during in situ experiments conducted at the SAXS beamline at the Elettra synchrotron facility. In particular, as-deposited mesostructured hafnia films showed to be highly sensitive, in terms of self-organisation of micelles and degree of order, to processing parameters such as relative humidity (RH) and external factors such as the synchrotron high-flux X-rays used in the in situ experiments. In particular, in a first set of experiments, mesostructured hafnia films were found to be highly sensitive to relative humidity changes in the deposition chamber, in the so-called tunable steady state. Changes in the relative humidity resulted in mesostructure assembly and de-assembly, observing order-to-disorder reversible transitions. Furthermore, a second set of experiments revealed the local mesostructure disruption and restoration, induced by changes in the X-ray incident beam. These phenomena were observed for the first time and were explained by entropic effects.

5.1.1 Experimental setup

Synthesis of mesostructured hafnia films   Mesoporous hafnia films can be synthesised starting from chloride precursors as the Hf source. Generally, the synthetic strategies to mesoporous transition metal oxides do not make use of alkoxides because of their high reactivity, which hinders the formation of an ordered mesostructure. Therefore, metal chlorides are often used as the precursors either

in hydrolytic or in non-hydrolytic synthetic pathways (see page 13). In the present case, the templating agent was triblock copolymer Pluronic F127 and the Hf source was anhydrous hafnium chloride ($HfCl_4$). A solution was prepared by the slow addition of $HfCl_4$ to an ethanol-surfactant mixture, water was then added to this sol under stirring. The molar ratios were:

$$HfCl_4 : EtOH : Pluronic\ F127 : H_2O = 1 : 40 : 0.005 : 20.$$

The substrates, previously cleaned with hydrofluoric acid, water, EtOH, and acetone, were dip-coated in the fresh solution (no ageing). The films were prepared by dip-coating in a controlled-humidity environment at the pulling rate of 2.3 mm·s^{-1} at room temperature. The RH during deposition was set to $\approx 20\%$. After deposition, the film were allowed to dry for about 1 minute, until the drying line disappeared. Soon afterwards, the films were exposed to high RH (≈ 80–90%) for around 5 seconds, after which they were aged for 24 hours in a controlled humidity environment (RH=50%) In previous experiments on mesostructured transition metal oxides (titania, zirconia, hafnia), exposure to high RH was found to affect critically both the optical quality of the films and the degree of order of the resulting mesostructure. This fact has been explained by the extended inorganic polycondensation induced by water which ensures homogeneity of the inorganic framework, resulting in less optical scattering and better optical quality. The high degree of order observed in films treated with high RH has been attributed to the creation of a well-defined "hybrid interface" between the organic (template) and the inorganic (framework) phases (see from page 45 onwards for details).

Experimental set-up at the SAXS beamline   The dip-coating system was a home-made device customised for in situ experiments (see Chapter 2, page 75 for a detailed description of the dip-coater used, and see page 72 for the SAXS beamline). In this dip-coater, the substrate is mounted on a fixed sample holder, whereas the beaker containing the solution is moved using a linear guide which is remotely controlled from the experimental hutch. Using this configuration, the sample remains in a fixed position to ensure that the selected area of the film is irradiated during the whole experiment, while the solution can be raised and lowered for the dip-coating process. The dip-coating apparatus is provided with a closed deposition chamber so that RH can be maintained constant during film deposition or varied through an air flow.

Because the deposition process requires RH to be varied in a wide range (20% to $\sim 80\%$ to 50%) the dip-coating chamber needs to be connected with a system flowing air with controlled RH. This is accomplished connecting a tube from an air compressor (dry air, RH$\approx 0\%$) to a bubbler containing hot water: in this way the air flow becomes saturated with water vapour (see Figure 5.1). In order to control RH, the tube with saturated water vapour is connected by means of a T-connector with a dry-air tube originating from the air compressor: the two air flows (high-RH and low-RH) are mixed and a tube carries the mixed flow from the T-connector to the dip-coating chamber. Two valves control the high-RH (through the bubbler) and low-RH (from compressor) air flows, so that humidity can be readily varied by opening or closing the two "wet air" and "dry air" valves. A humidity probe inside the deposition chamber is connected to a hygrometer in the control room, therefore an accurate readout of RH can be provided throughout the whole experiment.
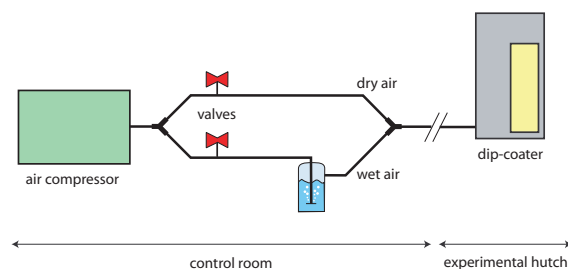
Figure 5.1. *Scheme of the mass flow controller used to vary RH in the deposition chamber during the in situ experiments on mesostructured hafnia films.*
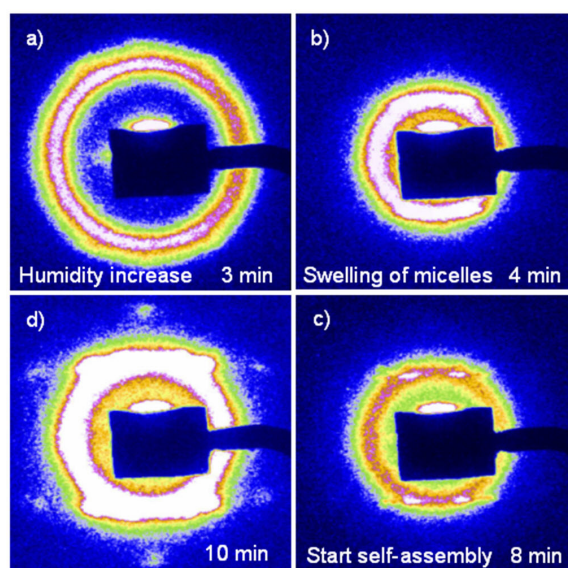

Figure 5.2. *Self-organisation induced by water adsorption and micelle swelling. The SAXS patterns are recorded at different times after dip-coating. The increase in humidity (a) causes the micelles to swell (b) and after 8 minutes self-organisation into an ordered mesophase is observed (c). In subfigure (d) the first order of diffraction spots is saturated and appears as a bright ring.*

5.1.2   In situ SAXS measurements

After preliminary experiments conducted to test the dip-coating and the controlled RH flow apparatus, we chose to work in transmission mode (incident X-ray impinging at 90° on the film), therefore we chose a thin substrate, i.e. a 50 μm-thick Si wafer. A Si substrate with this thickness is difficult to work with because it is very fragile and even the small pressure of tweezers can break it into fragments. However, thin Si substrates provide better conditions than cover microscope slide glass, in terms of signal-to-noise ratio.

Acquisition of SAXS diffraction patterns was started during dip-coating, as soon as the substrate was outside the solution vessel, with an integration time of 500 ms and a delay time of 1 s between two acquisitions. Because the storage time of a TIFF image file containing the two-dimensional scattering pattern to the computer hard drive is 500 ms, the total time between two acquisition was 2 s.

Figure 5.2 contains four selected diffraction patterns showing the different degrees of organisation in the mesostructured hafnia film. Figure 5.2 a shows the

as-deposited film: a diffraction ring appeared a few seconds after dip-coating, indicating the presence of disordered micellar structures with monodisperse size in the meso range. This phase is stable because in other experiments we have kept this disordered state by simply keeping low RH inside the deposition chamber. When high-RH air was pumped inside the deposition chamber ("dry air" valve close and "wet air" valve fully open) a sudden increase in the RH in the deposition chamber was displayed in the hygrometer readout (from 20% to ~80% in a few seconds). At the same time, a marked shrinkage in the diffraction ring could be observed (Figure 5.2 b). This ring shrinkage was attributed to the increase in the size of the disordered micelles in the film (as the micelles swell, the diffraction ring decreases its diameter), which was attributed to water adsorption in the hydrophilic crown at the organic-inorganic hybrid interface.[4,5] It is interesting to note that this structural change took place exactly when humidity increase was recorded by the hygrometer. The duration of the "wet air" flow was approximately 5 seconds and both valves were closed soon after the diffraction ring shrinkage was observed.

A few minutes later, diffraction spots appeared, accompanied by a decrease in RH (Figure 5.2 c). This decrease in RH was likely caused by the diffusion of vapours out of the deposition chamber: because the deposition chamber is not airtight, the system equilibrates with the external environment in the absence of a controlled air flow. After a few minutes we observed the presence of well-defined spots and no diffraction ring (Figure 5.2 d). This indicates a high degree of self-organisation if we consider that the setup is in transmission mode: the mesostructure not only has out-of-plane order, commonly observed in mesostructured films, but it also shows high in-plane order.

This experiment was repeated few times in order to ensure reproducibility, each time obtaining the same results. Interestingly, we noted that the disorder-order transition induced by RH changes is reversible: changing the humidity inside the deposition chamber from low to high RH (and vice versa) resulted in self-organisation and loss of order. These changes could be repeated a few times (at least 5 cycles) with little or no apparent loss of degree of order in the resulting mesostructure at high RH.

These experimental results show that micelle swelling is directly related to organisation and rearrangement of the mesophase. The overall process is shown in Figure 5.3: the precursor solution is an isotropic sol in which block copolymer concentration c is lower than the critical micelle concentration cmc. When the solvent evaporates, c becomes greater than cmc and micelles self-assemble. At this stage, when a weakly condensed film is formed, a disordered array of micelles can self-organise upon increase of the external humidity. Water absorption by the micelles causes their swelling and this effect pushes the system to self-organise. This phenomenon can be related to the *tunable steady state* (TSS), a particular state of as-deposited mesostructured films that allows for micellar reorganisation by external sources (such as RH, as in this case).[6] The system can therefore be driven towards order as long as the flexibility of the oxide network allows a rearrangement of the templating micelles when their size increases. When inorganic condensation leads to the formation of large oxo or hydroxo clusters, the TSS ends. The possibility of rearranging (order-disorder transitions) was observed for up to 5 hours since film deposition, which indicates a much longer TSS than that observed in silica (lasting approximately a few minutes). This is due to much faster condensation rate in TEOS than in chloride precursors.[7]
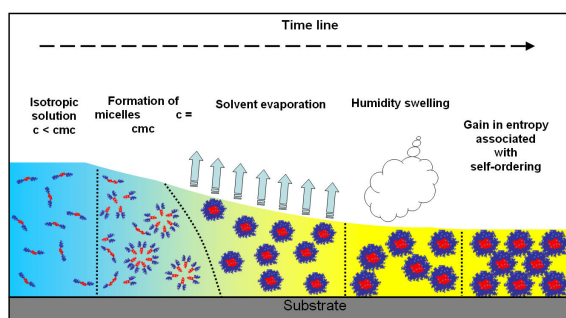
Figure 5.3. *Scheme of the self-organisation process taking place during the experiments on a mesostructured hafnia film.*

5.1.3 Mesophase symmetry

After these in situ experiments, mesostructured hafnia films were synthesised off-line following the same experimental procedure, including the treatment at high RH leading to self-organisation as observed in the in situ experiments, and were thermally treated at 150°C for 1 hour in order to stabilise the inorganic framework and inhibit further mesophase rearrangements (i.e. suppress the TSS). These films were studied by grazing incidence SAXS (GISAXS). The grazing incidence configuration was chosen because the films were deposited on thick substrates (500 μm-thick Si wafers). The GISAXS pattern of a mesostructured hafnia film treated at 150°C is shown in Figure 5.4 c.

The diffraction patterns were simulated with the software Nanocell, a code written for Mathematica® which outputs the simulated SAXS pattern of a mesostructure given initial parameters such as mesophase symmetry, d-spacings and experimental setup (see Chapter 2 on page 78). Different space groups were considered for the simulations, varying systematically the orientation of the unit cell with respect to the substrate. The only matching simulated patterns were found to be (1) a rhombohedral unit cell with $R\bar{3}m$ symmetry, oriented with the [111] 3-fold axis perpendicular to the substrate, (2) a face-centred cubic cell with $Fm\bar{3}m$ symmetry having the same orientation with respect to the substrate as the rhombohedral cell (Figure 5.5). In fact, these two descriptions are fully compatible, because a rhombohedral unit is the primitive cell of a FCC cell, provided that the angle between the axes of the rhombohedral cell α is 60°.[8]

The thermal shrinkage perpendicular to the substrate causes the variation of the cell parameters (axis a and angle α) if we consider the rhombohedral $R\bar{3}m$ cell; alternatively, if we consider the cubic $Fm\bar{3}m$ cell, a contraction along the [111] direction (i.e. 3-fold axis) is observed. These two descriptions can be considered equivalent, although the most correct choice from a crystallographic viewpoint is considered the rhombohedral $R\bar{3}m$ symmetry. The ordered mesophase can also be thought as composed of three different micelle planes in a close-packing stack with packing factor f=0.74 (see Figure 5.5).

The calculation of cell parameters for both as-deposited and thermally treated mesostructured hafnia films was done utilising a Mathematica® code written for the rhombohedral $R\bar{3}m$ symmetry, which is reported in detail in Appendix A. The cell parameters for the as-deposited film were $a = (20.8 \pm 2.0)$ nm and $\alpha = (62.0 \pm 6.2)°$. The constants for the film treated at 150°C were
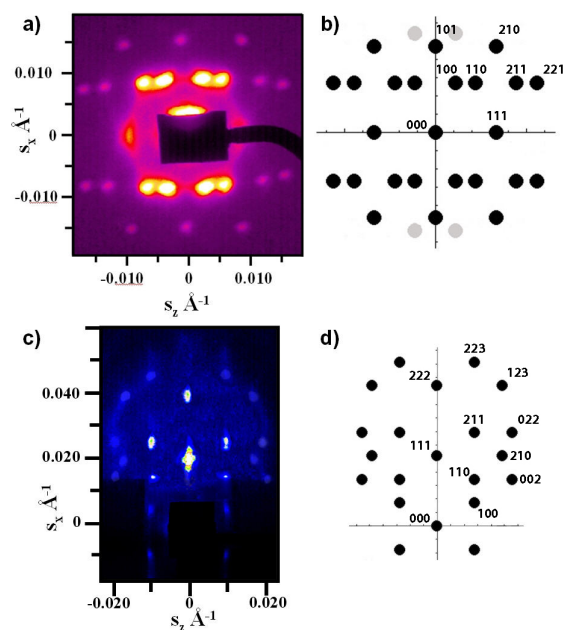
Figure 5.4. *Transmission mode SAXS pattern of an as-deposited hafnia film (a) and results of a Nanocell simulation using a $R\bar{3}m$ rhombohedral unit cell (b). Grazing incidence SAXS (GISAXS) pattern of a hafnia film treated at 150°C (c) and its Nanocell simulation for the same $R\bar{3}m$ unit cell (d).*

$a = (14.3 \pm 1.4)$ nm and $\alpha = (83.2 \pm 8.3)°$. This confirmed that a uniaxial shrinkage occurred during thermal treatment along the [111] direction. Even after a weak thermal treatment, the mesophase retained the same symmetry: this is in agreement with our findings because a uniaxial contraction of a rhombohedral cell along the [111] direction does not reduce the symmetry operations of this type of structure. Considering the reported error bar, the angle $\alpha = 62°$ calculated for the rhombohedral cell of the as-deposited film is close to that of the undistorted $Fm\bar{3}m$ cell, that is $\alpha = 60°$. This confirms that the rhombohedral structure of the as-deposited film can be described by a cubic $Fm\bar{3}m$ cell.

5.1.4 Self-organisation as an entropy-driven process

Self-assembly and self-organisation The synthesis of mesoporous films utilised in these experiments is known as evaporation-induced self-assembly (EISA). The underlying concept is that solvent evaporation causes an increase in the nonvolatile (inorganic and organic) species. This triggers both self-assembly because of the increase in surfactant concentration above the critical micellar concentration, and formation of bridged oxo or hydroxo species by the metal centres. However, this is in partial disagreement with our findings: the TSS duration is on the order of hours because the formation of an ordered structure can be observed even minutes after dip-coating. At the same time, we can reasonably assume that all solvent evaporated in the first minutes after dip-coating; therefore, the formation of an ordered mesostructure might appear uncorrelated to solvent evaporation. A solution to this contrast can be found in the fact that self-assembly describes the formation of micellar structures by the aggregation of surfactant molecules when $c > cmc$: this is observed in the first seconds after deposition, when solvent evaporation takes place
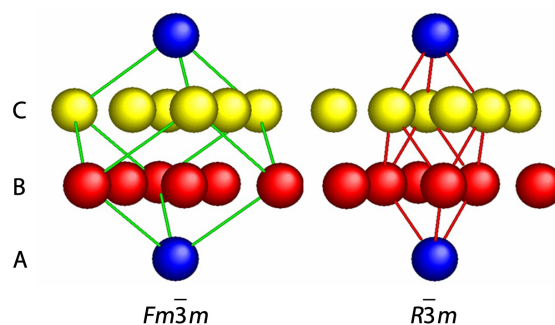
Figure 5.5. *Scheme of the mesostructure symmetry in a mesostructured hafnia film. Micelles are represented by the yellow spheres, the face-centred cubic $Fm\bar{3}m$ cell is drawn in green and the primitive rhombohedral $R\bar{3}m$ cell is drawn in red. Micelle layers (A, B, C) are shown on the left of the image.*

and can be considered to cause the self-assembly of disordered micelles (formation of a ring, Figure 5.2 a). We now consider another phenomenon, *self-organisation*, as separate from *self-assembly*, in that it involves the formation of ordered arrays of pre-formed micelles. Therefore a first conclusion is: self-assembly is triggered by solvent evaporation, but self-organisation is *not*, as we observe self-organisation even hours after solvent evaporation.

Another case where self-organisation is observed as a distinct phenomenon from self-assembly can be found in the synthesis of mesoporous tin oxide reported by Hillhouse's research group (see Chapter 1, page 52).[9] In this work, a mesostructure in tin oxide films is formed upon ageing at high RH for hours (delayed humidity treatment, DHT). In the cited publication the authors state "it is clear that the self-assembly process reported here is not EISA [. . .] The mesostructure is formed while the films are still in the high-humidity environment, in the presence of excess water incorporated during the DHT". However, no structural information on self-assembly regarding the first seconds and minutes after dip-coating is reported (interestingly, the authors state that in situ studies were planned at the time of writing).

Our experiments suggest a thermodynamic interpretation of the self-organisation of the process (self-assembly is still assumed to be driven by solvent evaporation). The film in its TSS is in a temporal window in which randomly distributed micelles can self-organise in ordered arrays in the absence of solvent evaporation. If we model the micelles as spheres in which interpenetration is forbidden and the interaction energy is zero, the enthalpy variation of the system during self-assembly can be neglected. This is a reasonable assumption because the spheres are not in contact due to inorganic species which condense on micellar hydrophilic surfaces.[10] It is important to stress that even if enthalpy plays an important role during solvent evaporation, once the micelles and the solid inorganic network are formed, we assume that it does not change significantly. As a consequence, only the *entropic* term in $\Delta G = \Delta H - T\Delta S$ should be responsible for the decrease in ΔG that pushes the system to self-organisation.

The counterintuitive idea that entropy is the source of order can be used to explain the experimental findings in the tunable state of self-organisation. In fact, the loss in entropy with ordering is more than compensated for by the gain in

entropy due to the increase in free volume* of the ordered films.[11,12] The swelling of micelles increases the volumetric fraction of the organic mesophase within the film, so that the micelles have lower translational entropy. In these conditions, the only way to maximise the entropy of the whole system is to increase free volume by packing the micelles in an ordered structure. Self-organisation is thus an entropy-driven process, provided that the inorganic framework is flexible enough to allow micelle self-organisation.

Degree of order   In mesostructured films the complexity of self-assembly and self-organisation is increased by the presence of inorganic NBBs that condense on the micelle surface to form a solid network. Self-organisation can be achieved provided that the condensation rate of the building units (inorganic or hybrid organic-inorganic) is much slower than the kinetics of micelle formation and ordering.[13] To date, the strong tendency for condensation of non-siliceous systems has been considered as the main obstacle to obtain highly ordered self-assembled mesostructured thin films.[14] The high reactivity of transition metal oxide precursors toward hydrolysis and condensation increases the extent of uncontrolled phase separation between the organic and the inorganic components. The tendency for condensation in sol-gel systems is a function of the atomic number of elements with the same valence, for instance, Si < Ti < Zr < Hf.[7,15,16] According to this theory, mesostructured hafnium oxide films should possess a lower degree of order than titanium or zirconium oxide mesostructured films. In a work by Brezesinski et al. the high reactivity of hafnia was identified as the cause of the lack in mesostructural order of the mesostructured hafnia films.[17] On the contrary, our findings show that self-assembled mesoporous hafnium oxide films have been reproducibly synthesised showing an unexpected high degree of order—even in-plane order was observed, which is a notable exception in the field of mesostructured films. Therefore our results suggest that other parameters than metal centre reactivity should be taken into account when predicting the degree of order in a mesostructured film.

5.1.5   Mesostructure damage induced by synchrotron radiation

During the in situ experiments on mesostructured hafnia, an interesting phenomenon was observed whilst the preview of SAXS acquisition was operating. The preview system allows to continuously capture and display SAXS patterns on the computer monitor, so as to follow structural evolutions in real-time. The interesting observation was that the mesostructure degree of order seemed to decrease with time: at first this was related to a change in RH that caused a mesophase transition towards a disordered state. A few adjustments were made to the experiments, for example RH was controlled more carefully, the solution vessel was removed from the chamber in order to prevent solvent and HCl vapours to come into contact with the film. However, the disordering phenomena remained and no satisfying explanation was provided. We had a clue of what was happening when we moved the sample a few mm to one of its sides, so that the incident beam probed a different region of the film: the mesostructure in this "new region" had a much higher degree of order with respect to the "old region", comparable to the degree of order of the "old region" before observing mesostructure degradation. We found that this

---

*The free volume is defined as the volume within which a given hard sphere centre can move without requiring alteration of the other sphere positions.

degradation was fully reproducible in mesostructured hafnia films: mesostructure degradation took place only in the irradiated area and did not affect the adjacent regions, so that after observing mesostructure degradation an ordered region could be detected simply by shifting the sample.

The most likely reason of this local mesostructure disruption phenomenon was assumed to be radiation damage induced by the incident X-rays. The preview system requires that a X-ray beam impinge on the sample continuously—typical values are 500 ms acquisition and 1500 ms delay, controlled by a fast shutter, therefore the sample was continuously irradiated with the incident X-ray beam. Furthermore, the effect was not observed when few acquisitions were made instead of many continuous acquisitions in preview mode. Another effect was visible in the irradiated samples: at the end of the experiments the films presented a change in colour in the irradiated region. In transmission mode, this was a spot having the same shape of the incident X-ray beam, whereas in grazing incidence configuration this was a stripe extending on the whole film.

We can formulate two hypotheses: (1) The block copolymer backbones are chemically broken by the incident X-rays, so that the micelles are disrupted. (2) A local increase in temperature causes micelles to de-assemble: *cmc* is highly sensitive to temperature and even a slight increase in temperature may cause the loss of self-assembly conditions, favouring the "single-chain state" of the unassembled molecules of surfactant. A number of publications support the first conclusion. In particular, damage to biological structures is often induced by high-flux synchrotron radiation due to the formation of free radicals from water molecules. The free radicals act as initiators for the de-polymerisation of these biological species (e.g. lipids, proteins).[18–20] Experiments are planned to elucidate the origin of this radiation damage.

To check whether the radiation affects the surface roughness or the total thickness of the film, we compared the morphology of both the irradiated and the unirradiated areas, finding that the roughness increases after X-ray irradiation (sampled on 10 different points on the surface). We related such difference with a loss of micellar organisation, which takes place without any crack or damage to the sample. Also, thickness is not affected by radiation: an atomic force microscopy (AFM) image was taken close to the border between the irradiated and unirradiated regions (Figure 5.7) showing no substantial difference on the average height of the surface. This provided evidence that the observed disordering phenomenon can be related to mesostructure de-assembly and does not consist in a mere ablation of the film from the substrate.

Even more surprisingly, we found that this mesostructure deformation was *reversible*. An experiment, the results of which are reported in Figure 5.6, showed that after mesostructure disruption, if the film was let at controlled RH for a certain amount of time with no irradiation, the mesostructure recovered a high degree of order. In other words, the mesostructure underwent a process of *re-organisation*.

The possibility of cycling between ordered and disordered states was confirmed by further experiments, although some hysteresis was observed, so that the phenomenon cannot be said to be fully reversible. This is caused by the stiffening of the inorganic network (polycondensation) which puts a time limit on the TSS and inhibits further micellar rearrangements. The mesostructure disruption-restoration phenomenon is of particular importance because—as in the previous case when mesophase changes were induced by RH variations—the self-organisation pro-
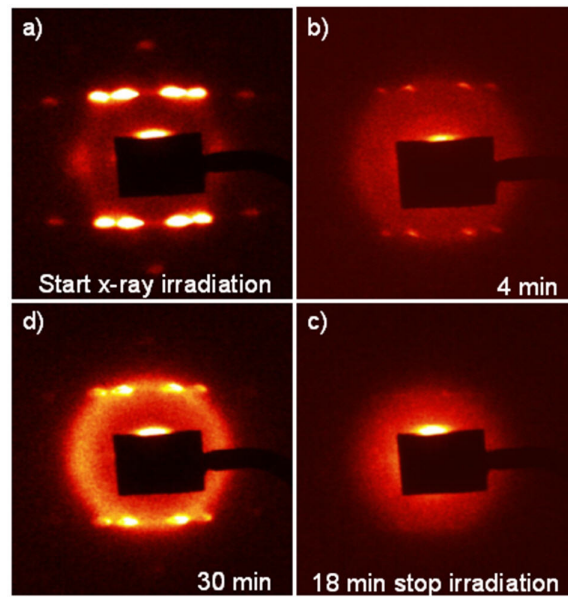
Figure 5.6. *Mesostructure disruption observed by SAXS in transmission mode. A high flux radiation causes a highly-organised hafnia film with a R̄3m symmetry (a) to lose partially the degree of order (b). After a few minutes of irradiation the order is almost completely lost (c) but an ordered mesostructure is observed again after switching off the X-ray flux and maintaining the film in stationary humidity and temperature conditions for some time (d).*
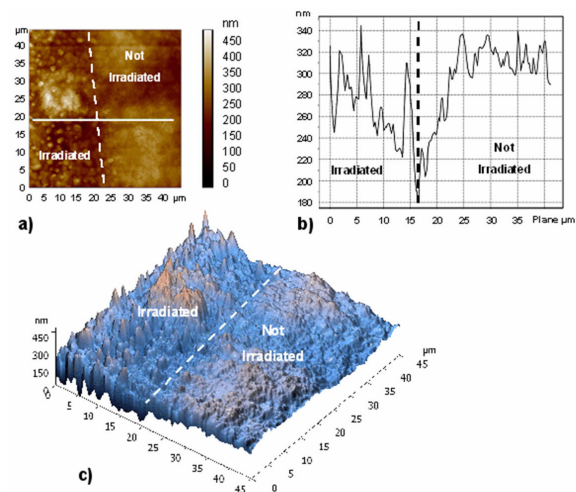

Figure 5.7. *AFM image of a mesostructured hafnia film after X-ray irradiation taken in contact mode on a film treated at 60°C for 40 min. Plane (a) and perspective (c) views of the boundary region between irradiated and unirradiated areas. The depth profile of the hafnia film across the irradiation boundary is also shown (b).*

cess is never pushed by solvent evaporation but it appears another entropy-driven process. If we admit that mesostructure disruption is caused by cleavage of the copolymer backbones, mesostructure restoration can be thought of involving the diffusion of undamaged block copolymer molecules and the self-assembly and self-organisation of new supramolecular structures. This is the most reasonable assumption but to date no experimental data have been acquired to provide support to this hypothesis, and further experiments are planned. In any case, self-assembly and self-organisation appear as separate mechanisms leading to different phenomena: formation of micelles and formation of order, respectively.

To sum up, self-assembly and self-organisation in mesostructured films appear as highly tunable processes: evaporation-induced self-assembly drives the templating species toward a first intermediate stage when micelles are formed upon solvent evaporation and increase of nonvolatile media. The flexible nature of the inorganic network, which is composed of oxo and hydroxo bridges and has a low degree of condensation, allows for micellar self-organisation driven by external parameters. These can be changes in relative humidity of high-flux X-rays, and they lead to entropic effects.

A direct application of this phenomenon is the possibility of inducing disordered regions into the mesostructured film with the aim, for example, to produce materials with a gap in the refractive index (after calcination, the mesoporous unirradiated region is expected to have a lower refractive index than the irradiated nonporous region). It is also possible to perform several write-erase cycles as long as the degree of condensation of the film allows mobility of the micelles. These changes in the mesophase become permanent once the mesostructure is thermally stabilised.

5.2   A novel simultaneous FTIR-SAXS in situ technique

5.2.1   Introduction

As we have seen, the formation of an ordered mesophase is a process resulting from a delicate balance between kinetic and thermodynamic effects. In the synthesis of mesoporous silica films, the ageing of the precursor solution affects the size of the inorganic starting units, resulting in higher or lower degrees of order. We have also shown that using hybrid silica precursors (organo-alkoxysilanes) it is possible to modify both the thermodynamics and the kinetics in mesostructure organisation, obtaining a mesophase with a higher degree of order.

Several new techniques have been developed with the purpose of studying the phenomena occurring during self-assembly. The most popular among these techniques is in situ SAXS using synchrotron radiation, which is used to assess structural changes and rearrangements in the mesostructure. However, this technique yields only structural information such as presence of an ordered mesostructure and the degree of order, but it does not allow collecting time-resolved data about the chemistry of the process. Spectroscopic information can be obtained only ex-situ in as-prepared films, but in this case the chemical information regarding the phenomena occurring during the dip-coating stage is lost. The self-assembly of the inorganic units is guided by the self-assembly of the amphiphilic block copolymer; this process is triggered by the fast solvent (water, ethanol) evaporation, which also pushes the inorganic oligomers close together and favours polycondensation.

Therefore, the lack of a spectroscopic in situ technique appears to be a weak point in the understanding of the process that leads to the formation of a mesostructure.

Several groups have successfully coupled SAXS with other in situ techniques to correlate the structural data and the chemical processes that occur during dip-coating. An interesting example is reported by Grosso and coworkers who performed time-resolved in situ GISAXS using synchrotron light combined with interferometry measurements on a mesostructured silica film templated by cetyltriethyl-lammonium bromide (CTAB).[21] This combined interferometry-SAXS technique allowed correlating mesophase organisation occurring during dip-coating with film thickness. Here, the evolution of thickness with time follows a triple regime, where a first rapid evaporation step is attributed to the evaporation of (mainly) ethanol; the second step is slower, due essentially to the departure of water, and a third regime involves the loss of residual water and ethanol molecules. However, the departure of solvent molecules is just an educated guess which is not supported by experimental data.

Another example of a combined technique was reported by Doshi et al. who performed time-resolved in situ GISAXS using synchrotron light combined with gravimetric analysis to study the self-assembly of a slowly evaporating cast film.[22]

In another work, in situ Karl Fischer titration measurements were used to estimate the content of water in as-deposited silica films as a function of RH, obtaining increasing $h = [H_2O]/[Si]$ values with increasing RH values, even though titrations were not made on films but on solutions, which were assumed to be representative of the corresponding films.[6]

Mass spectrometry of vapour fraction, Karl Fischer titration, ellipsometry and interferometry data acquired in situ on mesostructured titania thick films were used to follow the evolution of volatile species and film composition.[23] Crossing these data led to the comprehension of the role of each variable involved in the self-organisation. Thanks to these central works, fundamental solution and processing parameters, such as the manifold role of water and the importance of the modulable steady state, could be sorted out.

Time-resolved Fourier transform infrared spectroscopy (FTIR) can be used to monitor the chemical processes during self-assembly in cast films.[24] The FTIR technique is very effective to monitor the evaporation of water and ethanol and the polycondensation reactions in silica mesostructured materials, and it can be extended to the in situ analysis of mesostructured films during dip-coating, provided that the infrared spectrometer can be coupled with the dip-coater. In order to obtain structural and chemical information on the physicochemical processes occurring during dip-coating, we decided to couple the FTIR and the SAXS techniques at the synchrotron facility.

In this section we show the results of a preliminary experiment at the Elettra synchrotron, in which simultaneous in situ FTIR and SAXS experiments were conducted in order to study and correlate the structural and the chemical processes occurring during dip-coating of mesostructured silica films. The purpose of this section is to illustrate the potential of this technique in the study of mesostructured films, therefore we have selected as an example an experiment conducted on meso-structured organosilica films obtained from MTES-TEOS solutions (see page 96).

5.2.2 Experimental setup

The experimental setup is shown in Figure 5.8. FTIR measurements were performed using the optical system of the IRCube™ interferometer.[25] This is a very compact commercial spectrometer working in the middle infrared (mid-IR) spectroscopy produced by Bruker Optics, a Ge/KBr beamsplitter and a Globar source. The setup was designed so that simultaneous FTIR and SAXS measurements could be performed on the film, using the conventional Globar source and the synchrotron radiation, respectively. The optical components of the FTIR spectrometer were set up in a way that a parallel IR beam was focused by an additional external parabolic mirror onto the sample in transmission mode at normal incidence. The transmitted signal was reflected by a flat mirror towards another elliptical mirror focusing the signal onto the liquid nitrogen-cooled PC-MCT detector.

A GISAXS configuration requires that the correct angle of incidence be set carefully: the optimum angle of incidence α_i is slightly above the critical angle of a mesostructured film ($\approx$0.2°), and small variation off this optimum angle can deeply affect the GISAXS measurements, because too small α_i can cause total reflection, whereas too large α_i can cause insufficient scattering. The dip-coater's sample holder can be rotated so that the angle of incidence of the impinging X-ray can be readily varied. However, because accessing the experimental hutch during the experiment is forbidden, the sample holder rotation must be performed before the experiment is started. Therefore, we used a freshly-coated mesostructured silica sample for the adjustment of α_i, which was then left unaltered during the whole experiment by fixing the sample holder.

Following this experimental configuration, the incident IR and X-ray beams probe the very same region of the sample. The interval between successive acquisitions was set to 2 seconds, since from preliminary tests we evaluated that the time scale of these processes is on the order of seconds both in terms of self-assembly and chemical processes. The sequence of GISAXS and FTIR spectra acquisitions was simultaneously launched immediately after the solution vessel was lowered. FTIR data were collected using the Bruker OPUS™ software, and each FTIR spectrum was obtained by averaging 16 interferograms collected at a resolution of 8 cm^{-1}. Background was collected prior to each measurement session as the average of 100 spectra on a bare silicon substrate. The procedure followed in GISAXS data acquisition was the same used for the in situ experiments conducted on mesostructured hafnia films described in the previous section.

Here we present an in situ FTIR-SAXS experiment using the hybrid silica precursor solution described in Chapter 3. These hybrid systems are synthesised from a precursor solution where the Si source is a mixture of tetraethoxysilane (TEOS) and methoxy-triethoxysilane (MTES), and the templating agent is block copolymer Pluronic F127. The precursor solution was prepared as described previously: a solution containing 3.08 mL of EtOH, 2.84 mL of TEOS, 1.42 mL of MTES and 0.355 mL of HCl 0.768 M was stirred for 45 minutes, then added to a solution containing 15 mL of EtOH, 1.3 mL of HCl 0.057 M and 1.3 g of F127. The final solution was stirred for 10 minutes and used for dip-coating. The substrate was a 400 μm-thick, p-type B-doped (100) Si wafer. This substrate was chosen because it ensures transparency in the mid-IR range. Simultaneous FTIR and SAXS acquisitions were launched after lowering the solution vessel (pulling rate 2.3 mm·s^{-1}), as soon as the silicon substrate was fully coated. The relative humidity in the deposition chamber was set to $\approx$10% and kept throughout the whole experiment.
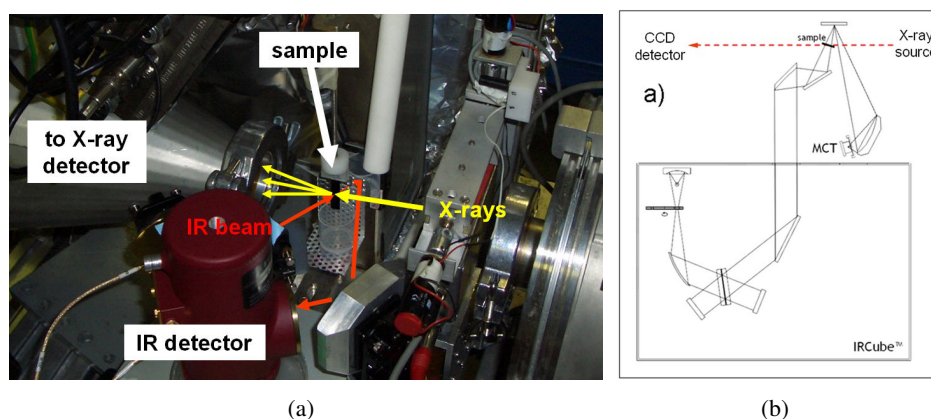
(a)   (b)

Figure 5.8. *(a) Photograph of the experimental simultaneous FTIR-SAXS apparatus at the Austrian SAXS beamline at the Elettra synchrotron. (b) Scheme of the experimental setup used for the experiments.*

5.2.3   Results

GISAXS results   Figure 5.9 shows the time-resolved GISAXS two-dimensional patterns recorded at intervals of two seconds. The first significant snapshots are shown, from $t = 0$ (acquisition start) to $t = 20$ sec. Another GISAXS snapshot, recorded at $t = 20$ min, is also reported. The GISAXS and FTIR spectra were recorded for times as long as 40 minutes from dip-coating. Within this time frame the RH inside the deposition chamber was maintained constant at $(10\pm5)\%$. The GISAXS patterns show that in the first 8 seconds no organisation of the mesophase takes place, and after 10 seconds the presence of a ring (dotted line in the figure) indicates that organisation is starting, even though a mesophase is still not well defined. At 12 seconds the detection of well-defined spots reveals the presence of an ordered mesostructure. Whereas these spots increase in sharpness and intensity with time, negligible changes are observed at times longer than 20 seconds. These in situ GISAXS data show only two diffraction spots, which makes the unambiguous identification of the space group impossible. This is because the integration time for each GISAXS pattern was limited to 500 ms in order to have good time resolution, and higher-order diffraction spots requiring longer integration times could not be recorded. Nevertheless, these spots could be used to quantify the degree of order of the mesophase.

FTIR results   Figure 5.10 shows the FTIR spectra recorded simultaneously with the GISAXS patterns shown in Figure 5.9. What was expected to be detected in this experiment was the kinetics of solvent and water evaporation. The raw spectra shown in Figure 5.10 appear well resolved and exhibit good signal-to-noise ratio even if they have not been smoothed and the baseline was not corrected. We can recognise two main regions, at high wavenumbers (3700–2800 cm^{-1}) and at low wavenumbers (1700–800 cm^{-1}) where different chemical species overlap. The first stages of the FTIR spectra are dominated by the vibrational modes attributed to ethanol. Its intense signals at 2973, 2927, 2885 cm^{-1}, at 1460–1270 cm^{-1}, at 1088 and 1050 cm^{-1}, and at 880 cm^{-1} allow following solvent evaporation with time. After about 8 seconds this process is completed (the residual signal after 10 seconds
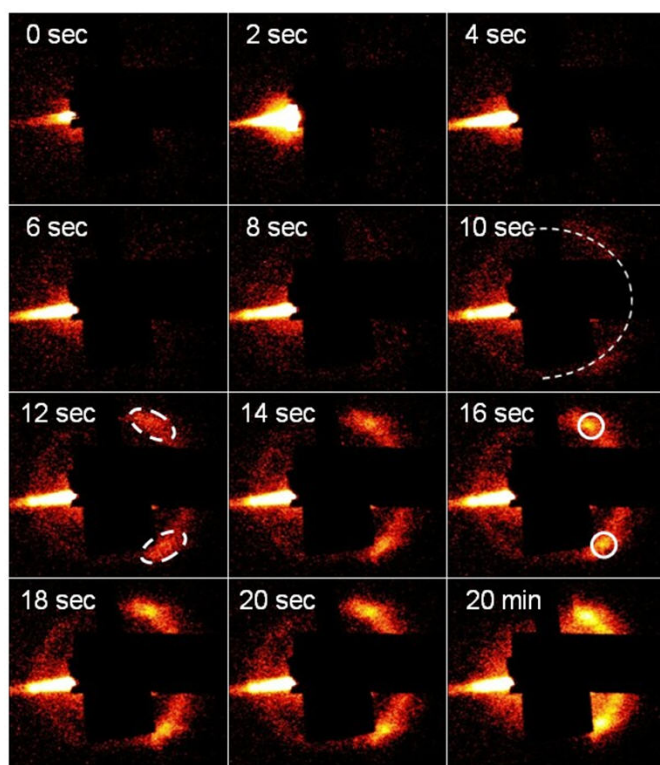
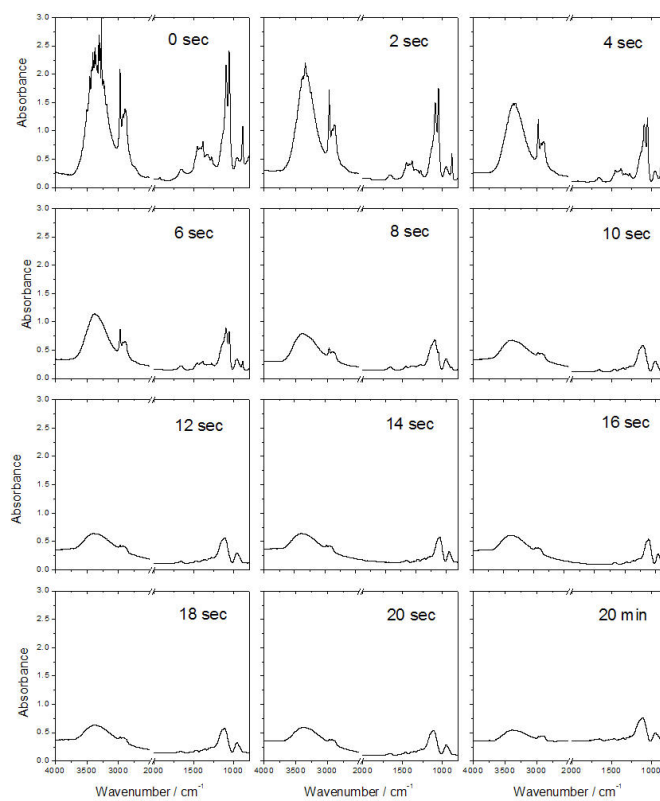**Figure 5.9.** *GISAXS images recorded at different times after the dip-coating.*

Figure 5.10. *Transmission FTIR absorption spectra recorded at different times after the dip-coating.*

observed in the C-H stretching region around 2700–3000 cm^{-1} was assigned to the surfactant). The decrease in intensity of the 1640 cm^{-1} vibrational mode attributed to water ($\nu_b(H_2O)$) indicates that evaporation of water is also observed in the first seconds of dip-coating, but after this fast initial stage, a slower evaporation rate follows.

5.2.4 Comparison between SAXS and FTIR data

Figure 5.11 shows the content of ethanol and water in the film as a function of time (dip-coating was set as $t = 0$). The content of ethanol and water was estimated considering the areas subtended by two specific absorption bands that are well resolved and not overlapped with other vibrational modes, that is around 880 and 1640 cm^{-1} for ethanol and water, respectively. The area of the two bands was plotted as a function of time, assuming that the areas at $t = 0$ correspond to 100% water and 100% ethanol in the film (Figure 5.11). From this graph, the evaporation of ethanol appears fast, following a linear trend: after 10 seconds the residual ethanol in the film can be approximated to 0%, so that the process can be considered to be complete. The evaporation of water has a more complex trend: (1) a fast initial evaporation in the first 2–3 seconds, similar to ethanol, is followed by (2) a slower intermediate stage between 3 and 6 sec, (3) then a third phase of water enrichment between 6 and 10 sec is followed by (4) another evaporation stage from 16 sec onwards. More specifically, at $t = 10$ sec, around 30% of the initial water is present in the film, whereas all ethanol is evaporated. At $t = 20$ sec, around 20% of the initial water is still detected in the film. The water enrichment stage (third point in the above description) is attributed to the polycondensation reactions that occur after ethanol evaporation.

From SAXS data, we observe that the organisation into an ordered mesophase starts only after ≈10 seconds. Comparing these structural data with the spectroscopic data from FTIR measurements, we infer that an ordered mesostructure is formed after ethanol evaporation is complete and 70% water has departed from the film: at this stage the SAXS diffraction spot intensity increases showing a sigmoidal trend with time (Figure 5.12). This graph shows the change in the average
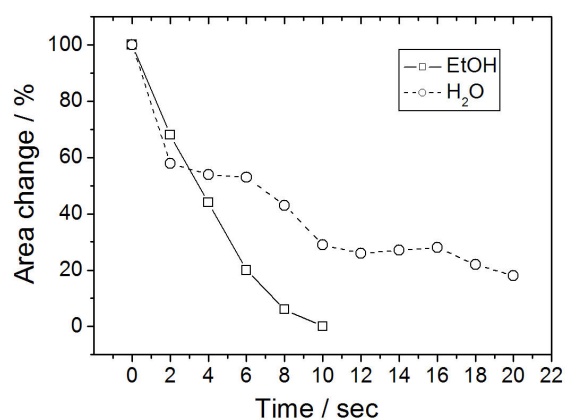

Figure 5.11. *Change in the area of the 1640 cm^{-1} band attributed to water and of the 880 cm^{-1} band attributed to ethanol as a function of time after dip-coating (compare with Figure 5.12).*
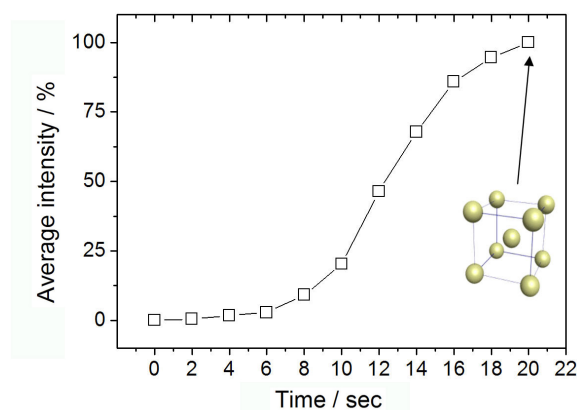
Figure 5.12. *Average intensity of a GISAXS diffraction spot as a function of time (compare with Figure 5.11).*

intensity of a SAXS diffraction spot (upper spot in the snapshots of Figure 5.9) as a function of time. To obtain these data, the intensity of a selected diffraction spot in a SAXS pattern was calculated as the average intensity calculated in a rectangular area around the spot, composed of 1148 pixels. These data were used for a semi-quantitative evaluation, in that they could not be normalised with respect to the intensity of the background. Nevertheless, this gave a reliable indication on how the mesophase evolves with time. The appearance of the asymmetric stretching ν_{as}(Si-O-Si) band at around 1100 cm^{-1} in the FTIR spectra after 10–12 seconds indicates that at this time polycondensation reactions are almost complete and an interconnected silica network is formed. However, at this stage the silica network is still flexible enough to allow spatial reorganisation of micelles.

It is worth to underline that mesophase organisation starts only after ethanol evaporation. This is in agreement with the well-known role of ethanol evaporation as the trigger to mesophase formation. However, as described in the introduction, there is no direct evidence of this, as there is no in situ experiment in the literature capable of providing simultaneous unambiguous spectroscopic and structural information on mesophase organisation. Therefore, this is the first time that evidence is provided regarding the time correlation between ethanol evaporation and mesophase formation. This is the most exciting finding of this FTIR-SAXS in situ technique.

The major advantage of this simultaneous FTIR and SAXS analysis is the possibility to discriminate between the evaporation rates of ethanol (or any other solvent) and water, as well as to obtain semiquantitative data that can be examined in the light of the structural data provided by SAXS. The discrimination between different chemical species can be readily attained by FTIR spectra, in that vibrational modes are attributed to different chemical species (e.g. the amount of free water, the degree of condensation of the inorganic walls).

In this case, it has been proved that the formation of an organised mesophase occurs after all ethanol and 70% of water have evaporated. At this stage, the presence of water in the film can be estimated as $h = $ [H$_2$O]/[Si] = 1.56 (i.e. 30% of h in the precursor solution), which is close to the values obtained through other in situ experimental techniques such as Karl-Fischer titration (see 5.2.1). This leads us to identify another application of the present technique, in that the water content

(expressed as h) can be simply calculated from FTIR data, and correlated quantitatively with RH. As we have said, this has been done previously by means of rough estimates from Karl-Fischer titrations on cast films rather on dip-coated films, but the FTIR-SAXS technique can be considered to be more accurate.

Other advantages of this FTIR-SAXS combined technique are that it is not invasive, can be applied to thin films instead of thick films, cast drops or solutions, and does not require altering the chemistry of the self-assembling system. It also takes into account the presence of atmospheric water, as a reference background is taken prior to each FTIR measurement session.

5.2.5   Conclusions and future perspectives

To summarise, in this section we have presented a new combined FTIR-SAXS technique, where the IR source is a conventional Globar lamp, and monochromated synchrotron light is used as the X-ray source. This technique has been applied to the study of mesostructured silica films with an experiment providing insight on basic structural and chemical aspects of self-assembly. In particular, the formation of an ordered mesostructure was correlated with ethanol and water evaporation from the film; the amount of residual water within the film was estimated to be 30% in correspondence to the onset of self-assembly, whereas all ethanol had already departed from the film. This opens a new affordable route to calculate the amount of residual solvent in the films. Besides, the presence of water vapour in the environment is accounted for by the background spectrum, acquired prior to each measurement session. This is important because a direct correlation can be established between the RH value in the deposition chamber and the quantity of water present in the film: this correlation was previously studied in the literature, but using experimental techniques based on thick films or cast films, whose behaviour is quite different from thin films obtained by dip-coating and studied by in situ SAXS. Recently, we have reproduced the same triple regime in the in situ FTIR study on a ethanol or water-ethanol evaporating cast droplet.[26] In this work, multiple evaporation steps were associated to water adsorption from the atmosphere, and water and ethanol evaporation from the droplet. It will be interesting to compare the data obtained in this study with those provided by FTIR-SAXS in situ measurements and those found in the literature.

More in general, the simultaneous recording of different types of information allows correlating different phenomena that contribute to a complex process such as self-assembly in mesostructured films. This is particularly relevant when the kinetics of some chemical processes can affect other chemical or physical processes involved in the phenomenon.

Another main advantage provided by the in situ FTIR-SAXS technique is that different vibrational modes can be attributed to different species in the FTIR spectra (provided that they do not overlap). Therefore, different chemical information can be obtained, for example on water content, ethanol content, inorganic condensation, copolymer content, etc. This experiment also opens many important perspectives in other research areas, for example the real-time and in situ detection of the radiation damage induced in biological systems and tissues.

References

[1] P. Dubček. Nanostructure as seen by the SAXS. *Vacuum*, **2005**, *80*, 92–97.

[2] C. J. Brinker, Y. Lu, A. Sellinger, H. Fan. Evaporation-induced self-assembly: Nanostructures made easy. *Adv. Mater.*, **1999**, *11*, 579–585.

[3] G. Soler-Illia, E. L. Crepaldi, D. Grosso, C. Sanchez. Block copolymer-templated mesoporous oxides. *Curr. Opinion Colloid Interf. Sci.*, **2003**, *8*, 109–126.

[4] E. L. Crepaldi, G. Soler-Illia, D. Grosso, C. Sanchez. Nanocrystallised titania and zirconia mesoporous thin films exhibiting enhanced thermal stability. *New J. Chem.*, **2003**, *27*, 9–13.

[5] G. Soler-Illia, E. Scolan, A. Louis, P.-A. Albouy, C. Sanchez. Design of meso-structured titanium oxo based hybrid organic-inorganic networks. *New J. Chem.*, **2001**, *25*, 156–165.

[6] F. Cagnol, D. Grosso, G. Soler-Illia, E. L. Crepaldi, F. Babonneau, H. Amenitsch, C. Sanchez. Humidity-controlled mesostructuration in CTAB-templated silica thin film processing. The existence of a modulable steady state. *J. Mater. Chem.*, **2003**, *13*, 61–66.

[7] C. J. Brinker, G. W. Scherer. *Sol-gel science: The physics and chemistry of sol-gel processing*. Academic Press, San Diego, 1992.

[8] C. Hammond. *Introduzione alla cristallografia*. Zanichelli, Bologna, 1994.

[9] C. N. Urade, H. W. Hillhouse. Synthesis of thermally stable highly ordered nanoporous tin oxide thin films with a 3D face-centered orthorhombic nanostructure. *J. Phys. Chem. B*, **2005**, *109*, 10538–10541.

[10] C. Sanchez, G. Soler-Illia, F. Ribot, D. Grosso. Design of functional nano-structured materials through the use of controlled hybrid organic-inorganic interfaces. *C. R. Chimie*, **2003**, *6*, 1131–1151.

[11] A. G. Yodh, K.-H. Lin, J. C. Crocker, A. D. Dinsmore, R. Verma, P. D. Kaplan. Entropically driven self-assembly and interaction in suspension. *Phil. Trans. R. Soc. Lond. A*, **2001**, *359*, 921–937.

[12] H. N. W. Lekkerkerker, A. Stroobants. Ordering entropy. *Nature*, **1998**, *393*, 305–306.

[13] Q. Huo, D. I. Margolese, U. Ciesla, D. G. Demuth, P. Feng, T. E. Gier, P. Sieger, A. Firouzi, B. F. Chmelka, F. Schüth, G. D. Stucky. Organization of organic molecules with inorganic molecular species into nanocomposite biphase arrays. *Chem. Mater.*, **1994**, *6*, 1176–1191.

[14] G. Soler-Illia, C. Sanchez, B. Lebeau, J. Patarin. Chemical strategies to design textured materials: From microporous and mesoporous oxides to nanonetworks and hierarchical structures. *Chem. Rev.*, **2002**, *102*, 4093–4138.

[15] J. Livage, M. Henry, C. Sanchez. Sol-gel chemistry of transition metal oxides. *Prog. Solid State Chem.*, **1988**, *18*, 259–341.

[16] J. D. Wright, N. A. J. M. Sommerdijk. *Sol-gel materials: Chemistry and applications*. CRC Press, Boca Raton, 2001.

[17] T. Brezesinski, B. Smarsly, K. Iimura, D. Grosso, C. Boissiàˆre, H. Amenitsch, M. Antonietti, C. Sanchez. Self-assembly and crystallization behavior of mesoporous, crystalline HfO_2 thin films: A model system for the generation of mesostructured transition-metal oxides. *Small*, **2005**, *1*, 889–898.

[18] J. Murray, E. Garman. Investigation of possible free-radical scavengers and metrics for radiation damage in protein cryocrystallography. *J. Synchrotron Rad.*, **2002**, *9*, 347–354.

[19] A. Cheng, M. Caffrey. Free radical mediated X-ray damage of model membranes. *Biophys. J.*, **1996**, *70*, 2212–2222.

[20] A. G. Richter, J. Wang, R. Guico, K. Shull. X-radiation damage of polymer thin films. *Argonne Nat'l Laboratory Report*, **1999**.

[21] D. Grosso, F. Babonneau, P.-A. Albouy, H. Amenitsch, A. R. Balkenende, A. Brunet-Bruneau, J. Rivory. An in situ study of mesostructured CTAB-silica film formation during dip coating using time-resolved SAXS and interferometry measurements. *Chem. Mater.*, **2002**, *14*, 931–939.

[22] D. A. Doshi, A. Gibaud, V. Goletto, M. Lu, H. Gerung, B. Ocko, S. M. Han, C. J. Brinker. Peering into the self-assembly of surfactant templated thin-film silica mesophases. *J. Am. Chem. Soc.*, **2003**, *125*, 11646–11655.

[23] E. L. Crepaldi, G. Soler-Illia, D. Grosso, F. Cagnol, F. Ribot, C. Sanchez. Controlled formation of highly organized mesoporous titania thin films: from mesostructured hybrids to mesoporous anatase TiO_2. *J. Am. Chem. Soc.*, **2003**, *125*, 9770–9786.

[24] P. Innocenzi, T. Kidchob, J. Mio Bertolo, M. Piccinini, M. Cestelli Guidi, A. Marcelli. Time-resolved infrared spectroscopy as an in situ tool to study the kinetics during self-assembly of mesostructured films. *J. Phys. Chem. B*, **2006**, *110*, 10837–10841.

[25] http://www.brukeroptics.com/ftir/ircube.htm (accessed December 2007).

[26] P. Innocenzi, L. Malfatti, S. Costacurta, T. Kidchob, M. Piccinini, A. Marcelli. Evaporation of ethanol and ethanol-water mixtures studied by time-resolved infrared spectroscopy. *Submitted to J. Phys. Chem. A*.

Appendix A

Mesophase symmetry and cell parameter calculation

A.1 Description of symmetry in mesoporous materials

Ordered mesoporous and mesostructured materials are characterised by the spatial periodicity of matter (inorganic walls, mesopores) similar to periodicity of atoms in a crystalline material. As a consequence, a notation already in use in crystallography was adopted to classify the periodicity of mesostructure. In this section we give a brief overview on the concepts revolving around symmetry in crystalline materials, introducing the Hermann-Mauguin notation of space groups which is used in the description of mesostructure.

Crystalline materials are characterised by a repetition in space of identical *unit cells*. Each unit cell exists in an identical orientation and is related to the next one by translation along one of three *crystallographic axes*. We can choose any point in this pattern and then proceed to mark all other points which have an identical environment: this geometrical array of points defines a *lattice*. There are 14 lattice types in three-dimensional space (Bravais lattice types), which are P triclinic, P,C monoclinic, P,C,I,F orthorhombic, P,I tetragonal, P,I,F cubic, rhombohedral, P hexagonal. The capital letters describe centring of the lattice. P: primitive, F: face-centred, I: body-centred, C: base-centred.

However, the complete symmetry of a structure is not defined by the lattice alone, since the arrangement of the atoms around each lattice point may also be symmetric. Therefore, each set of symmetry operations (or symmetry elements) about a point, without translational repetition, defines a *point group*. In other words, a unit cell is invariant under the operations that describe its point group. These point symmetry elements are *n*-fold rotational axes, reflection (mirror) planes, glide planes, inversion and screw operation. In three-dimensional space there are 32 point groups. Combined with the 14 translational elements (i.e. the Bravais lattice types), they give 230 *space groups*.

Different notations are possible to indicate the 230 space groups. The most commonly used in crystallography is the *Hermann-Mauguin* notation, which is also the most used in the structural description of mesoporous materials. The Hermann-Mauguin notation consists of a set of symbols. The first symbol describes the centring of the Bravais lattice (P, A, B, C, I, R or F). The next symbols describe the mirror perpendicular and the axes parallel to each symmetry direction. In case a mirror coexists with a symmetry axis in the same direction, the two symbols are separated by a fractional (/) sign. For example, $2/m$ describes a

monoclinic lattice with a two-fold rotational axis parallel to a mirror plane. The inversion operation, when present, is never indicated in the notation (except in the triclinic system, where it is the only symmetry element), but it is indicated by the combination of an axis and a mirror, as in this case. The Hermann-Mauguin symbols are in most cases written in their short form, for example *mmm* is written in place of $2/m\,2/m\,2/m$. Another example of a space group notation that we have encountered in this work is $Fm\bar{3}m$, which corresponds to a face-centred (F) cubic lattice with a 3-fold rotoinversion axis ($\bar{3}$), where a rotoinversion axis corresponds to a *n*-fold rotation operation followed by inversion.

A.2   Cell parameter calculation

This section provides detail on the methods adopted for cell parameter calculation in the study of a mesostructure with SAXS data. The starting point of such analysis is the attribution of a SAXS pattern to a symmetry group with *hkl* indexation of the diffraction spot. Next, the d-spacing values can be calculated by directly clicking on the diffraction pattern in the Fit2d GUI once the sample-to-detector distance is known (this is done in the calibration step, see Chapter 2).

If needed, the s_x and s_y coordinates of the spots in a SAXS pattern are also calculated. This is also accomplished with Fit2d: the x, y coordinates of each spot on the detector (expressed in pixels) are easily output by the software by direct clicking on the image in the GUI, and the s_x, s_y values are calculated with the calibration ring of the silver behenate standard (which is measured in each session). The ring corresponds to a known lattice constant, therefore the corresponding s_x and s_y values can be obtained by the fitting of the calibration ring with the equation of a circumference:

$$y = \frac{1}{\Delta s_y}\sqrt{\frac{1}{d^2} - x^2 \Delta s_x^2},\qquad\text{(A.1)}$$

where the values of Δs_x and Δs_y are the free parameters which are varied in the curve fitting. This is performed using Origin's "Advanced fitting tool" function with two free parameters (P1 and P2) using the expression:

y=(1/P2)*sqrt(*drs*-(x*P1)^2),

where *drs* is the squared reciprocal of the silver behenate d-spacing $1/d_{\text{AgBeh}}^2$, or 2.934079E-4. Figure A.1 shows the results of such fitting procedure.

Once these values have been obtained, they can be loaded in Mathematica® from a CSV (comma-separated values) file and analysed. The following equation is used:

$$\frac{1}{d_{hkl}^2} = \frac{h^2}{a^2} + \frac{k^2}{b^2} + \frac{l^2}{c^2}.\qquad\text{(A.2)}$$

where *h*, *k*, *l* are the Miller indexes relative to one spot, *d* is the d-spacing relative to that spot and *a*, *b*, *c* are the cell constant that have to be calculated. For each symmetry group, simpler equations can be derived (e.g. in cubic systems $a = b = c$, so that Equation A.2 can be simplified by $a = d\sqrt{h^2 + k^2 + l^2}$).

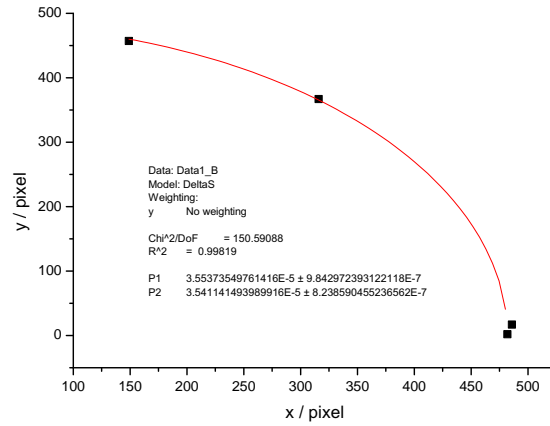In the following pages we report on the codes developed for Mathematica,

Data: Data1_B
Model: DeltaS
Weighting:
y   No weighting

Chi^2/DoF   = 150.59088
R^2   = 0.99819

P1   3.55373549761416E-5 ± 9.842972393122118E-7
P2   3.541141493989916E-5 ± 8.238590455236562E-7

Figure A.1. *Output of an Origin calibration procedure for the calculation of Δs_x and Δs_y*

describing examples of calculations for the cubic $Im\overline{3}m$, tetragonal $I4/mmm$ and rhombohedral $R\overline{3}m$ symmetries.

Cubic Regarding the $Im\overline{3}m$ cell, the cell parameter a is calculated as the average of the a values, calculated according to each experimental spot. In this case the only input values needed are the Miller indices and the d-spacing values for each spot:

$$a_{avg} = \frac{1}{n} \sum_{i=1}^{n} a_i \qquad (A.3)$$

where a_{avg} is the average value of the cell constant a calculated according to every spot, n is the number of experimental spot in the pattern and a_i is the cell constant value calculated according to the i-th spot. The error is calculated as the standard deviation:

$$\sigma = \sqrt{\frac{1}{n} \sum_{i=1}^{n} \left(a_i^{th} - a_i^{exp}\right)^2} \qquad (A.4)$$

where σ is the standard deviation, a_i^{th} is the cell constant calculated for a spot simulated using the equation $a = d\sqrt{h^2 + k^2 + l^2}$ and a_i^{exp} is the cell constant calculated for the experimental spot.

Tetragonal In the $I4/mmm$ case, the input values are x, y, d, h, k, l, ΔS_x, ΔS_y (the last two are needed to convert the spot positions in the detector to the corresponding s_x and s_y values. Once these values are loaded, a simulated diffraction pattern is created using Equation A.2. In the tetragonal case, $c = b$, so there are only two cell constant, a and c. We can therefore decouple the two a and c values and use the following equations:

$$S^2(a,c) = \sum_{i=1}^{n} \left[s_x^{i,exp} - s_x^{i,th}(a,h_i,k_i) \right]^2 + \sum_{i=1}^{n} \left[s_y^{i,exp} - s_y^{i,th}(c,l_i) \right]^2 = S^2(a) + S^2(c),$$

$$s_x^{i,th} = \frac{\sqrt{h_i^2 + k_i^2}}{a}, \ s_y^{i,th} = \frac{l_i}{c}$$

$$(A.5)$$

where $S^2(a,c) = S^2(a) + S^2(c)$ is an error function which quantifies the difference between the experimental spots $s_x^{i,exp}, s_y^{i,exp}$ and the simulated spots $s_x^{i,th}, s_y^{i,th}$. Different spot patterns are simulated according to different cell parameter values a and c which are varied in a given range. Thus, the error function $S^2(a,c)$ is sampled in this range and its minimum gives the best fit of the cell parameters. The difference with the previous case (cubic cell) is substantial: whereas in the $Im\overline{3}m$ case the cell parameter a was calculated from the single d-spacing values of each spot, in the $I4/mmm$ case the cell constants are calculated from the spot positions in the reciprocal space s_x and s_y.

Rhombohedral   The approach used for the $R\overline{3}m$ cell is similar: the cell parameters a and α are varied in the d-spacing equation valid for the rhombohedral system, which can be derived from Equation A.2:

$$\frac{1}{d_{hkl}^2} = \frac{(h^2 + k^2 + l^2)\sin^2\alpha + 2(hk + kl + lh)(cos^2\alpha - \cos\alpha)}{a^2(1 + 2\cos^3\alpha - 3\cos^2\alpha)}. \qquad (A.6)$$

An error function $f_{err}(a_i, \alpha_i)$ is defined as the difference between the theoretical and the experimental d-spacings calculated for each spot. This error function is then passed to a global error function $f_{global}(a, \alpha)$, which is defined as:

$$f_{global}(a, \alpha) = \sqrt{\frac{1}{n}\sum_{i=1}^{n} f_{err}^2(a_i, \alpha_i)} \qquad (A.7)$$

and which is minimised to find the best fit of the cell parameters a and α.

Cubic Im$\overline{3}$m

Input from file

```
Off[General::spell]
```

■ Import data as list into variable ImportedData

```
ImportedData = Import["C:\SAXS\dati.csv", "CSV"]
```

{{22, , , }, {1, 1, 0, 107.62}, {3, 2, 1, 41.43},
 {1, 3, 0, 49.42}, {1, 2, 1, 63.96}, {2, 0, 0, 80.98}, {1, 0, 1, 119.05},
 {-1, 1, 0, 119.37}, {2, 2, 2, 46.02}, {1, 1, 2, 67.78}, {0, 0, 2, 67.78},
 {1, 3, 2, 42.82}, {0, 3, 1, 51.43}, {0, 2, 2, 51.43}, {2, -1, 1, 68.91},
 {-1, 1, 2, 69.97}, {-1, 3, 0, 52.34}, {1, 2, 3, 52.34}, {-1, 3, 2, 44.56},
 {0, 1, 3, 53.76}, {-2, 2, 0, 59.56}, {-2, 2, 2, 48.73}, {2, -1, 3, 45.33}}

■ Moves values from ImportedData into variables Spots, h, k, l, dExp

```
Spots = ImportedData[[1]][[1]];
(* Assign first number of list to variable Spots (n. of spots in the .csv file) *)
For[i = 2, i ≤ Spots + 1,
 (* Start "for" cycle from second line, end at line Spots+1 *)
 h[i - 1] = ImportedData[[i]][[1]];      (* Assign Miller indexes values: h, k, l *)
 k[i - 1] = ImportedData[[i]][[2]];
 l[i - 1] = ImportedData[[i]][[3]];
 dExp[i - 1] = ImportedData[[i]][[4]];
 (* Assign experimental d-spacing values relative to each spot *)
 i ++]
```

- ## Show data in matrix form

      `MatrixForm[ImportedData]`

$$\begin{pmatrix} 22 & & & \\ 1 & 1 & 0 & 107.62 \\ 3 & 2 & 1 & 41.43 \\ 1 & 3 & 0 & 49.42 \\ 1 & 2 & 1 & 63.96 \\ 2 & 0 & 0 & 80.98 \\ 1 & 0 & 1 & 119.05 \\ -1 & 1 & 0 & 119.37 \\ 2 & 2 & 2 & 46.02 \\ 1 & 1 & 2 & 67.78 \\ 0 & 0 & 2 & 67.78 \\ 1 & 3 & 2 & 42.82 \\ 0 & 3 & 1 & 51.43 \\ 0 & 2 & 2 & 51.43 \\ 2 & -1 & 1 & 68.91 \\ -1 & 1 & 2 & 69.97 \\ -1 & 3 & 0 & 52.34 \\ 1 & 2 & 3 & 52.34 \\ -1 & 3 & 2 & 44.56 \\ 0 & 1 & 3 & 53.76 \\ -2 & 2 & 0 & 59.56 \\ -2 & 2 & 2 & 48.73 \\ 2 & -1 & 3 & 45.33 \end{pmatrix}$$

Cell parameter calculation

- ## Calculate a as the average of the single a values which are calculated from the d-spacing relative to each spot

```
For[i = 1, i ≤ Spots,
 a[i] = dExp[i] √h[i]^2 + k[i]^2 + l[i]^2 ;
 i++]
```

$$\mathtt{aAverage} := \frac{1}{\mathtt{Spots}} \sum_{i=1}^{\mathtt{Spots}} \mathtt{a[i]}$$

- ## Calculate the error on a as standard deviation of the single calculated a values

$$\mathtt{StdDev} = \sqrt{\frac{1}{\mathtt{Spots}} \sum_{i=1}^{\mathtt{Spots}} (\mathtt{a[i]} - \mathtt{aAverage})\text{^}2}$$

`11.2323`

Output solutions

```
Print["Solution: a = (", aAverage, "±", StdDev, ")Å"]
```

Solution: a = (163.353±11.2323)Å

Tetragonal I4/mmm

Input from file

```
Off[General::spell]
```

■ Import data as list into variable ImportedData

```
ImportedData = Import["C:\SAXS\inputtetra.csv", "CSV"]
```

{{15, 506, 186, 0.000053, 0.0000532}, {0, 0, 2, 498, 395},
 {0, 0, 4, 501, 603}, {0, 0, 6, 498, 812}, {1, 0, 1, 625, 376},
 {1, 0, 1, 385, 371}, {1, 0, 3, 623, 503}, {1, 0, 3, 385, 500},
 {1, 0, 5, 617, 712}, {1, 0, 5, 377, 704}, {2, 0, 4, 739, 606}, {2, 0, 4, 261, 601},
 {2, 0, 2, 742, 408}, {2, 0, 2, 266, 397}, {3, 0, 3, 871, 495}, {3, 0, 3, 144, 500}}

■ Move values from ImportedData into variables Spots, h, k, l, dExp

```
Spots = ImportedData[[1]][[1]];
(* First number of list is assigned to variable Spots (total n. of spots) *)
BCx = ImportedData[[1]][[2]];
BCy = ImportedData[[1]][[3]];
ΔSx = ImportedData[[1]][[4]];
ΔSy = ImportedData[[1]][[5]];
For[i = 1, i ≤ Spots,
 (* Begin "for" cycle at second line, end at line Spots+1 *)
 h[i] = ImportedData[[i + 1]][[1]];  (* Assign values to Miller indexes h, k, l *)
 k[i] = ImportedData[[i + 1]][[2]];
 l[i] = ImportedData[[i + 1]][[3]];
 xExp[i] = (ImportedData[[i + 1]][[4]] - BCx) * ΔSx;
 yExp[i] = (ImportedData[[i + 1]][[5]] - BCy) * ΔSy;
 i++]
```

```
Table[{xExp[i], yExp[i]}, {i, Spots}] (* Plot experimental data in a sx, sy graph *)
```

{{-0.000424, 0.0111188}, {-0.000265, 0.0221844}, {-0.000424, 0.0333032},
 {0.006307, 0.010108}, {-0.006413, 0.009842}, {0.006201, 0.0168644},
 {-0.006413, 0.0167048}, {0.005883, 0.0279832}, {-0.006837, 0.0275576},
 {0.012349, 0.022344}, {-0.012985, 0.022078}, {0.012508, 0.0118104},
 {-0.01272, 0.0112252}, {0.019345, 0.0164388}, {-0.019186, 0.0167048}}

ListPlot[Table[{xExp[i], yExp[i]}, {i, Spots}], PlotStyle → PointSize[0.02]]
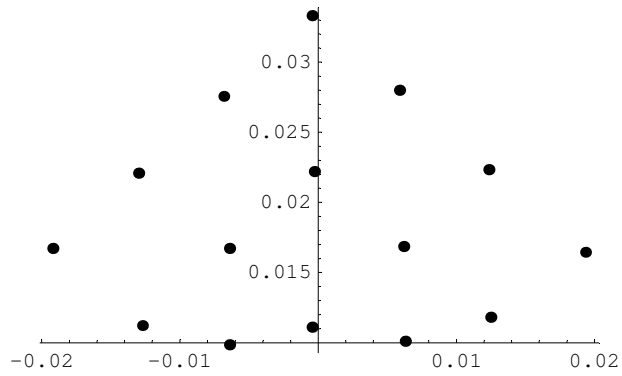
- Graphics -

■ Show data in matrix form

MatrixForm[ImportedData]

$$
\begin{pmatrix}
15 & 506 & 186 & 0.000053 & 0.0000532 \\
0 & 0 & 2 & 498 & 395 \\
0 & 0 & 4 & 501 & 603 \\
0 & 0 & 6 & 498 & 812 \\
1 & 0 & 1 & 625 & 376 \\
1 & 0 & 1 & 385 & 371 \\
1 & 0 & 3 & 623 & 503 \\
1 & 0 & 3 & 385 & 500 \\
1 & 0 & 5 & 617 & 712 \\
1 & 0 & 5 & 377 & 704 \\
2 & 0 & 4 & 739 & 606 \\
2 & 0 & 4 & 261 & 601 \\
2 & 0 & 2 & 742 & 408 \\
2 & 0 & 2 & 266 & 397 \\
3 & 0 & 3 & 871 & 495 \\
3 & 0 & 3 & 144 & 500
\end{pmatrix}
$$

Generic functions

- **Define an error function Sq[a_,c_] (actually its square) given by the quadratic difference between experimental d-spacing and theoretical d-spacing**

```
Clear[i]
```

$$xTh[i\_] = \frac{\sqrt{h[i]^2 + k[i]^2}}{a}$$

$$yTh[i\_] = \frac{l[i]}{c}$$

$$Sq[a\_, c\_] = \sum_{i=1}^{Spots} \left(Abs[xExp[i]] - \frac{\sqrt{h[i]^2 + k[i]^2}}{a} \right)^2 + \sum_{i=1}^{Spots} \left(yExp[i] - \frac{l[i]}{c} \right)^2$$

$$\frac{\sqrt{h[i]^2 + k[i]^2}}{a}$$

$$\frac{l[i]}{c}$$

$$4.29777 \times 10^{-7} + \left(0.019186 - \frac{3}{a}\right)^2 + \left(0.019345 - \frac{3}{a}\right)^2 + \left(0.012349 - \frac{2}{a}\right)^2 + \left(0.012508 - \frac{2}{a}\right)^2 +$$

$$\left(0.01272 - \frac{2}{a}\right)^2 + \left(0.012985 - \frac{2}{a}\right)^2 + \left(0.005883 - \frac{1}{a}\right)^2 + \left(0.006201 - \frac{1}{a}\right)^2 + \left(0.006307 - \frac{1}{a}\right)^2 +$$
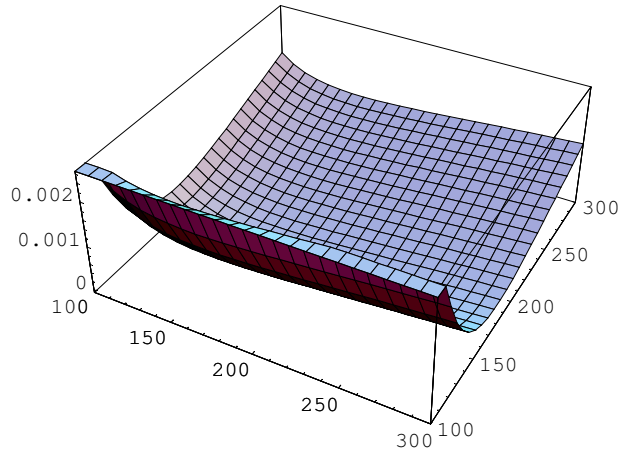
$$2\left(0.006413 - \frac{1}{a}\right)^2 + \left(0.006837 - \frac{1}{a}\right)^2 + \left(0.0333032 - \frac{6}{c}\right)^2 + \left(0.0275576 - \frac{5}{c}\right)^2 +$$

$$\left(0.0279832 - \frac{5}{c}\right)^2 + \left(0.022078 - \frac{4}{c}\right)^2 + \left(0.0221844 - \frac{4}{c}\right)^2 + \left(0.022344 - \frac{4}{c}\right)^2 +$$

$$\left(0.0164388 - \frac{3}{c}\right)^2 + 2\left(0.0167048 - \frac{3}{c}\right)^2 + \left(0.0168644 - \frac{3}{c}\right)^2 + \left(0.0111188 - \frac{2}{c}\right)^2 +$$

$$\left(0.0112252 - \frac{2}{c}\right)^2 + \left(0.0118104 - \frac{2}{c}\right)^2 + \left(0.009842 - \frac{1}{c}\right)^2 + \left(0.010108 - \frac{1}{c}\right)^2$$

```
Plot3D[Sq[a, c], {a, 100, 300}, {c, 100, 300}]
(* Plot Sq[a_,c_] with variable a and c *)
```
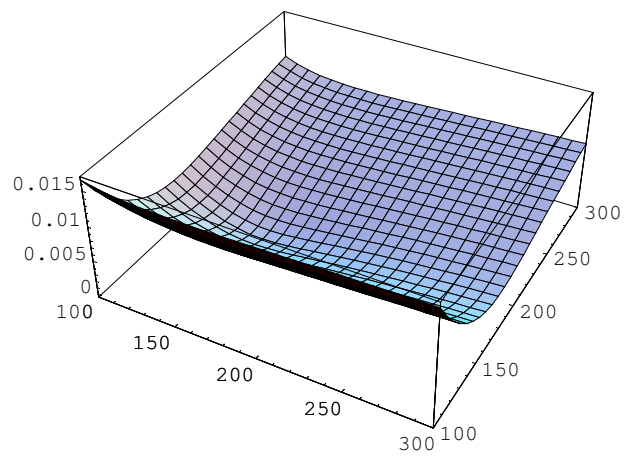

- SurfaceGraphics -

$$\texttt{ErrorFunction[a\_, c\_]} = \sqrt{\frac{1}{\texttt{Spots}} \; \texttt{Sq[a, c]}}$$

```
 (* Returns the error function given by the quadratic average of Sq[a_,c_] *)
```

$$\frac{1}{\sqrt{15}} \left(\sqrt{\left(4.29777 \times 10^{-7} + \left(0.019186 - \frac{3}{a} \right)^2 + \left(0.019345 - \frac{3}{a} \right)^2 + \right.} \right.$$

$$\left(0.012349 - \frac{2}{a} \right)^2 + \left(0.012508 - \frac{2}{a} \right)^2 + \left(0.01272 - \frac{2}{a} \right)^2 + \left(0.012985 - \frac{2}{a} \right)^2 +$$

$$\left(0.005883 - \frac{1}{a} \right)^2 + \left(0.006201 - \frac{1}{a} \right)^2 + \left(0.006307 - \frac{1}{a} \right)^2 + 2 \left(0.006413 - \frac{1}{a} \right)^2 +$$

$$\left(0.006837 - \frac{1}{a} \right)^2 + \left(0.0333032 - \frac{6}{c} \right)^2 + \left(0.0275576 - \frac{5}{c} \right)^2 + \left(0.0279832 - \frac{5}{c} \right)^2 +$$

$$\left(0.022078 - \frac{4}{c} \right)^2 + \left(0.0221844 - \frac{4}{c} \right)^2 + \left(0.022344 - \frac{4}{c} \right)^2 + \left(0.0164388 - \frac{3}{c} \right)^2 +$$

$$2 \left(0.0167048 - \frac{3}{c} \right)^2 + \left(0.0168644 - \frac{3}{c} \right)^2 + \left(0.0111188 - \frac{2}{c} \right)^2 +$$

$$\left. \left. \left(0.0112252 - \frac{2}{c} \right)^2 + \left(0.0118104 - \frac{2}{c} \right)^2 + \left(0.009842 - \frac{1}{c} \right)^2 + \left(0.010108 - \frac{1}{c} \right)^2 \right) \right)$$

```
Plot3D[ErrorFunction[a, c], {a, 100, 300}, {c, 100, 300}]
(* Plot the error function and find a minimum in a,c by visual inspection *)
```


- SurfaceGraphics -

Find and output solutions

```
Solutions = FindMinimum[ErrorFunction[a, c], {{a, 200, 100, 300}, {c, 200, 100, 300}}]
 (* Minimise error function to find best fit of a and c *)
```

{0.00164348, {a → 157.004, c → 178.235}}

```
aMinimum = a /. Solutions[[2, 1]]
cMinimum = c /. Solutions[[2, 2]]
```

157.004

178.235

```
ErrorMinimum = Solutions[[1]]
```

0.00164348

Errors

- **ErrorFunction represents the standard deviation calculated as quadratic sum of the differences between theoretical Sx and calculated Sx, and theoretical Sy and calculated Sy, divided by the number of spot, square root. Therefore its minimum represents the standard deviation of the distances in the reciprocal space between calculated and experimental spots.**

- **This returns a value in the reciprocal space. We can imagine this value as the radius of a circle representing the indetermination around the coordinates a, c. Therefore we calculate a, c corresponding to this error.**

```
aWorst = 1 / (1 / aMinimum + ErrorMinimum)
```

```
124.801
```

```
aMinimum
```

```
157.004
```

```
aError = Abs[aWorst - aMinimum]   (* Error on a *)
```

```
32.2027
```

```
cWorst = 1 / (1 / cMinimum + ErrorMinimum)
cMinimum
cError = Abs[cWorst - cMinimum] (* Error on c *)
```

```
137.854
```

```
178.235
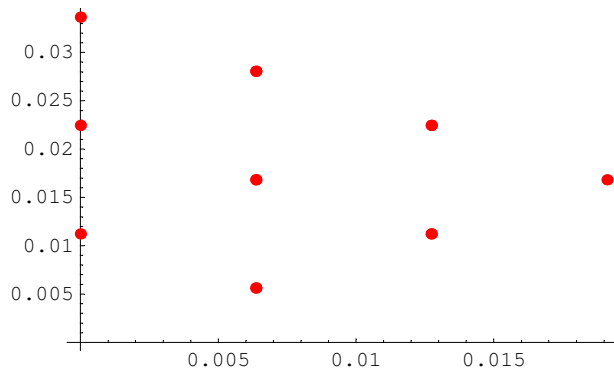```

```
40.3809
```

Some graphs

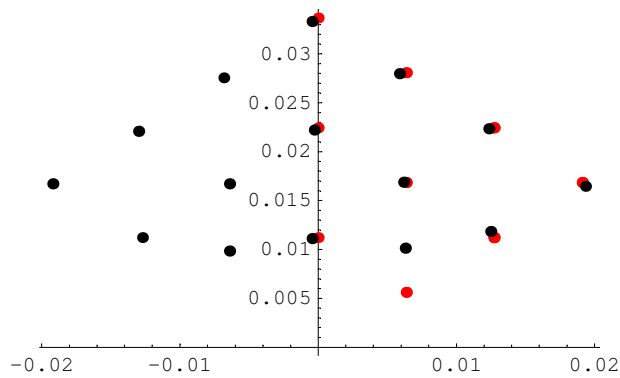- ## Simulated data from the best fit of (a,c)

```
p1 = ListPlot[Table[{ Sqrt[h[i]^2 + k[i]^2] / aMinimum , l[i] / cMinimum }, {i, Spots}],
   PlotStyle → {PointSize[0.02], Red}]
```

$$p1 = \text{ListPlot}\left[\text{Table}\left[\left\{\frac{\sqrt{h[i]^2 + k[i]^2}}{\text{aMinimum}}, \frac{l[i]}{\text{cMinimum}}\right\}, \{i, \text{Spots}\}\right],\right.$$
$$\left.\text{PlotStyle} \to \{\text{PointSize}[0.02], \text{Red}\}\right]$$

- Graphics -

- ## Simulated and experimental data are superimposed in a single graph

```
Show[p1, p2]
```

- Graphics -

Rhombohedral R$\overline{3}$m

Input from file

```
Off[General::spell]
```

▪ Import data as list into variable ImportedData

```
ImportedData = Import["C:\SAXS\R3m.csv", "CSV"]
```

{{3, , , }, {1, 0, 0, 165}, {1, 1, 1, 145}, {2, 1, 0, 90}}

▪ Move values from ImportedData into variables Spots, h, k, l, dExp

```
Spots = ImportedData[[1]][[1]];
(* First of list is assigned to variable Spots (n. of  spots in input CSV file) *)
For[i = 1, i ≤ Spots,
 (* Cycle "for" from second to Spots+1 line *)
 h[i] = ImportedData[[i + 1]][[1]];      (* Assign h, k, l *)
 k[i] = ImportedData[[i + 1]][[2]];
 l[i] = ImportedData[[i + 1]][[3]];
 dExp[h[i], k[i], l[i]] = ImportedData[[i + 1]][[4]];
 (* Assign values of experimental d values relative to each spot *)
 i ++]
```

▪ Show data in matrix form

```
MatrixForm[ImportedData]
```

$$\begin{pmatrix} 3 & & & \\ 1 & 0 & 0 & 165 \\ 1 & 1 & 1 & 145 \\ 2 & 1 & 0 & 90 \end{pmatrix}$$

Generic functions

▪ Function d^2 for rombohedral unit cell

```
dSquare[a_, α_, h_, k_, l_] = (a^2 (1 + 2 Cos[α]^3 - 3 Cos[α]^2)) /
  ((h^2 + k^2 + l^2) * Sin[α]^2 + 2 (h k + k l + l h) (Cos[α]^2 - Cos[α]))
```

$$\frac{a^2 \ (1 - 3 \, \text{Cos}[\alpha]^2 + 2 \, \text{Cos}[\alpha]^3)}{2 \ (h\,k + h\,l + k\,l) \ (-\text{Cos}[\alpha] + \text{Cos}[\alpha]^2) + (h^2 + k^2 + l^2) \, \text{Sin}[\alpha]^2}$$

- **Define an error function Sq[a_,c_] (actually its square) given by the quadratic difference between experimental d-spacing and theoretical d-spacing as calculated from the previous equation**

```
Err[a_, α_, h_, k_, l_] = dExp[h, k, l] - Sqrt[dSquare[a, α, h, k, l]]
```

$$\text{dExp}[h, k, l] - \sqrt{\frac{a^2\ (1 - 3\ \text{Cos}[\alpha]^2 + 2\ \text{Cos}[\alpha]^3)}{2\ (h\,k + h\,l + k\,l)\ (-\text{Cos}[\alpha] + \text{Cos}[\alpha]^2) + (h^2 + k^2 + l^2)\ \text{Sin}[\alpha]^2}}$$

Cell parameter calculation

- **Assign an error function to each spot based on the previous definition**

```
For[i = 1, i ≤ Spots,
 SpotErrorFunction[a_, α_][i] = (Err[a, α, h[i], k[i], l[i]]);
 i++]
```

- **Define a global error function (ErrorFunction) given by the quadratic sum of the single-spot error functions (SpotErrorFunction) divided by the number of spots (std. deviation)**
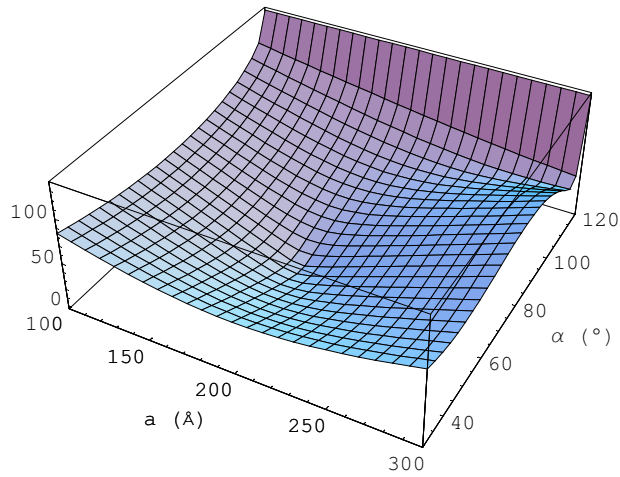
```
ErrF = 0;
Temp = 0;
For[i = 1, i ≤ Spots,
 Temp = ErrF;
 ErrF = Temp + SpotErrorFunction[a, α][i]^2;
 i++]
```

$$\text{ErrorFunction}[a\_, \alpha\_] = \sqrt{\frac{1}{\text{Spots}}\ \text{ErrF}}$$

$$\frac{1}{\sqrt{3}}\left(\sqrt{\left(\left(165 - \sqrt{a^2\ (1 - 3\ \text{Cos}[\alpha]^2 + 2\ \text{Cos}[\alpha]^3)\ \text{Csc}[\alpha]^2}\right)^2 + \right.}\right.$$

$$\left.\left(145 - \sqrt{\frac{a^2\ (1 - 3\ \text{Cos}[\alpha]^2 + 2\ \text{Cos}[\alpha]^3)}{6\ (-\text{Cos}[\alpha] + \text{Cos}[\alpha]^2) + 3\ \text{Sin}[\alpha]^2}}\right)^2 + \right.$$

$$\left.\left.\left(90 - \sqrt{\frac{a^2\ (1 - 3\ \text{Cos}[\alpha]^2 + 2\ \text{Cos}[\alpha]^3)}{4\ (-\text{Cos}[\alpha] + \text{Cos}[\alpha]^2) + 5\ \text{Sin}[\alpha]^2}}\right)^2\right)\right)$$

▪ Plot ErrorFunction

```
Plot3D[ErrorFunction[a, α Degree], {a, 100, 300},
 {α, 30, 120}, AxesLabel → {"a (Å)", "α (°)", ""}]
```


- SurfaceGraphics -

```
ContourPlot[ErrorFunction[a, α °], {a, 100, 300}, {α, 30, 120}, Contours → 15]
```
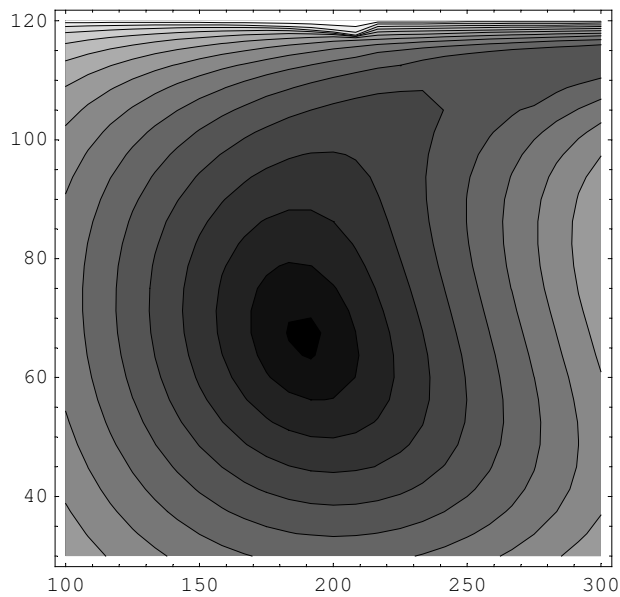

- ContourGraphics -

■ **Find a minimum in ErrorFunction varying a and α in a specified range {start,min,max}. Variables aMinimum and αMinimum contain the values of a, α corresponding to the minimum of ErrorFunction. Variabile ErrorMinimum contains the value of ErrorFunction calculated for aMinimum and αMinimum**

```
Minimum = FindMinimum[ErrorFunction[a, α], {{a, 160, 150, 250}, {α, 60 °, 30 °, 90 °}}]
(* position "2" is that of {a,α} *)

{3.22744, {a → 189.058, α → 1.16948}}


aMinimum = a /. Minimum[[2, 1]]
αMinimum = α /. Minimum[[2, 2]]

189.058

1.16948


ErrorMinimum = Minimum[[1]]
  (* this minimum is the std deviation in d-spacing, threfore in REAL space *)

3.22744
```

Intersection method for error calculation

■ **This method calculates the standard deviation as the differences between the single and the global error functions. The differences are summed quadratically and then divided by the number of spots. The result is a value δz that is summed to the minimum of ErrorFunction and gives zIntersec. A plane parallel to xy, z=zIntersec, intersecates the curve of ErrorFunction and defines a curve parallel to xy (see last graph): this curve represents the maximum variations of parameters a ed α that determine the error.**

■ **Calculate the differences between the global and the single error functions**

```
Deviation = Range[Spots] ; (* creates and initialise list Deviation *)

For[i = 1, i ≤ Spots,
Deviation[[i]] =
  Abs[SpotErrorFunction[aMinimum, αMinimum][i] - ErrorFunction[aMinimum, αMinimum]];
(*Print[i," ",Deviation[[i]]]*)
i ++]
```

- **Quadratic sum of the deviations**

$$\delta z = \sqrt{\frac{1}{\text{Spots}} \sum_{i=1}^{\text{Spots}} \text{Deviation}[[i]]\^2}$$

3.94362

- **Intersecate curve ErrorFunction with a plane parallel to xy passing by a distance equal to Delta from the bottom of the curve. Intersectionin the two points corresponding to aMinimum and αMinimum.**

```
zIntersec = ErrorMinimum + δz;
aMax = a /. FindRoot[ErrorFunction[a, αMinimum] == zIntersec, {a, aMinimum}];
αMax = α /. FindRoot[ErrorFunction[aMinimum, α] == zIntersec, {α, αMinimum}];
aError = Abs[aMinimum - aMax];
αError = Abs[αMinimum - αMax] / °;
```
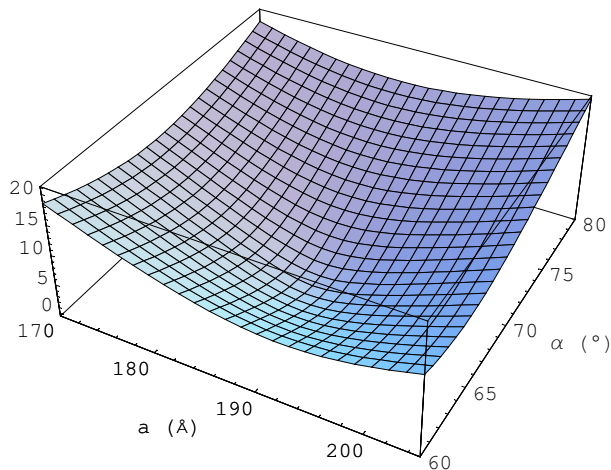
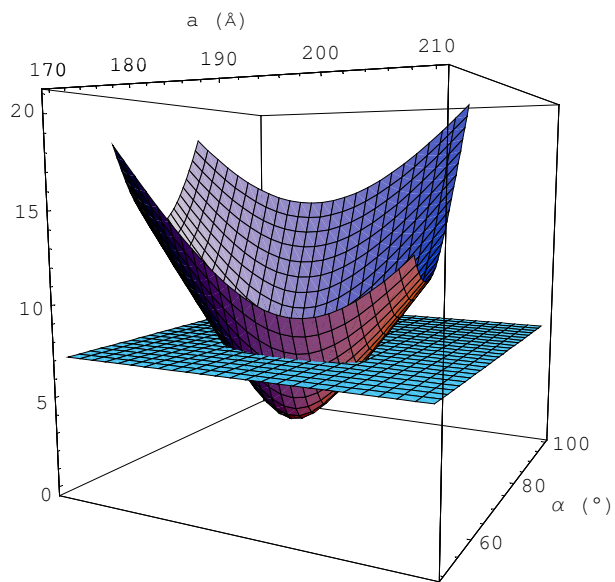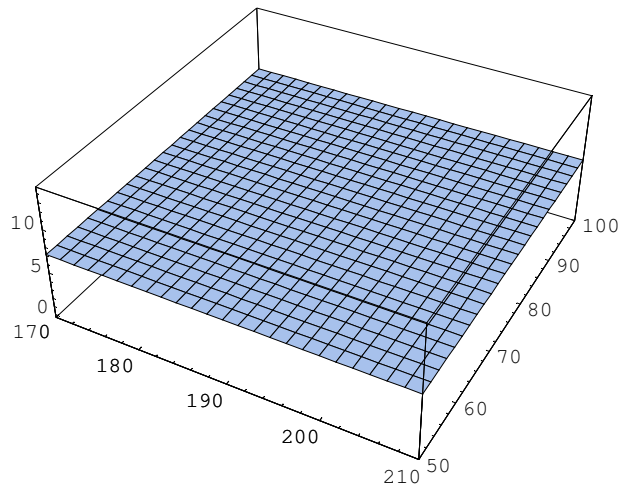## Solutions and graphs: ErrorFunction, zIntersec, intersection of the two

```
p1 = Plot3D[ErrorFunction[a, α Degree], {a, 170, 205}, {α, 60, 80},
    AxesLabel → {"a (Å)", "α (°)", ""}]; (* First graph is EfforFunction *)
p2 = Plot3D[zIntersec, {a, 170, 210}, {α, 50, 100}, ColorOutput → RGBColor];
(* second graph is zIntersec *)
Show[p1, p2, ViewPoint → {1, -2, 0.3}, BoxRatios → {1, 1, 1}]
```

Appendix B

Materials, self-assembly and biology

B.1 Better materials through biology

A notable example of a self-assembled biological system which is often addressed to when considering the synthesis of porous materials is diatom, a photosynthetic unicellular species of alga enclosed by a shell of silica (Figure B.1 a). The outer shell is made of porous silica: this architecture provides structural stiffness and permits the intake of nourishment through the interconnections between the pores. These siliceous architectures form through the self-assembly of proteins, which act as the structuring agents that regulate nucleation, growth, morphology and orientation of the inorganic silica particles from dilute solutions of silicic acid. In this case, the self-assembled structure serves as a template for the construction of a rigid inorganic framework with protective function. The skeleton that constituted the mineral framework of such living species sedimented at the bottom of the sea in the course of millions of years, and large deposits of diatomaceous earth emerged after geologic turmoil. This chalk-like sedimentary rock is now widely used in industry owing to its filtering properties, for example in sugar refining and in purification of water in swimming pools.[1]

In general, the formation of inorganic structures (oxides, sulfides, silica, carbonates and phosphates) that is directed by organic species in living organisms is called *biomineralisation*. This term includes all biochemical processes leading to the formation of mineralised parts in living organisms.[2] Although the starting point for the concentration and transformation of components in an aqueous medium to form crystals is generally assumed to be an aqueous solution containing dissolved ions, there is increasing evidence that clusters, nanoscale amorphous precipitates, and other complex precursors in the aqueous phase may play an important role in crystallisation.[3] Notable examples are the formation of skeleton, teeth, bones: all of these biological inorganic structures can be considered to form through self-assembly processes involving the assembly of inorganic precursors guided by macromolecules such as collagen, glycoproteins, chitin and polysaccharides.[4]

Nature abounds in biomineralised self-assembled systems, whose architectures have been optimised in millions of years in order to ensure the best functional (e.g. optical and chemical sensing) and structural (e.g. housing, motion) properties, with the least expenditure in terms of biological raw materials. Essentially, the optimisation of these properties served to enhance the chances of survival, therefore they

were slowly refined by evolution. An interesting example is nacre (mother-of-pearl), whose shells are made of hard thick plates of aragonite and calcite intercalated with thin and soft stress-dissipating protein β-sheets. This particular "brick and mortar" composite structure renders fracture toughness 1000 times higher than regular calcite crystals (Figure B.1 b) and can be exploited for anything that needs to be lightweight and fracture-resistant. Since organisms have spent millions of years optimising structural materials for better performances, materials scientists interested in the design of functional materials should be curious about the smart solutions that nature provided to problems which are similar to those they have to cope with daily.

Nature can thus drive inspiration for the synthesis of new materials. Given the countless range of existing biological architectures, it should be clear that the study of biomineralisation and other self-assembly processes in nature could enable us to formulate new strategies towards the synthesis of novel structural and functional materials.

Because biological processes occur generally in very mild conditions (i.e. in aqueous solvents, at ambient temperature and pressure and with low precursor concentrations) they can be imported into the chemistry lab in what is commonly referred to as *soft chemistry*, i.e. involving chemical reactions at ambient temperature and pressure, starting from molecular or colloidal precursors. Such an approach to synthesis, inspired by the study of natural phenomena and taking advantage of natural principles, goes under the name of *biomimetic approach*.[5,6] In fact, the aim of *biomimicry* is not quite to copy a process or an architecture already existing in nature or merely synthesise a material from biological templates, but to get inspiration and to use the knowledge derived from the study of natural systems as a guide for the design of new syntheses, materials, architectures. Inspiration arises from recognising the analogies between the way biology assembles materials with a particular function, as in the case of the nacre mentioned previously, and the way we can portend to similar things through materials chemistry in order to fabricate materials with well-designed structures, properties and functions. In this sense, it would be more correct to speak of *bio-inspired* materials chemistry, rather than biomimetic.[7]

Being inspired by the study of nature is not a new concept. Leonardo da Vinci
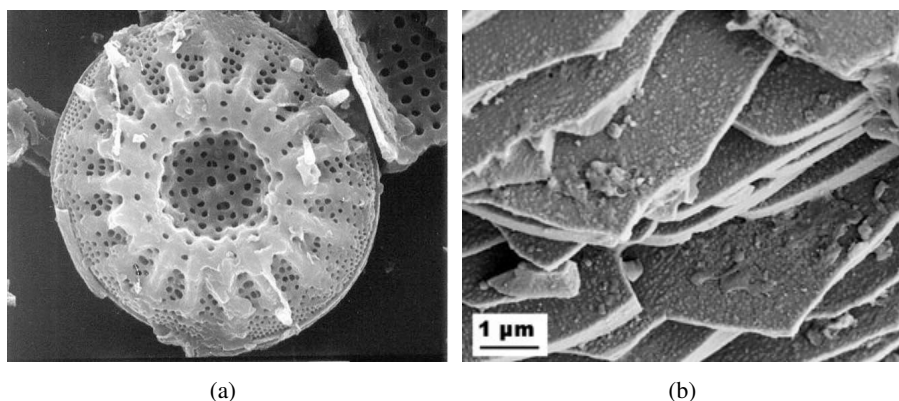

(a)   (b)

Figure B.1. *(a) SEM image of a diatom. (b) SEM image of the brick-and-mortar structure of a nacre.*

used to study natural phenomena and animal anatomy, upon which he based the construction of his machines and engineering works. However, it is only in the last decades that a deep awareness has arisen, that nature can offer countless models which we can turn to for inspiration. The pioneering works by Pieter Harting in 1873[8] and D. W. Thompson in 1917[9] are generally considered to be the first works where biomineralisation processes were described in detail and direct observations were reported on the shape of microscopic organisms in the successful attempt to explain the morphogenesis of biominerals. In particular, Dutch zoologist and microscopist Pieter Harting succeeded in making perfect replicas of some natural calcareous forms by reacting calcium and carbonate salts in biological media like albumen and gelatin, thus discovering that natural architectures were not merely inorganic in their origin. Thanks to the discovery that these structures could be synthesised in the laboratory, Harting's work is considered to mark the beginning of biomimetic inorganic chemistry.

B.2 Self-assembly in biology

Self-assembly is a process of paramount importance in biological systems, because it lies at the basis of the formation and the evolution of biological systems. For example, cell walls are bilayer membranes built by the self-assembly of biological amphiphilic polymers called phospholipids. Another remarkable example is the synthesis of proteins within the cell: ribosomes are synthesising units that build different types of proteins (multi-purpose elements that serve as structural units, signalling agents, enzymes, etc.) in a self-assembling process encoded in the different portions of DNA. In its essence, a DNA code is transcribed into RNA, then RNA is decoded by transfer RNA (^{t}RNA) molecules, which bear conjugate amino acids. These loaded ^{t}RNA molecules dock into the ribosome, and add their amino acid molecules one by one to the growing polypeptide chain which constitutes the protein. These can be considered self-assembly processes in that they are not driven by external forces and lead to an ordered functional structure.

In Chapter 5 we have described two phenomena occurring during the synthesis of mesostructured HfO_2 films: (1) a disorder-to-order transition of the mesophase induced by atmospheric humidity, (2) mesostructure disruption upon exposure to X-rays. These two phenomena are reversibile as long as inorganic condensation does not hinder mesophase rearrangements: changing relative humidity to high and low values in the deposition chamber causes the mesostructure to self-organise and disrupt, respectively; X-rays cause the disruption of the ordered mesostructure, which is restored when the radiation is turned off. These properties can be thought as a (much simpler) synthetic equivalent of the reversibility property of a living organism: once the external perturbation is over, the system returns to the initial equilibrium state. Even if these restoration phenomena are much more complex in living systems than in the mentioned experiments, it is interesting to compare the self-organisation behaviours in these two systems. After all, an outlook on the properties of self-organising systems can drive inspiration for new materials.

Many properties of biological systems (e.g. adaptability, reproduction, nourishing) are possible due to the labile character of the bonds in self-assembled units (typically, weak interactions such as electrostatic forces and Van der Waals interactions). Weak bonds can be broken with little energetic expenditure and reform with as little amount of energy, in order to adapt to the new thermodynamic equilib-

rium conditions. As a consequence, several properties of biological systems can be traced back to the general properties of self-assembled systems. Let us consider as an example the self-healing property of a living organism that intervenes when its internal organisation is somehow disrupted by an external agent. Self-healing corresponds to the *reversibility* property of a self-assembled system, which shows the tendency to return to its original state once the perturbation from the environment has ceased.

A living system is clearly much more complex than a self-assembled system obtained in the laboratory. Furthermore, a living structure is always *far* from thermodynamic equilibrium. This apparent contradiction can be solved considering self-assembly as a dynamic process, where a metastable ordered state is maintained through the supply of energy from the environment in the form of food and the elimination of metabolic products. Therefore, self-assembly can be classified as either *static* or *dynamic*. In static self-assembly the ordered state forms as the system approaches equilibrium, reducing its free energy, whereas in dynamic self-assembly forming and maintaining the ordered state requires dissipation of free energy but not an approach to equilibrium.

Stretching this definition of dynamic self-assembly to include the phenomena related to self-organisation, we get to the bottom line: what are we, if not dynamic self-assembled and self-organised systems, striving to stay out of thermodynamic equilibrium as long as we can?

References

[1] F. E. Round, R. M. Crawford. *The diatoms. Biology and morphology of the genera.* Cambridge University Press, UK, 1990.

[2] S. Mann. *Biomineralization. Principles and concepts in bioinorganic materials chemistry.* Oxford University Press, Oxford, 2001.

[3] A. Navrotsky. Energetic clues to pathways to biomineralization: Precursors, clusters, and nanoparticles. *Proc. Natl. Acad. Sci U.S.A.*, **2004**, *101*, 12096–12101.

[4] H. Colfen, S. Mann. Higher-order organization by mesoscale self-assembly and trasformation of hybrid nanostructures. *Angew. Chem. Int. Ed. Engl.*, **2003**, *42*, 2350–2365.

[5] S. Mann, S. L. Burkett, S. A. Davis, C. E. Fowler, N. H. Mendelson, S. D. Sims, D. Walsh, N. T. Whilton. Sol-gel synthesis of organized matter. *Chem. Mater.*, **1997**, *9*, 2300–2310.

[6] C. Sanchez, H. Arribart, M. M. Giraud Guille. Biomimetism and bioinspiration as tools for the design of innovative materials and systems. *Nature Materials*, **2005**, *4*, 277–288.

[7] E. Dujardin, S. Mann. Bio-inspired materials chemistry. *Adv. Mater.*, **2002**, *14*, 775–788.

[8] P. Harting. *Natuurkd. Verh. Koninkl. Acad.*, **1873**, *13*, 1.

[9] D. W. Thompson. *On growth and form.* Dover Publications, New York, 1992.

Appendix C

Publications and collaborations

C.1   Publications in peer-reviewed journals

[1] P. Falcaro, S. Costacurta, G. Mattei, H. Amenitsch, A. Marcelli, M. Cestelli Guidi, M. Piccinini, A. Nucara, L. Malfatti, T. Kidchob, P. Innocenzi. Highly ordered "defect-free" self-assembled hybrid films with a tetragonal mesostructure. *J. Am. Chem. Soc.*, **2005**, *127*, 3838–3846.

[2] P. Innocenzi, L. Malfatti, T. Kidchob, P. Falcaro, S. Costacurta, M. Guglielmi, G. Mattei, V. Bello, H. Amenitsch. Thermal-induced phase transitions in self-assembled mesostructured films studied by small-angle X-ray scattering. *J. Synchrotron Rad.*, **2005**, *12*, 734–738.

[3] D. Buso, P. Falcaro, S. Costacurta, M. Guglielmi, A. Martucci, P. Innocenzi, L. Malfatti, V. Bello, G. Mattei, C. Sada, H. Amenitsch, I. Gerdova, A. HachÃ©. PbS-doped mesostructured silica films with high optical nonlinearity. *Chem. Mater.*, **2005**, *17*, 4965–4970.

[4] L. Malfatti, T. Kidchob, S. Costacurta, P. Falcaro, P. Schiavuta, H. Amenitsch, P. Innocenzi. Highly ordered self-assembled mesostructured hafnia thin films: An example of rewritable mesostructure. *Chem. Mater.*, **2006**, *18*, 4553–4560.

[5] P. Innocenzi, L. Malfatti, T. Kidchob, S. Costacurta, P. Falcaro, M. Piccinini, A. Marcelli, P. Morini, D. Sali, H. Amenitsch. Simultaneous in-situ and time-resolved infrared and small angle X-ray scattering analysis. *J. Phys. Chem. C*, **2007**, *111*, 5345–5350.

[6] L. Malfatti, T. Kidchob, P. Falcaro, S. Costacurta, M. Piccinini, M. Cestelli Guidi, A. Marcelli, A. Corrias, M. F. Casula, H. Amenitsch, P. Innocenzi. Highly ordered self-assembled mesostructured membranes: porous structure and pore surface coverage. *Microp. Mesop. Materials*, **2007**, *103*, 113–122.

[7] S. Costacurta, L. Biasetto, E. Pippel, J. Woltersdorf, P. Colombo. Hierarchical porosity components by infiltration of a ceramic foam. *J. Am. Cer. Soc.*, **2007**, *90*, 2172–2177.

[8] S. Costacurta, L. Malfatti, P. Falcaro, P. Innocenzi. Photocurable silica hybrid organic-inorganic films for photonic applications. *J. Sol-Gel. Sci. Technol.*, **2007**, *44*, 59–64.

[9] P. Falcaro, S. Costacurta, L. Malfatti, T. Kidchob, M. F. Casula, M. Piccinini, A. Marcelli, B. Marmiroli, H. Amenitsch, P. Schiavuta, P. Innocenzi. Fabrication of mesoporous functionalized arrays by integrating deep X-ray lithog-

raphy with dip-pen writing. *Adv. Mater., in press.*

[10] M. Mazaj, S. Costacurta, N. Zabukovec Logar, G. Mali, N. Novak Tusar, P. Innocenzi, L. Malfatti, F. Thibault-Starzyk, H. Amenitsch, V. Kaučič, G. Soler-Illia. Mesoporous aluminophosphate thin films with cubic pore arrangement. *Submitted to Langmuir.*

[11] S. Costacurta, L. Malfatti, P. Innocenzi, H. Amenitsch, A. Masili, A. Corrias, M. F. Casula. Confined growth of iron cobalt nanocrystals in mesoporous silica thin films: FeCo-SiO$_2$ nanocomposites. *Submitted to Micropor. Mesopor. Mater.*

[12] P. Innocenzi, L. Malfatti, S. Costacurta, T. Kidchob, M. Piccinini, A. Marcelli. Evaporation of ethanol and ethanol-water mixtures studied by time-resolved infrared spectroscopy. *Submitted to J. Phys. Chem. A.*

C.2 Ongoing collaborations

The following collaborations were developed thanks to the research work done at the Laboratory led by Prof. Plinio Innocenzi in Alghero (University of Sassari, Sardinia). I am much indebted to the following persons for exciting work done together, interesting discussion and good time spent together.

Heinz Amenitsch, Benedetta Marmiroli: Institute of Biophysics and Nanosystems, Graz, Austria

Paolo Falcaro, Piero Schiavuta, Paolo Scopece: CIVEN, Coordinamento Interuniversitario Veneto per le Nanotecnologie, Venezia

Masahide Takahashi: Institute for Chemical Research, Kyoto University, Japan

Maria Francesca Casula: Dipartimento di Scienze Chimiche, Università di Cagliari

Galo Soler-Illia: Unidad de Actividad Química, CNEA, Buenos Aires, Argentina

Matjaz Mazaj: National Institute of Chemistry, Ljubljana, Slovenia

David Grosso, Florence Babonneau: Laboratoire de Chimie de la Matière Condensée, Université Pierre et Marie Curie, Parigi, France

Michele Maggini: Dipartimento di Chimica Organica, Università di Padova

Massimo Piccinini, Augusto Marcelli: INFN Istituto Nazionale di Fisica Nucleare, Laboratori Nazionali di Frascati, Roma

Diego Sali: Bruker Optics, Milano

Bruno Alonso: CRMHT, Centre de Recherche sur les Matériaux à Haute Température, CNRS Orléans, France

```
(\/)
(0.o)
(> <)
```

Ringraziamenti

Moltissime persone incontrate nel corso di questi tre anni di dottorato hanno dato un contributo alla mia formazione professionale e personale—ciascuno a proprio modo, nel bene e nel male.

Prima di tutti, ringrazio di cuore il papà e la mamma per essere sempre stati al mio fianco incondizionatamente e per avermi assecondato nelle mie scelte. Grazie inoltre a tutta la mia famiglia ed i parenti (fratello, nonno, zii, cugini).

Grazie ad una persona speciale, per ~~avermi sopportato~~ essere stata sempre al mio fianco e per aver appoggiato le mie scelte, specialmente in questo lungo anno ad Alghero. Grazie, Vale!
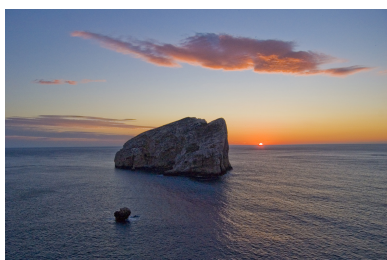
Capo Caccia, Alghero.

Ringraziamenti molto sentiti vanno a coloro che in tutti questi anni (tesi + dottorato) mi sono stati più vicini, ovvero ~~Bizarre e Male Peloso~~ Luca e Paolo. Un ringraziamento speciale va a Plinio, che è stato un faro di riferimento in tempi bui, grazie per aver creduto in me ed avermi offerto la possibilità di svolgere parte del mio lavoro ad Alghero. Con tutti voi, spero di continuare la amicizia e la collaborazione per altre avventure (*espandersi o morire!*). Ringrazio poi le persone incontrate ad Alghero e dintorni: Tongjit, Sonia, Angela, Roberta, Maria Francesca, Stefania, Cristiana, Vanna, Barbara (ah, le sarde!!). In particolare, grazie a Masa per avermi insegnato molte cose sulla scienza, oltre ~~al gergo scurrile~~ alle espressioni basilari della lingua giapponese («Anata wa okama sensei des ka?»). Ed ecco una persona senza la quale avrei odiato Elettra: grazie al buon Heinz e a tutto lo staff della beamline SAXS ad Elettra, per le notti insonni ad Elettra e ovviamente per le abbuffate da Mahnič.

Grazie a Massimo per avermi concesso la possibilità di svolgere il dottorato di ricerca presso l'Ateneo padovano. A Padova, i miei ringraziamenti sono dovuti a Paolo e Lisa, Giovanni e Valentina, Michele, Ilaria, per gli interessanti lavori fatti insieme.

Beamline scientist feeding user.

Un ringraziamento sentito va alla top list dei mesoporosi: in primis il mitico Galo (King of ~~Maricones~~ Mesoporous) per il suo contagioso entusiasmo; l'inafferrabile David; il biblico Jeff per le conversazioni molto intriganti a Montpellier. E tutte le persone con cui ho collaborato e in alcuni casi stretto amicizia: Jack l'australiano, Alex l'americano, Massimo, Matjaz. Infine, grazie a Luca e tutto lo staff capeggiato dal Signor Male (!). Grazie a Giacomo per aver stampato questa tesi. Grazie al consorzio Cosmolab per aver finanziato ~~i miei numerosi voli di Stato~~ le mie ricerche.

–Ste